Structural and Magnetic Properties of Indium Substituted Nickel-Zinc Ferrites Synthesized via Reverse Micelle Technique

by

Sangeeta Thakur

A THESIS SUBMITTED IN THE FULFILLMENT OF THE REQUIREMENTS

FOR THE DEGREE OF

DOCTOR OF PHILOSOPHY

IN

PHYSICS

JAYPEE UNIVERSITY OF INFORMATION TECHNOLOGY
WAKNAGHAT, H.P. (INDIA)
Feb. 2010

DEDICATED
TO MY
LOVING PARENTS
&
SISTER

Jaypee University of
Information Technology
Waknaghat-173 215
Solan, Himachal Pradesh
Phone No.: 91-1792-239227
Fax No.: 91-1792-245362

CERTIFICATE

This is to certify that the Ph.D. thesis titled **"Structural and Magnetic Properties of Indium substituted Nickel-Zinc Ferrites Synthesized via Reverse Micelle Technique"** submitted to Department of Physics Jaypee University of Information Technology, contains the bonafied record of the work carried out by Ms. Sangeeta Thakur, who has completed the necessary work for her degree of **Doctor of Philosophy in Physics.** Candidate carried out the work reported in this thesis under our joint supervision and guidance. This work has not been submitted for any other degree or diploma.

Date: 16 Feb., 2010

Prof. (Dr.) S. C. Katyal
Head
Department of Physics

Prof. (Dr.) Mahavir Singh
Department of Physics
Shimla-171005

ABSTRACT

Work presented in this thesis describes studies on structural, magnetic and Mössbauer spectroscopy characterization on nano and bulk samples of pure nickel-zinc ferrite having basic composition $Ni_{0.58}Zn_{0.42}Fe_2O_4$ and indium doped nickel-zinc ferrite ($Ni_{0.58}Zn_{0.42}In_xFe_{2-x}O_4$, x = 0.1, 0.2, 0.3) samples. Nano ferrite particles have been prepared by reverse micelle technique. Bulk samples in this study are prepared by annealing the reverse micelle synthesized nanoparticles at high temperature 1473 K. Prepared bulk and different size nanoparticles have been characterized using X-ray diffraction (XRD), transmission electron microscopy (TEM) and Fourier transform infrared spectroscopy (FTIR) studies. ^{57}Fe Mössbauer measurements have been made in the temperature range from 5-300 K for determining the cation redistribution and hyperfine parameters. For studying the magnetic behavior dc magnetization have been performed using vibrating sample magnetometer and SQUID magnetometer, whereas to study the dynamic behavior ac susceptibility measurements have been performed.

A brief description of the thesis, which has been divided into seven chapters, is given below. General introduction of ferrite and their classification, historical development of ferrite, their nano particles and the addition of metal impurities to ferrite particles is described in chapter 1. A brief introduction of general properties of ferrite nanoparticles has also given. Various applications of ferrite particles, motivation and objective of the thesis have also been included in this chapter.

Chapter 2 presents the theoretical concepts used/developed in this work. Various models have been described to understand the magnetism of ferrite and nanoferrite particles. A brief description of technique used for preparation of nanocrystalline ferrite samples is included.

Chapter 3 describes the various experimental techniques used for the preparation and characterization of nano and bulk samples.

Chapter 4 focuses on the study of structural properties of nano and bulk samples using X-ray diffraction, transmission electron microscopy and fourier transform infrared spectroscopy measurements.

Chapter 5 includes the experimental results and observations obtained by Mössbauer spectroscopy. Effect of indium concentration, particles size and temperature

on the Mössbauer parameters of nickel-zinc ferrite sample has been described. A comparative study on nano and bulk samples has also been illustrated.

Chapter 6 describes magnetic properties of nano and bulk samples using super conducting quantum interference device (SQUID) magnetometer, vibrating sample magnetometer (VSM) and ac susceptometer. Effect of particle size and indium concentration on the magnetic properties of nickel-zinc ferrite particles has been described. The thermal variation of magnetization in high fields in terms of a modified Bloch's law, the role of interactions on the static and dynamic properties of nano samples have also been discussed.

Chapter 7 represents the summary and conclusions obtained through various studies. Suggestions for the future work on the samples studied have been included in this chapter.

List of Publications

(1) **Sangeeta Thakur**, S. C. Katyal, M. Singh "Improvement in electric and dielectric properties of nano ferrites synthesized via reverse micelle technique" published in **Applied Physics Letters, 2007**, vol. 91 Iss. 26, pp. 262501-03.

(2) **Sangeeta Thakur**, S. C. Katyal, M. Singh "Structural and magnetic properties of nano nickel- zinc ferrite synthesized by reverse micelle technique" published in **Journal of Magnetism and Magnetic Materials**, **2009** vol. 321, pp. 1-7.

(3) **Sangeeta Thakur**, S. C. Katyal, A. Gupta, V. R. Reddy, M. Singh "Room temperature ferromagnetic ordering in indium substituted nano nickel zinc ferrite" published in **Journal of Applied Physics**, **2009,** vol. 105, pp 1**.**
Also selected by virtual Journal of Nanoscience and Technology.

(4) **Sangeeta Thakur**, S. C. Katyal, A. Gupta, V. R. Reddy, S. K. Sharma, M. Knobel, M. Singh "Nickel-zinc ferrite from reverse micelle process: structural and magnetic properties, Mössbauer spectroscopy characterization" published in **Journal of Physical Chemistry C**, **2009**, vol. 113, pp. 20785-20794.

(5) **Sangeeta Thakur**, S. C. Katyal, A. Gupta, V. R. Reddy, M. Singh "Characterization of magnetic nano materials by Mössbauer spectroscopy" **IOP Conference Series** in press**.**

Presentations in Conferences/Workshop:

(1) B. S. Chauhan, Gagan Kumar, Satish Verma, **Sangeeta Thakur**, S. C. Katyal, M. Singh, "Low temperature processing and enhancement of electrical properties of mixed Mg-Mn ferrites" presented at **DAE-SSP** Symposium **BARC** Mumbai from 5-9 Dec., **2005.**

(2) **Sangeeta Thakur**, Meenakshi Kanthwal, S. C. Katyal, M. Singh, "Effect of oxidising agent on magnetic and electrical structural properties of nano Mn-Zn ferrites" presented at **Indo-Singapore symposium** at **IIT Bombay** from 24-26 Feb., **2006.**

(3) **Sangeeta Thakur**, S. C. Katyal, M. Singh, "Superparamagnetic properties of nano Ni-Zn ferrite synthesized via reverse micelle technique" presented at 52nd DAE Solid State Physics Symposium at **University of Mysore**, from 27-31 Dec., **2007**.

(4) **Sangeeta Thakur,** S. C. Katyal**,** M. Singh, "Effect of indium substitution on magnetic properties of nano nickel zinc ferrite" presented in 53rd DAE Solid State Physics Symposium **at DAE-SSP** Symposium **BARC** Mumbai from 16-20 Dec., **2008.**

(5) **Sangeeta Thakur,** S. C. Katyal, M. Singh, "Structural and Magnetic properties of indium doped nano nickel-zinc ferrite synthesized by reverse micelle Technique"

presented in International conference on magnetic materials and their applications for 21st century at NPL **DELHI INDIA** from 21-23 Oct., **2008**.

(6) **Sangeeta Thakur**, S. C. Katyal, A. Gupta, V. R. Reddy, M. Singh, "Room temperature ferromagnetic ordering in indium substituted nano nickel zinc ferrite" presented in International conference on Magnetism and magnetic material at **AUSTIN, TEXAS, USA** from Nov. 10-14, **2008.**

(7) **Sangeeta Thakur,** Patrick Quéffélec, Jean Löaec Mattei, M. Singh, S. C. Katyal, "Technological role of indium in nickel-zinc nano ferrites synthesized via reverse micelle technique" presented in International conference on multifunctional oxide materials at **Himachal Pradesh University Shimla**, April 16-18. **2009.**

(8) **Sangeeta Thakur**, S. C. Katyal, A. Gupta, V. R. Reddy, M. Singh, "Characterization of indium doped nano nickel-zinc ferrite by Mössbauer spectroscopy" presented in workshop on oxide materials **IUAC Delhi** from 12-13th May, **2009**

(9) **Sangeeta Thakur**, S. C. Katyal, A. Gupta, V. R. Reddy, M. Singh, "Characterization of Magnetic Nano Materials by Mössbauer Spectroscopy" presented in International conference on the application of Mössbauer effect at **AUSTRIA Vienna** from **19-24 July**, **2009**.

(10) **Sangeeta Thakur**, S. C. Katyal, A. Gupta, V. R. Reddy, M. Singh, "Nickel-zinc-indium ferrite: magnetic properties and Mössbauer Spectroscopy Characterization" presented in International conference on electroceramics at Delhi University from **Dec. 13-17**, **2009.**

CONTENTS

LIST OF TABLES

LIST OF FIGURES

CHAPTER 1

INTRODUCTION

Magnetism and magnetic materials have a long and illustrious history. In the modern era magnetism influences many aspects of our lives. Magnetic materials and magnetic phenomenon inconspicuously appear in many complex devices. One of such well known magnetic material family is ferrite.

1.1 Ferrites

"*Ferrites represent a class of magnetic materials with a plethora of fascinating, intrinsic functionalities. The intriguing interplay of charge, spin, and orbital ordering in these systems superimposed by lattice effects opens a scientifically rewarding playground for both fundamental and application-oriented research. In particular, the possibility of externally modifying the properties of these complex oxides and thus potentially generating novel practical applications opens a new perspective*."

Ferrites are the mixed metal oxides containing iron oxide as their main component. Though, ferrites are known to exist since hundreds of years, the research in ferrites was initiated at the end of Second World War. Kato & Takei [1], Kawai [2] and Snoek [3] were the first to start work on ferrimagnetic materials. In 1945 Snoek [4] laid the foundation of the science and technology of ferrites. The paper by Néel in 1948 [5] in which theory of a new class of magnetic materials, ferrimagnets, was put forward, initiated a great stream of experimental and theoretical investigations of ferrites and other ferrimagnets. Ferrite possesses good magnetic properties along with very high d.c. resistivity [6]. Among various magnetic materials, ferrites are the best in high frequency circuits and they cannot be replaced by other magnetic elements. In addition, they are relatively inexpensive. Ferrites have found wide applications as effective magnetic materials in radio engineering, microwave technology and some other fields of technology. They are extensively used as core materials for inductances and transformers in telecommunication industry, audio and video recording heads, memory devices, digital systems, tapes and electronic devices which are operated from low to high frequency range. The increasing demand due to the specific applications of ferrites have changed remarkably and kept pace with the developments in electronic technologies. Therefore, the diversity of applications make ferrites an active area of research. It is well known that changing its composition or the method or condition of preparation could modify the

properties of ferrites. Materials science and technology have been steadily applied to improve properties as well as new products by appropriate choice of composition and method of preparation.

1.1.1 Classification of ferrites

Depending on the nature of magnetic behavior of the ferrite materials, they are classified into two broad categories, soft ferrites and hard ferrites. Soft ferrites are easy to magnetize and demagnetize and have low coercive fields. Hard ferrites retain their magnetization once they are magnetized, having large coercive field and are used for permanent magnet. Soft ferrites are used to construct electromagnet. The characterization of soft and hard ferrites in general is based upon some important factors like:

(a) The residual magnetism (remanence/coercivity), M_R that the material retains when the external magnetic field is removed.

(b) The saturation flux or the maximum magnetic field that can be induced in the materials i.e., saturation magnetization M_s.

(c) The demagnetization field or the value of the external magnetic field applied in the negative direction that removes the residual magnetic field i.e. coercive force H_c [7].

Taking into the crystal structure and the magnetic ordering, ferrites can be grouped into four different categories [8] namely spinel, garnet, magnetoplumbite and ortho ferrites (Table 1.1).

Table 1.1 Different types of ferrites with their structures, chemical formula and examples

Type	Structure	General Formula	Examples
Spinel	Cubic	MFe_2O_4	M = Ni, Zn, Mn Mg, Cu, Co, Li
Garnet	Cubic	$Ln_3Fe_3O_{12}$	Ln = Y, Sm, Eu, Gd Tb, Dy, Ho, Er
Magnetoplumite	Hexagonal	$MFe_{12}O_{19}$	M = Ba, Sr
Orthoferrite	Pervoskite	$LnFeO_3$	Ln = same as in garnet

The spinel ferrites are named after the naturally occurring mineral spinel, having the chemical formula $MgAl_2O_4$ and the general chemical formula written as MFe_2O_4, where M is a divalent transition metal or a suitable combination of these ions. The spinel lattice is composed of a close packed oxygen arrangement in which 32 oxygen ions form the unit cell (the smallest repeating unit in the crystal network). These anions are packed in a face centered cubic (FCC) arrangement leaving two kinds of spaces between anions: tetrahedrally coordinated sites (A), surrounded by four nearest oxygen atoms, and octahedrally coordinated sites (B), surrounded by six nearest neighbor oxygen atoms. These are illustrated in figure 1.1. In total, there are 64 tetrahedral sites and 32 octahedral sites in the unit cell, of which only 8 tetrahedral sites and 16 octahedral sites are occupied, resulting in a structure that is electrically neutral [9,10].

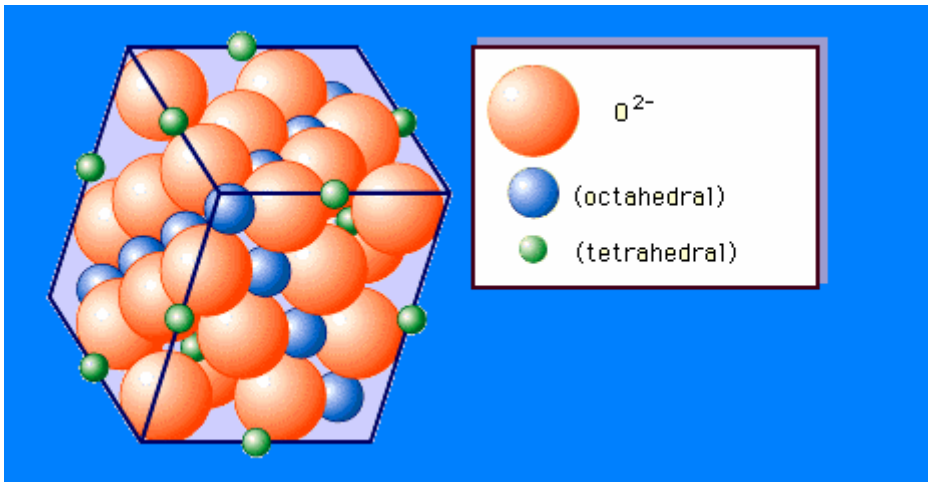

Figure 1.1 *Schematic of two subcells of a unit cell of the spinel structure, showing octahedral and tetrahedral sites*

The localization of ions either in the tetrahedral or octahedral sites depends fundamentally on the ion and lattice sizes. Also it has been observed to depend on the temperature and the orbital preference for specific coordination. The ionic distribution of this kind of structure may be represented by eqn. (1.1)

$$(M_x^{2+} Fe_{1-x}^{3+}) [M_{1-x}^{2+} Fe_{1+x}^{3+}] O_4^{2-} \quad \text{.....(1.1)}$$

where the cations enclosed by parenthesis occupy tetrahedral sites comprising the tetrahedral sublattice, while the cations enclosed by the square bracket occupy octahedral sites comprising the octahedral sublattice and x is the inversion parameter and x = 0 and 1 stand for the inverse and normal spinel and for mixed spinel, $0 < x < 1$. The factors, which

can influence the distribution of the metal ions over tetrahedral and octahedral sites: the electronic configuration of the metal ions, the ionic radii and the electrostatic energy of the spinel lattice and more recently the preparation condition [11,12].

1.2 Nanoferrites

Nanoscience is an ever expanding field of scientific research that involves materials that have at least one dimension in the nanometer size regime. What is usually termed "Nanostructured systems" mainly comprises those materials, whose properties are determined by entities (particles, crystallites or clusters) with characteristic lengths between 1 to 100 nm in at least two dimensions. The field of nanoscience encompasses various types of materials such as thin films (1 dimensional), nanotubes (2 dimensional), and nanoparticles (3 dimensional). Nanosized materials can display enhanced surface and size dependent properties. Although the unique properties of nanosized materials have been known as far back as 1700's (e.g. Venetian glass blowers used colloidal gold to produce a red color), recognition of size related properties was not achieved until the past 60 years. It is the pursuit of novel size related properties that fuels nanoscience research. Nanostructured materials represent a fast evolving application of recent research in physics and chemistry. Among the most promising nanomaterials being developed are magnetic nanomaterials including magnetic nanoparticles and magnetic nanosensors.

In recent years the scientific literature has been replete with reports of magnetic nanoparticle synthesis, properties and novel applications [13,14]. This has largely been driven by the hope, and in some instances realization, of surface enhanced properties. By producing materials on the nanoscale, there exists the possibility that surface based properties (e.g. catalysis and reactivity), magnetism, and electronic properties may be enhanced. In most nanoparticulate materials, and specifically in the case of metal oxides, there are several properties can be influenced by the particle size.

In nanoparticle systems the surface disorder can influence the lattice symmetry and cell parameters throughout the particle due to the limitation in the size of the particle itself [15,16]. The thermodynamic stability can also change due to decreasing size and this in turn can induce modification of the cell parameters and/or structural

transformations. Structures that are not stable in the bulk can be at the nanoscale range; for example γ-Al_2O_3 [17], MoO_x oxides [18] and $BaTiO_3$ [19].

In case of magnetic nanoparticles, the disruption in crystal structure at the surface can greatly influence the magnetic properties [20,21]. The truncation of the lattice at the surface weakens exchange interactions, and in many cases reduces coupling with neighboring particles. In particular, for magnetic oxide systems such as spinel ferrites the magnetic exchange is dependent on the cation-anion-cation bond angles that are affected by the surface truncation. The bond bending commonly experienced on surfaces can produce profound changes in the magnetic properties of nanoparticles and the solids based on these particles [22,23].

Interest in nanosized spinel ferrites has greatly increased in the past few years due to their importance in understanding the fundamentals in nanomagnetism [24] and their wide range of applications such as high-density data storage, ferrofluid technology, sensor technology, spintronics, magnetocaloric refrigeration, heterogeneous catalysis, magnetically guided drug delivery and magnetic resonance imaging [14,24-27]. The physics of nanoscale magnetic particles is an area of enduring interest. From a fundamental perspective the study of nanoparticles sheds light on how bulk properties transforms to atomic as size decreases. In fact, the behavior of bulk magnetic materials is determined and influenced by the formation of domains and domain wall movement. The magnetic behavior of bulk materials is complicated by the fact that domain wall moment can be impeded or pinned by impurities, grain boundaries, etc. due to this; a direct correlation between the observed magnetic behavior and the quantum origins of magnetism is not readily achievable. However, if the size of the magnetic materials is decreased below a critical characteristic length, domain formation is no longer energetically favored and the particles behave like single domains [28]. Moreover, the large surface fraction opens the opportunity for manipulation of properties via interfacial interaction. Knowledge of these fundamental properties is essential for creative use of nanoparticles in important technical applications [29-33].

Magnetism is the result of inert-atomic exchange and in case of nanoferrites, this requires well defined bond angles and lengths, and hence, the particles must be crystalline. A successful synthetic technique for this system should produce particles that

are single crystallites. The surface of any crystallite, however, by its very nature is disordered. An amorphous outer layer of the particles may be detrimental to the magnetic properties. In systems such as core shell nanoparticles minimizing the effect of the "amorphous layer" may be important not only from a chemical point of view, but also in terms of enhancing the magnetic properties.

Many disciplines including biology, physics, chemistry and engineering are pursuing a wide variety of methodologies for producing nanomaterials. To carefully study and exploit the potential and possibilities associated with nanomaterials, the key point is to create well-defined, monodisperse structures of predictable size, shape, crystallinity, and morphology through a straightforward synthesis. As is well known, in the preparation of nanocrystalline oxide samples, mainly following two approaches: (1) Top to bottom approach: physical methods (2) Bottom to top approach: chemical methods are followed.

Physical methods are commercially attractive because it is generally easier to produce larger volumes of product, but they tend to impact physical stresses in the materials which can require further processing and result in wider size distributions. The most popular physical methods are ball milling, laser pyrolysis and plasma torch. Chemical techniques are generally better for the synthesis of mixed cation nanoparticles because they can provide control over the particle stoichiometry, shape, size distribution, crystallinity and phase purity [13]. Numerous chemical methods have been developed that have proven viable for the synthesis of nanoparticles. The most popular chemical methods of synthesis of nanomaterials [34-40] include formation through a chimie douce solution chemistry methodology, a sol-gel processing mechanism, the use of microemulsions, the utilization of hydrothermal and solvothermal methods, the kinetic control of growth through the use of capping reagents, the application of template inspired methodologies, and lastly, biomimetic synthesis. These methods have their own set of advantages and disadvantages in terms of ease of preparation, duration of synthesis, extent of instrumentation required and also the availability of the precursors and their economic viability. In contrast to physical methods, which often require breaking a larger sample into smaller components, these methods grow particles from the constituent atoms. In general, these synthesis routes utilize some form of solution chemistry thereby

providing pathways to kinetically stable phases that can be different from those obtained using traditional bulk preparation methods [17-19,41]. As a result, chemical methods are sometimes used to produce a pre-cursor material which is then annealed to yield the final product.

Energy-efficient synthesis and processing routes of nanocrystalline spinel ferrites are prerequisite for technological applications [14]. Among many types of preparation and processing techniques, reverse micelles, which are essentially nanosized aqueous droplets that exist in microemulsions with certain compositions, are known to present an excellent medium for the synthesis of nanoparticles [42-44]. It is the inherent ability of this reaction system to control the size and size distribution that makes it attractive for the synthesis of nanoparticles [45].

As magnetic materials, soft ferrites are best suited for high frequency applications. Among soft spinel ferrites nickel-zinc ferrites are found to be very attractive and versatile magnetic materials, which have applications in both low and high frequency devices and play significant role in technological applications such as microwave devices, power transformers in electronics, rod antennas, read/write heads for high speed digital tapes etc. because of their high resistivity [46], low dielectric losses, high curie temperature and chemical stability. Structural and magnetic properties of nickel-zinc ferrites are highly sensitive to composition, sintering condition, grain size, type and amount of additives, impurities and the preparation methodology [47-49]. The various compositions of the bulk system $Ni_{1-x}Zn_xFe_2O_4$ (x = 0.1, 0.2, 0.3, 0.4, 0.5, 0.6, 0.7, 0.8, 0.9) [50-59] have been investigated and reported in literature. This system has also been extensively studied for various properties as well as for structural and characterization techniques in nanometric range. The material can be synthesized by numerous different chemical and physical methods [60-70]. A very few numbers of investigations have been made on structural and magnetic properties of nickel-zinc ferrite particles synthesized via reverse micelle technique [71-75].

A large number of investigations have been made on trivalent impurities (Al^{3+}, Cr^{3+}, In^{3+}) substituted spinel ferrite to understand their magnetic and electric properties [53,67,76-81]. It has been shown that the magnetic and other properties of ferrite particles can be upgraded by incorporating suitable diamagnetic impurities [53,78-81]. Very little

work has been reported on the Mössbauer investigations in case of trivalent indium (In^{3+}) ions doped in stoichiometric compositions of nickel-zinc ferrites. Parvatheeswara Rao et al [80] have studied the substitution of indium ions in the nickel-zinc system. They found that saturation magnetization increases slightly for a certain concentration of indium ions thereafter it decreases. Their assertion on this type of anomalous behavior of magnetization as a function of indium ions concentration in nickel-zinc ferrite systems was corroborated by the experiments of Lakshman et al [78] and Ghosh et al [79] on indium substituted Mg-Mn ferrite. They interpreted this effect in terms of distribution of the indium ions behavior at tetrahedral and octahedral sites. Kirichok et al [76] have studied the Mössbauer investigations of magnesium ferrite doped with indium ions. They found that indium ions replace primarily the iron ions in the tetra-positions and with further increase in concentration of indium ions they partially occupy octa-positions.

Very little work has been reported on the bulk ferrite particles prepared by annealing nano particles at high temperature [62,64,67,81-83]. Upadhyay et al [64] have investigated nickel-zinc ferrite ($Ni_{1-x}Zn_xFe_2O_4$, x = 0.0, 0.25, 0.50, 0.75, 1.0) systems prepared by chemical precipitation followed by hydrothermal treatment, using Mössbauer spectroscopy and found that the occupancy of nano particles returns to normal values after heat treatment.

1.3 Aim of present work and outline of thesis

In the present work, we have chosen nickel-zinc ferrite as basic material. Due to the inherent ability of reverse micelle technique to control the size and size distribution of nanoparticles in comparison to other techniques, we have chosen this technique for synthesis of nanoparticles. Among the different possible compositions of nickel-zinc ferrites, low value of dielectric constant and dielectric loss obtained in $Ni_{0.58}Zn_{0.42}Fe_2O_4$ ferrites show its applicability at high frequencies [46]. The $Ni_{0.58}Zn_{0.42}Fe_2O_4$ has, therefore, been used as the basic ferrite material. We have successively substituted diamagnetic In^{3+} ions in place of Fe^{3+} ions to achieve a possible upgrading of the magnetic properties. Bulk samples have been prepared by annealing the reverse micelle synthesized nanoparticles at high temperature (~1473 K).

The magnetic hyperfine structure of the nickel-zinc ferrites $Ni_{1-x}Zn_xFe_2O_4$ have been the subjects of many years [51-53,58], but we have not found any Mössbauer investigations on nano nickel-zinc ferrite systems synthesized via reverse micelle technique. It would be interesting to investigate the site preference of nickel and zinc ions in nickel-zinc ferrite system where one of the cations has a strong preference for tetrahedral and the other for octahedral sites. It is widely appreciated that the cation distribution in spinel ferrites, upon which many physical and chemical properties depend, are a complex function of processing parameters and depends on the preparation method of the material [84,85]. It should be emphasized that in most of the papers on reverse micelle synthesis of spinel ferrites [71-75,86,87], not much work has been done to determine the structure of oxides, finite size effect and interparticle interactions among the nanoparticles. Especially, the evaluation of the cation distribution in reverse micelle synthesized spinel ferrites from Mössbauer spectra and/or X-ray diffraction patterns is not as straightforward as is frequently claimed in the literature. Because of the importance of the site inversion phenomena, we have first focused on the structural change at nano level. Once these site inversion phenomena are understood and controlled, we can use our particles for size dependent studies. We have investigated in detail the thermal and nanoparticle size dependence of the high field magnetization of ferrite particles. The small size of the nanoparticles indeed leads to enhanced finite-size and surface spin effects. We have analyzed the thermal variations of magnetization in high fields to investigate the finite-size effect and an extra surface contribution. The magnetic behavior of nanoparticles is strongly affected also by interparticle interactions. The magnetic interactions can be due to dipolar coupling and exchange coupling among surface atoms and play a fundamental role in the physics of these systems [88-90]. The role of interactions on the static and dynamic properties of ferrite nanoparticles is investigated.

To our knowledge, no systematic and comparative study of nano and bulk nickel-zinc ferrite and indium doped nickel-zinc ferrite samples prepared by reverse micelle technique has been reported yet. The structural, magnetic and Mössbauer characterization of the prepared nano and bulk samples is carried out using different techniques.

Considering all the above mentioned points, the present thesis aims

- To prepare uniform and spherical nanoparticles of nickel-zinc ferrite ($Ni_{0.58}Zn_{0.42}Fe_2O_4$) and indium doped nickel-zinc ferrite ($Ni_{0.58}Zn_{0.42}In_xFe_{2-x}O_4$, x = 0.1, 0.2, 0.3) samples via reverse micelle technique followed by annealing at high temperature to make bulk samples.
- To study the effect of pH value of precipitation on the formation of spinel phase and on the particle size.
- To see the effect of co-substitution of diamagnetic (In^{3+}) ion at iron (Fe^{3+}) site in nickel-zinc ferrite system to understand the various magnetic exchange interactions.
- To study the structural properties of nano and bulk ferrite particles using X-ray diffraction, transmission electron microscopy (TEM), far-infrared transmission spectra (FTIR).
- To obtain the quantitative structural information about the nonequilibrium cation distribution and the noncollinear spin arrangement in nanosized particles using in-field Mössbauer spectroscopy.
- To study the magnetic properties of nano and bulk ferrite systems using super conducting quantum interference magnetometer (SQUID) and vibrating sample magnetometer (VSM).
- To see the effects of the particle size and indium concentration on the physical properties of nano samples viz. surface effects, cation distribution, superparamagnetic relaxation, interparticle interaction, saturation magnetization, and coercivity.
- To study the finite size effect and an extra surface contribution at low temperature using Bloch's law.
- To study the spin dynamics in nano particles using ac susceptibility measurements and role of interactions on the static and dynamic properties of nanoparticles using different models.

From the application point of view, a comparative study of nano and bulk samples is also carried out.

This thesis is divided into seven chapters.

Chapter 1 contains the introduction to ferrites, nanoferrites, literature survey, aim of the present work and outline of the thesis.

Chapter 2 presents the theoretical concepts used/developed in this work. Various models have been described to understand the magnetism of ferrite and nanoferrite particles. A brief description of technique used for preparation of nanocrystalline ferrite samples is included.

Chapter 3 describes the various experimental techniques used for the preparation and characterization of nano and bulk samples.

Chapter 4 focuses on the study of structural properties of nano and bulk samples using X-ray diffraction, transmission electron microscopy and fourier transform infrared spectroscopy measurements.

Chapter 5 includes the experimental results and observations obtained by Mössbauer spectroscopy. Effect of indium concentration, particles size and temperature on the Mössbauer parameters of nickel-zinc ferrite sample has been described. A comparative study on nano and bulk samples has also been illustrated.

Chapter 6 describes magnetic properties of nano and bulk samples using super conducting quantum interference device (SQUID) magnetometer, vibrating sample magnetometer (VSM) and ac susceptometer. Effect of particle size and indium concentration on the magnetic properties of nickel-zinc ferrite particles has been described. The thermal variation of magnetization in high fields in terms of a modified Bloch's law, the role of interactions on the static and dynamic properties of nano samples have also been discussed.

Chapter 7 represents the summary and conclusions obtained through various studies. Suggestions for the future work on the samples studied have also been included in this chapter.

References

[1] Kato V. and Takei T. *J. Inst. Elect. Engrs*. **1933**, 53, 408.

[2] Kawai M. *J. Soc. Chem. Ind. Jpn.* **1934**, 37, 392.

[3] Snoek J. L. *Physica* **1936**, 3, 463.

[4] Snoek J. L. *New development in ferromagnetic materials* New York, Amsterdam, Elsevier **1947**.

[5] Neel L. *Ann. Phys.* (Paris) **1948**, 3, 13.

[6] Snelling E. C. *Soft ferrites-Properties and Applications* Butterworths and Co Ltd., London **1988**.

[7] Kladnig W. F. and Zenger M. *Modern ferrites technologies and products* United Nations International Development Organization, September, **1992**.

[8] Viswanathan B. and Murthy V. R. K. *Ferrite Materials: Science and Technology* New Delhi, Narosa Publishing House, **1990**.

[9] Goldman A. *Modern Ferrite Technology* New York, Van Nostrand Reinhold, **1990**.

[10] Spaldin N. *Magnetic materials: Fundamental and device applications* Cambridge, Cambridge University Press, **2003**.

[11] Corliss L. M., Hasting J. M. and Verwey E. J. *Jr. Chem. Phys*. **1953**, 90, 1013.

[12] Sawataki G. A., Wounde F. V. D. and Morish A. H. *J. Appl. Phys*. **1962**, 39, 1204.

[13] Cushing B. L., Kolesnichenko V. L. and O'Connor C. J. *Chem. Rev.* **2004**, 104, 3893.

[14] Willard M. A., Kurihara L. K., Carpenter E. E., Calvin S. and Haris V. G. *Int. Mater. Rev.* **2004**, 49, 125.

[15] Ayyub P., Palkar V. R., Chattopadhyay S. and Multani M. *Phys. Rev. B* **1995**, 51, 6135.

[16] Schoiswohl J., Kresse G., Srurnev S., Sock M., Ramsey M. G. and Netzer F. P. *Phys. Rev. Lett.* **2004**, 92, 20.

[17] McHale J. M., Auroux A., Perrotta A. J. and Navrostsky A. *Science* **1997**, 277, 788.

[18] Song Z., Cai T. H., Chang Z. P., Liu G., Rodriguez J. A. and Hrbek J. *J. Am. Chem. Soc.* **2003**, 125, 8059.

[19] Uchino K., Sadanaga E. and Hirose T. *J. Am. Chem. Soc.* **1989**, 72, 1555.

[20] Dormann J. L. *Mater. Sci. Engg. A* **1993**, 168, 217.

[21] Kodama R. H. and Berkowitz A. E. *Phys. Rev. B* **1999**, 59, 6321.

[22] Dormann J. L., Fiorani D. and Tronc E. *Adv. Chem. Phys*. **1997**, 98, 283.

[23] Gangopadhyay S., Hadjipanayiis G. C., Sorensen C. M. and Klabunde K. J. *IEEE Trans. Magn.* **1993**, 29, 2619.

[24] Zhou C., Schulthess T. C. and Landau D. P. *J. Appl. Phys.* **2006**, 99, 08H906.

[25] Wang Z. L., Liu Y. and Zhang Z. *Handbook of Nanophase and Nanostructured Materials Vol. 3* New York, Kluwer Academic/Plenum Publishers, **2002**.

[26] Sugimoto M. *J. Am. Ceram. Soc.* **1999**, 82, 269.

[27] Lüders U., Barthélémy A., Bibes M., Bouzehouane K., Fusil S., Jacquet E., Contour J- P., Bobo J-F., Fntcuberta J. and Fert A. *Adv. Mater*. **2006**, 18, 1733.

[28] Kittel C. *Phys. Rev.* **1946**, 70, 965.

[29] Dorman J. L. and Fiorani D. *Magnetic properties of Fine particles* North-Holland, Amsterdam, **1992**.

[30] Lu L., Sui M. L. and Lu K. *Science* **2000**, 287, 1463.

[31] Raj K., Moskowitz R. and Casciari R. *J. Magn. Magn. Mater*. **1995**, 149, 174.

[32] Ozaki M. *Mater. Res. Bull.* XIV **1989**, 35.

[33] Gleiter H. *Nanostruct. Mater*. **1992**, 1, 1.

[34] Hu J., Odom T. W. and Lieber C. M. *Acc. Chem. Res*. **1999**, 32, 435

[35] Patzke G. R., Krumeich F. and Nesper R. *Angew Chem. Int. Ed*. **2002**, 41, 2446.

[36] Puntes V. F., Krishnan K. M. and Alivisatos A. P. *Science* **2001**, 291, 2115.

[37] Mo M., Zeng J., Liu X., Yu W., Zhang S. and Qian Y. *Adv. Mater.* **2002**, 14, 1658.

[38] Limmer S. J., Seraji S., Forbess M. J., Wu Y., Chou T. P., Nguyen C. and Cao G. Z. *Adv. Mater.* **2001**, 13, 1269.

[39] Mbindyo J. K. N., Mallouk T. E., Mattzela J. B., Kratochvilova I., Razavi B., Jackson T. N. and Mayer T. S. *J. Am. Chem. Soc*. **2002**, 124, 4020.

[40] Ginzburg M., Fournier-Bidoz S., Coombs N., Ozin G. A. and Manners I. *Chem. Commun.* **2002**, 3022.

[41] Gleiter H. *Nanostruct. Mater*. **1995**, 6, 3.

[42] Yener D. O. and Giesche H. *J. Am. Ceram. Soc.* **2001**, 84, 1987.

[43] Nanni A. and Dei L. *Langmuir* **2003**, 19, 933.

[44] Gan L. M., Zhang L. H., Chan H. S. O., Chew C. H. and Loo B. H. *J. Mater. Sci.*

1996, *31*, 1071.

[45] Pileni M. P. *J. Am. Chem. Soc.* **2003**, 225, U18.

[46] Thakur S., Katyal S. C. and Singh M. *Appl. Phys. Lett.* **2007**, 91, 262501.

[47] Caltun O. F., Spinu L. and Stancu Al. *J. Magn. Magn. Mater.* **2002**, 242–245, 160.

[48] Dias A. and Moreira R. L. *J. Magn. Magn. Mater.* **1997**, 172, L9.

[49] Scrinivasan T. T. and Ravindranathan P. *J. Appl. Phys.* **1988**, 63, 3789.

[50] Satya Murthy N. S., Natera M. G., Youssef S. I. and Begum R. J. *Phys. Rev.* **1969**, 181, 969.

[51] Leung L. K., Evans B. J. and Morrish A. H. *Phys. Rev. B* **1973**, 8, 29.

[52] Uen T. M. and Tseng P. K. *Phys. Rev. B* **1982**, 25, 1848.

[53] Srivastava R. C., Khan D. C. and Das A. R. *Phys. Rev. B* **1990**, 41, 12514.

[54] Kumar P. S. A., Shrotri J. J., Kulkarni S. D., Deshpande C. E. and Date S. K. *Mater. Lett.* **1996**, 27, 293.

[55] Srinivasan G., Laletsin V. M., Hayes R., Puddubnaya N., Rasmussen E. T. and Fekel D. J. *Solid State Comun.* **2002**, 124, 373.

[56] Costa A. C. F. M., Tortella E., Morelli M. R. and Kiminami R. H. G. A. *J. Magn. Magn. Mater.* **2003**, 256, 174.

[57] Srinivasan G., DeVreugd C. P., Flattery C. S., Labtsin V. M. and Paddubnaya N. *Appl. Phys. Lett.* **2004**, 85, 2550.

[58] Irvine J. T. S., Huanosta A., Valenzuela R. and West A. R. *J. Am. Ceram. Soc.* **2005**, 73, 729.

[59] Sorescu M., Diamandescu L., Ramesh P. D., Roy R., Daly A. and Bruno Z. *Mater. Chem. Phys*. **2007**, 101, 410.

[60] Lee J. H., Maeng D. Y., Kim Y. S. and Won C. W. *J. Mater. Sci. Lett.* **1999**, 18, 1029.

[61] Albuquerque A. S., Ardisson J., Macedo W. A. A. and Alves M. C. M. *J. Appl. Phys.*

2000, 87, 4352.

[62] Yang D., Lavoie L. K., Zhnag Y. and Shihui Ge *J. Appl. Phys.* **2003**, 93, 7492.

[63] Wu K. H. and Huang W. C. *J. Solid State Chem.* **2004**, 177, 3052.

[64] Upadhyay C., Verma H. C. and Anand S. *J. Appl. Phys*. **2004**, 95, 5746.

[65] Mouallem-Bahout M., Bertrand S. and Peńa O. *J. Solid State Chem.* **2005**, 178, 1080.

[66] Hwang C., Tsai J., Huang T., Peng H. and Chen S. *J. Solid State Chem.* **2005**, 178, 382.

[67] Singhal S., Barthwal S. K. and Chandra K. *J. Magn. Magn. Mater*. **2006**, 296, 94.

[68] Rao B. P., Rao G. S. N., Mahesh A., Murthy Y. L. N., Hong S. M. and Kim C. *J. Appl. Phys*. **2007**, 101, 123902.

[69] Deka S. and Joy P. A. *J. Am. Ceram. Soc.* **2007**, 90, 1494.

[70] Lopez G. P., Silvetti S. P., Aguirre M. del C. and Condo A. M. *J. Alloys Comp.* **2009**, 487, 646.

[71] Uskokovi V. and Drofenik M. *Materiali in Technolije* **2003**, 37, 129.

[72] Morrison S. A., Cahill C. L., Carpente E. E., Calvin S., Swaminathan R., McHenry M. E. and Harris V. G. *J. Appl. Phys*. **2004**, 95, 6392.

[73] Kale A., Nathani H., Srivastava R. S. and Misra R. D. K. *Mater. Sci. Tech.* **2004**, 20, 999.

[74] Gubbala S., Nathani H., Koizol K. and Misra R. D. K. *Physica B* **2004**, 348, 317.

[75] Uskokovi V., Drofenik M. and Ban I. *J. Magn. Magn. Mater.* **2004**, 284, 294.

[76] Kirichok P. P. and Antoshchuk A. I. *Physica* **1977**, 29, 86

[77] Sankpal A. M., Suryavanshi S. S., Kakatkar S. V., Tengshe G. G., Patil R. S., Chaudhari N. D. and Sawant S. R. *J. Magn. Magn. Mater*. **1998**, 186, 349.

[78] Lakshman A., Rao K. H. and Mendiratta R. G. *J. Magn. Magn. Mater*. **2002**, 250, 92.

[79] Ghosh S., Nambissan P. M. G. and Bhattacharya R. *Phys. Lett. A* **2004**, 325, 301.

[80] Parvatheeswara B. and Rao K. H. *J. Magn. Magn. Mater.* **2005**, 292, 44.

[81] Date S. K., Joy P. A., Kumar P. S. A., Sahoo B. and Keune W. *Phys. Stat. Sol. (c)* **2004**, 1, 3495.

[82] Kumar S. and Patil K. C. *J. Solid State Chem.* **1992**, 99, 12.

[83] Naughton B. T. and Clarke D. R. *J. Am. Ceramic Soc.* **2007**, 90, 3541.

[84] Šepelák V., Feldhoff A., Heitjans P., Krumeich F., Menzel D., Litterst F. J., Bergmann I. and Becker K. D. *Chem. Mater*. **2006**, 18, 3057.

[85] Šepelák V., Bergmann I., Feldhoff A., Heitjans P., Krumeich F., Menzel D.,

Litterst F. J., Campbell S. J. and Becker K. D. *J. Phys. Chem. C* **2007**, 111, 5026.

[86] Vestal C. R. and Zhang Z. J. *Int. J. of Nanotechnology* **2004,** 1, 240.

[87] Hochepied J. F., Bonville P. and Pileni M. P. *J. Phys. Chem. B* **2000,** 104, 905.

[88] Lee P. R. and Banfield J. F. *Science* **1988**, 281, 969.

[89] Banfield J. F., Welch S. A., Zhang H., Ebert T. T. and Lee P. R. *Science* **2000**, 289, 751.

[90] Mendes P. M., Chen Y., Palmer R. E., Nikitin K., Fitzmaurice D. and Preece J. A. *J. Phys.: Condens. Matter* **2003**, 15, S3047.

CHAPTER 2

THEORETICAL BACKGROUND

Commercial use of ferrites is generally based on two important characteristics: their electrical resistivity and their magnetic properties. Any investigation into ferrites therefore requires an understanding of magnetics and how to characterize it. Nanomagnetism has a special role to play as magnetic properties depend uniquely on both dimensionality and lengthscales. This chapter presents the theoretical concepts used/developed in this work. Various models have been described to understand the magnetism of ferrite and nanoferrite particles. A brief description of technique used for preparation of nanocrystalline ferrite samples is included.

2.1 Magnetism of ferrites

2.1.1 Magnetic interactions

In order to study the origin and nature of the magnetic behavior associated with spinel ferrites, there are mainly three types of magnetic interactions, which are possible between the metal ions at tetrahedral (A) and octahedral (B) sites through the intermediate oxygen ions (O^{2-}) i.e., superexchange interaction (Figure 2.1).

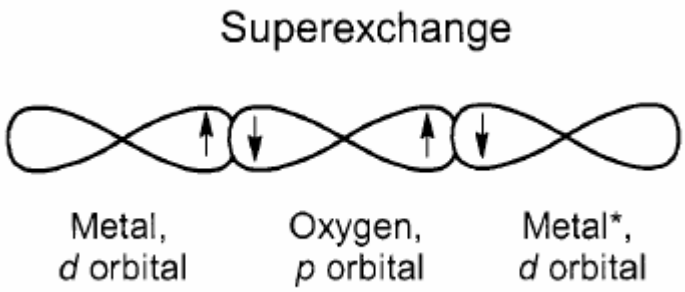

Figure 2.1 *Illustration of electron coupling via superexchange from one metal atom to another (metal*) through an oxygen atom*

These are A-A, A-B, and B-B interactions as suggested by Anderson [1]. Since cation-cation distances are large, direct interactions are negligible. It has been verified experimentally that these interaction energies are negative favoring antiferromagnetism when the d orbital of the metal ions are half filled or more than half filled, while a positive interaction accompanied by ferrimagnetism results when d orbitals is less than half filled.

The magnitude of the interaction energy between two magnetic ions M and M´ depends upon

(a) the distances from these ions to the oxygen ions through which interaction occurs.

(b) the angle M-O-M´ represented by θ as shown in figure 2.2.

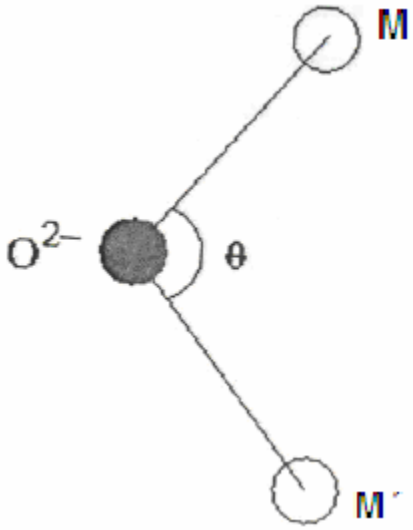

Figure 2.2 *M-O-M´ angles in ferrites*

For θ =180^{o}, where the interatomic distance is shortest, the exchange energy is found to be highest. The energy decreases rapidly with increasing the distance and decreasing the angle towards 90^{o}.

In spinel structure, the A-O-B angle is in the neighborhood of 180^{o}, while A-O-A and B-O-B angles are closer to 90^{o}. Thus, with A-O-B interaction predominating, the spins of the (A) and (B) site ions will be oppositely magnetized with a resultant magnetic moment equal to the difference between those of (A) and (B) site ions. To explain the magnetic properties of spinel ferrites quantitatively, it is necessary to know what sorts of ions are involved and which ion occupies which site. The more unpaired valence electrons a cation has, the larger is its contribution to the magnetic moment. In case of magnetite system, the trivalent iron has five unpaired electrons, while the divalent iron has four. Since magnetite is an inverse spinel the overall magnetic moment decreases when compared to a theoretical normal spinel of the same material. In order to increase the

overall magnetic moment in ferrites, such as nickel ferrites are often doped with zinc to produce nickel-zinc ferrite particles.

As zinc ions have preference to (A) site and the fact that divalent zinc has no free valence electrons (d^{10}), the inclusion of zinc increases the overall magnetic moment. However, it has also been mentioned that magnetic coupling of the (A) sites with the (B) sites occurs due to superexchange through neighboring oxygen atoms, which is not possible if either cation does not have unpaired electrons. This means that there is a limit in the benefits of doping with zinc, and studies have shown that the magnetic moment begins to decline once the inclusion of zinc in the (A) sites is greater than 50 % [2].

Gorter [3] gave various possible configurations of the ion pair in spinel ferrites with favorable distances and angles for an effective magnetic interaction. In general, it is found that the magnitude of A-B, B-B and A-A interactions are negative with $|A\text{-}B| >> |B\text{-}B| >> |A\text{-}A|$.

2.1.2 Magnetic ordering in spinel ferrites

Ferromagnetism occurs due to the sublattice magnetic ordering. The magnetic properties of spinel ferrites are governed by the types of magnetic ions residing on (A) and (B) sites and relative strength of intersublattice, J_{AB}, and intrasublattice, J_{BB}, J_{AA}. When the A-B interaction is the dominant one i.e. $J_{AB} > J_{BB} > J_{AA}$, then the spins have the collinear structure in which moments on the (A) site are antiparrallel to the moment on the (B) site. When A-A (or B-B) interaction is comparable to A-B interaction then the spins have non-collinear (canted) structure. Spinel ferrites allow variety of magnetic disorder and frustration to be introduced. The competition between the various magnetic interactions occurs in a variety of magnetic structure due to the unsatisfied magnetic bonds. The magnetic properties of ferrites are accounted through several models like Neel's model, Yafet Kittel Model, random canting model and localized canting model. A brief description of the Neel's model and the Yafet Kittel model is given here.

2.1.2.1 Neel's model

This model [4] is based on the following assumptions:

(i) Two sublattice exist, tetrahedral (A) and octahedral (B).

(ii) One type of magnetic ion exists and a fraction of these ions appears on (B) sites.

(iii) An internal Weiss molecular field acts on the ions.

(iv) A-B or B-A interactions are equal and predominant over A-A and B-B interaction. Therefore, the net observed moment is the difference between the two average sublattice magnetic moments. This theory can also be applicable to the mixed ferrites. The ionic distribution is written as

$$(M_x^{2+} Fe_{1-x}^{3+})^A [M'^{2+}_{1-x} Fe_{1+x}^{3+}]^B O_4^{2-} \quad \text{.....(2.1)}$$

M and M′ are metallic ions. With Neel's configuration the saturation moment at 0 K is given by

$$M_s \text{ (in } \mu_B) = M_{(B)} - M_{(A)} \text{.....(2.2)}$$

where $M_{(B)}$ and $M_{(A)}$ are the magnetic moments at (B) and (A) sites respectively.

$$\text{or } M_s \text{ (in } \mu_B) = \{2(1-x)S_m' + 5\,(1+x)\}^{(B)} - \{5\,(1-x) + 2xS_m\}^{(A)} \text{..... (2.3)}$$

where S_m and S_m' are the spin quantum number of the respective ions and the orbital angular momenta are assumed to be quenched and μ_B is the Bohr magneton. However, Neel's predominant assumption fails to explain the behavior of pure $ZnFe_2O_4$. $ZnFe_2O_4$ has the normal spinel structure; Zn^{2+} being non-magnetic, the (A) site ions carry no magnetic moment. Thus B-B interaction gives rise to antiferromagnetic ordering in the (B) lattice. The discrepancies of the experimental data and Neel's theory were tried to explain through some statistical models with exchange linkage approach [5,6], considering number of nearest magnetic neighbors contributing to magnetization. Further, modifications to the same approach were attempted by Ishikawa, Novik and Geller etc. [7-9].

2.1.2.2 Yafet Kittel model

Yafet and Kittel extended the Neel's theory to take into account the antiferromagnetic A-A and B-B interactions that may not be negligible in comparison to the A-B interactions. They suggested that in spinel ferrites, non-magnetic sublattice in

one sublattice leads to the non-collinear or canted spin arrangement on the other sub lattice. Consequently, this results in the splitting of (B) sublattice into two mainly (B_1) and (B_2) with equal magnetic moment at an angle θ_{YK} with the direction of net magnetization of (B) sublattice at 0 K.

Figure 2.3 shows the angle between different moments and their directions. The occurrence of splitting is determined by the interactions responsible for the ordering. To calculate the uniform canting angle θ_{YK}, a split sublattice model was developed by Yafet and Kittel [10]. Now the modified formula will be

$$M_s(\mu_B) = M_{(B)} \text{ Cos } \theta_{YK} - M_{(A)} \quad \text{.....(2.4)}$$

With increase in angle θ_{YK}, Cos θ_{YK} decreases leading to the decrease in the magnetic moment.

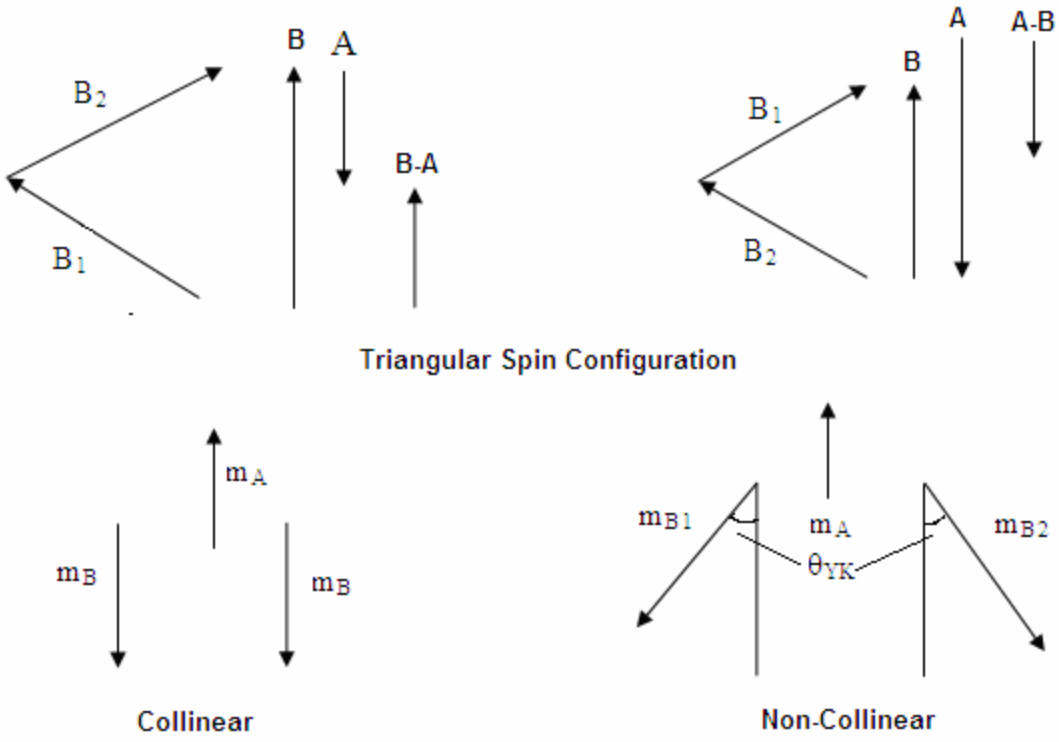

Figure 2.3 *Configuration of the ion pairs in spinel ferrites*

2.2 Magnetics of nanoparticles

The behavior of bulk magnetic materials is determined and influenced by the formation of domains and domain wall movement. The magnetic behavior of bulk materials is complicated by the fact that domain wall moment can be impeded or pinned

by impurities, grain boundaries, etc. Due to this, a direct correlation between the observed magnetic behavior and the quantum origins of magnetism is not readily achievable. However, if the size of the magnetic materials is decreased below a critical characteristic length, domain formation is no longer energetically favored and the particles behave like single domains [11]. Moreover, the large surface fraction opens the opportunity for manipulation of properties via interfacial interaction. Knowledge of these fundamental properties is essential for creative use of nanoparticles in important technical applications [12-16].

The most spectacular effect of the size reduction of a magnetic particle lies in the superparamagnetism (SPM) phenomena [17-19]. Briefly, superparamagnetism occur when the thermal fluctuations or an applied field can easily move the magnetic moments of the nanoparticle away from the easy axis, the preferred crystallographic axes for the magnetic moment to point along. In such a situation, each particle behaves like a paramagnetic atom, but with a giant magnetic moment as there is a still well-defined magnetic order in each nanoparticle [20]. Their existence was first predicted by Neel [17]. The simplest model to account for the relaxation time of the thermal fluctuations of the magnetization of a particle with uniaxial anisotropy is given by eqn.,

$$\tau = \tau_0 \exp\left(\frac{E_A}{k_B T}\right) \quad \text{.....(2.5)}$$

where E_A is the energy barrier to moment reversal and k_BT is the thermal energy. For non-interacting particles, the pre-exponential factor τ_o is of the order of 10^{-9}-10^{-12} s and weakly dependent on temperature [21]. This energy barrier has several origins, including both intrinsic and extrinsic effects such as the magentocrystalline and shape anisotropies, respectively; but in the simplest cases, it has a uniaxial form given by

$$E_A = KV \sin^2 \theta \quad \text{.....(2.6)}$$

where K is the anisotropy energy density and V is the particle volume and θ is the angle between the magnetization and easy direction. Either $\theta = 0^o$ or 180^o is a direction of minimum energy. These directions are separated by an energy barrier of the height. It is also important to recognize that observations of superparamagnetism are implicitly dependent not just on temperature, but also on the measurement time τ_m of the experimental technique used. If $\tau << \tau_m$, the flipping is fast relative to the experimental

time and the particles appear to be paramagnetic; while if $\tau >> \tau_m$, the flipping is slow and quasi-static properties are observed-the so called 'blocked state' of the system. A blocking temperature T_B is defined as the mid point between these two states, where $\tau = \tau_m$.

Later Brown [21] and Aharoni [22] studied the dependence of superparamagnetic relaxation time on the magnetic field parallel to the easy axis of the particles and found that the relaxation time decreases with the increasing magnetic field, which yield a decrease in the blocking temperature. The first attempt to introduce interactions in the Neel-Brown model was made by Shtrikman and Wohlfarth [23] for the relaxation time in the weak interaction limit, of the form,

$$\tau = \tau_0 \exp\left(\frac{E_A}{k_B(T_B - T_0)}\right) \text{.....(2.7)}$$

where T_o is an effective temperature, which accounts for the interaction effects. A more general approach was developed by Dormann et al [24]. This model correctly reproduces the variation of blocking temperature (T_B), deduced from ac susceptibility and Mössbauer spectroscopy as a function of the observation time of the experiment. The increase of the T_B with strength of the dipolar interactions has been predicted by this model and confirmed experimentally [25-28]. In a third model proposed by Morup and Trone [29] for the weak interaction limit, the opposite dependence of T_B with the strength of the interactions is predicted. This behavior was experimentally confirmed by Mössbauer spectroscopy in the samples of γ-Fe_2O_3 particles [29] and suggested two magnetic regimes, governed by opposite dependencies of T_B occur in interacting fine particles. It was shown that at high temperature and/or for weak interactions, T_B signals the onset of a blocked state and T_B decreases as the interaction increase. In contrast, at high temperatures and/or strong interactions, a transition occurs from superparamagnetic state to a collective state, which shows most of the feature of typical spin glass state. In this case, T_B is associated with a freezing process and it increases with the interactions.

Surface effects in a nanoparticle are of great importance due to increase in the surface to volume ratio since they dominate the magnetic properties and become more important with decreasing size of the particle. Consequently, the ideal picture of a superspin formed by the collinear arrangement of all spins of the particle is no longer

valid, and the misalignment of the surface spins yields strong deviations from the bulk behavior. This is also true for particles of many ferrimagnetic oxides with strong exchange interactions, in which magnetically competing sublattices usually exist. In these cases, broken bonds and defects at the surface layer destabilize magnetic order giving rise to magnetic frustration, which is enhanced with the strength of the magnetic interactions. Consequently, the profile of magnetization is not uniform across the particle, the surface layer being more demagnetized than the core spins. In fact, even strong exchange interactions in the surface responsible for the coordination defects and is found that in a particle of diameter of the order of 8 nm, 50 % (in the γ-Fe_2O_3 nanoparticles) of atoms lie on the surface, and therefore the effect of the latter cannot be ignored. In early models this fact was explained by postulating the existence of a dead magnetic layer giving no contribution to the magnetization of the particle [30]. Coey et al [31] proposed the existence of a random canting of the surface spins due to the competing antiferromagnetic interactions between sublattices to account for the reduction in M_s observed in γ-Fe_2O_3 nanoparticles. A further verification of the existence of spin canting in nanoparticles of different ferrimagnetic oxides (γ-Fe_2O_3, $CoFe_2O_4$, $CuFe_2O_4$, $NiFe_2O_4$) was studied by using Mössbauer spectroscopy [31,32], polarized [33] and inelastic neutron scattering [34] and ferromagnetic resonance [35]. However, in contrast with original suggestion by Coey that spin canting occurs mainly at the surface layer due to magnetic frustration, some work based on Mössbauer spectroscopy supports the idea that it is a finite size effect, which is uniform throughout the particle [36-40]. Indeed, the origin of spin misalignment observed in ferrimagnetic nanoparticles is still under discussion and there is not a complete understanding of the phenomenon. A model has been proposed by Kodama et al [38] and Martinez et al [41] suggesting the existence of a magnetically ordered core surrounded by a surface layer of canted spins, which undergoes a spin-glass like transition to a frozen state below a certain temperature, T_f. It creates an exchange field acting over the ordered core of the particle, which could be responsible for the shifting of the M-H curves after a field-cooled (FC) process by a mechanism similar to that giving rise exchange bias in layered structure [42,43]. The existence of a frozen state at the particle surface has been experimentally established by different techniques [41,44-48].

A micromagnetic model at atomic scale proposed by Kodama et al [44,46] and several numerical simulations of a single domain ferrimagnetic particle with a variety of assumptions but with the common condition of free boundaries at the surface [49-64] have evidenced the non-uniformity of the magnetization profile across the ferrimagnetic particle, with fast decreasing towards the surface. These results demonstrate that the non-uniform profile of the particle magnetization is merely a surface effect. However, enhancement in magnetic anisotropy [60], vacancies and broken exchange bonds at the particle surface have to be included in these models in order to induce enough magnetic disorder so as to freeze the disordered surface layer which give rise to spin-glass behavior [46,51]. Hence, surface and finite size effects seem not to be significant as to produce the spin glass state, even in the case of ferrimagnetic particles with competing antiferromagnetic sublattices, surface anisotropy and disorder being necessary additional ingredients. In nanoparticles with a randomly distribution of easy axis, interparticle interactions are a additional source of magnetic disorder that may lead to a frozen collective state of particle spins at low temperature, apart from the effects of the surface to core exchange coupling. Indeed, both processes may occur in parallel contributing simultaneously to the spin-glass behavior in ferrite nanoparticles. The main types of magnetic interactions, which can be found in nanoparticle systems, are: (a) dipole-dipole interactions, which always exist; and (b) exchange interactions through the surface of the particles which are in close contact. Taking into account the anisotropic character of dipolar interactions, which may favor the ferromagnetic, or antiferromagnetic alignment of the particle spins depending on the geometry; nanoparticles systems have all the necessary ingredients to give rise to a spin glass behavior namely, random distribution of local easy axes and frustration of magnetic interactions.

2.2.1 Size dependent magnetic properties

The one of the most important and interesting property of spinel ferrite which provides them a scope for the wide practical application is the magnetic properties they possess. The different critical parameters assessed for application purpose are saturation magnetization, coercive field, remanence, magnetic losses, magnetic susceptibility, transition temperature etc.

In this section, we are giving a brief discussion on the dependence of magnetic behavior viz., saturation magnetization, coercivity, transition temperature etc. on the particle size.

2.2.2 Effect of particle size on saturation magnetization (M_s)

The reduction of the saturation magnetization, M_s is a common experimental observation in many nanoparticle systems [30,61]. In general, the saturation magnetization, M_s in particularly shows a monotonic decrease with decreasing particle size [62]. For example, the saturation magnetization for the evaporated fine iron (Fe) particles (~20 nm) has been reported in the range of 10-90 % of the bulk value depending upon the particle size [63]. Decreasing the particle size from 20 to 6 nm, the M_s value decreases from 190 to 25 emu/g, which are 86.4 % and 11.4 % of the bulk saturation moment respectively [64]. A strong decrease of M_s with decreasing particle size [30,65-67] has also been observed for fine oxides of iron. Berkowitz [30] showed that the M_s of the fine γ-Fe_2O_3 particle is 30 emu/g, where as the theoretical bulk value is 73 emu/g. It has been also observed that M_s decreases from 16 emu/g to a value 3.8 emu/g when the particle size decreased from 8 to 4 nm in case of γ-Fe_2O_3 fine particles [67]. In case of natural ferrite, Fe_3O_4 nanoparticles, Sato et al [68] and Abu-Aljarayesh [69] observed a reduction of M_s to 80 % and 38 % of the theoretical value (92 emu/g), when the size reduced to 15 nm and 8.5 nm respectively. Similar results have also been reported in many spinel ferrite nanoparticles [70-76]. In fact, the observation of reduction in M_s is unanimously agreed upon, the explanation proposed by various peoples for the same has been quite contradicting. In early models put by Berkowitz [30] this fact was explained by assuming the existence of a dead magnetic layer at the surface of the particles. According to this model, the saturation magnetization M_s is

$$M_s = M_0\left(1-\frac{6t}{D}\right) \qquad \text{.....(2.8)}$$

where M_0 is the bulk saturation moment at room temperature, t is the thickness of the layer and D is the particle diameter. The thickness of the dead layer was found to be ~0.6 nm in case of $MnFe_2O_4$ ferrite nanoparticles having size in the range 6 to 25 nm [66,77-79]. Further, a random canting of the surface spins caused by competing antiferromagnetic interactions between sublattices was proposed by Coey et al [31] and

Morrish et al [77] to account for the reduction of M_s in γ-Fe_2O_3 ferrimagnetic particles. It was observed that even a magnetic field of 50 kOe was not enough to align all the spins in the field direction of particles of 6 nm in diameter. The existence of canted spins was subsequently verified in different nanoparticle systems of ferrimagnetic oxides [31-33, 44,78] $NiFe_2O_4$, γ-Fe_2O_3, $CuFe_2O_4$, $CoFe_2O_4$ using Mössbauer spectroscopy [31,32].

In contrast, from other studies based on Mössbauer spectroscopy, it has been suggested that spin canting is not a surface effect, but rather a finite size effect, which is uniform throughout the whole volume of the particle [36-39,79]. This consequently causes a substantial decrease of M_s when compared with that of bulk material. The spin canting as a surface effect has also been disputed by Pankhurst [36] and he claimed that the lower M_s values are due to non-saturation of magnetization because of random distribution of the fine particles with enhanced value of magnetocrystalline anisotropy. In spite of these alternate explanations to the spin canting effects, recent experiment [41,44] seems to support the idea of surface effect domination in the nano-sized particles.

In addition to these effects, cation redistribution at chemically inequivalent sites has been proposed in certain nanoparticles of spinel ferrites [67,80-83]. In $MnFe_2O_4$ nanoparticles, many authors have reported that reduction of M_s with decreasing particle size is due to an increasing fraction of the Mn ions in the octahedral site [80,84,85]. Chen et al [79] have attributed the decrease of M_s in nanoparticles of $MnFe_2O_4$ to the surface effects rather than to the cation-redistribution although they have observed the distribution of Mn ions in tetrahedral and octahedral sites. In addition with the reduction of M_s with the size observed in nanoparticles of ferromagnetic and antiferromagnetic oxides, several experimental results [86-96] and theoretical models have shown a clear enhancement of M_s in ferromagnetic metallic nanoparticles, which has been attributed to the surface atoms, whose atomic environment is very different as compared with the core atoms [97-102]. Sepelak et al [103] have observed a clear enhancement of magnetization in milled $MgFe_2O_4$ ferrite and attributed to the mechanically induced cation re-distribution. Bhowmik et al [104] have also observed a similar kind of results in case of mechanically milled $Co_{0.2}Zn_{0.8}Fe_2O_4$ spinel oxide and correlate the enhancement of magnetization of nanoparticles to the inverse of spin canting effect i.e., the lowering of octahedral site spin canting by milling of bulk sample.

2.2.3 Effect of particle size on coercivity (H_c)

Like the saturation moment M_s, the coercivity of the nanoparticles has a striking dependence on their size [105,106]. Figure 2.4 shows schematically the variation of coercivity H_c with particle diameter. In case of larger size particles, there is a tendency towards multi-domain structure formation, which results in a decrease in the value of H_c due to domain wall (DW) motion in an applied field (Figure 2.4). In multi-domain region, magnetization is related to the motion of domains and the size-dependence of coercivity is experimentally given by [105]

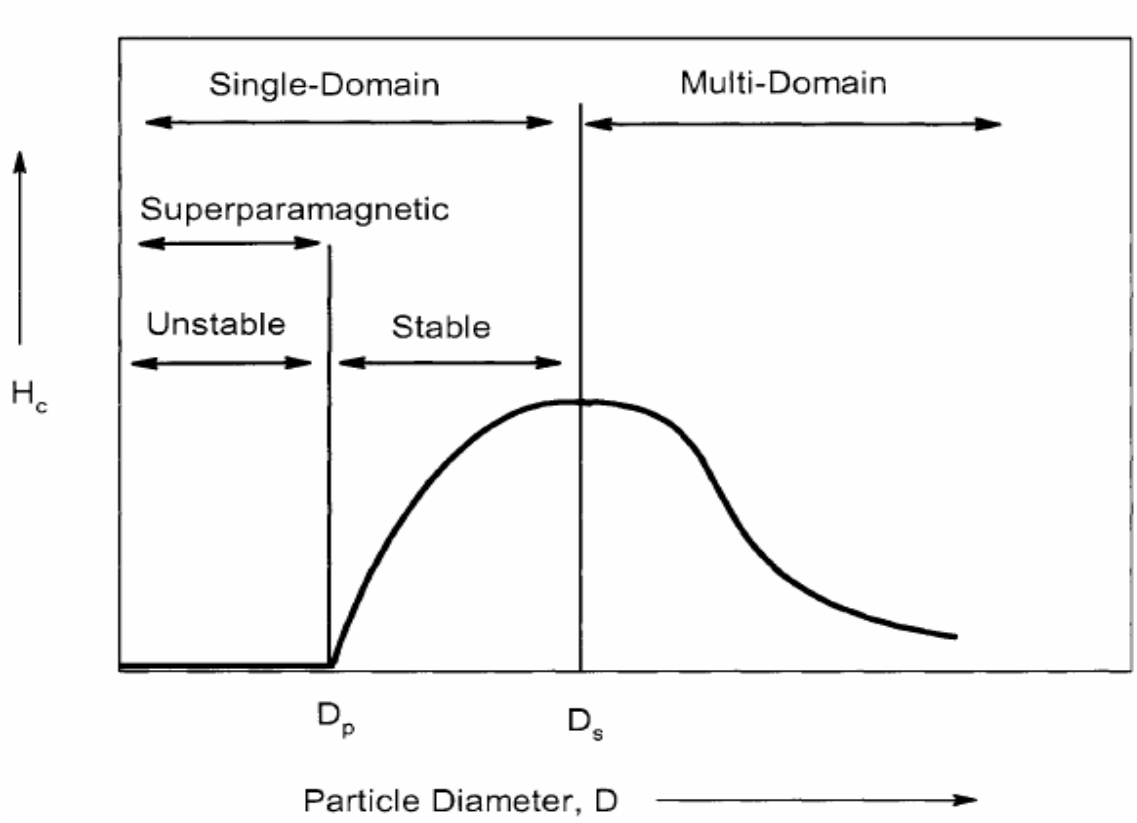

Figure 2.4 *Schematic variation of coercivity with particle diameter.*

$$H_c = a + \frac{b}{D} \quad \ldots\ldots\ldots\ldots\ldots\ldots\ldots\ldots\ldots(2.9)$$

where a and b are constant. As the particle diameter decreases, the coercivity increases. Below a critical diameter (D_s), the particles become a single domain and the coercivity

reaches a maximum. Below D_s, the coercivity decreases with decreasing particle size because of thermal effects. The relation is given by [105]

$$H_c = g - \left(\frac{h}{D^{\frac{3}{2}}} \right) \text{.....(2.10)}$$

where g and h are constants. Below a critical diameter (D_p), thermal effects are strong enough to spontaneously demagnetize a previously saturated assembly of particles and the coercivity becomes zero and superparamagnetism develops. In this range of particle sizes, the energy barrier to flip the magnetic moment of the particles becomes comparable to the thermal energy. In such a situation, the relaxation time is faster than the characteristics time window of the experimental set up. The superparamagnetic behavior is clearly evidenced from the absence of M-H curve above the blocking temperature and the appearance of a quadrupole doublet in the Mössbauer spectra.

The enhancement of coercivity in nanoparticle systems in comparison to their bulk counterparts has been reported by many authors in literature [63-64,107]. For example, evaporated fine particles of iron (~20 nm) have been reported to have coercivities up to two orders of magnitudes higher than the bulk value [63]. In this system, a maximum value of H_c obtained at room temperature is 1140 Oe for a particle of size 21.4 nm [64]. When the particle size reduced to 13 nm, the H_c value decreases to 900 Oe. With further reduction of the particle size, H_c reduces drastically and attains a zero value for particles of size ~7 nm and hence shows superparamagnetic effect. Similar results have also been observed in nanoparticles of γ-Fe_2O_3 [107]. Nanocrystalline $Ni_{0.5}Zn_{0.5}Fe_2O_4$ sample with particle size in the range of 15-29 nm shows H_c in the range of 14-45 Oe [108] that are two orders of magnitude higher than that reported for bulk [2]. In ferromagnetic systems, it has been shown that the coercivity H_c steeply increases with particle diameter following a D^6 power law up to 50 nm and H_c then goes through a maximum and decreases again for particle size below 150 nm according to the well known 1/D law for polycrystalline magnets [109]. Different models have been proposed to explain the complex behavior of H_c with particle size. For example, non-magnetic grain boundary model has been proposed to explain the 1/D law for polycrystalline

particles [110-112] whereas the linear increase in H_c with particle size in nanoparticle range has been explained through Stoner-Wohlfarth theory [113].

According to Stoner-Wohlfarth theory, the coercivity H_c of a single domain particle is given by

$$H_c = \frac{2K}{M_s \mu_0} \quad \text{.....(2.11)}$$

where μ_0 is a universal constant of permeability in free space, K is the anisotropy constant and M_s is the saturation moment of the nanoparticle [114]. Above the blocking temperature, the magnetocrystalline anisotropy is overcome by thermal energy and K can be considered as zero. The nanoparticles do not display magnetization hysteresis behavior with $H_c = 0$. Below the blocking temperature, M_s increases when the particle size increases. However, K, increases faster than M_s and H_c increases linearly with particle size.

2.3 Synthesis of ferrite particles in nano and bulk scale:

To carefully study and exploit the potential and possibilities associated with nanomaterials, the key point is to create well-defined, monodisperse structures of predictable size, shape, crystallinity, and morphology through a straightforward synthesis. All the samples of nickel-zinc ferrite particles and indium doped nickel-zinc ferrite nanoparticles in the present study were prepared using bottom to top approach employing reverse micelle synthesis.

Reverse micelles, which are essentially nanosized aqueous droplet that exist in microemulsions with certain compositions, are known to present an excellent medium for the synthesis of nanoparticles with uniform morphology [115-117]. It is the inherent ability of this reaction system to control the size and size distribution that makes it attractive for the synthesis of nanoparticles [118]. The fundamentals of this technique and its applicability to ferrite synthesis are presented in the following sections.

2.3.1 Micelle fundamental

An emulsion is formed when two immiscible solvents, such as water and oil, are mixed together to produce a stable suspension of one within the other [119]. Generally

this is facilitated by the use of a surfactant, which is a linear molecule that has an affinity for both the solvents. In the case of water and oil, the surfactant has one end that is hydrophobic and one that is hydrophilic as illustrated in figure 2.5 (a). The surfactant serves as the boundary between the two liquid phases (Figure 2.5b) [119].

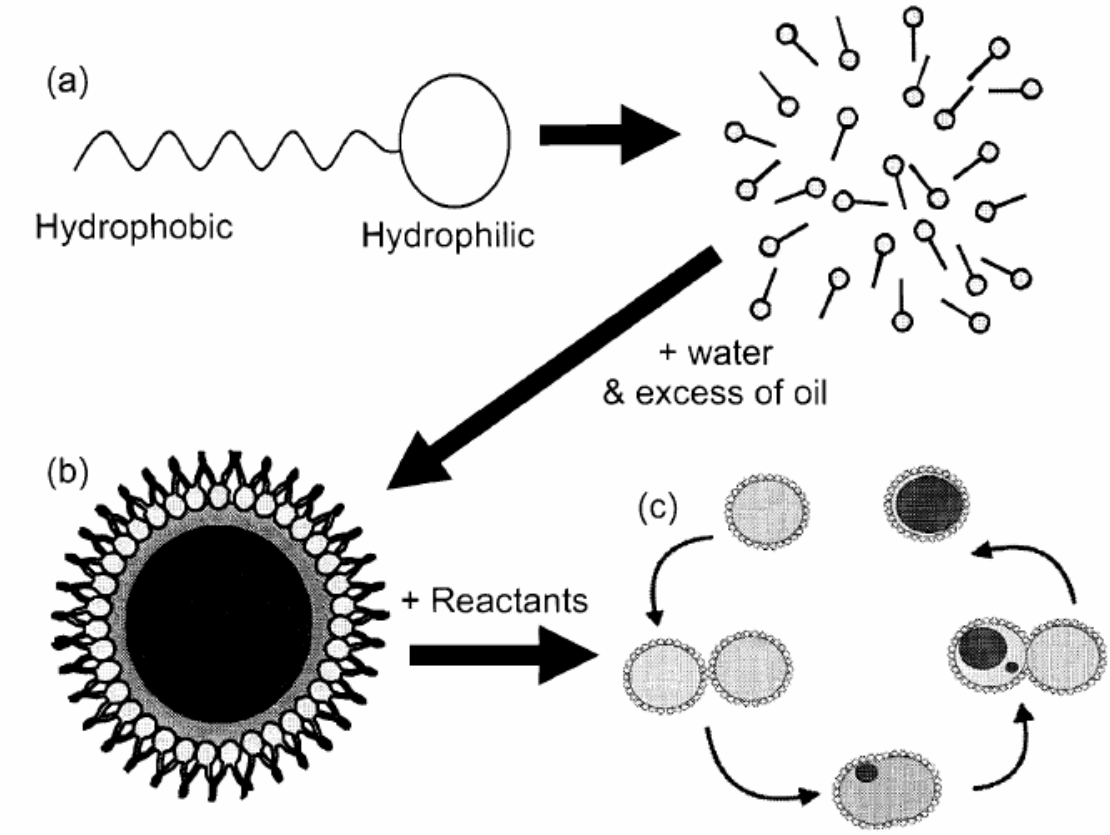

Figure 2.5 *Illustration of a reverse micelle system (a) The surfactant has a hydrophobic 'tail' and hydrophilic 'head' (b) Mixed with water and an excess of oil, a reverse micelle is formed (c) Reactants contained within reverse micelles mix and share contents allowing the reaction to take place*

Micelle can be found in two forms and although the term micelle is often used to describe either type, strictly speaking a micelle is the region within the emulsion regime in which the oil forms spheres surrounded by surfactant within a large volume of water [120]. Reverse micelle are then the analogue of this with the surfactant coated aqueous spheres contained within a volume of oil. When the surfactant concentration is increased to a level such that there are large numbers of surfactant molecules on the surface, then these molecules start forming reverse micelles, leading to decrease in the surface tension.

In a reverse micelle the hydrophilic groups are in contact with each other and hence their interaction with the non polar solvent molecules is minimized. The formation of reverse micelles continues with an increase in surfactant concentration until a critical micelle concentration is reached. Once this critical micelle concentration is reached, a further increase in the surfactant will not alter the surface tension. When the concentration of the surfactant in a non polar solvent is greater than the critical micelle concentration, then the introduction of a polar solvent (water) in a minute quantities leads to its spontaneous dispersion in billions of tiny and almost spherical nanoscopic droplets. The surfactant molecules accumulate at the surface of water drops with the hydrophilic groups facing inwards. The hydrophilic groups are kept away from the non-polar solvent, thereby minimizing the energy of the system. The small water droplets encapsulated in reverse micelles play the role of micro reactors, providing an isolated space for the reaction to take place. The reaction occurs simultaneously in the large number of micro reactors, with consequent nucleation and growth of billions of particles. Now it is this water pool that makes the reverse micelle favorable for the synthesis of nanoparticles because the water pool is in nanometer size which can be controlled by controlling the water content.

These reverse micelles serve as a useful system for growing nanoparticles based on aqueous, room temperature reactions. Reactions progress within the water pool which then restrict the growth of the particles and limit their size (Figure. 2.5c). Studies of micelle systems have demonstrated that the water pools are uniform in size [121-125], thereby providing an environment in which to produce uniform nanoparticles of a given size [124].

The ratio of surfactant, water and oil governs what phase the mixture will form. A phase diagram of these three components, as seen in figure 2.6, illustrates the regions in which both micelles and reverse micelles are formed. While the region of the phase diagram in which reverse micelle formation can occur seems small, a large number of reverse micelle sizes can be produced within this area [125]. Although individual phase diagram are valid only for specific water-oil-surfactant systems, some traits are common to all such systems [126]. When surfactant and water are mixed in oil in proportion corresponding to the reverse micelle region of the phase diagram, the water and surfactant self-assemble to form reverse micelles of uniform sized aqueous spheres. In

the case of reverse micelles, as the water to surfactant ratio is increased the micelles become larger.

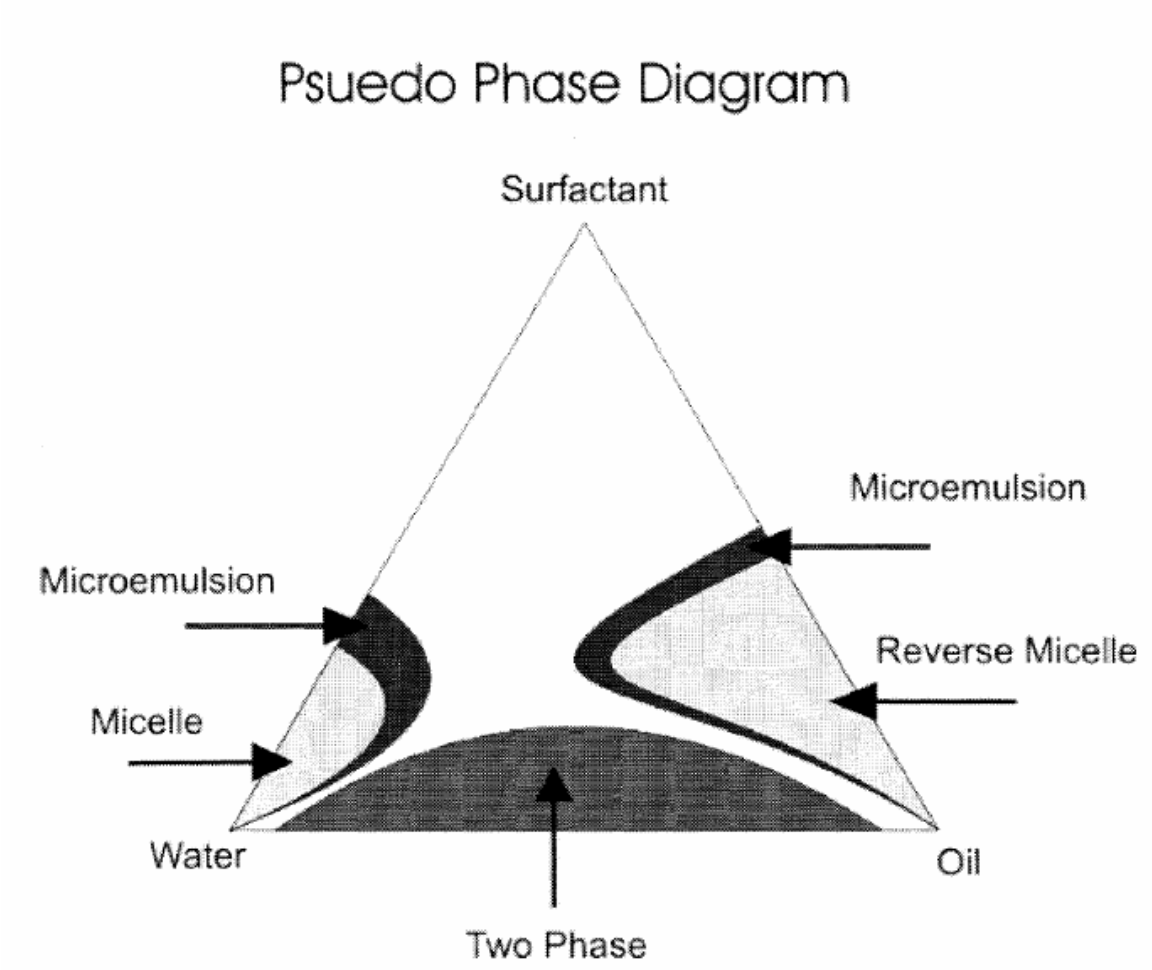

Figure 2.6 *A phase diagram illustrating the effects of the water/oil/surfactant ratio on the solution phase*

2.3.2 Synthesis in reverse micelles

Reverse micelle systems lend themselves to aqueous, room-temperature reactions [127,128]. Co-precipitation and reduction reactions done under these conditions are therefore easily adapted to reverse micelle synthesis [129]. Reactants are dissolved in water and then mixed with surfactant and oil to produce reverse micelle solutions containing the various components. As the reaction proceeds the reverse micelles restrict the growth of particles [130]. In conjunction with the size uniformity of the aqueous spheres this

produces nanoparticles (from 5 to 30 nm in size [131]) with a narrow particle size distribution.

When the reactant solutions are mixed, particle growth within the micelles occurs via reactant exchange of neighboring water pools (Figure 2.5c) [132]. Thinking of the micelles as spongy spheres, three things can happen when two micelles come into contact: 1) they can collide and bounce off one another; 2) they can stick to one another; 3) or they can merge into a "super" micelle and in the process share their contents. The lifetime of the micelle exchange is of the order of micro seconds [133]. This is a few orders of magnitude longer than their contents require to form nanosized particles [124,127,134]. The surfactant, oil phase, and to a lesser degree the concentration of micelles per unit volume, can have a significant influence on the rate and nature of the micelle interactions. This in turn can lead to differences in reaction rates, particles growth and size [135,136].

There are three basic types of surfactant systems that have been employed for synthesizing ferrites (Figure 2.7) with the difference being determined by the nature of the hydrophilic segment.

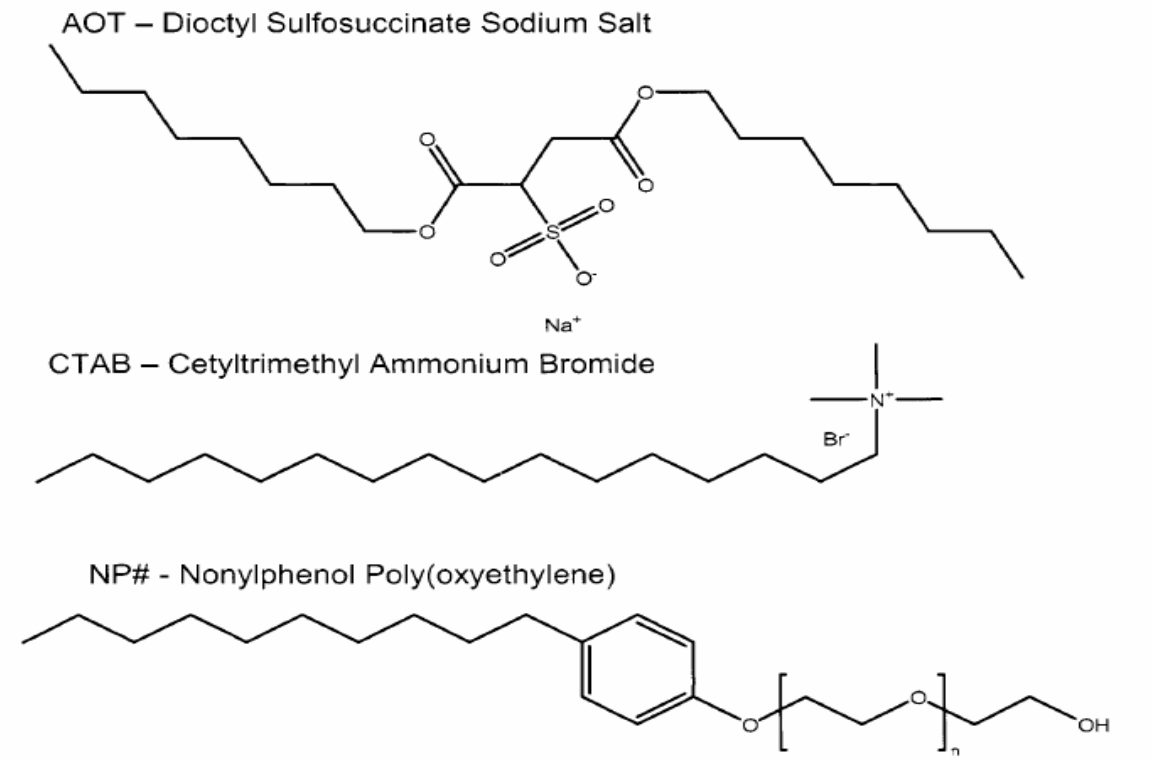

Figure 2.7 *Chemical structure of three common surfactants*

Careful consideration of a number of factors is advisable when selecting a suitable surfactant, starting with the reactants and reaction conditions. The surfactant should be chemically inert with respect to all other components of the microemulsion. This is particularly relevant when the system contains oxidizing or reducing agents. On this matter, both cetyl trimethylammonium bromide (CTAB) and sodium bis (2-ethylhexyl) sulfosuccinate (AOT) are stable against mild oxidizers, like dilute H_2O_2 and mild reducing agents, such as hydrazine. By far, the most extensively studied surfactant is sodium dioctylsulfosuccinate (AOT) which contains an anionic hydrophilic group [125, 137-140]. AOT generally offers a wider range of resultant nanoparticle size. Because of its two branched hydrocarbon chains (Figure 2.8), this molecule possess a high ratio of hydrophobic tail volume to head group surface area, which is predicted to be a key factor in reverse micelle formation [141]. Also it does not require co-surfactants to form reverse micelles.

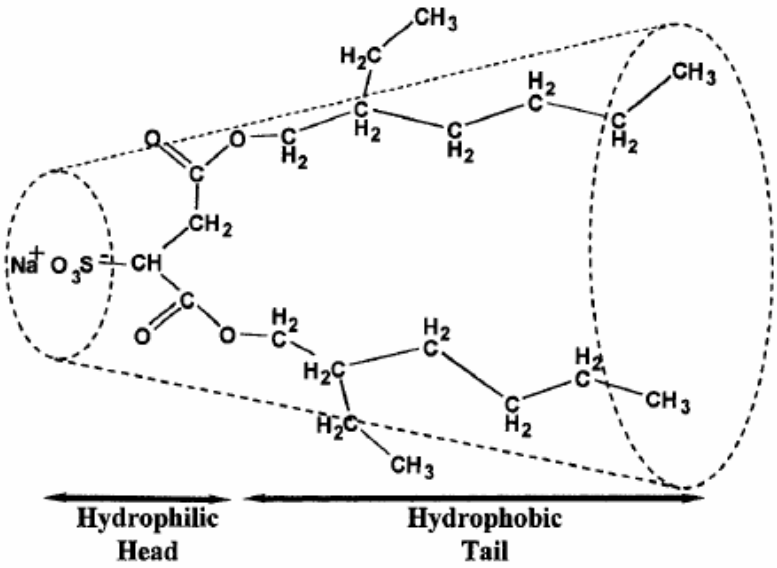

Figure 2.8 *Molecular structure of sodium bis(2-ethylhexyl) sulfosuccinate (AOT) surfactant. The dotted lines represent the cone-like packing structure of the twin tail surfactant*

The AOT/isooctane reverse micelle system has been well characterized [124,126] and widely employed in the successful synthesis of numerous nanomaterials including simple ferrites such as $Ni_{0.5}Zn_{0.5}Fe_2O_4$ particles. It was therefore determined to use AOT as a

starting point in the development of a synthetic technique for production of the nano nickel-zinc ferrite particles. Once this technique had been realized, the next step would be the adaptation of this synthesis to other ferrite systems to evaluate their effect described herein.

2.4 X-ray diffraction

X-ray diffraction technique is used for the realization of structural property and can be employed exclusively to categorize the crystalline phase in the sample. The fundamental of X-ray diffraction is best explained by the Bragg's equation which places the condition for the constructive interference for the scattered X-ray from the successive atomic planes formed by the crystal lattice of the material. The Bragg's condition is given by:

$$2d \sin\theta = n\lambda \quad \text{.....(2.12)}$$

where,

θ = Angle that X-rays make with the sample surface

d = Inter-planar spacing

λ = Wavelength of incident radiation

n = Order of diffraction

These spectra can also give us information about the average particle/grain size, lattice parameter, crystal structure of the samples, etc.

2.4.1 Indexing and determination of lattice constants, particle size

The indexing of pattern has been done by using the powder X-ray software developed by Chen Dong [142]. If one has knowledge of the crystal structure, then different 'a' values of lattice constants are tried so that all peaks are assigned (h, k, l) values. Secondly, the exact 2θ values at which reflections are observed are noted carefully and then with the help of Bragg's law in the form:

$$a = \frac{(\lambda/2)\left[h^2+k^2+l^2\right]^{1/2}}{\sin\theta} \quad \text{.....(2.13)}$$

the corresponding 'a' values are calculated and compared with that observed using the powder X-ray software.

In order for a crystal to diffract at all, the reflection plane must meet the incident X-ray beam at one of the specified angles. It is necessary in order that the X-ray reflected from the different points on these planes reach the detector in phase. When the diffracting planes are large, contain thousand of parallel planes, this condition is satisfied very accurately and hence the diffraction maxima are sharp. However, in case of smaller crystallites, this condition is somewhat relaxed due to the smaller number of co-operating planes. Therefore, when the crystallites are so small that they contain only a few planes in phase, diffraction by these planes is no longer valid for producing sharp diffraction minima. In general, reduction in crystallites size affects the broadening of the peaks. If the path difference between rays scattered from the first two planes differs only slightly by an integral multiple of wavelength then the planes scattering a ray exactly out of phase with the ray from the first plane will lie deep within the crystal. As the crystal is too much small that this plane does not exit then complete cancellation of all the scattered rays will not exit this means that there is a correlation between the amount of out of phaseness that can be tolerated and the size of the crystal. Therefore the broadening of the peak depends upon the particle size, which can be calculated [143,144]. The particle size D was determined from the broadening of X-ray diffraction peaks using the Debye-Scherrer eqn. [145],

$$D = \frac{k\,\lambda}{FWHM * Cos\theta_{hkl}} \quad \text{.....(2.14)}$$

where D is the particle size in Å, k is the shape factor (usually taken as 0.9), λ is the X-ray wavelength (1.54 Å for Cu-K_α), FWHM is the full width at half maximum and θ is the Bragg's angle in degrees.

2.5 Mössbauer spectroscopy

Mössbauer spectroscopy can give very precise information about the chemical, structural, magnetic and time-dependent properties of a material. Key to the success of the technique is the discovery of recoilless gamma ray emission and absorption, now referred to as the 'Mössbauer Effect', named after its discoverer Rudolph Mössbauer,

who first observed the effect in 1957 and received the Nobel Prize in Physics in 1961 for his work.

The Mössbauer effect provides information about the local magnetic and electronic environment of Mössbauer nuclei (i.e. ^{57}Fe or ^{119}Sn) in a sample. Since this technique does not require the application of an external field, it is possible to observe very weak magnetic interactions, without the perturbing effect of the external field [146,147]. The principle of the Mössbauer effect is essentially the observation of fine structure in the transition between different nuclear energy levels, *e.g.* of ^{57}Fe or ^{119}Sn nuclei, by means of nuclear resonance absorption or fluorescence radiation. In the experiment a source containing ^{57}Co nuclei provides a convenient supply of excited ^{57}Fe nuclei, which decay into the ground state accompanied by a gamma ray emission (Figure 2.9). When the gamma ray energy matches precisely the energy gap in the sample being studied, a nuclear transition occurs in absorption. For this purpose the source moves with a certain velocity v and the frequency of the gamma ray can be slightly adjusted because of the Doppler effect. Because of the high frequency of the gamma photon, the Doppler shifts can be quite significant. In this way one can probe any splitting in the ground state in the source or absorber nucleus which might result from magnetic or other interactions. Figure 2.9 shows the absorption peak occurring at $v = 0$, since source and absorber are identical. The energy levels in the absorbing nuclei can be modified by their environment in three main ways: by the isomer shift, quadrupole splitting and magnetic splitting.

2.5.1. Isomer shift

The isomer shift arises due to the slight change in the Coulomb interaction between the nuclear and electronic charge distributions over the nuclear volume which is associated with the slight increase of the ^{57}Fe nucleus in the I =3/2 state. In a Mössbauer spectrum the isomer shift is the velocity of the center of gravity of the spectrum with respect to zero velocity. As the isomer shift is proportional to the s-electron density of the nucleus, this can be used to gain information about the valence state of the Mössbauer atom or of charge transfer, and is also useful to detect lattice expansion/compressions, as these also change the electronic density [148]. The hyperfine splitting scheme for the ^{57}Fe

Mössbauer transition induced by Coulomb interaction (isomer shift) is shown in figure 2.9 (a).

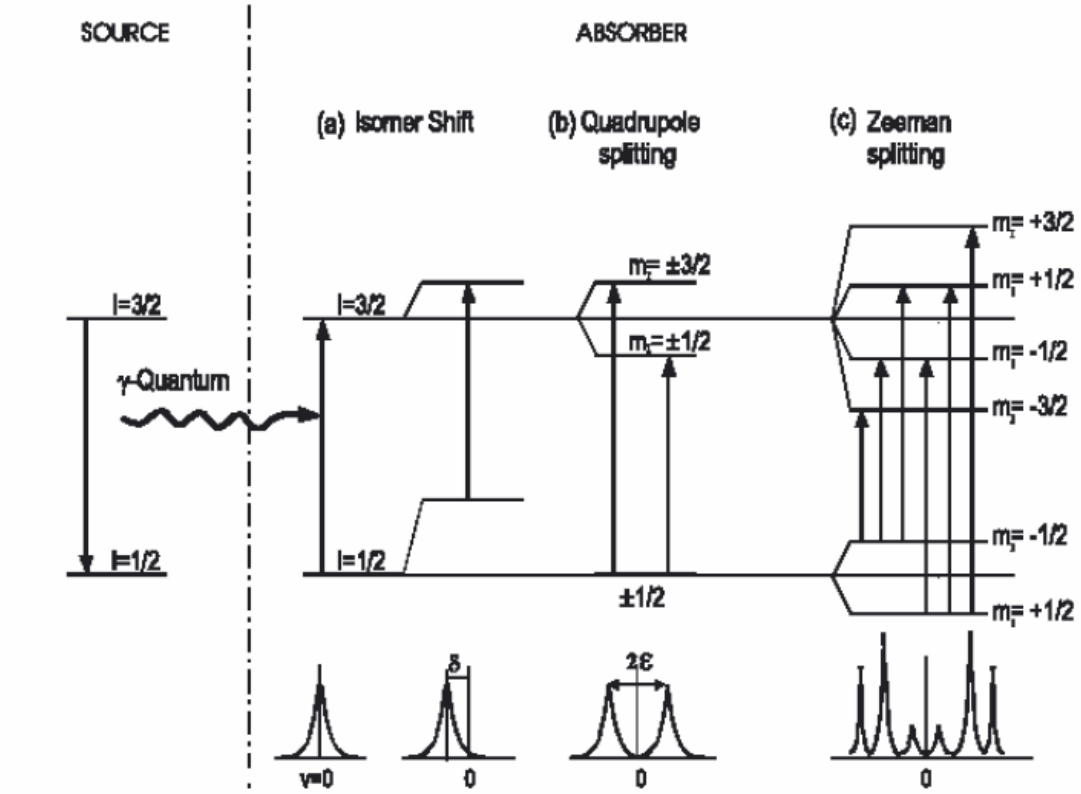

Figure 2.9 *Hyperfine splitting scheme for the ^{57}Fe Mössbauer transition induced by (a) Coulomb interaction (isomer shift), (b) quadrupole interaction and (c) magnetic dipole (Zeeman) interaction between the nucleus and the electrons*

2.5.2. Quadrupole splitting

If the nucleus is subjected to an electric field gradient, the interaction between the nuclear quadrupole moment and the electric field gradient splits the excited I = 3/2 state into a doublet, and a two line Mössbauer spectrum is produced and the splitting is called quadrupole splitting [149]. Its applications are the investigations of local symmetry around the Mössbauer atom and the configuration of its valence electrons. The quadrupole splitting scheme for the ^{57}Fe Mössbauer transition induced by Coulomb interaction is shown in figure 2.9 (b).

2.5.3. Magnetic or Zeeman splitting

In the presence of a magnetic field the nuclear spin moment experiences a dipolar interaction with the magnetic field i.e. Zeeman splitting. There are many sources of magnetic fields that can be experienced by the nucleus. The total effective magnetic field B_{eff} of the Mössbauer nucleus is given by: $B_{eff} = B_{contact} + B_{orbital} + B_{dipolar} + B_{applied}$, [150-155] the first three terms being due to the atom's own partially filled electron shells. $B_{contact}$ is due to the spin on those electrons polarising the spin density at the nucleus, $B_{orbital}$ is due to the orbital moment on those electrons, and $B_{dipolar}$ is the dipolar field due to the spin of those electrons. This effect can be used to detect magnetic exchange interactions and local magnetic fields. This kind of splitting is illustrated in figure 2.9 (c).

2.5.4 Line width and line shape

The values of experimentally determined full width at half maximum (FWHM), Γ_{ex}, and the nuclear transition energy, E_θ yield the following expression for resonance absorption which is generally shows a Lorentzian shape:

$$I(E) = \frac{\Gamma_{ex}}{2\pi}\left[(E_\theta - E_\gamma)^2 + \left(\frac{1}{2}\Gamma_{ex}{}^2\right)\right]^{-1} \quad \text{.....(2.15)}$$

where E_γ is the gamma ray energy and E_θ is equal to the difference between energy of excited state (E_{ex}) and ground state (E_{gd}). The line width of the emission or absorption lines is inversely proportional to the mean life time τ of the excited state $\Gamma\tau = h/2\pi$ where h is Planck's constant. The half width of 14.4 keV transition of ^{57}Fe nucleus is equal to 4.5×10^{-9} eV corresponding to 0.19 mm/s velocity between source and absorber. The broadening of lines of Mössbauer spectra is mainly attributed to the relaxation effects [156], presence of lattice defects, which may be uniformly or non-uniformly distributed near the source atom, mechanical vibrations of spectrometer, larger thickness of absorber, large solid angle, low resolution, quadrupole shifts etc. [157]. The broadening of various lines can be used to draw important inferences about the internal structure and environment around the Mössbauer nuclei.

2.5.5 Relaxation effects

The internal magnetic field at a nuclear site is proportional to the resultant spin of the ion, which may change due to several possible mechanisms. This affects the hyperfine interactions giving rise to the relaxation phenomenon [158], which is responsible for producing line broadening and growth of inner lines at the cost of outer lines of the magnetic hyperfine spectrum [159,160]. During the process of spin fluctuation, an ion either absorbs or emits an energy quantum equal to the difference in energy between the ionic spin states. The main process responsible for the spin fluctuation can be grouped as [161-163],

(i) Electronic spin relaxation

(ii) Superparamagnetic fluctuations

The electronic spin relaxation arises when the ionic spin exchange energy with the neighboring spins or lattice phonons. In this process, the ion fluctuates from one spin state to another and stays there for a time, called electronic relaxation time, before making a transition to some other state. Depending upon the agency with which ion exchanges energy, the electronic relaxation mechanism may further be classified as follow:

(a) Spin-spin relaxation, and

(b) Spin-lattice relaxation.

In spin-spin relaxation mechanism, the ion exchanges energy with another paramagnetic ion with which it is coupled through dipolar or exchange interaction. In spin-lattice relaxation process, the ionic spin exchanges energy with lattice vibrations. The lattice vibrations modulate the crystalline electric field and thus affect the orbital motion of electron of the ion [164,165]. This in turn acts on spin state through spin-orbit coupling. The spin-phonon interaction then proceeds indirectly via spin-orbit and orbit-lattice interactions, as the spin of the ion is not sensitive to the electric field directly. The spin-spin relaxation time is generally very small as compared to spin-lattice relaxation time and it is the spin-lattice relaxation time that governs the time required for transition from one orientation of the net spin (S_Z) to another. Lowering the temperature also increases this relaxation time. The time dependence of the nuclear magnetic field at the site of the nucleus follows the time dependence of S_Z. In ferromagnetic and antiferromagnetic

materials the interactions between the spins are so strong that these create a preferred direction for S_Z. It has been shown that the observed magnetic hyperfine spectra can be understood using a spin wave treatment [166].

Superparamagnetic spin fluctuations in a solid are exhibited by physically small magnetic particles or by small regions called clusters, which are more magnetic than the rest of the solid or are magnetically de-coupled from the rest of the solid. In such a case the magnetization vector of the particle or cluster starts fluctuating randomly among easy direction of magnetization in the presence of the thermal energy [167].

2.5.6 In-field Mössbauer spectroscopy

An application of an external magnetic field brings us an other important knowledge about the structure of ferrites and an arrangement of the magnetic moments. It allows to separate sufficiently the Mössbauer lines belonging to iron atoms in the tetrahedral and octahedral sites of ferrite. If there exists a non-collinear spin configuration as for example, Yafet-Kittel type or helical spin structure, then the lines 2 and 5 of the Mössbauer sextet do not disappear. If, however, the spins alignment is of Neel type or deviation from the Neel type in the sense that spins are oppositely directed within the sublattices, then the lines 2 and 5 must disappear, as the atomic spin moments on the (A) site and (B) site of a collinear ferrimagnetic align parallel and antiparallel to the applied magnetic field. In the presence of the external magnetic field applied parallel to the γ-ray direction, the effective magnetic field, B_{eff} , at the ^{57}Fe nucleus is expressed as a vector sum of the hyperfine magnetic field, B_{hf}, and the external magnetic field, B_{ext}, i.e. $B_{eff} = B_{hf} + B_{ext}$. The effective field is thus inclined at an angle Ψ to the γ-ray direction. It follows that $B^2_{hf} = B^2_{eff} + B^2_{ext} - 2\ B_{ext}\ B_{eff}\ Cos\Psi$. The direction of hyperfine field is, however, antiparallel to the orientation of the magnetic moment of the iron atom which is explained to be a result of the prevailing negative Fermi contact term. The line intensities (i.e. the areas of the peaks in a magnetic sextet), proportional to the Clebsch-Gordan coefficients are then commonly given by

$$A_{1,6}\ (\Psi) = 3\ (1+ \cos^2 \Psi)$$

$$A_{2,5}\ (\Psi) = 4\ \sin^2 \Psi$$

$$A_{3,4}\ (\Psi) = 1+ \cos^2 \Psi,$$

where A_{ij} is the intensity of the line i or j (i, j = 1, 6; 2, 5; 3, 4). The intensities of the lines in the magnetically split spectrum are thus in the ratio of 3: x : 1:1 : x: 3 with $x = 4\sin^2 \Psi/(1+\cos^2 \Psi)$. The value of Ψ is then usually calculated from

$$\Psi = \arcsin \{6r/(4+3r)\}^{1/2}$$

Or equivalently form

$$\Psi = \arccos\{(4-s)/(4+s)\}^{1/2}$$

where $r = A_{2,5}/A_{1,6}$ and $s = A_{2,5}/A_{3,4}$, respectively. When some spins in the particle are not fully align in a direction of the external magnetic field, $A_{2,5} \neq 0$ and it implicates that $\Psi \neq 0$. NORMOS (SITE/DIST) fitting package [168] was used for fitting of the data, which contains code to read and write the data files.

References

[1] Anderson P. W. *Phys. Rev*. **1950**, 79, 350.

[2] Smit J. and Wijn H. P. J. *Ferrites* New York, John Wiley and Sons, **1959**.

[3] Gorter E. W. *Philips. Res. Rept*. **1954**, 9, 321.

[4] Neel L. *Ann. Phys.* (Paris) **1948**, 3, 137.

[5] Gilleo M. A. *Phys. Rev.* **1958**, 109, 777.

[6] Gilleo M. A. *J. Phys. Chem. Solids.* **1960**, 13, 33.

[7] Ishikawa Y. *J. Phys. Soc. Japan* **1962**, 17, 1877.

[8] Nowik I. *J. Appl. Phys*. **1969**, 40, 872.

[9] Geller S. *Phys. Rev.* **1969**, 181, 980.

[10] Yafet Y. and Kittel C. *Phys. Rev.* **1952**, 87, 290.

[11] Kittel C. *Phys. Rev.* **1946**, 70, 965.

[12] Dorman J. L. and Fiorani D. (eds.) *Magnetic properties of Fine particles* North-Holland, Amsterdam, **1992**.

[13] Lu L., Sui M. L. and Lu K. *Science* **2000**, 287, 1463.

[14] Raj K., Moskowitz R. and Casciari R. *J. Magn. Magn. Mater*. **1995**, 149, 174.

[15] Ozaki M. *Mater. Res. Bull.* XIV **1989**, 35.

[16] Gleiter H. *Nanostruct. Mater*. **1992**, 1, 1.

[17] Neel L. *Ann. Geophys.* **1949**, 5, 99.

[18] Bean C. P. and Livingston J. D. *J. Appl. Phys.* **1959**, 30 S, 120S-129S.

[19] Dormann J. L. *Revue Phys. Appl.* **1981**, 16, 275.

[20] Morrish A. H. *The Physical Principles of Magnetism* New York, Wiley, **1965**.

[21] Brown W. F. *Jr. Phys. Rev.* **1963**, 130, 1677.

[22] Aharoni A. *Phys. Rev.* **1969**, 177, 793.

[23] Shtrikman S. and Wohlfarth E. P. *Phys. Lett. A* **1981**, 85, 467.

[24] Dormann J. L., Bessais L. and Fiorani D. *J. Phys. C: Solid State Phys*. **1988**, 21, 2015.

[25] Dormann J. L., Cherkaoui R., Pinu L., Nogues M., Lucari L., D´Orazio F., Fiorani D., Garcia A., Tronc E. and Jolivet J. P. *J. Magn. Magn. Mater.* **1998**, 187, L139.

[26] Luo W., Nagel S. R., Rosenbaum T. F. and Rosensweig R. E. *Phys. Rev. Lett.* **1991**, 67, 2721.

[27] Zhang J., Boyd C. and Luo W. *Phys. Rev. Lett.* **1996**, 77, 390.

[28] Vincent V., Yuan Y., Hamman J., Hurdequint H. and Guevara F. J. *J. Magn. Magn. Mater.* **1996**, 161, 209.

[29] Morup S. and Tronc E. *Phys. Rev. Lett.* **1994**, 72, 3278.

[30] Berkowitz A. E., Shuele W. J. and Flanders P. J. *J. Appl. Phys.* **1968**, 39, 1261.

[31] Coey J. M. D. *Phys. Rev. Lett*. **1971**, 27, 1140.

[32] Haneda K., Kojima H., Morrish A. H., Picone J. and Wakai K. *J. Appl. Phys.* **1982**, 53, 2686.

[33] Lin D., Nunes A. C., Majkrzak C. F. and Berkowitz A. E. *J. Magn. Magn. Mater*. **1995**, 145, 343.

[34] Gazeau F., Dubois E., Hennion M., Perzynski R. and Raikher Yu L. *Europhys. Lett*. **1997**, 40, 575.

[35] Gazeau F., Bacri J. C., Gendron F., Perzynski R., Raikher Yu L., Stepanov V. I. and Dubois E. *J. Magn. Magn. Mater.* **1998**, 186, 175.

[36] Pankhurst Q. A. and Pollard R. J. *Phys. Rev. Lett.* **1991**, 67, 248.

[37] Parker F.T., Foster M. W., Margulies D. T. and Berkowitz A. E. *Phys. Rev. B* **1993**, 47, 7885.

[38] Kodama R. H., Makhlouf S. A. and Berkowitz A. E. *Phys. Rev. Lett.* **1997**, 79, 1393.

[39] Linderoth S., Hendriksen P. V., Bodker F., Wells S., Davis K., Charles S. W. and Morup S. *J. Appl. Phys*. **1994**, 75, 6583.

[40] Morales M. P., Serna C. J., Bodker F. and Morup S. *J. Phys.: Condens. Matter*. **1999**, 11, 3058.

[41] Martinez B., Obradors X., Balcells LI, Rounanet A. and Monty C. *Phys. Rev. Lett.* **1998**, 80, 181.

[42] Nogues J. and Schuller I. K. *J. Magn. Magn. Mater.* **1999**, 192, 203.

[43] Stamps R. L. *J. Phys. D.: Appl. Phys.* **2000**, 33, R247.

[44] Kodama R. H., Berkowitz A. E., McNiff E. J. and Foner S. *Phys. Rev. Lett.* **1996**, 77, 394.

[45] Muro M. G. D., Battle X. and Labarta A. *Phys. Rev. B* **1999**, 59, 13584.

[46] Kodama R. H. and Berkowitz A. E. *Phys. Rev. B* **1999**, 59, 6321.

[47] Kodama R. H., Berkowitz A. E., McNiff E. J. and Foner S. *J. Appl. Phys.* **1997**, 81, 5552.

[48] Koksharov Yu A., Gubin S. P., Kosobudsky I. D., Yurkov G. Yu, Pankratov D. A., Ponomarenko L. A., Mikheev M. G., Beltran M., Khodoskovsky and Tishin A. M. *Phys. Rev. B* **2000**, 63, 12407.

[49] Dimitrov D. A. and Wysin G. M. *Phys. Rev. B* **1994**, 50, 3077.

[50] Dimitrov D. A. and Wysin G. M. *Phys. Rev. B* **1995**, 51, 11947.

[51] Kachkachi H., Ezzir A., Nogues M. and Tronc. E. *Euro Phys. J. B.* **2000**, 14, 681.

[52] Kachkachi H. and Dimian M. *J. Appl. Phys.* **2002**, 91, 7625.

[53] Kachkachi H. and Dimian M. *Phys. Rev. B* **2002**, 66, 174419.

[54] Labay Y., Crisan O., Berger L., Greeneche J. M. and Coey J. M. D. *J. Appl. Phys.* **2002**, 91, 8715.

[55] Trohidou K. N. and Blackman J. A. *Phys. Rev. B* **1990**, 41, 9345.

[56] Kerhrakos D. and Trohidou K. N. *J. Magn. Magn. Mater.* **1998**, 177-181, 943.

[57] Zianni X., Trohidou K. N. and Blackman J. A. *J. Appl. Phys*. **1997**, 81, 4739.

[58] Zianni X. and Trohidou K. N. *J. Appl. Phys.* **1999**, 85, 1050.

[59] Trohidou K. N., Zianni X. and Blackman J. A. *J. Appl. Phys.* **1998**, 84, 2795.

[60] Neel L. *J. Phys. Radium* **1954**, 15, 225.

[61] Dormann J. L., Fiorani D. and Tronc E. *Advan: Chem. Phys.* **1997**, XCVIII, 283.

[62] Rozman M. and Drofenik M. *J. Am. Ceram. Soc*. **1995**, 78, 2449.

[63] Tasaki A., Takao M. and Okunaga H. *Japn. J. Appl. Phys*. **1974**, 13, 27.

[64] Hadjipanayis G. C., Tang X., Gangopadhyay S., Yiping L., Sorensen C. M., Klabinde K. J., Kostikas A. and Papaefthymiou V. *Studies of Magnetic Properties of Fine particles and their Relevance to Material Science* eds. by Dorman J. L. and Fiorani D. Amsterdam, Elsevier Science Publishers **1992**.

[65] Martinez B., Riog A., Molins E., Gonzalez-Carreno T. and Serna C. J. *J. Appl. Phys.* **1998**, 83, 3256.

[66] Barei J. C., Perzinsky R., Salin D., Cabuil V. and Masart V. *J. Magn. Magn. Mater.* **1986**, 62, 36.

[67] Vollath D., Szabo D. V., Taylor R. D. and Willis J. O. *J. Mater. Res.* **1997**, 12, 2175.

[68] Sato T., Iijima T., Seki M. and Ingaki N. *J. Magn. Magn. Mater.* **1987**, 65, 252.

[69] Abu-Aljarayesh, Al-Bayrakdar A. and Mahmood S. H. *J. Magn. Magn. Mater*. **1993**, 123, 267.

[70] Gajbhiye N. S. *Metals Mater. Process.* **1998,** 10, 247.

[71] Berkowitz A. E., Lahut J. A., Jacobs I. S., Levison L. M. and Forester D. E. *Phys. Rev. Lett.* **1975**, 34, 594.

[72] Berkowitz A. E., Lahut J. A. and VanBuren C. E. *IEEE Trans. Magn.* **1980**, 16, 184.

[73] Morrish A. H. and Haneda K. *J. Appl. Phys*. **1981**, 52, 2496.

[74] Zheng M., Wu X. C., Zou B. S. and Wang Y. J. *J. Magn. Magn. Mater.* **1998**, 183, 152.

[75] Tang Z. X., Sorenson C. M., Klabunde K. J. and Hadjipanayis G. C. *Phys. Rev. Lett*. **1991**, 67, 3602.

[76] Chen J. P., Sorenson C. M., Klabunde K. J., Hadjipanayis G. C., Delvin E. and Kostikas A. *Phys. Rev. B* **1996**, 54, 9288.

[77] Morrish A. H., Haneda K. and Schurer P. J. *J. Phys. (Paris)* **1976**, 57,C6-301.

[78] Jiang J. Z., Goya G. F. and Rechenberg H. R. *J. Phys. Condens. Mater*. **1999**, 11, 4063.

[79] Morales M. P., Serna C. J., Bodker F. and Morup S. *J. Phys.: Condens. Matter*. **1997**, 9, 5461.

[80] Lotgering F. K. *Philips Res. Rep.* **1965**, 20, 320.

[81] Brabers V. A. M. *J. Phys. Chem. Solid*s **1971**, 32, 2118.

[82] Simsova J. and Simsa Z. *Czech J. Phys. B* **1974**, 24, 449.

[83] Pannaparayil T., Marande R., Komarneni S. and Samkar S. G. *J. Appl. Phys.* **1988**, 64, 5641.

[84] Morrish A. H., Li Z.W. and Zhou Z. X. *J. Phys.* (Paris) **1997**, C1, 513.

[85] Sawatzky G. A., Wounde F. V. D. and Morrish A. H. *Phys. Rev*. **1969**, 187, 747.

[86] Lingenza S., Szynkarczuk M. and Miracka M. *J. Magn. Magn. Mater.* **1980**, 15-18, 1433.

[87] Respaud M., Broto J. M., Rakoto H., Fert A. R., Thomas L. Barbara B., Verelst M., Snoeck E., Lecante P., Mosset A., Osuna J., Ould T. E., Amiens C. and Chaudret B. *Phys. Rev. B* **1998**, 57, 2925.

[88] Cox D. M., Trevor D. J., Whetten R. L., Rohlfing E. A. and Kaldor A. *Phys. Rev. B* **1985***,* 32, 7290.

[89] Luborsky F. E. and Lawrence P. E. *J. Appl. Phys.* **1961**, 32, 2315.

[90] Furubayashi T., Nakatani I. and Saegusa N. *J. Phys. Soc. Japan* **1995**, 56, 11527.

[91] Chen J. P., Sorenson C. M., Klabunde K. J. and Hadjipanayis *Phys. Rev. B* **1995**, 51, 11527.

[92] Heer W. A. de, Milani P. and Chatelain A. *Phys. Rev. Lett.* **1990**, 65, 488.

[93] Buecher J. P., Douglass D. C. and Bloomfield L. A. *Phys. Rev. Lett.* **1991**, 66, 3052.

[94] Douglass D. C., Cox A. J., Bucker J. P. and Boomfield A. *Phys. Rev. B* **1993**, 47, 12874.

[95] Cox A. J., Louderback J. G. and Bloomfield A. *Phys. Rev. Lett*. **1993**, 71, 923.

[96] Bilas L. M. L., Chatelain A. and Herr-de W. A. *Science* **1994**, 265, 1682.

[97] Feng L., Press M. R., Khanna S. N. and Jena P. *Phys. Rev. B* **1989**, 39, 6914.

[98] Merikoski J., Timonen J., Mnninen M. and Jena P. *Phys. Rev. Lett*. **1991**, 66, 398.

[99] Khanna S. N. and Linderoth S. *Phys. Rev. Lett.* **1991**, 67, 742.

[100] Reddy R. V., Khanna S. N. and Dunlap B. I. *Phys. Rev. Lett.* **1993**, 70, 3323.

[101] Zhi-quing L. and Bing-Lin Gu. *Phys. Rev. B* **1993**, 47, 13611.

[102] Kaiming D., Jinlong Y., Chuanyun X. and Klein W. *Phys. Rev. B* **1996**, 54, 2191.

[103] Sepelak V., Baabe D., Mienert D., Litterst F. J. and Becker K. D. *Scripta Mater.* **2003**, 48, 961.

[104] Bhowmik R. N., Ranganathan R., Sarkar S., Bansal C. and Nagarajan R. *Phys. Rev.*

B **2003**, 68, 134433.

[105] Cullity B. D. *Introduction to Magnetic Materials*, Addision-Wesley, Reading, M A, **1972**.

[106] Wohlfarth E. P. in Magnetism: *A Treatise on Modern Theory and Materials* New York, Academic Press, **1963**.

[107] Bate G. *Ferromagnetic Materials* edited by E. P. Wohlfarth, North-Holland Publishing Co. Hauge Vol.2 **1980**.

[108] Pal M., Brahma P., Hakravorty D., Bhattacharya D. and Maiti H. S. *J. Magn. Magn. Mater.* **1996**, 164, 256.

[109] Herzer G. *IEEE Trans. Mag*. **1990,** 26, 1397.

[110] Smit J. *Adv. Ceram.* **1986**, 16, 1.

[111] Visser E. G. and Johnson M. T. *J. Magn. Magn. Mater.* **1991**, 101, 143.

[112] Rikukawa H. *IEEE Trans. Magn.* **1982**, 18, 1535.

[113] Chikazumi S. *Physics of Ferromagnetism* 2nd edition, New York, Oxford University Press, **1997**.

[114] Leslie-Pelecky D. L. and Rieke R. D. *Chem. Mater.* **1996**, 8, 1770.

[115] Yener D. O. and Giesche H. *J. Am. Ceram. Soc*. **2001**, 84**,** 1987.

[116] Nanni A. and Dei L. *Langmuir* **2003**, 19, 933.

[117] Gan L. M., Zhang L. H., Chan H. S. O., Chew C. H. and Loo B. H. *J. Mater. Sci.* **1996**, 31, 1071.

[118] Pileni M. P. *Am. Chem. Soc.* **2003**, 225, U18.

[119] Wennerstrom H., Soderman O., Olsson U. and Lindman B. *Colloids and Surface A* **1997**, 123-124, 13-26.

[120] Winsor P. A. *Chem. Rev.* **1963**, 68, 1.

[121] Eastoe J., Fragneto G., Robinson B. H., Towey T. F., Heenan R. K. and Leng F. J. *J. Chem. Soc. Faraday Trans.* **1992**, 88, 461-471.

[122] Eastoe J., Steytler D. C., Robinson B. H., Heenan R. K. and North A. N. *J. Chem. Soc. Faraday Trans.* **1994**, 90, 2497-2504.

[123] Eastoe J., Chatfield S. and Heenan R. *Langmuir* **1994**, 10, 1650-1653.

[124] Pileni M.P. *Structure and reactivity in reverse micelles* Amsterdam, Elsevier, **1989**.

[125] Zulauf M. and Eicke H-F. *J. Phys. Chem.* **1979**, 83, 480-486.

[126] Wennerstrom H. *Colloids and Surfaces A: Physicochemical and Engineering Aspects* **2000**, 167, 209-214.

[127] Pileni M. P. *J. Phys. Chem.* **1993**, 97, 6961.

[128] Sims J., Kumbhar A., Lin J., Agnoli F., Carpenter E., Sangregorio C., Frommen C., Kolesnichenko V. and O'Connor C. *J. Molecular Crystals and Liquid Crystals* **2002**, 379, 113.

[129] Lin X. M., Sorensen C. M., Klaunde K. J. M and Hadjipanayis G. C. *Langmuir* **1998**, 14, 7140.

[130] Rivas J., Quintela M. L., Perez J. L. and Liz L. *IEEE Trans. Magn.* **1993**, 29, 2655.

[131] O'Connor C. J., Seip C. T., Carpenter E. E., Li S. C. and John V. T. *Nanostruc. Mater.* **1999**, 12, 65.

[132] Eicke H. F. *Water-in-oil microemulsion phenomenon: In surfactants in solution* eds. Mittal K. and Lindman L. New York, Plenum Press, **1984**, 3, 1533.

[133] Wennerstrom H., Morris J. and Olsson U. *Langmuir* **1997**, 13, 6972.

[134] Pileni M. P. *Advan. Colloid and Inetrface Science* **1993**, 46, 139.

[135] Cason J. P., Miller M. E., Thompson J. B. and Roberts C. B. *J. Phys. Chem. B* **2001**, 105, 2297.

[136] Kitchens C. L., Mcleod M. C. and Roberts C. B. *J. Phys. Chem. B* **2003**, 107, 11331.

[137] Eastoe J., Robinson B. H., Steytler D. C. and Thronleeson D. *Advan. Colloid and Inetrface Science* **1991**, 36, 1.

[138] Petit C., Lixon P. and Pileni M. P. *Langmuir* **1991**, 7, 2620.

[139] Pileni M. P., Zemb T. and Petit C. *Chem. Phys. Lett.* **1985**, 118, 414.

[140] Jain T. K., Varsheny M. and MAitra A. *J. Phys. Chem.* **1989**, 93, 7409.

[141] Mitchelle D. J. and Ninham B. W. *J. Chem. Soc. Faraday Trans.* 2, **1981**, 77, 601.

[142] Dong C. *J. Appl. Cryst*. **1999**, 32, 838.

[143] Kulg H. P. and Alexander L. E. *X-ray Diffraction Procedures*, 2nd Edition, New York, John Wiley & Sons Inc. **1974**.

[144] *International Tables for X-ray Crystallography* Birmingham U. K., Kynoch Press Vol. I **1952**, Vol. II **1959** and Vol. III **1962**.

[145] Cullity B. D. *Elements of X-ray Diffraction* Addison-Wesley Publ. Co. **1978**.

[146] Sauer Ch. and Zinn W. *Magnetic Multilayers* eds. Bennet L. H. and Watson R. E., Singapore, World Scientific, **1993**.

[147] Wegener H. *Der Mössbauer Effect und seine Anwendung in Physik und Chemie* Germany, Bibliograph. Institut Mannheim, **1966**.

[148] Cohen M. H. and Reif F. *Solid State Physics* **1957**, 5, 321.

[149] Marshall W. and Johnson C. E. *J. Phys. Radium* **1962**, 23, 733.

[150] Wounde F. V. D. and Sawatzky G. A. *Phys. Rev. B* **1971**, 4, 3159.

[151] Wounde F. V. *Mössbauer Spectroscopy and Magnetic Properties of Iron Compounds* Ph. D. Thesis, The Netherlands, Groningen University, **1966**.

[152] Wounde F. V. D. *Phys. Stat. Solidi.* **1966**, 17, 417.

[153] Perlow G. J., Johnson C. E. and Marshall W. *Phys. Rev.* **1965**, 140A, 875.

[154] Sharp E. J. and Miller J. E. *J. Appl. Phys.* **1969**, 40, 4680.

[155] Sharp E. J. and Miller J. E. *J. Appl. Phys.* **1970**, 41, 4718.

[156] O' Connor D. A. *Nucl. Inst. and Meth. B* **1963**, 21, 318.

[157] Kanjilal D., Chopra S., Narayanan M. M., Iyer I. S., Jha V., Joshi R. and Datta S. K. *Nucl. Instr. and Meth. B* **1993**, 238, 97.

[158] Bancroft G. M. *Mössbauer Spectroscopy* U. K., McGraw Hill Co. Ltd., **1973**.

[159] Wickman H. H. *Mössbauer Effect Methodology* Vol. 2, ed. I. J. Gruverman New York, Plenum Press, **1966**.

[160] Goldanskii V. I. and Makarov E. F. *Chemical Applications of Mössbauer Spectroscopy* eds. Golanskii V. I. and Herber R. H., New York, Academic Press, **1986**.

[161] Srivastava C. M., Shringi S. N. and Srivastava R. G. *Phys. Rev. B* **1976**, 14, 2032.

[162] Srivastava C. M., Shringi S. N. and Srivastava R. G. *Phys. Rev. B* **1976**, 14, 2041.

[163] Raj P. and Kulshreshta S. K. *Phys. Stat. Solidi* **1971**, 4A, 501.

[164] Kroning R. de L. *Physics* **1939**, 6, 33.

[165] Vleck J. H. V. *J. Chem. Phys.* **1939**, 7, 72.

[166] Woude F. V. D. and Dekker A. *J. Phys. Stat. Solidi* **1965**, 9, 775.

[167] Breen D. P., Krupka D. C. and Williams F. I. B. *Phys. Rev.* **1969**, 179, 241.

[168] Brand R. A., Lauer J. and Keune W. Phys. Rev. B **1984**, 31, 1630.

CHAPTER 3

EXPERIMENTAL METHODS

This chapter presents a brief description of generalized procedure for preparation of nanocrystalline ferrite samples and the experimental techniques employed in characterizing the samples under study. It is divided into two parts (i) Sample preparation techniques in its nano-sized form by reverse micelle technique (ii) Different characterization techniques which have been used for the study of structural, Mössbauer and magnetic properties of these materials.

3.1 Synthesis of nano ferrite particles

The AOT/isooctane reverse micelle system has been well characterized and widely employed in the successful synthesis of numerous nanomaterials including spinel ferrites such as $Ni_{0.5}Zn_{0.5}Fe_2O_4$ particles [1-3]. It was therefore determined to use AOT as a starting point in the development of a synthetic technique for production of the nano nickel-zinc ferrite particles. Once this technique had been realized, the next step would be the adaptation of this synthesis to indium doped nickel-zinc ferrite systems to evaluate their effect described herein.

The samples were prepared from stoichiometric amounts of respective metal chlorides. Synthesis protocol to obtain high quality ferrite samples in their nano and bulk form is elaborately discussed below.

The following chemicals were used in the synthesis procedure: $FeCl_2.4H_2O$ (Merk, 99.9%), $NiCl_2.6H_20$ (Merk, 95%), $ZnCl_2$ (Merk), $InCl_3$ (Merk), sodium dioctyl sulfosuccinate AOT (Aldrich, 99.99%) as a surfactant: isooctane (Qualigens, 99.9%) as the oil phase, hydrochloric acid (HCl), double distilled water as the aqueous phase, NH_4OH (25wt%) as a precipitating agent and methanol (99%) as a washing agent.

Figure 3.1 shows the schematic diagram for the synthesis of nanoferrite particles by reverse micelle technique. For the AOT\isooctane reverse micelle system, a stock solution of 0.56*M* AOT was prepared in isooctane. An aqueous phase was then prepared using 0.07*M* $FeCl_2.4H_2O$, 0.02*M* $NiCl_2.6H_20$ and 0.02*M* $ZnCl_2$ to make $Ni_{0.58}Zn_{0.42}Fe_2O_4$ nanoparticles. Using a divalent iron salt as a precursor component, pH of the aqueous metal ion solution was set as 1.2 to avoid early oxidation of ferrous ions. First microemulsion was prepared by adding aqueous phase containing ions into AOT/isooctane. The size of the water pools in reverse micelle can be controlled by

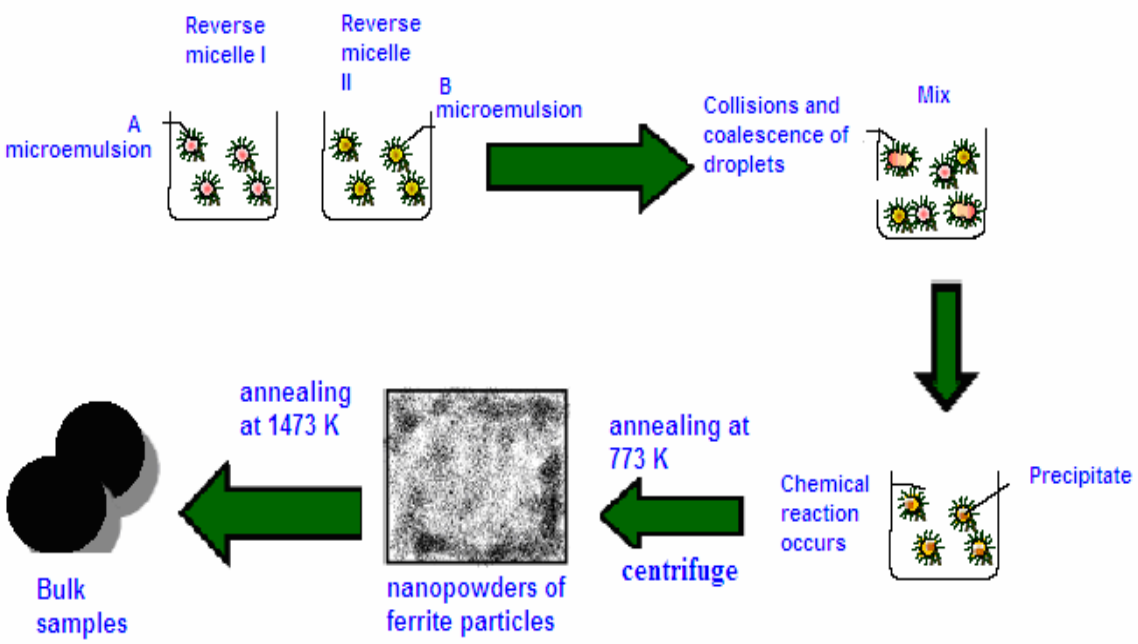

Figure 3.1 *Synthesis of nanoparticles by reverse micelle technique*

adjusting ω which is water to surfactant concentration ratio. The relative volume of AOT solution to water was 6:1, which corresponds to the ratio of water to surfactant (ω = $[H_2O]/[AOT]$) as 15.5. Second microemulsion was prepared by mixing ammonia solution into AOT/isooctane, keeping ω at 13.5. The ammonia solution was used to adjust the pH of the aqueous metal solution to induce precipitation and oxidation within the water pools. Both the microemulsions were agitated and then sonicated until each was visibly clear. Second microemulsion was added at once into the first microemulsion. Initially a green color forms, which over a period of a few minutes, turns reddish. The reaction was rapidly stirred for 2 h to ensure complete reaction. Excess of methanol was added to disrupt the micelles and remove surfactant from the particles. This mixture was centrifuged and the supernatant removed. The material was washed and centrifuged repeatedly with methanol until the AOT was removed and then dried overnight in an oven followed by calcination for 4 h at 773 K. Samples were prepared at different pH values (1) pH < 9.6 (2) pH = 9.6 (3) pH = 10.96 (4) pH =11.40. In order to achieve a higher pH value the amount of ammonia in second microemulsion was increased, keeping ω same for all cases. Measurement of pH values during the aging times of the

mixed precursor and precipitating microemulsions were performed by using Elico pH meter LI 127 model at room temperature.

Additionally indium doped nickel-zinc ferrite ($Ni_{0.58}Zn_{0.42}In_xFe_{2-x}O_4$, x = 0.1, 0.2, 0.3) particles were prepared by taking $InCl_3$ in aqueous solution of other metal reactants such that total molarity of the solution remains constant ~0.1*M* and performing the same procedure as described above. Various synthesis experiments were performed at different pH values to get the pure spinel phase. Particle size was increased by increasing the pH value. The w = $[H_20]$/[AOT] ratio was kept constant in all experiments.

Bulk samples were prepared by heating reverse micelle synthesized nanoparticles at high temperature (~1473 K) for 4 h. This is of importance not only for basic science but also because of possible high-temperature applications of reverse micelle synthesized ferrites.

3.2 X-ray diffraction

X-ray diffraction analysis was used to study the crystallinity of powder samples. This method can be used for phase identification, particle and unit cell size determination. When an electromagnetic wave enters a crystal it will be scattered by the electrons inside. For certain angles of incidence there will be constructive interference between the different scatters, but for most of the angles destructive interference will cancel the diffracted beams. By measuring at which angles the constructive interference occur, it is possible to learn about the geometrical ordering of the atoms inside the crystal [4-6]. X-ray diffraction is a useful nondestructive method of structure analysis. The most common uses of X-ray diffraction in our type of work are:

- to check if the sample consists of a single phase.
- to check the crystallinity of the sample.
- to see whether the sample is polycrystalline or a single crystal
- to measure the particle size.

X-ray diffraction is the most widely used basic structural characterization technique for studying the samples which are in their respective powder form. In normal θ-2θ scan mode, a beam of monochromatic X-rays is made to incident on the sample, making an angle θ with the sample surface. The detector motion is coupled with that of

the X-ray source so that it is always kept at a position at an angle of 2θ with the incident direction of the X-ray beam. The spectrum is recorded as intensity vs. 2θ. The schematic of X-ray diffractometer is shown in figure 3.2.

This technique is based on Bragg's law of diffraction. The X-rays get diffracted from the crystal planes when the Bragg's diffraction condition is satisfied, as given by:

$$2d \sin \theta = n \lambda \ldots\ldots\ldots\ldots\ldots\ldots\ldots\ldots (3.1)$$

where, d is the interplaner spacing, n is the order of diffraction, λ is the wavelength of X-ray and θ is the incident angle.

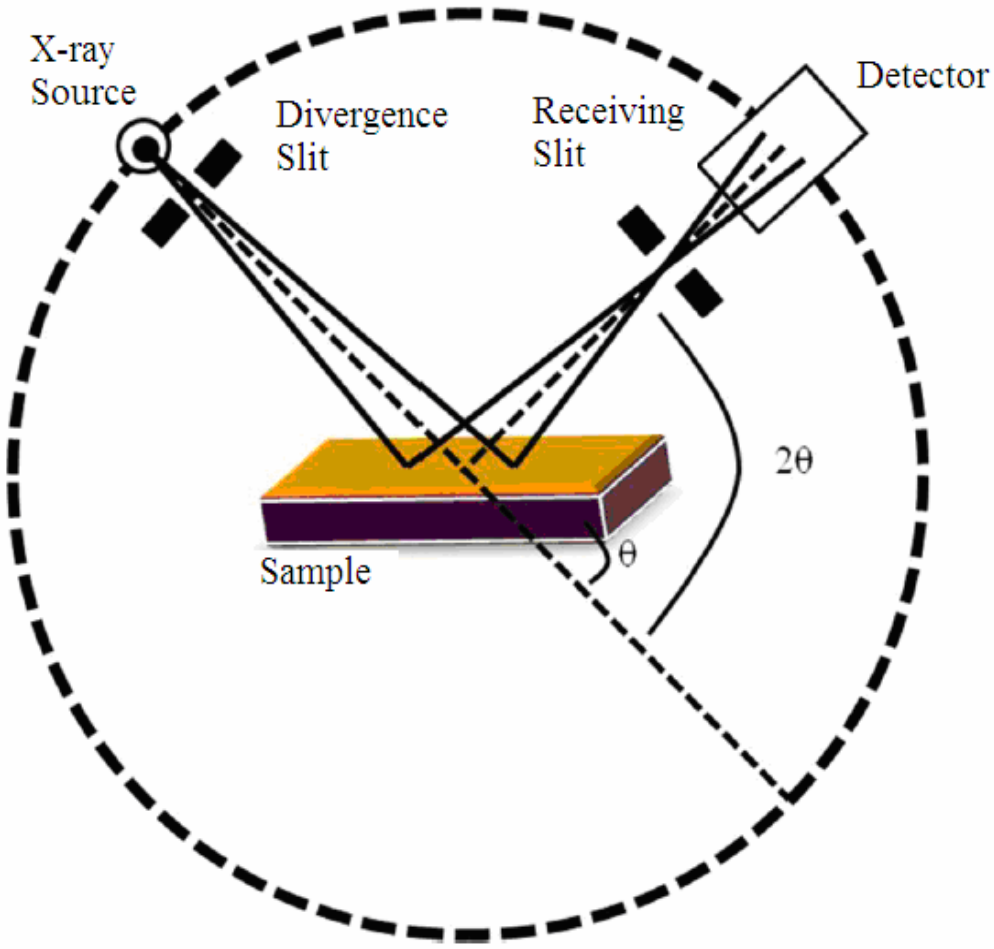

Figure 3.2 *Schematic of X-ray diffractometer*

To satisfy Bragg's law during the experiment it is necessary to scan either wavelength (λ) or angle (θ). The variation in angle 2θ brings different atomic planes into position for reflection. Thus for a particular set of planes, the first order diffraction occurs at a particular value of 2θ, the detector counts increase, and a peak gets recorded. By comparing the peak positions in the X-ray diffraction spectrum with the standard data, one can obtain the knowledge about phases present in the sample. Sharper peaks indicate better crystallinity of the film. These spectra can also give us information about the average particle/grain size, lattice parameter, crystal structure of the samples, etc. By measuring the shift in the diffraction peak position (and hence lattice constants), one can get an idea of the strains present in the sample. A typical block diagram of a powder X-ray diffraction unit is shown in figure 3.3.

In the present work, the X-ray diffraction patterns for the powders were carried out on rotating anode X-ray generator (Rigaku) at SAIF Chandigarh. X-ray diffraction technique was used in the range of 20^{o}–70^{o} using Cu-K_{α} (λ= 1.54184 Å) radiation source.

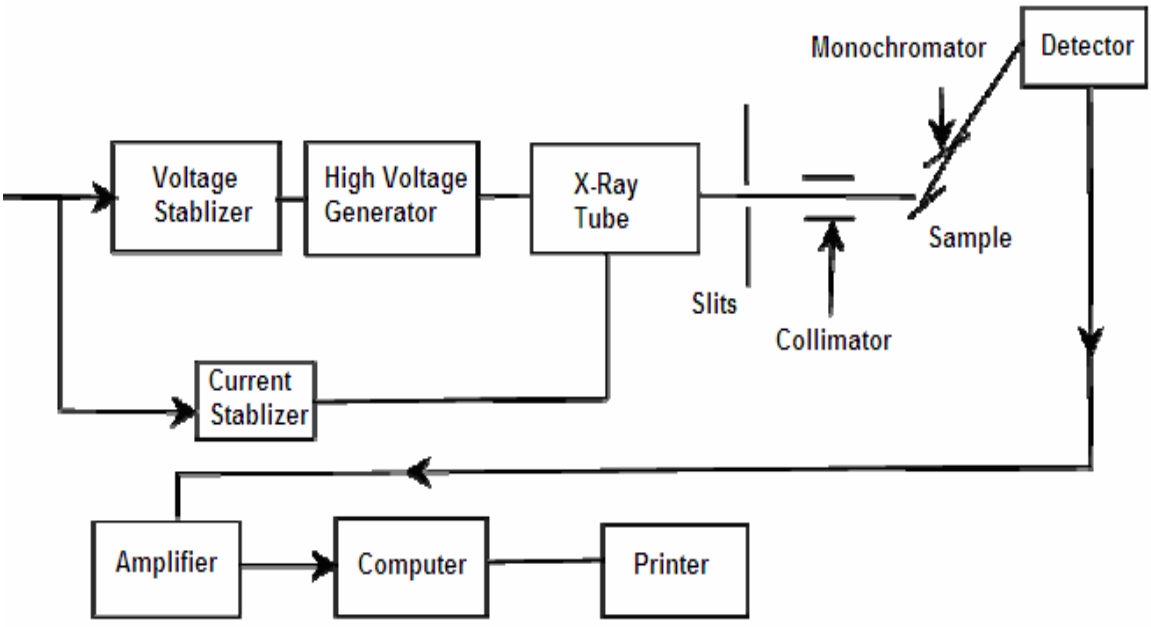

Figure 3.3 *A typical block diagram of a powder X-ray diffraction Unit*

3.3 Transmission electron microscopy

Transmission electron microscopy (TEM) yields information on the morphology, composition and crystallographic information on a very fine scale. Transmission electron microscopy work the same way as a slide projector where a beam of electrons (like the light) is being shined through the specimen (like the slide) and whatever part is transmitted is projected onto a phosphor screen to yield an image from where the morphology can be extracted. A crystalline material interacts with the electron beam mostly by diffraction rather than absorption, although the intensity of the transmitted beam is still affected by the volume and density of the material through which it passes. The intensity of the diffraction depends on the orientation of the planes of atoms in a crystal relative to the electron beam. At certain angles the electron beam is diffracted strongly, sending electrons away from the axis of the incoming beam, while at other angles the beam is largely transmitted. A high contrast image can therefore be formed by blocking electrons deflected away from the optical axis of the microscope and by placing the aperture to allow only unscattered electrons through. This produces a variation in the electron intensity that reveals information on the crystal structure, and can be viewed on a fluorescent screen, or recorded on photographic film or captured electronically.

Transmission electron microscopy (TEM) is a very sensitive instrument, for studying the grain size and morphology of nanoparticles at higher magnification, higher resolution and depth of focus compared to an optical microscope. Transmission electron microscopy consists of following important sections: illumination system, specimen stage, imaging system, image recording system. These sections are illustrated in the block diagram of the electron microscope shown in figure 3.4. For transmission electron microscopy investigations, powders were crushed in a mortar, dispersed in methanol, and fixed on a copper-supported carbon film.

In this work, transmission electron microscopy is performed at SAIF Chandigarh on a Hitachi microscope (H-7500) 120 kV equipped with CCD camera. This instrument has the resolution of 0.36 nm (point to point) with 40-120 kV operating voltage. It has electron diffraction, tungsten filament, low dose function, high contrast mode with ergodynamic look. The specific features of the instrument are: maximum field of views at

x700 with dual picture modes, auto-navigation and largest possible field with mose contrast and auto pre-irradiation mode (APIS).

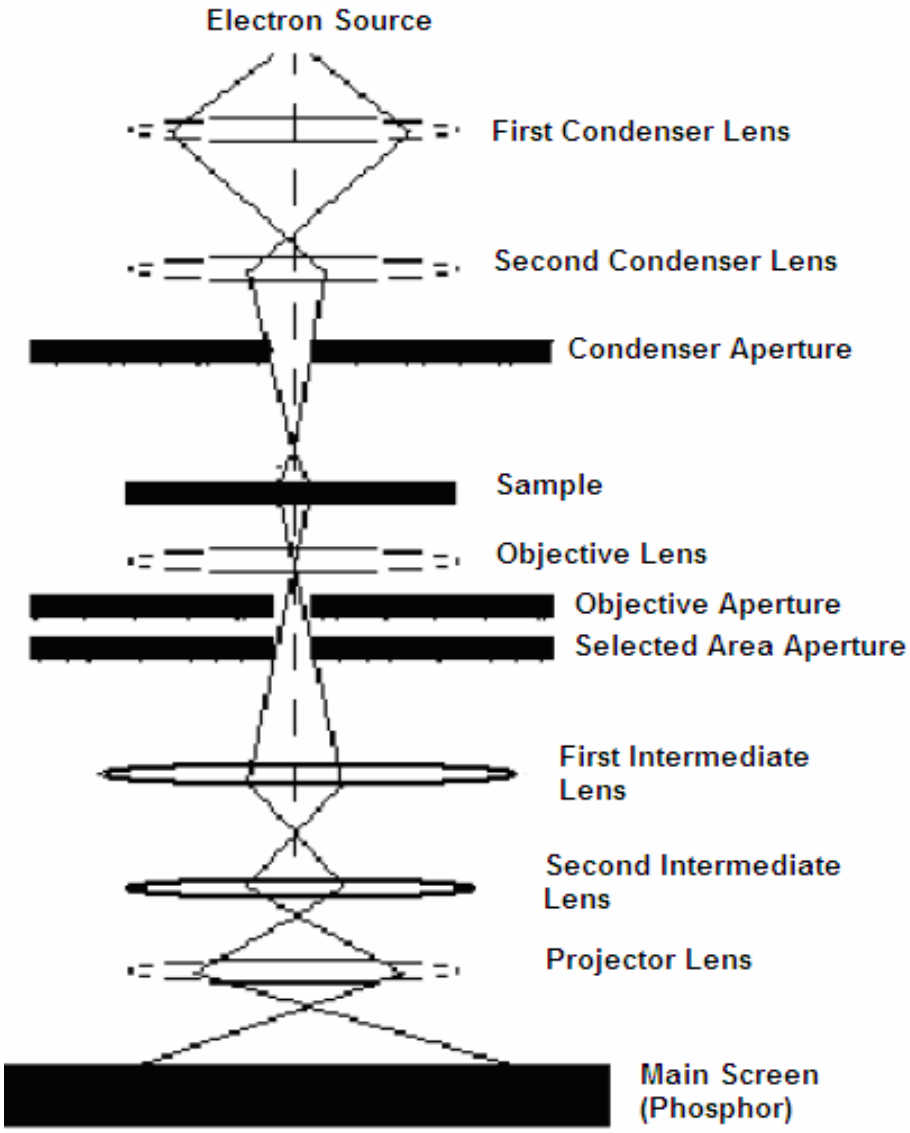

Figure 3.4 *A block diagram of transmission electron microscope*

3.4 Fourier transform infrared (FTIR) spectroscopy

Spectroscopy is the study of the interaction of electromagnetic radiation with a chemical substance. When radiation passes through a sample (solid, liquid or gas) certain frequencies of the radiation are absorbed by the molecules of the substance leading to the molecular vibrations.

Infrared (IR) spectroscopy is a powerful tool for probing the vibrational motion of atoms in a molecule which are greatly influenced by the masses of atoms, their geometrical arrangement and strength of their chemical bonds. Infrared spectra involve IR radiation, which results from transition between quantized vibrational states and provides complementary information of molecular vibrations. It consist of a spectral region from red end of visible spectrum (12500 cm^{-1}; 0.8 mm) to the microwave (10 cm^{-1}; 1000 mm) in the electromagnetic spectrum and based upon both application and instrumentation involved is conveniently divided into near-IR (12500 to 4000 cm^{-1}), mid-IR (4000-400 cm^{-1}) and far-IR (400-10 cm^{-1}). A typical spectrometer mainly comprises of (a) radiation source, (b) optical path and monochromator, (c) radiation detector and (d) sample holder.

Modern fourier transform IR spectrometers are superior to the dispersive IR spectrometers. An FTIR is a method of obtaining infrared spectra by first collecting an interferogram of a sample signal using an interferometer, then performing a fourier transform on the interferogram to obtain the spectrum. An FTIR spectrometer is a spectral instrument that collects and digitizes the interferogram, performs the fourier transform function and displays the spectrum. The main component in the FTIR spectrometer is an interferometer. This device splits and recombines a beam of light such that the recombined beam produces a wavelength-dependent interference pattern or an interferogram. The Michelson interferometer is most commonly used. Figure 3.5 shows schematics of the Michelson interferometer.

A Michelson interferometer consists of two mirrors and a beam splitter positioned at an angle of 45^{o} to the mirrors. A KBr beam splitter coated with germanium is typically used for mid IR region. Incident light strikes the beam splitter so that half of the light is transmitted through the beam splitter and half is reflected to the mirrors. The two components are then reflected back and recombined at the beam splitter with half of the light passing on towards the sampling areas and half traveling back toward the source. The signal at the detector is a cosine wave. In general, the function of the interferometer is to disperse the radiation provided by the IR source into its component frequencies. With polychromatic light (radiation with more than a single wavelength), the output signal is the sum of all the cosine waves which is the fourier transform of the spectrum or

an interferogram. This signal is the sum of the three cosine wave signals from each frequency separately. The interferogram contains the basic information on frequencies and intensities characteristic of a spectrum but in a form that is not directly interpretable. Thus, the information is converted to a more familiar form, a spectrum, using fourier transform methods.

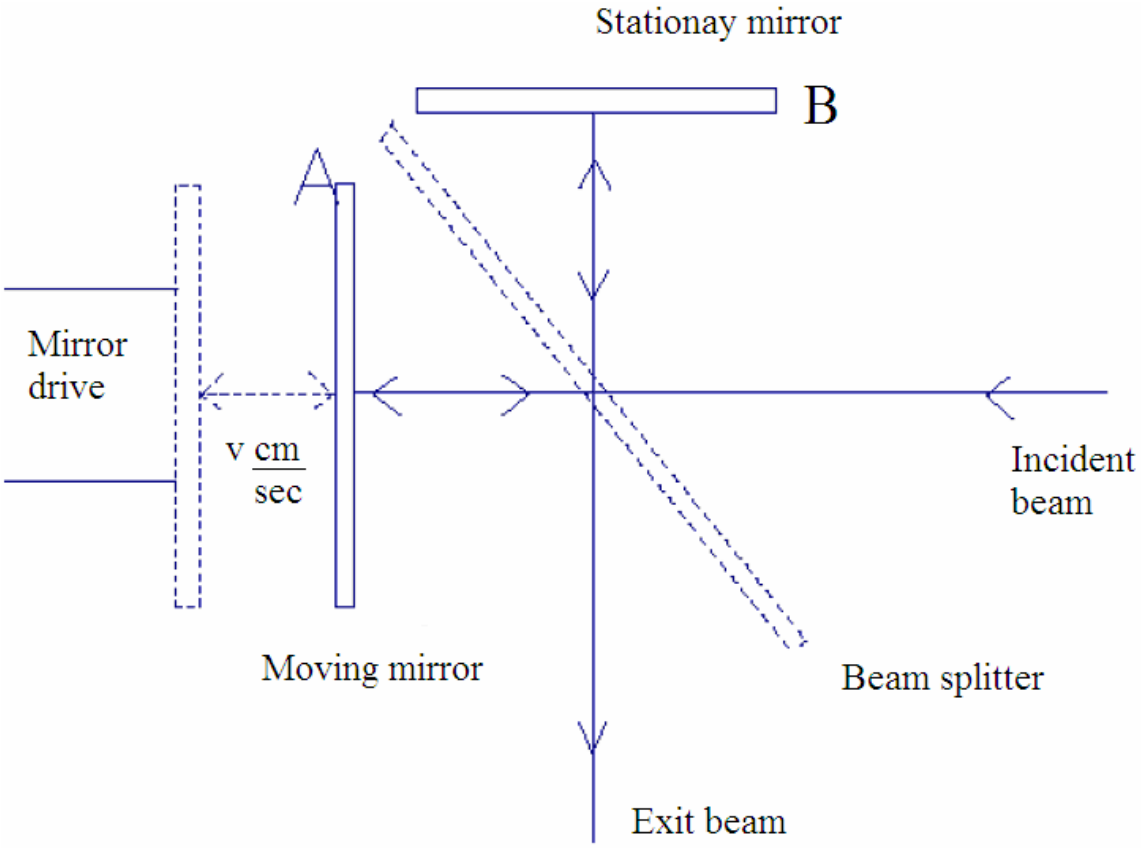

Figure 3.5 *Schematic diagram of a FTIR spectrometer*

In the present work fourier transform infrared spectroscopy (FTIR) measurements were made on a Bruker Model Vertex 70 spectrophotometer from 400 to 4000 cm^{-1} using KBr pellet method, at IUC-UGC, consortium for scientific research, Indore.

3.5 Mössbauer spectroscopy

^{57}Fe Mössbauer spectroscopy uses a radioactive source of ^{57}Co. The decay scheme of this isotope is shown in figure 3.6. The half-life of ^{57}Co is 271.7 days and decays by electron capture to the excited state of ^{57}Fe. This excited state decays to I = 3/2 excited state (14.4 keV) or to I = ½ ground state by gamma rays emission. The 14.4 keV state decays to the ground state by gamma rays emission or internal conversion. The half-life of 14.4 keV excited state is 97.8 ns, giving a Mössbauer gamma ray with a line width of 0.097 mm/s and the line width of a resonant emission and absorption event is thus

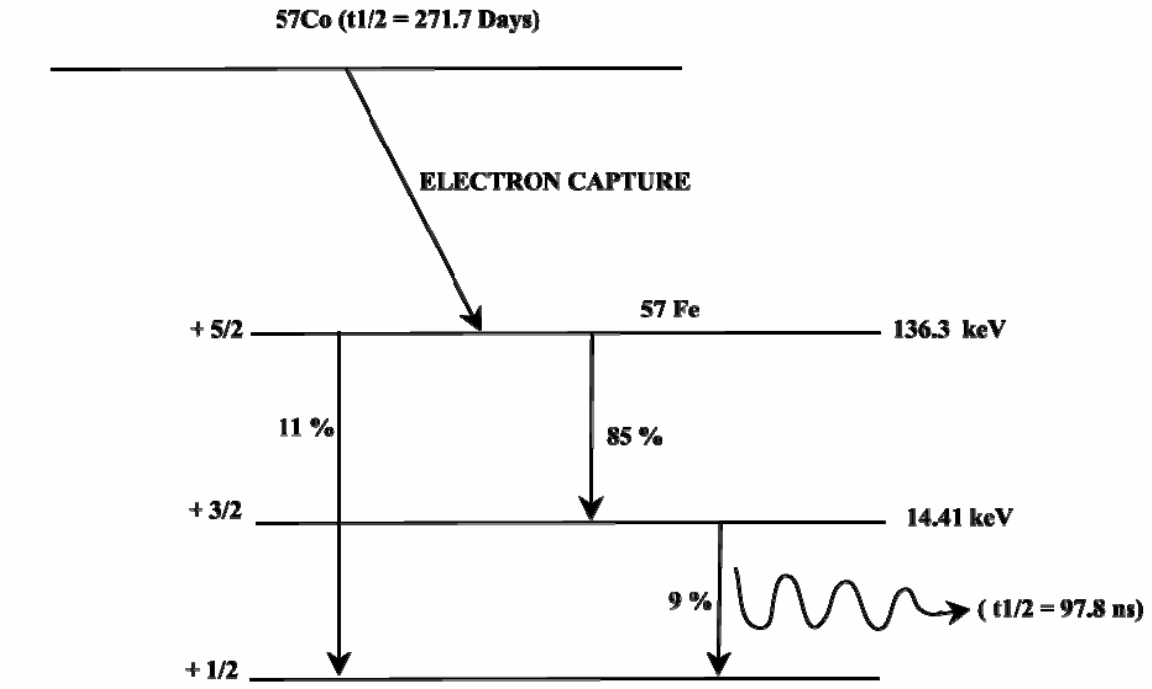

Figure 3.6 *Schematic diagram of a simple Mössbauer spectrometer*

0.19 mm/s in perfect condition. The source used in the present work is fabricated by diffusing ^{57}Co atoms in rhodium foil matrix and provides a solid environment for the ^{57}Co atoms with a high recoil-free fraction. The source velocity is controlled by a transducer, which oscillated with constant acceleration. Waveform generator sends a reference waveform to the drive amplifier, via a D/A converter (Figure 3.7). This signal is sent to the vibrator, where it is converted to a mechanical oscillation of the drive shaft and source. A small coil within the vibrator provides a feedback signal to correct any deviations from the reference wave form. The detector here is a proportional counter

containing a 90 % of argon and 10 % of methane gas. It uses an applied voltage of –2.0 to –2.5 keV and has 65 % efficiency for gamma rays.

The pulse magnitude from the detector is directly proportional to the gamma rays energy and is sorted by a single channel analyzer after amplification. This allows the selection of Mössbauer gamma ray from any other radiation emitted from the source. The detector counts and source velocity are synchronized by a microprocessor system. The

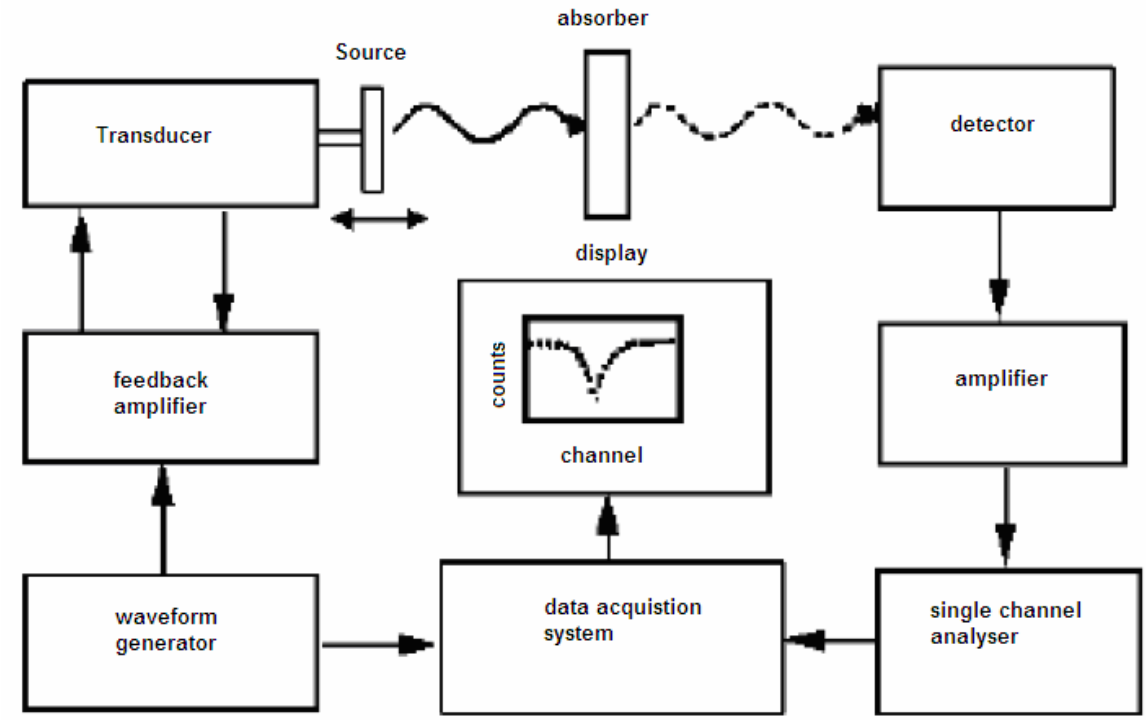

Figure 3.7 *A block diagram of a typical Mössbauer spectrometer*

counts accumulate 512 channels for one cycle, which contain two complete spectra, one for positive acceleration and one for negative acceleration of the source. As the acceleration is constant the time interval is equal for all the velocity intervals, hence each channel records for the same amount of time. During the analysis the full spectrum is folded around a center point to produce a single spectrum. This increases the number of counts and hence gives better statistics and also flattens the background profile produced by difference in intensity of the source radiation as the source moves relative to absorber and detector. The raw data is collected by a data acquisition computer system, which can be further used for analysis. The spectrum is folded and a theoretical spectrum is

calculated according to specified hyperfine parameters and is compared to the data. The minimum deviation (χ^2) between the theoretical spectrum and the experimental spectrum gives the best fit. The analysis programs vary the parameters of the theoretical spectrum to find a minimum in χ^2. As there are number of minima of χ^2 that can be obtained from various points in parameter space, the resulting fits must then be checked for consistent parameters to ensure a fit that is physically valid. NORMOS (SITE/DIST) [7] fitting package was used for fitting of the data, which contains code to read and write the data files. This can produce doublets and the double sextets using Lorentzian line shapes. This program uses the VA02A routine for χ^2 minimization. The routines can be fit with multiple hyperfine fields or quadrupole splitting distribution blocks as well as multiple crystalline sites.

To analyze the recorded spectra, the spectrometer needs to be calibrated. The three main calibration parameters are the velocity scale, the center point of the spectrum and a linearity of the velocity/time profile of the oscillation compared to a standard reference. The calibration is performed using a spectrum recorded from a α-Fe foil at room temperature and fitted with the NORMOS (SITE/DIST) fitting package. The velocity scale is calibrated using the well-defined line positions of the sextet from iron. The center of this iron spectrum at room temperature is taken as the reference point (0.0 mm/s) for isomer shift values of the sample spectra.

In the present work, Mössbauer spectroscopy studies were performed on the nano and bulk samples at IUC-UGC, consortium for scientific research, Indore. Mössbauer absorbers of thickness ~20 mg/cm^2 were prepared using powdered materials. Spreading the 20-30 mg fine powders in a copper ring of 1 cm diameter on a thin aluminum foil and fixing the powder using GE Varnish/vacuum grease achieved the uniform thickness of the absorber. Low temperature and in-field ^{57}Fe Mössbauer measurements were carried out using Janis made of superconducting magnet. In-field Mössbauer spectra were recorded at 5 K in the presence of an external magnetic field of 5 T applied parallel to the γ-ray direction.

3.6 Magnetic studies: magnetometry

The study of magnetic properties of materials is a basic requirement for understanding electronic behavior in condensed matter. Magnetometry is a general term referring to the magnetic property measurements of a particular system. The dc magnetometer and the ac susceptometer are two entirely different techniques that provide different ways of investigating the magnetic properties. Both these techniques rely on sensing coils used to measure the change in the magnetic flux due to magnetized sample. The basic difference between these two techniques resides in how the flux variation is achieved. In a dc magnetization measurement, a sample is subjected to and magnetized by a static dc field usually arising from an iron core or superconducting magnet. The sample is then moved relative to a detection coil that is used to measure variations in flux due to magnetized sample. On the other hand, in ac measurements, the sample is centered within a coil while driven with an external ac field. This produces a time varying magnetization, inducing a voltage that a second detection coil senses. Usually a lock-in amplifier is used to analyze this signal which is related to the materials ac magnetic properties. Various techniques of magnetometry can be used to measure the magnetic properties of the materials. Vibrating sample magnetometer and superconducting quantum interference device (SQUID) are well-known methods to measure the magnetization of the materials.

3.6.1 Vibrating sample magnetometer

Vibrating sample magnetometer (VSM) is a powerful technique for determination of magnetization and hysteresis loop of nano and bulk sample [8]. The operation of the vibrating sample magnetometer is based on the flux change in a coil when a sample having non-zero magnetic moment is vibrated near it. The schematic of the vibrating sample magnetometer is shown in figure 3.8.

The sample to be studied is fixed in a sample holder which is located at one end of the rod whose other end is attached to a mechanical vibrator which vibrates typically with a frequency of 82 Hz, and with amplitude of about 0.1 mm. The direction of vibration is kept perpendicular to that of the magnetic field generated by an electromagnet. The oscillating magnetic field, resulted from the vibrating sample,

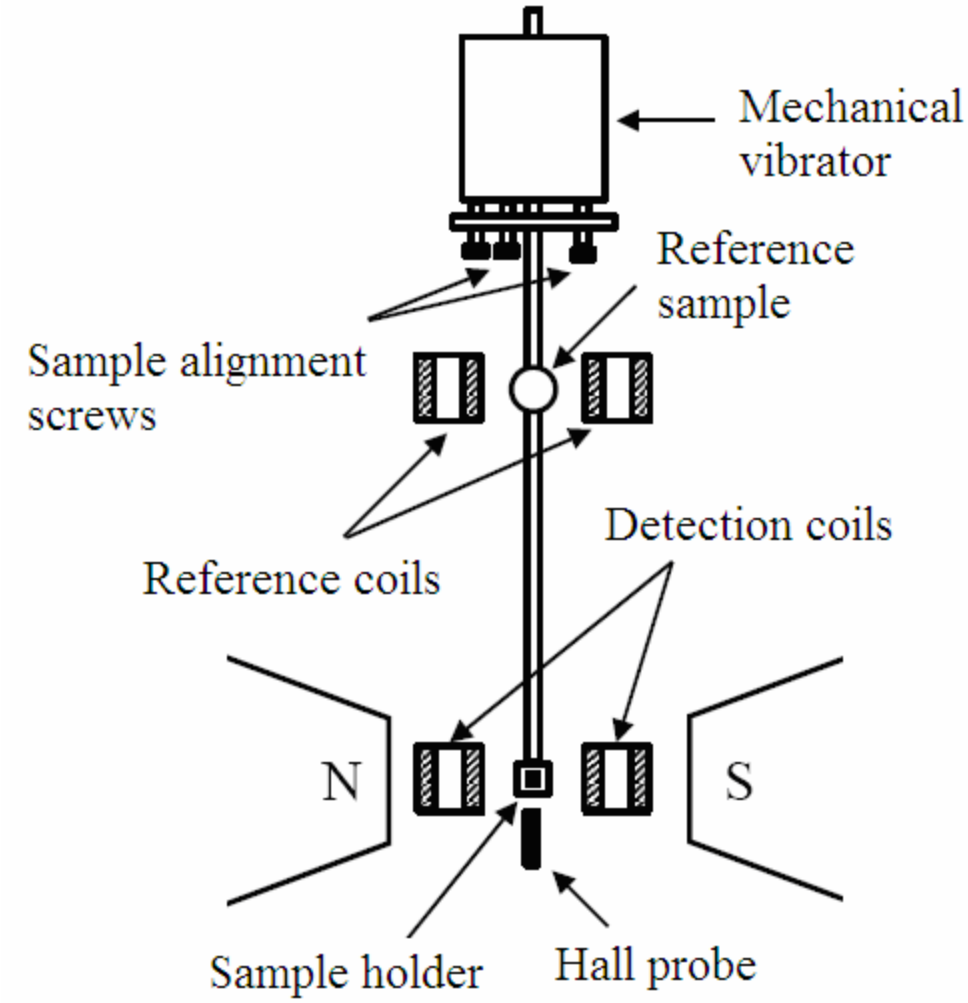

Figure 3.8 *Schematic of the vibrating sample magnetometer*

generates an alternating e.m.f. in the detection coils kept near the sample. The vibrating rod also carries a reference specimen, in the form of a small permanent magnet, near its upper end and its oscillations induce e.m.f. in the reference coils. The difference between the voltage of the detection and reference coils, which is directly proportional to the magnetic moment of the sample is measured and is expressed in terms of the magnetic moment (i.e. in emu). For sample with known mass or dimensions, its magnetization can be measured either in units of emu/gm or emu/cm^3. It is very sensitive technique; it can detect a change in the magnetic moment as small as 5 x 10^{-5} emu. The block diagram of vibrating sample magnetometer is shown in figure 3.9

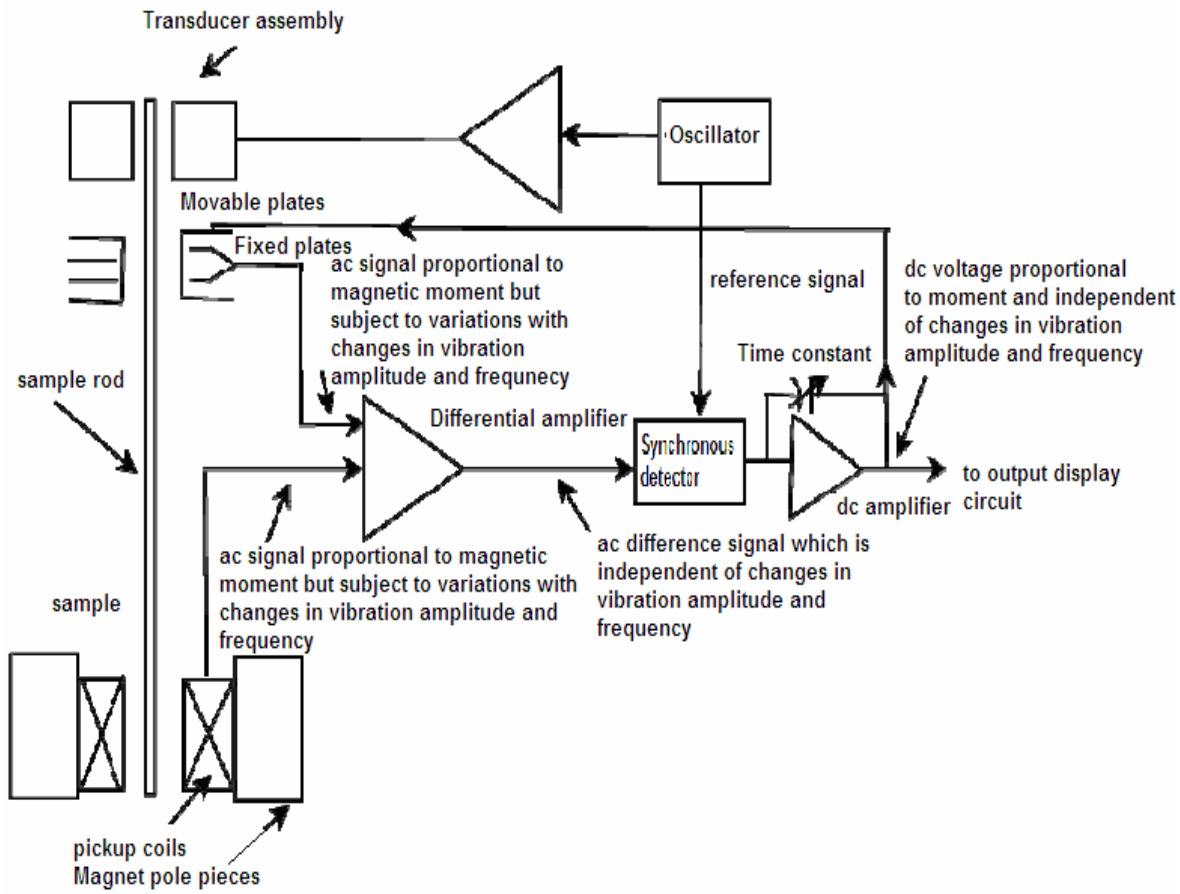

Figure 3.9 *Block diagram of the vibrating sample magnetometer*

In the present work, measurements were performed using a quantum design (USA), 14 T physical property measurement system (vibrating sample magnetometer PPMS-VSM), at IUC-UGC, consortium for scientific research, Indore. For the measurement using VSM, the powered sample were weighted, pressed into a small quartz container and finally mounted at the end of a rigid ceramic rod. To avoid the movement of the powders inside the tube they were compacted using Teflon tape. The stability of the instrument is ± 0.05 % for fixed coil geometry, the absolute accuracy is 2 % and the reproducibility is better than 1 %. The least measurable moment is better than of the order of 10^{-4} emu. For recoding magnetization measurements at lower temperatures range from 77-300 K, a closed cycle refrigerator has been used.

3.6.2 Superconducting quantum interference device (SQUID) magnetometry

Magnetometers based on the SQUID technology are presently the most sensitive instruments to measure magnetic moments of liquid or solid state samples. State of the art systems are capable of measuring magnetic moments of the order of 10^{-7} emu (10^{-10} Am^2) and even below. Essentially two modes of operation exist. First, as a magnetometer, it measures the static magnetic moment (m), at various applied fields (H*)*, and temperatures (T). When normalized to the volume of the sample one obtains the average magnetization (M). SQUID magnetometers are used in various fields of research such as in the study of superconductors, biological materials, thin magnetic films, magnetic nanostructures, magnetic fluids and geological materials.

The SQUID magnetometer is one of the extremely low impedance, high sensitivity flux detector capable of operating over a wide range of frequencies. It uses the properties of electron-pair wave coherence and Josephson junctions to detect very small magnetic fields. In a SQUID based magnetometer; a magnetic sample passes through a set of sensing coils. The sensing coils are comprised of superconducting coils separated by thin insulating layers that are less than 30 Å thick. The insulating layers are called Josephson junctions after Brian Josephson who, in 1962, showed that Cooper pairs (electron pairs in superconducting materials) in superconductors could tunnel through an insulating layer or weak link between the superconductors [9]. A dc-SQUID is comprised of two Josephson junctions connected in parallel (Figure 3.10). A current is passed through the superconductors and when no magnetic sample is present the Cooper pairs weakly interfere as they pass through the Josephson junctions. This interference is caused by phase shifts (δ_A and δ_B) of the Cooper pairs passing through junctions A and B respectively. However, when a magnetized sample passes through the center of the SQUID device, the magnetic flux changes the interference (phase difference) of the cooper pairs. Ultimately, the total current passing through the superconducting loops (I) changes as a result of any magnetic flux (B) through the loops by the relationship

$$I = 2 I_0 \sin\delta_0 \cos\left(\frac{e}{h}\int B.dS\right) \qquad \text{.....(3.2)}$$

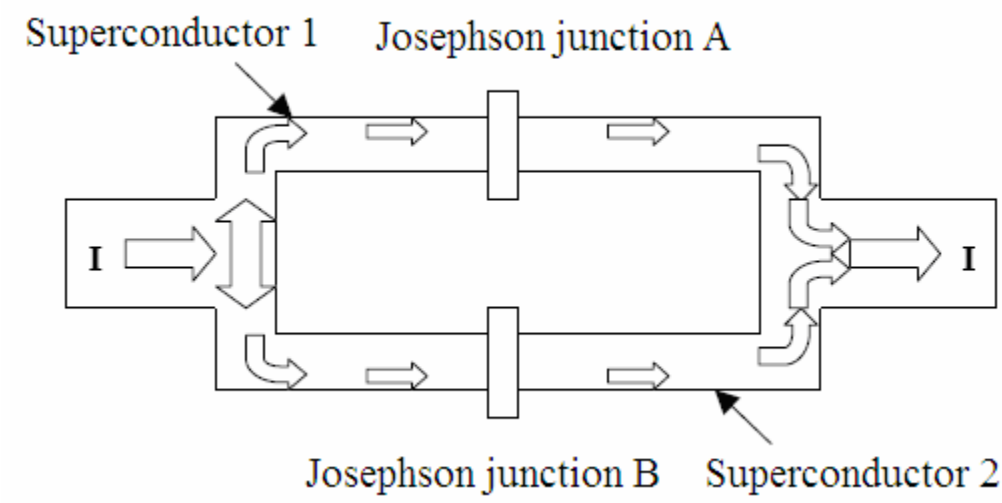

Figure 3.10 *Schematic diagrams of SQUID sensing device*

where I_0 is the initial current, δ_0 is a constant phase shift, *e* is the charge of an electron, h is Planck's constant and *S* is area of the superconducting loops [10]. The current change causes a change in voltage, which is amplified by a coil coupled to the SQUID and converted into a current with equal and opposite flux [11]. The sensitivity of the SQUID magnetometer is directly related to its ability to measure the phase difference of Cooper pairs. SQUID magnetometers are also very precise, allowing for reproducible standard deviations of the order of 10^{-3} to 10^{-6} emu for six averaged measurements. The schematic diagram of SQUID magnetometer is shown in figure 3.11.

In the present work, SQUID measurements were performed on the nano and bulk samples at Instituto de Fisica Gleb Wataghin, Universidade Estadual de Campinas (UNICAMP) Campinas, Brazil. For the measurements using SQUID magnetometer, the powered samples were mounted within a plastic straw and connected to one end of a sample rod, which is inserted into the dewar filled with liquid helium. The other end is attached to a stepper motor, which is used to position the sample within the center of the SQUID pick up coils. The magnetization measurements on bulk and nanoparticle samples were performed using a quantum design MPMS XL SQUID magnetometer.

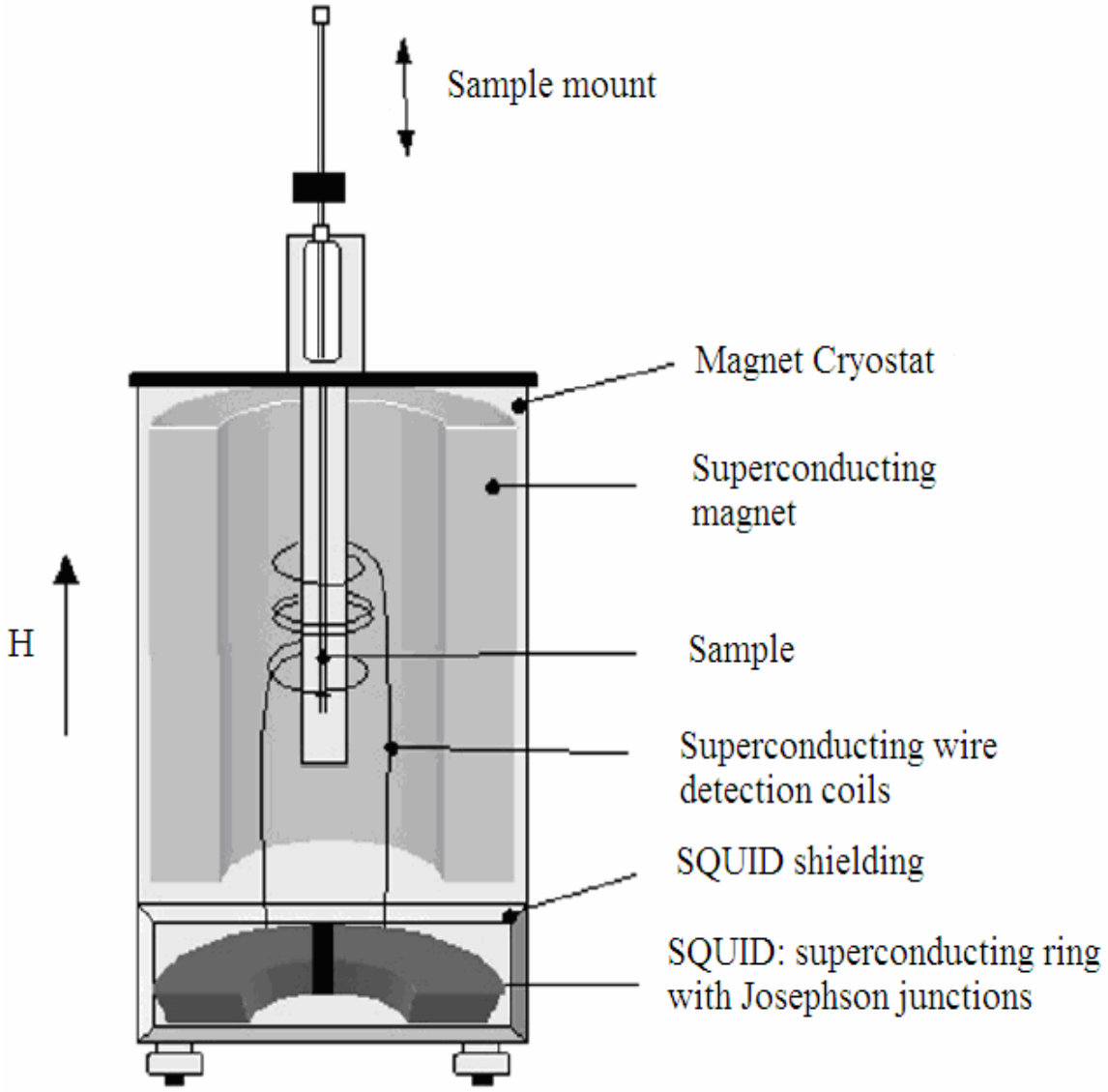

Figure 3.11 *Schematic diagram of SQUID magnetometer*

3.6.3 AC suscepetometer

An ac susceptometer is a unique tool, which is capable of measuring susceptibility under very small magnetic fields, with or without a dc bias field. It can also be used to measure the magnetic susceptibility as a function of frequency and temperatures, and is capable to separate the real part χ' and imaginary part χ'' of the complex susceptibility.

The basic principle for measuring the ac susceptibility of a sample is the change in inductance of a coil or in the mutual inductance of a pair of identical and coaxial coils connected in series but oppositely wound when the sample is inserted in it. Change in

inductance is proportional to the susceptibility of a sample. Generally, at lowest frequencies of the oscillating field, it is beneficial to use the mutual inductance technique. For this, two coils can be used: one (primary) for producing the ac field and the other (secondary) as the mutual inductance coil for detecting signal. The secondary coil is placed either within or wound on the top of primary (Figure 3.12). Then, an ac field and

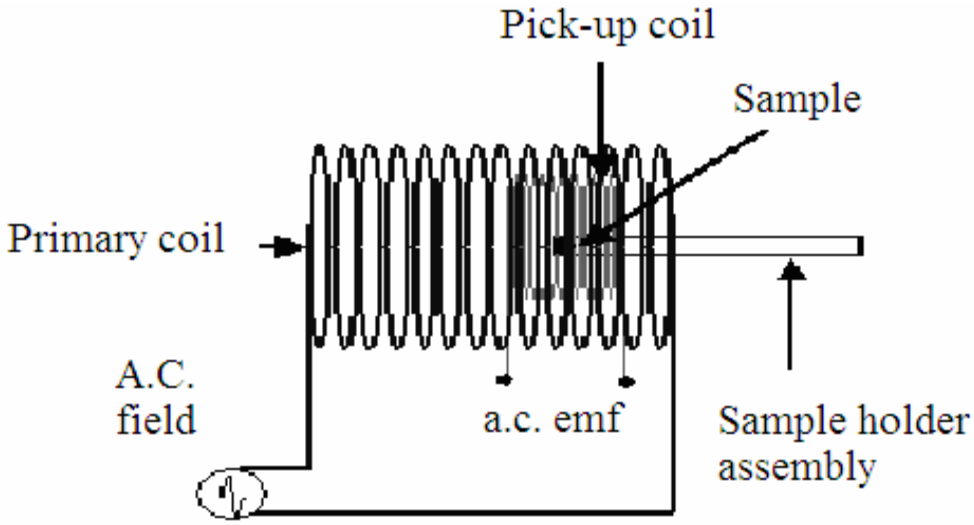

Figure 3.12 *Schematic diagram of the ac suscepetometer*

the magnetodynamics can be studied through the complex susceptibility ($\chi' + \chi''$). The real part χ' represents the component of the susceptibility that is in phase with the applied ac field, while χ'' represent the component that is out of phase and are measured by phase sensitive detection of the voltage induce across the secondary coil, when the sample is moved from the centre of one of the identical coils to the center of another. The block diagram of the ac suscepetometer set up is shown in figure 3.13.

In the present work, ac susceptibility measurements were performed on the nano samples at IUC-UGC, consortium for scientific research, Indore. For the measurements of ac susceptibility, the powered samples were weight, pressed into a small quartz container and finally mounted at the end of a sapphire rod. To avoid the movement of the powders inside the tube, they were compacted using Teflon tape.

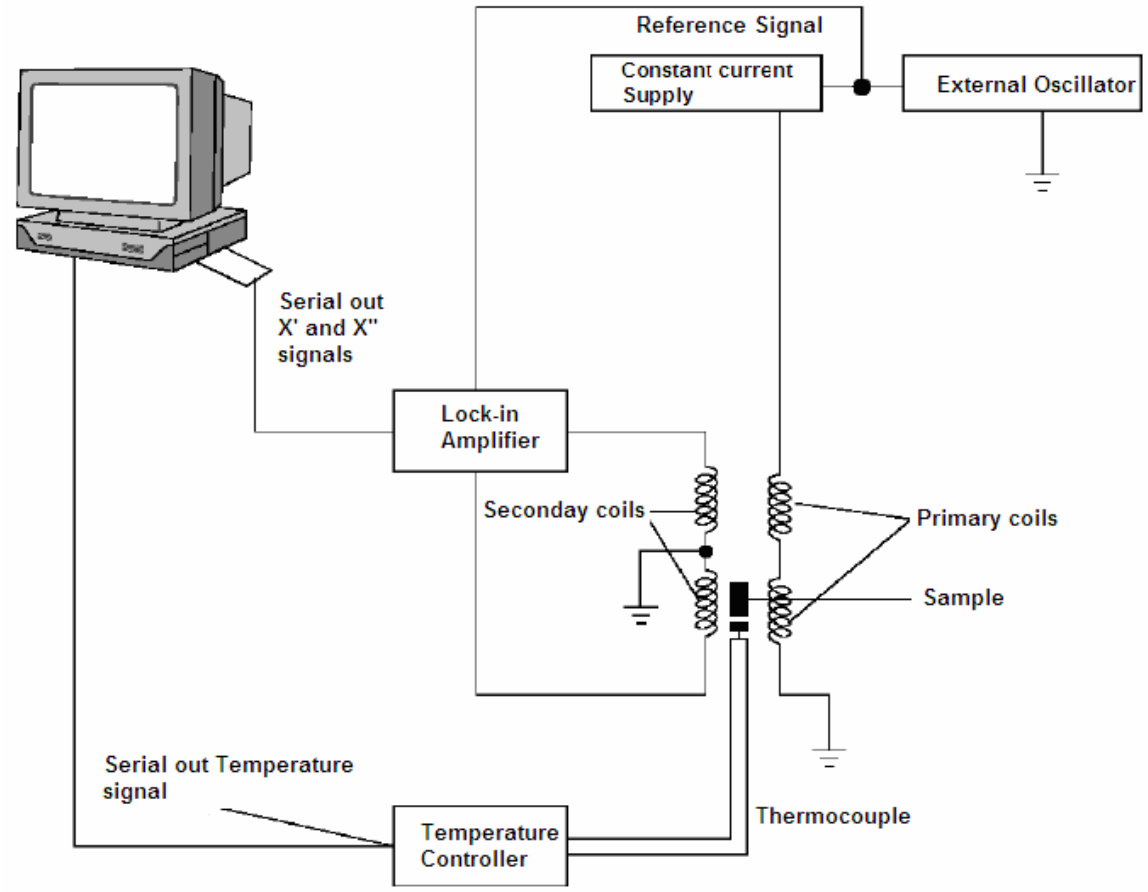

Figure 3.13 *Block diagram of the ac suscepetometer*

3.6.4 Temperature dependent zero field cooled (ZFC) and field-cooled (FC) magnetization

The transition temperature (T_B) of a magnetic material is an important factor as it governs the classification of a material as ferro-, ferri-or superparamagnetic. Zero-field-cooled (ZFC) and field-cooled (FC) magnetization versus temperature (M vs. T) measurements are commonly used to determine T_B, also known as the blocking temperature, of magnetic materials. The blocking temperature (T_B) is a measure of the thermal energy required to overcome the superexchange transition and is defined as the temperature at which the nanoparticles do not relax during the time of measurement; they are blocked

In these measurements, a sample is cooled from room temperature to 5 K in zero applied magnetic field. Then a small magnetic field is applied and the sample is warmed up to temperature 300 K (zero field-cooled measurement) and the magnetic moment is recorded. In the field-cooled measurements, the sample is cooled from 300 K to 5 K in the presence of field, where upon the temperature is again increased to 300 K and the magnetic moment is recorded. In the ZFC measurement, the magnetic dipoles of the sample are random at room temperature and remain random upon cooling. At 5 K, the dipoles do not have enough thermal energy to rotate. As the temperature is increased k_BT, increases and the magnetic dipoles align in the direction of the applied magnetic field resulting in an increase in the magnetic moment. In the field cooled measurement, the magnetic dipoles are aligned at 300 K and are cooled to 5 K in this configuration. As the temperature is increased, k_BT provides the energy for the magnetic dipoles to randomize resulting in a decrease in the magnetic moment. The point at which the ZFC and FC curves meet is called the separation point. Below the blocking temperature, there is sufficient thermal energy to randomize the magnetic dipoles and a material behaves like a paramagnetic. ZFC-FC measurements are done in the presence of various applied fields.

3.6.5 Room and low temperature magnetization vs. applied magnetic field measurements

Magnetization vs. applied magnetic field measurement (hysteresis curves measurements) is a time dependent measurement of the magnetic moment of a sample as the magnetic field is increased and decreased in a hysteresis fashion. Hysteresis loops provide information such as saturation magnetization (M_s), remanence magnetization (M_R) and coercivity (H_c) for a given material. These values are specific to the temperature at which hysteresis loop experiment is performed as the magnetic moment of a sample can depend on the temperature. Hysteresis loop experiments were performed at different temperatures for nanoparticles at 300 K, 200 K, 120 K, 80 K and 5 K beginning at zero applied magnetic fields. For bulk particles hysteresis loops measurements were carried out at 300 K and 5 K.

M_s was determined by observing the magnetic moment of the sample at the largest applied magnetic field. M_R was determined by locating the point on the y-axis, where there was a magnetization in zero applied magnetic field. H_c was determined by

locating the point on the x-axis where the magnetization was zero in an applied magnetic field. (Figure 3.14)

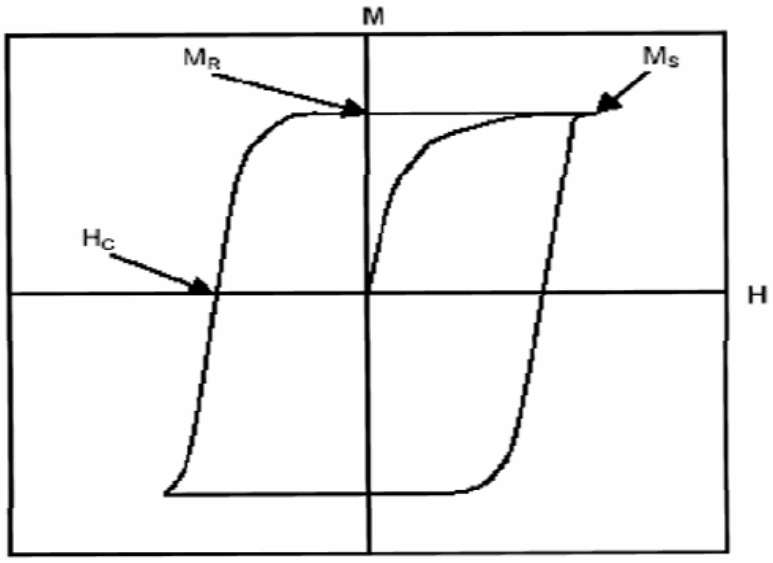

Figure 3.14 *Hysteresis curves (M-H) indicating the location of the point of interest*

3.6.6 Variation of magnetization with temperature in presence of high field

In order to account for the finite size effect and effective Bloch law formalism we have measured spontaneous magnetization vs. temperature for bulk samples in the presence of high field (~5 T) on a SQUID magnetometer. Variation of magnetization in the presence of high field (5 T) with temperature is studied in the cooling cycle.

3.6.7 AC susceptibility vs. temperature at different frequencies

The ac susceptibility is a powerful technique for exploring the nature of the magnetic transitions such as ferromagnetic, antiferromagnetic, superparamagnetic, freezing and spins glass transitions. The measurement of ac susceptibility as a function of temperature at different frequencies is very fruitful in studying the dynamical behavior of the systems like spin glasses, superparamagnet and also their relaxation time in magnetic moments. In a spin-glass, the magnetic spins experience random interactions with other magnetic spins, resulting in a state that is highly irreversible and metastable. This spin-glass state is realized below a freezing temperature, which is determined by measuring

the real part χ' versus temperature, a curve which reveals a cusp at the freezing temperature. Furthermore, the location of cusp is dependent on the frequency of the ac susceptibility measurements, a feature that is not present in other magnetic systems and therefore confirms the spin-glass phase. On the other hand in case of superparamagnetic particles, above the blocking temperature T_B, the imaginary part χ'' is small and the real χ' follows the Curie law (χ' vs. $1/T_B$), as expected for paramagnetic behavior. From such a measurement, one can check that the particles are truly non-interacting by verifying the dependence of $1/T_B$ on the measurement time as given by Neel-Brown theory (chapter 2) and the departure from this theory indicates strong interparticle interactions.

References

[1] Morrison S. A., Cahill C. L., Carpente E. E., Calvin S., Swaminathan R., McHenry M. E. and Harris V. G. *J. Appl. Phys*. **2004**, 95, 6392.

[2] Kale A., Nathani H., Srivastava R. S. and Misra R. D. K. *Mater. Sci. Tech.* **2004**, 20, 999.

[3] Gubbala S., Nathani H., Koizol K. and Misra R. D. K. *Physica B* **2004**, 348, 317.

[4] Cullity B. D. *Elements of X-ray Diffraction* Addison-Wesley Publ. Co. **1978**.

[5] Warren B. E. *X-ray diffraction* Courier Dover Publications New York, **1990**.

[6] James R. W. *The Optical Principles of the Diffraction of X-rays* London, G. Bell and Sons, **1948**.

[7] Brand R. A., Lauer J. and Keune W. Phys. Rev. B **1984**, 31, 1630.

[8] Foner S. *Vibrating Sample Magnetometer* Rev. Sci. Inst. **1958**, 30, 548.

[9] Castellano M. G. *Macroscopic quantum behavior of Superconducting Quantum Interference Devices* Fortschr. Phys., **2003**, 51, 288-294.

[10] Ibach H. and Luth H. *Solid state Physics: An Introduction to Principles of Materials* Science 2nd ed., New York, Springer, **1995**.

[11] Jiles D. *Introduction to Magnetism and Magnetic Materials* New York, Chapmann and Hall, **1991**.

CHAPTER 4

STRUCTURAL PROPERTIES OF NANO AND BULK FERRITE SAMPLES

Magnetic properties of nano ferrites are highly sensitive to their nanostructural properties like grain size, grain distributions, phase, imperfections, particle size distribution and environment of the ions. Therefore structural studies like X-ray diffraction (XRD), transmission electron microscopy (TEM) and Fourier transform infrared spectroscopy (FTIR) are essential to probe the nanostructural features of the system. The present chapter was taken up to study the structural properties of nickel-zinc ferrite ($Ni_{0.58}Zn_{0.42}Fe_2O_4$) and indium doped nickel-zinc ferrite ($Ni_{0.58}Zn_{0.42}In_xFe_{2-x}O_4$, x = 0.1, 0.2, 0.3) samples at nano and bulk scale.

X-ray diffraction analysis was used to study the crystallinity of powder samples. This method can be used for phase identification, particle and unit cell size determination. In the present work, the X-ray diffraction patterns for the ferrite samples were taken in the range of 20^o–70^o with a step size of 0.05^o (2θ) with 5 s counting time at each step using Cu-K_α (λ = 1.54184 Å) radiation source. Transmission electron microscopy (TEM) is a very sensitive instrument, for studying the grain size and morphology of nanoparticles at higher magnification, higher resolution and depth of focus compared to an optical microscope. For transmission electron microscopy investigations, powders were crushed in a mortar, dispersed in methanol, and fixed on a copper-supported carbon film. Fourier transforms infrared spectroscopy (FTIR) was used to characterize the local environment of ions. Fourier transform infrared spectroscopy was recorded on a Bruker Model Vertex 70 spectrophotometer from 400 to 4000 cm^{-1} using KBr pellet method.

Results and discussion

4.1 X-ray diffraction (XRD)

Nickel-zinc ferrite ($Ni_{0.58}Zn_{0.42}Fe_2O_4$) particles and indium doped nickel-zinc ferrite $Ni_{0.58}Zn_{0.42}In_xFe_{2-x}O_4$ (x = 0.1, 0.2, 0.3) particles were synthesized via reverse micelle technique. Various synthesis experiments were performed at different pH value to get the pure spinel phase. The w = $[H_20]/[AOT]$ ratio was kept constant in all experiments. Figure 4.1 shows the X-ray powder diffraction patterns of nano $Ni_{0.58}Zn_{0.42}Fe_2O_4$ sample with pH value at (a) pH < 9.6 (b) pH = 9.6 (c) pH = 10.96 and (d) pH = 11.40. The X-ray diffraction patterns show that the amount of precipitating

agent used plays a crucial role in the process of synthesizing the nano nickel-zinc ferrite particles. Analysis of the X-ray diffraction pattern revealed a match with PDF # 08-0234 [1], indicating the single spinel phase structure at pH = 9.6 (Figure 4.1b). Below this value of 9.6, a second phase of goethite (α-FeOOH) also appears with spinel phase (Figure 4.1a). However, the sample synthesized at higher pH value (10.96) contains traces of hematite in addition to spinel phase (Figure 4.1c). At pH = 11.40, dominant phase formed is of hematite (Figure 4.1d). Use of lesser amount of precipitating agent as compared to the stoichiometric amount needed to precipitate the precursor cations in the formation of divalent hydroxide, leads to the formation of goethite [2]. Two concurrent reactions depending on hydroxide ion concentration take place. The first reaction is the formation of goethite (α-FeOOH), which persists as an intermediate compound in the formation of ferrite at pH value < 9.6. The second reaction is associated with the oxidation of hydroxide and incorporation of Fe^{3+} into nickel-zinc ferrite particles.

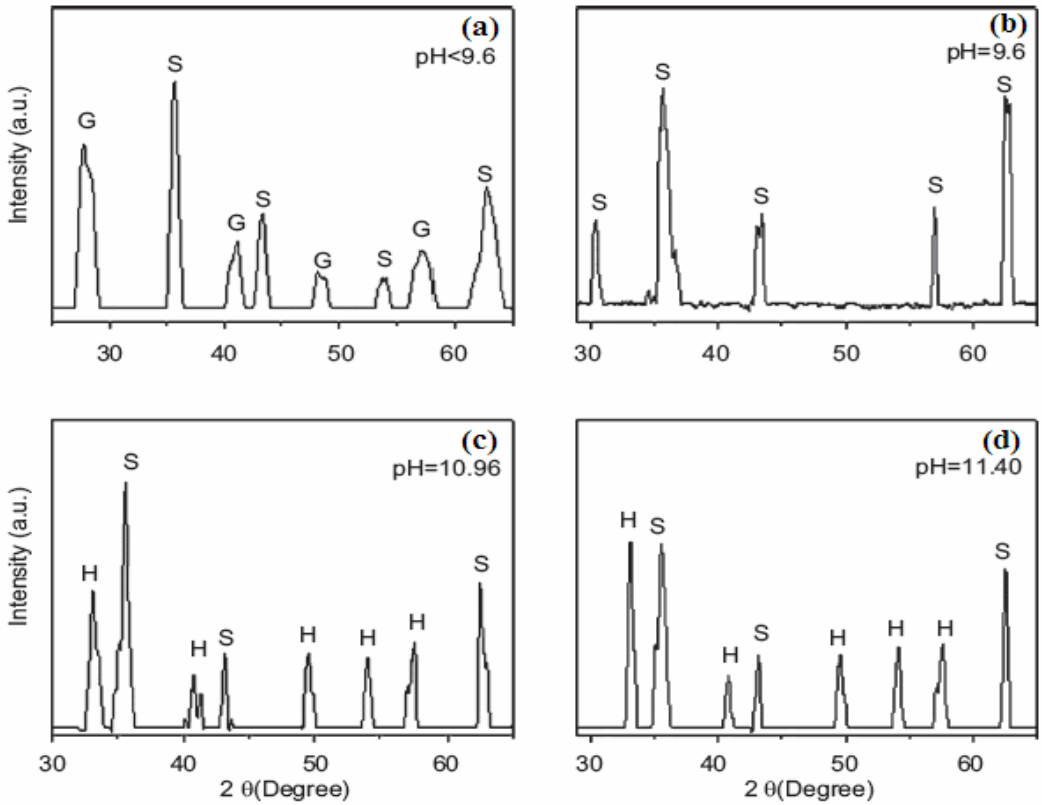

Figure 4.1 *XRD patterns with increase in pH value of nano nickel-zinc ferrite (a) shows the formation of goethite phase (G) with the spinel phase (S) for pH < 9.6 while (b) shows the pure single spinel phase formed at pH =9.6, (c-d) shows the formation of hematite phase (H) with the spinel phase for pH =10.96, pH =11.40*

Simplified chemical reactions for both processes can be written as:

$$2\ Fe^{2+} + 4\ OH^- + ½\ O_2 \longrightarrow 2\ FeOOH + H_2O\text{…… ……..(4.1)}$$

$$0.58Ni^{2+} + 0.42Zn^{2+} + 2\ Fe^{2+} + 6\ OH^- + ½\ O_2 \longrightarrow Ni_{0.58}Zn_{0.42}Fe_2O_4 + 3H_2O\text{……} \quad (4.2)$$

However at higher pH value (10.96), zinc hydroxide is partially dissolved and its deposition is incomplete, because of its amphoteric nature [3]. As a result the sample prepared at pH > 9.6 contains traces of hematite in addition to spinel phase which can clearly be seen in figure 4.1 (c-d). For any reverse micelle process, pH affected the crystallization of the product. Based on the above experiments, the suitable reaction conditions for the synthesis of well crystallized nano $Ni_{0.58}Zn_{0.42}Fe_2O_4$ (N_0) sample were obtained.

Figure 4.2 shows the X-ray diffraction patterns of indium doped nickel-zinc

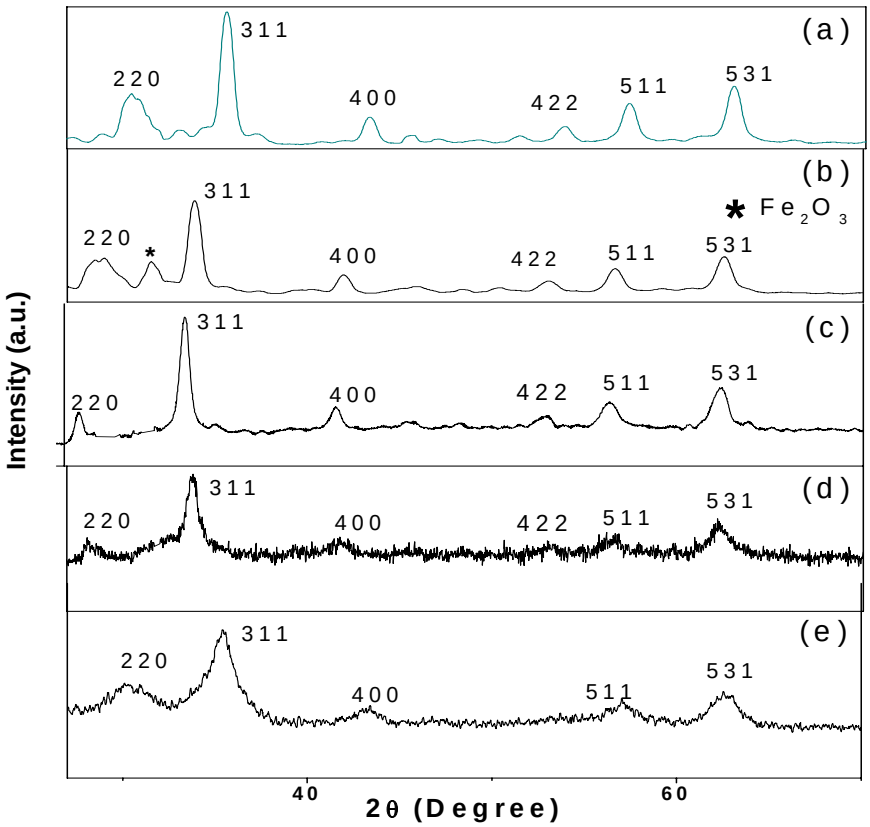

Figure 4.2 *XRD patterns of nickel-zinc-indium ferrite nanoparticles (a) N_1 (b) N_2 (c) N_3 (d) N_4 (e) N_5*

ferrite particles. At pH = 10.6, for $Ni_{0.58}Zn_{0.42}In_{0.1}Fe_{1.9}O_4$ (N_1) sample, the analysis of the material revealed a match with PDF # 08-0234 [1], indicating the single spinel phase structure. However at the same pH value (10.6), $Ni_{0.58}Zn_{0.42}In_{0.2}Fe_{1.8}O_4$ (N_2) sample contains slight trace of hematite (Fe_2O_3) in addition to spinel phase (Figure 4.2b). To get the pure spinel phase we have decreased the pH value of the precipitation, keeping w = [H_20]/[AOT] ratio constant in all experiments [4]. At pH = 9.0, $Ni_{0.58}Zn_{0.42}In_{0.1}Fe_{1.9}O_4$ (N_3) and $Ni_{0.58}Zn_{0.42}In_{0.2}Fe_{1.8}O_4$ (N_4) nanosamples are successfully synthesized showing the pure spinel phase structure (Figure 4.2c-d). For getting the single spinel phase structure of $Ni_{0.58}Zn_{0.42}In_{0.3}Fe_{1.7}O_4$ (N_5) sample, we have again decreased the pH value (~8.2) of the precipitation (Figure 4.2e). Table 4.1 shows the different compositions of ferrite particles prepared at different pH values.

Table 4.1 Composition of ferrite particles and pH value of precipitation, N: Nano samples, S: Bulk samples

Sample	Composition	pH
N_0	$Ni_{0.58}Zn_{0.42}Fe_2O_4$	9.6
N_1	$Ni_{0.58}Zn_{0.42}In_{0.1}Fe_{1.9}O_4$	10.6
N_2	$Ni_{0.58}Zn_{0.42}In_{0.2}Fe_{1.8}O_4$	10.6
N_3	$Ni_{0.58}Zn_{0.42}In_{0.1}Fe_{1.9}O_4$	9.0
N_4	$Ni_{0.58}Zn_{0.42}In_{0.2}Fe_{1.8}O_4$	9.0
N_5	$Ni_{0.58}Zn_{0.42}In_{0.3}Fe_{1.7}O_4$	8.2
S_0	$Ni_{0.58}Zn_{0.42}Fe_2O_4$	-
S_1	$Ni_{0.58}Zn_{0.42}In_{0.1}Fe_{1.9}O_4$	-
S_2	$Ni_{0.58}Zn_{0.42}In_{0.2}Fe_{1.8}O_4$	-
S_3	$Ni_{0.58}Zn_{0.42}In_{0.3}Fe_{1.7}O_4$	-

Bulk samples were prepared by annealing the pure spinel phase N_0, N_3, N_4 and N_5 nanosamples (almost same particle size) at 1473 K for 4 h. Figure 4.3 shows the X-ray patterns of bulk samples $Ni_{0.58}Zn_{0.42}Fe_2O_4$ (S_0), $Ni_{0.58}Zn_{0.42}In_{0.1}Fe_{1.9}O_4$ (S_1), $Ni_{0.58}Zn_{0.42}In_{0.2}Fe_{1.8}O_4$ (S_2) and $Ni_{0.58}Zn_{0.42}In_{0.3}Fe_{1.7}O_4$ (S_3). Even after heat treatment analysis of the bulk samples revealed a match with PDF # 08-0234, indicating the single spinel phase structure. While for $Ni_{0.58}Zn_{0.42}In_{0.3}Fe_{1.7}O_4$ (S_3) sample, this heat treatment is not enough to make its bulk particles from $Ni_{0.58}Zn_{0.42}In_{0.3}Fe_{1.7}O_4$ (N_5) sample. Therefore, sample is heated at much more higher temperature (1673 K) for getting the bulk particles.

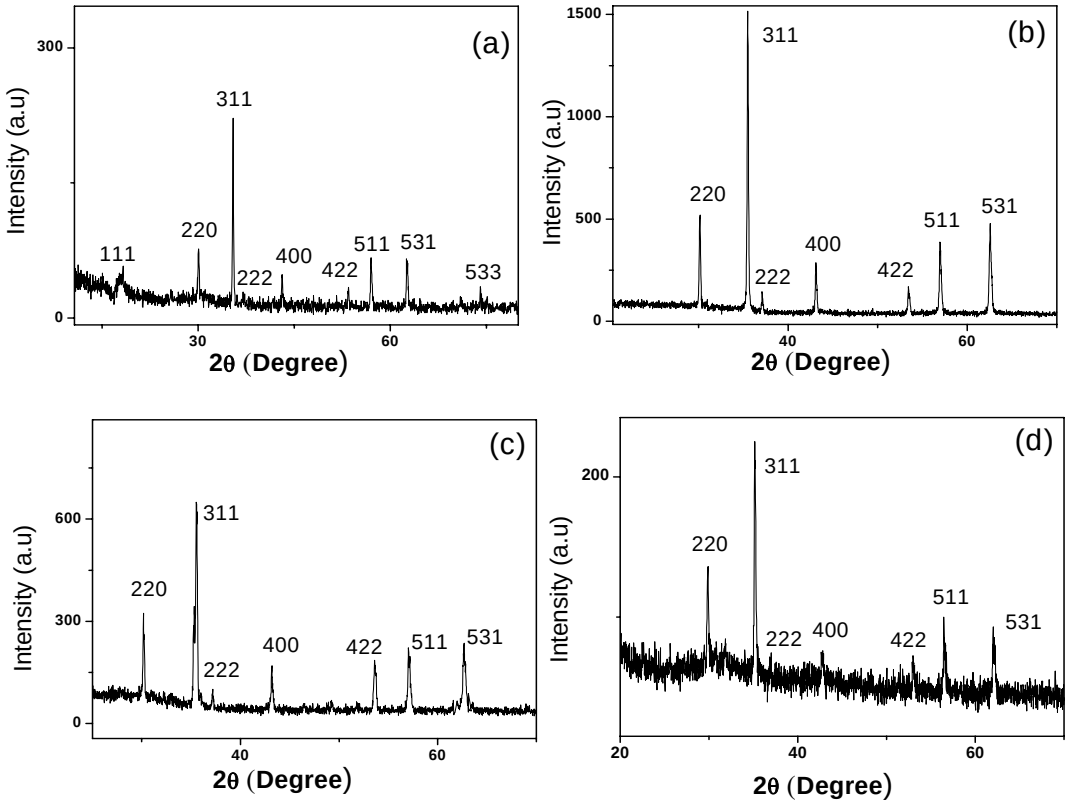

Figure 4.3 *XRD patterns of annealed samples (a) S_0 (b) S_1 (c) S_2 (d) S_3*

The values of lattice constants were determined from the observed positions of peaks using the well-known Bragg's law in the form:

$$a = \frac{(\lambda/2)\left[h^2+k^2+l^2\right]^{1/2}}{\sin\theta} \qquad \text{.....(4.3)}$$

where, (h, k, l) are the miller indices, λ is the wavelength and θ is the angle of corresponding maximum of diffraction. The obtained lattice constant of bulk $Ni_{0.58}Zn_{0.42}Fe_2O_4$ sample is 8.380 Å, a value that is in good agreement with the results published for nickel-zinc ferrite particles [5,6].

From the X-ray diffraction patterns of nanoparticles, it is evident that reflection lines are quite broad as compared to annealed samples. The average particle size was calculated using Debye-Scherrer's eqn. (4.4) [7],

$$D = \frac{k\lambda}{FWHM * Cos\theta_{hkl}} \qquad \text{..... (4.4)}$$

where D is the particle size in Å, k is the shape factor (usually taken as 0.9), λ is the X-ray wavelength (1.54 Å) and θ is Bragg's angle in degrees. The maximum intensity peak (311) was used to find the full width at half the maximum. Using eqn. (4.4), crystallite size of 8.4, 14, 17 nm were determined at pH = 9.6, 10.96, 11.40 respectively for nano $Ni_{0.58}Zn_{0.42}Fe_2O_4$ samples. Table 4.2 shows the particle size, lattice constants and unit cell volume for the bulk as well as nano samples. For reverse micelle process, pH affected the crystallization of the product. In case of nano samples, particle size increases with increase in pH value. This increase in the particle size with increase in the precipitating pH value has already been noticed for other types of ferrites synthesized via wet approaches [8]. The changes in the kinetic stability induced by increased pH values of the solution, which leads to the flocculation of smaller particles into larger aggregates, was attributed to this phenomenon [9]. For annealed (bulk) samples particle size increased to ~0.1 μm except for $Ni_{0.58}Zn_{0.42}In_{0.3}Fe_{1.7}O_4$ sample whose particle size is in nanoscale ~56 nm.

Table 4.2 Particle size, lattice constant and unit cell volume for the nano as well as bulk samples

Sample	Particle size	Lattice constant (Å)	Unit cell Volume ($Å^3$)
N_0	8.4 nm	8.361	584.486
N_1	15.0 nm	8.446	602.494
N_2	15.0 nm	8.432	599.503
N_3	8.7 nm	8.375	587.427
N_4	8.3 nm	8.382	588.901
N_5	8.0 nm	8.387	589.956
S_0	~ 0.1 μ m	8.380	588.380
S_1	~ 0.1 μ m	8.387	589.956
S_2	~ 0.1 μ m	8.390	590.589
S_3	~ 56 nm	8.424	597.798

The lattice constant is found to increase with the increase in indium concentration throughout except for $Ni_{0.58}Zn_{0.42}In_{0.2}Fe_{1.8}O_4$ (~15 nm) sample. The variation can be understood on the basis of the ionic radius of the substituted cation. Since the ionic radius of indium ions (0.91 Å) is larger than that of Fe^{3+} ions (0.67 Å), the substitution is expected to increase the lattice constant with increase in indium (In^{3+}) ions concentration. When the larger indium ions enter the lattice, the unit cell expands while preventing the overall cubic symmetry. This is true as long as the lattice constant increases with the substituent concentration. However, during synthesis if indium ions dissociate from the lattice, a second phase will be formed, which can decrease the lattice constant. The observed decrease in the lattice constant for $Ni_{0.58}Zn_{0.42}In_{0.2}Fe_{1.8}O_4$ (~15 nm) sample is thought to be a result of dissociation of indium ions from the lattice so as to form a second phase. However, the presence of such additional phases in minor concentration might not be seen in X-ray diffraction patterns due to the limitation of the resolution of the instrument.

It has been observed that whether the lattice constants expand or contract with the reduction in size and by how much, appears to depend primarily on the nature of interatomic bonds. Lattice constants increase for $Ni_{0.58}Zn_{0.42}In_{0.1}Fe_{1.9}O_4$ (~15 nm) and $Ni_{0.58}Zn_{0.42}In_{0.2}Fe_{1.8}O_4$ (~15 nm) samples in comparison to bulk samples. In most transition metal oxides, a slight decrease in the particle size is accompanied by an increase in the unit cell volume. For example, the unit cell volume of 8 nm γ-Fe_2O_3 nanoparticles was found to be 2.6 % larger than the bulk cell volume [10]. This happens because the ions in the outermost layer of a nanoparticle are incompletely coordinated and hence forms an electric dipole, resulting roughly a parallel array of dipoles originating in the boundary layer of each particle. The repulsive inert-dipolar forces would tend to increase the lattice constant. Anderson et al. [11] have also reported that it may be due to the small particle size and the interface structure with a large surface/volume fraction.

However, lattice parameters are seen to decrease for samples having very small crystallite sizes. The lower value of lattice constant observed in case of $Ni_{0.58}Zn_{0.42}Fe_2O_4$ (8.4 nm), $Ni_{0.58}Zn_{0.42}In_{0.1}Fe_{1.9}O_4$ (8.7 nm), $Ni_{0.58}Zn_{0.42}In_{0.2}Fe_{1.8}O_4$ (8.3 nm) and $Ni_{0.58}Zn_{0.42}In_{0.3}Fe_{1.7}O_4$ (8.0 nm) samples in comparison to that obtained for bulk samples

could be due to the excessive lattice strain caused by the very high surface/volume ratio known to affect nanocrystalline properties [12].

4.2 Transmission electron microscopy

Transmission electron microscopy (TEM) images for the nanoparticle samples are shown in figure 4.4. Figure 4.4 (a) is the transmission electron microscopy image of $Ni_{0.58}Zn_{0.42}Fe_2O_4$ (N_o) sample, showing spherical particles, with particle size distribution in the range, 8-12 nm. The electron diffraction pattern (inset of Figure 4.4a) shows a ring superimposed with spot, revealed the polycrystallinity of individual crystallites and also confirmed the formation of spinel cubic ferrite. The dark field image is indicative of a very fine, less than 10 nm, grain size inside the crystallites. Figure 4.4 (b-c) shows transmission electron microscopy images for $Ni_{0.58}Zn_{0.42}In_{0.1}Fe_{1.9}O_4$ (N_1) and $Ni_{0.58}Zn_{0.42}In_{0.2}Fe_{1.8}O_4$ (N_2) samples at pH = 10.6. Particles are spherical, with particle size distribution in the range 15-25 nm. While at pH = 9.0, transmission electron microscopy images (Figure 4.4d-e) show that nanoparticles consist of crystallites mostly in the 8-12 nm size range for $Ni_{0.58}Zn_{0.42}In_{0.1}Fe_{1.9}O_4$ (N_3) and $Ni_{0.58}Zn_{0.42}In_{0.2}Fe_{1.8}O_4$ (N_4) samples. Smooth region in the middle shows the background, which appears slightly dark because of a fine layer of surfactant coated on the carbon film. Figure 4.4 (f) shows the transmission electron microscopy image of $Ni_{0.58}Zn_{0.42}In_{0.3}Fe_{1.7}O_4$ (N_5) sample, with a narrow particle size distribution in the range 5-8 nm.

Transmission electron microscopy images are also recorded for annealed samples at 1473 K. Annealed samples have size increased to ~0.1 μm (Figure 4.5) except for $Ni_{0.58}Zn_{0.42}In_{0.3}Fe_{1.7}O_4$ (S_3) sample, which shows the anomalous behavior. Transmission electron microscopy image of $Ni_{0.58}Zn_{0.42}In_{0.3}Fe_{1.7}O_4$ bulk sample shows that even after annealing the sample at much higher temperature (1673 K), particle size remains in nanorange ~50-81 nm. Transmission electron microscopy results are in reasonable agreement with the X-ray diffraction determined crystallite size.

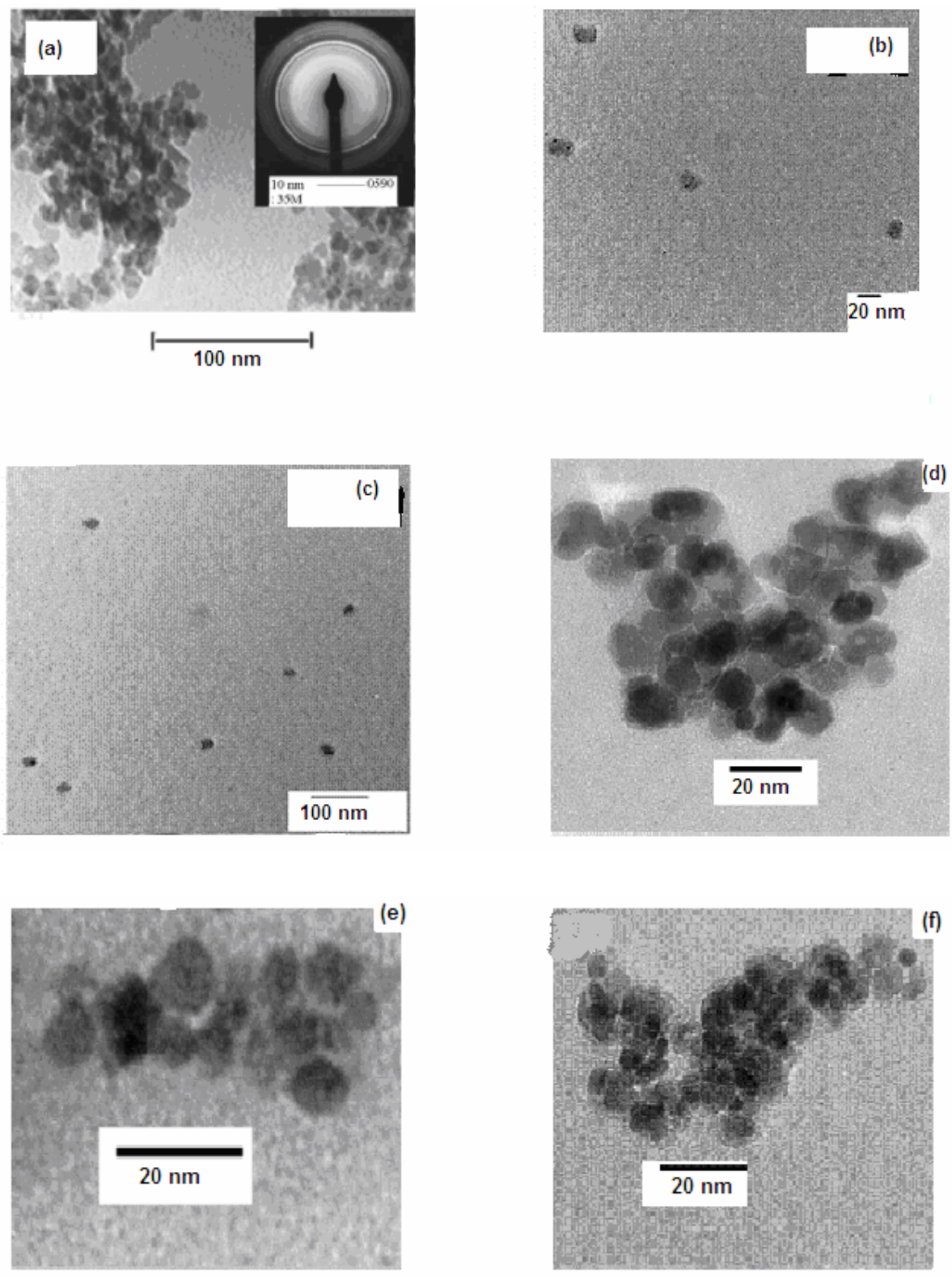

Figure 4.4 *TEM images of (a) N_0 (b) N_1 (c) N_2 (d) N_3 (e) N_4 (f) N_5 nanosamples*

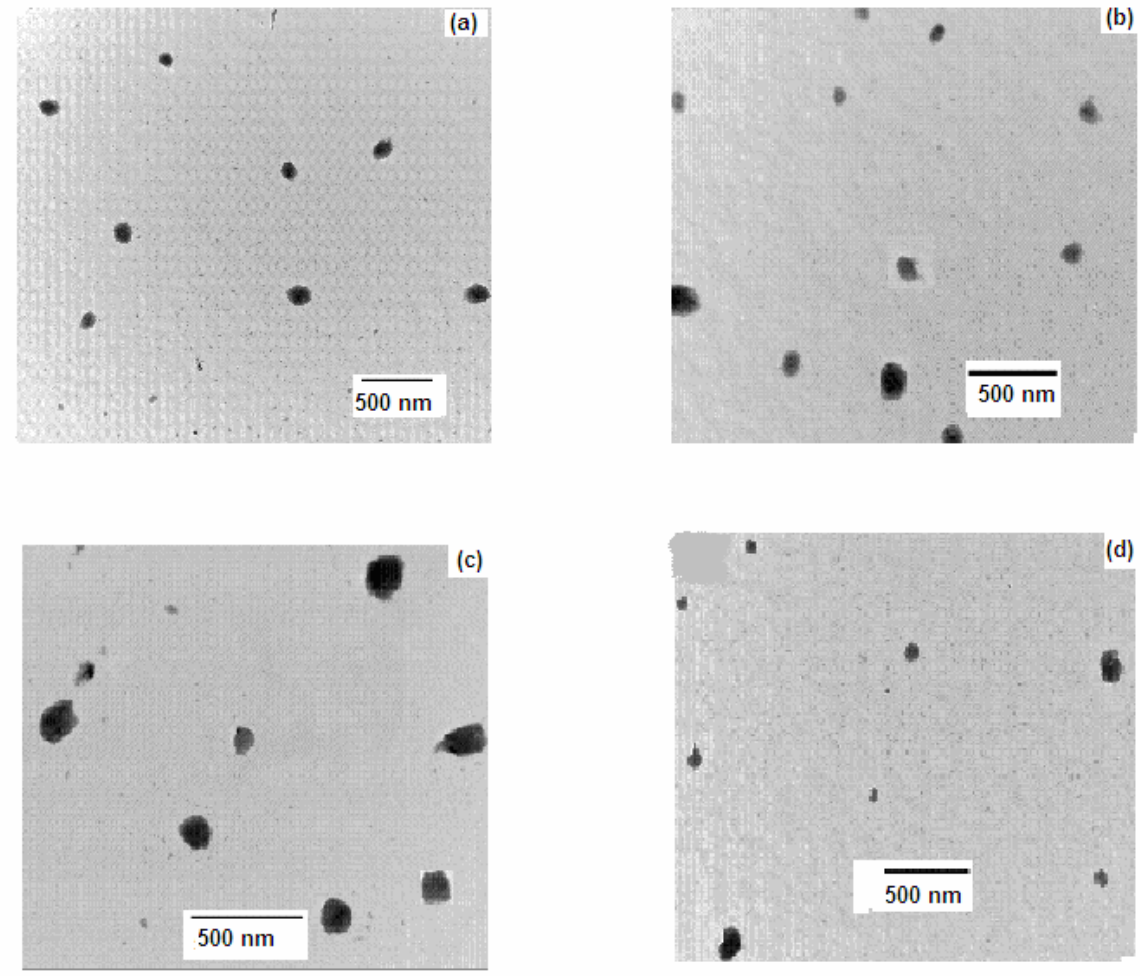

Figure 4.5 *TEM images of (a) S_0 (b) S_1 (c) S_2 (d) S_3 bulk samples*

4.3 Fourier transform infrared spectroscopy

Figure 4.6 shows the room temperature infrared spectra for nickel-zinc ferrite and indium doped nickel-zinc ferrite nanoparticles. The spectra are recorded in the range 400 cm^{-1} up to 4000 cm^{-1}. In the range 1000–100 cm^{-1}, the infrared bands of solids are usually assigned to vibration of ions in the crystal lattice [13]. Two main broad metals-oxygen bands are seen in the infrared spectra of all spinels and ferrites in particular. The highest one, v1, generally observed in the range 550-600 cm^{-1}, corresponds to intrinsic stretching vibration of the metal at the tetrahedral site, $M_{tetra} \leftrightarrow O$ [14]. It can be observed that the higher frequency bands lie at ~ 590, 609, 616, 610, 618, 620 cm^{-1} for N_0, N_1, N_2, N_3, N_4 and N_5 respectively. This confirmed that the structure remains cubic spinel after indium substitution. The broad absorption band around 1131 cm^{-1} corresponds to interlayer

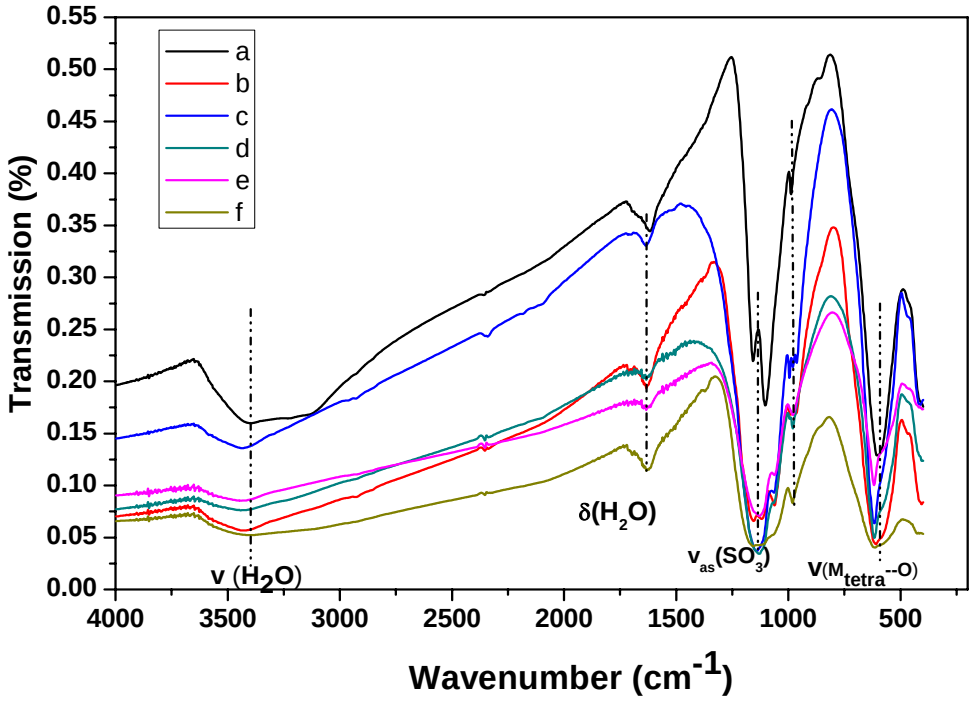

Figure 4.6 *IR absorption spectra of (a) N_0 (b) N_1 (c) N_2 (d) N_3 (e) N_4 (f) N_5 nano samples*

sulfate ions [15]. The absorption band corresponding to water deformation, $\delta(H_2O)$, is recorded around 1624 cm^{-1}, is less intensive [16] and the H_2O absorption band at ~900-1000 cm^{-1} indicates hydrogen bridges. Broad absorption band between 3500 and 3127 cm^{-1} centered around 3433 cm^{-1} is due to O↔H stretching vibration interacting through hydrogen (H) bands [17]. On the basis of detailed analysis of infrared spectra for $Ni_{0.58}Zn_{0.42}In_xFe_{2-x}O_4$ samples more information can be obtained. It can be seen from figure 4.6 that the introduction of indium ion induces significant positive frequency shift of about 16 cm^{-1} for tetrahedral site, showing off that indium is incorporated into the structure. The frequency shift observed are reasonably due to the replacement of Fe^{3+} ions with In^{3+} ions having larger ionic radius and higher atomic weight at tetrahedral sites in the ferrite lattice, which affects the Fe^{3+}— O^{2-} stretching vibration. Special attention has been pointed at the IR absorption spectra for sample heated at high temperature (Figure 4.7). In the spectra we can observe that the peaks are very sharp. The presence of broad absorption band at 1131 cm^{-1} indicates that sulphate ions are still present in the

system. The broadness is interpreted as lowering of symmetry of the sulphate ions after heat treatment. There are two weak and broad absorption bands around 1400 cm^{-1} and 1600 cm^{-1} corresponding to the presence of small amount of residual carbon in the samples. The strong peak at 1710 cm^{-1} is due to the C = O stretching bond. The peaks at 2927 cm^{-1} and 2857 cm^{-1} are due to the asymmetric and symmetric vibrations of the CH_2 group. Our nano sample is covered by a layer of surfactant, the carbonization of the surfactant at high temperature results in extra bands in bulk samples in comparison to nano samples.

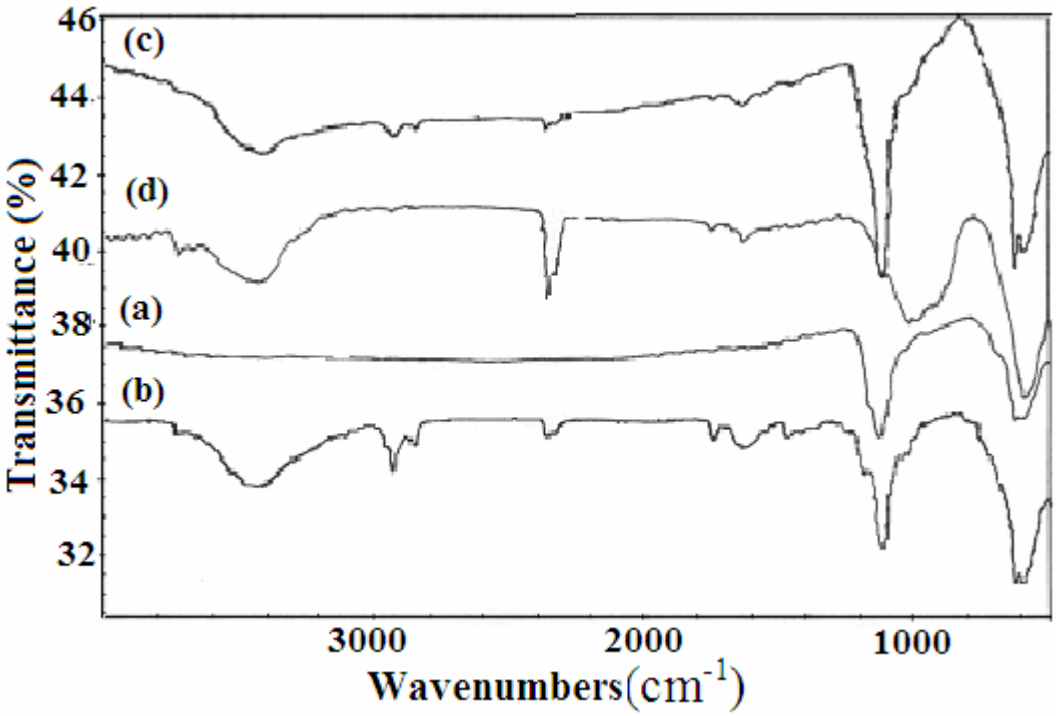

Figure 4.7 *IR absorption spectra of (a) S_0 (b) S_1 (c) S_2 (d) S_3 bulk samples*

Conclusion

We have performed a study on structural properties of pure nickel-zinc ferrite ($Ni_{0.58}Zn_{0.42}Fe_2O_4$) sample and indium doped nickel-zinc ferrite ($Ni_{0.58}Zn_{0.42}In_xFe_{2-x}O_4$) samples synthesized by reverse micelle technique followed by annealing at high temperature to make bulk samples, using X-ray diffraction, transmission electron microscopy and fourier transform infrared spectroscopy measurements. X-ray diffraction

studies confirms the formation of nano samples and the persistence of the spinel phase upto 1473 K. Reverse micelle technique has been found to be appropriate for the synthesis of nanostructured nickel-zinc ferrite particles. In order to yield spinel phase, the pH value of the precipitation was controlled. The average particle size has been found to increase with the pH value of the precipitation. Excessive lattice strain caused by the very high surface/volume ratio results in lattice constant smaller for nano samples $Ni_{0.58}Zn_{0.42}Fe_2O_4$ (8.4 nm), $Ni_{0.58}Zn_{0.42}In_{0.1}Fe_{1.9}O_4$ (8.7 nm), $Ni_{0.58}Zn_{0.42}In_{0.2}Fe_{1.8}O_4$ (8.3 nm) and $Ni_{0.58}Zn_{0.42}In_{0.3}Fe_{1.7}O_4$ (8.0 nm) as compared to bulk samples. Transmission electron microscopy shows that the nano samples synthesized via reverse micelle technique have spherical size and narrow particle size distribution, while in case of annealed samples monodisperse particles are obtained. $Ni_{0.58}Zn_{0.42}In_{0.3}Fe_{1.7}O_4$ sample shows the anomalous behavior having particle size in nanoscale ~56 nm even after heat treatment. Transmission electron microscopy results are in reasonable agreement with the X-ray diffraction determined crystallite size.

Fourier transform infrared spectra confirmed that the structure remains cubic spinel after indium substitution. The frequency shift observed are reasonably due to the replacement of iron (Fe^{3+}) ions with indium (In^{3+}) ions having larger ionic radius and higher atomic weight at tetrahedral sites in the ferrite lattice, which affects the Fe^{3+}—O^{2-} stretching vibration. The carbonization of the surfactant at high temperature results in extra bands in bulk samples in comparison to nano samples.

To our knowledge, this is the first report which highlights the structural properties of indium doped nickel-zinc ferrite particles synthesized by reverse micelle technique. This approach offers several advantages because of possible high-temperature applications of reverse micelle synthesized ferrites.

References

[1] Joint Committee on Powder Diffraction Standards (JCPDS) Powder Diffraction File (PDF), International centre for Diffraction Data, Newtown Square, PA, **2004**.

[2] Uskokovic V., Drofenik M. and Ban I. *J. Magn. Magn. Mater.* **2004**, 284, 294.

[3] Rath C., Sahu K. K., Anand S., Date S. K., Mishra N. C. and Das R. P. *J. Magn. Magn. Mater.* **1999**, 202, 77.

[4] Thakur S., Katyal S. C. and Singh M *J. Magn. Magn. Mater*. **2009**, 321, 1-7.

[5] El-Sayed A. M. *Ceram. Inter.* **2002**, 28, 363-367.

[6] Priyadharsini P., Pradeep A., Samtrasive rao P. and Chandrasekaran G. *Mater. Chem. Phys.* **2009**, 116, 207-213.

[7] Cullity B. D. *Elements of X-ray diffraction* 2nd ed., Addison-Wesley Publishing Company Inc. **1978**.

[8] Jiao X., Chen D. and Hu Y. *Mater. Res. Bull*. **2002**, 37, 1583.

[9] Yener D. O. and Giesche H. *J. Am. Ceram. Soc.* **2001**, 84, 1987.

[10] Ayyub P., Mulatani M. S., Barma M., Palkar V. R. and Vijaraghavan R. *J. Physics C: Solid State Phys.* **1997**, 21, 1851.

[11] Anderson D. and Robert L. M. *J. Magn. Magn. Mater.* **1997**, 172, 29.

[12] Hartridge A., Bhattacharya A. K., Sengupta M., Majumdar C. K., Das D. and Chintalapudi S. N. *J. Magn. Magn. Mater.* **1997**, 176, L89-L92.

[13] Brabers V. A. M. *Phys. Stat. Sol.* **1969**, 33, 563.

[14] Waldron R. D. *Phys. Rev.* **1955**, 99, 1727.

[15] Li F., Liu X., Yang Q., Liu J., Evans D. G. and Duan X. *Mater. Res. Bull.* **2005**, 40, 1244.

[16] Hernandez-Moreno M. J., Ulibarri M. A. and Rendon J. L. *Phys. Chem. Min.* **1985**, 12, 34.

[17] Hair M. L. *J. Non-Cryst. Solids* **1975**, 19, 299.

CHAPTER 5

MÖSSBAUER SPECTROSCOPY CHARACTERIZATION OF NANO AND BULK FERRITE SAMPLES

Mössbauer spectroscopy is a nondestructive technique suitable for the study of structure at nanolevel. The ^{57}Fe Mössbauer spectra are sensitive to the local environment of the iron atoms in the crystal lattice. From the Mössbauer parameters the following information can be obtained: valence state, identification of nonequivalent iron positions in a crystal lattice, type of coordination of iron in its individual positions, level of ordering and stoichiometry, cation distribution and magnetic ordering.

In this chapter, we have presented the Mössbauer spectroscopy characterization on nano and bulk samples at room temperature (300 K) and low temperature (5 K). In most of the papers on reverse micelle synthesis of spinel ferrites [1-4], not much work has been done to determine the structure of oxides with the help of Mössbauer spectroscopy. Especially, the evaluation of the cation distribution in reverse micelle synthesized spinel ferrites from Mössbauer spectra and/or X-ray diffraction patterns is not as straightforward as is frequently claimed in the literature. The hyperfine interactions in tetrahedral (A) and octahedral (B) sites of a nanoscale spinel ferrite usually do not differ substantially and possess a more or less distributive character [5]. Under these conditions, it can happen that the (A) and (B) Mössbauer subspectra are difficult to resolve because of strongly overlapping lines. The use of both large external magnetic fields and low temperature is indispensable in many cases in order to allow for a unanimous separation of the contributions from both sites [6,7]. Thus, cation distributions merely determined from Mössbauer spectra without application of an external magnetic field have to be considered with reserve, especially when conclusions are drawn from spectra with low resolution or bad statistics. In this chapter, quantitative structural information is obtained on both the nonequilibrium cation distribution and the noncollinear spin arrangement in nanosized nickel-zinc ferrite ($Ni_{0.58}Zn_{0.42}Fe_2O_4$) and indium substituted nickel-zinc ferrite ($Ni_{0.58}Zn_{0.42}In_xFe_{2-x}O_4$, x = 0.1, 0.2, 0.3) particles. Effect of indium concentration and particles size on the Mössbauer parameters has been studied. We have also studied the correlation between the particle size and hyperfine field. These studies will surely facilitate the understanding and controlling of the magnetic properties of nanoparticles.

^{57}Fe Mössbauer measurements were carried out in transmission mode with $^{57}Co/Rh$ radioactive source in constant acceleration mode using standard PC-based

Mössbauer spectrometer equipped with Weissel velocity drive. Low temperature and in-field ^{57}Fe Mössbauer measurements were carried out using Janis made of superconducting magnet. Mössbauer spectra were recorded at T = 300 K and 5 K. In-field Mössbauer spectra were recorded at 5 K in the presence of an external magnetic field of 5 T applied parallel to the γ-ray direction. Velocity calibration is done with natural iron absorber. The spectra were well analyzed using a least square-fitting programme NORMOS (SITE/DIST) developed by R. A. Brand [8]. The degree of inversion, λ was calculated from the Mössbauer subspectral intensities, $I_{(A)}/I_{(B)} = f_{(A)}/f_{(B)}*\{\lambda /(2 - \lambda)\}$, assuming that the ratio of the recoilless fractions is $f_{(B)}/f_{(A)} = 1$ at 5 K and $f_{(B)}/f_{(A)} = 0.94$ at room temperature [9]. The average canting angle (Ψ), was calculated from the ratio of the intensities of lines 2 and 3 from each subspectra, I_2/I_3, according to $\Psi = \arccos\{(4-I_2/I_3)/(4+ I_2/I_3)\}^{1/2}$ [10].

Results and discussion

5.1 Mössbauer spectra of nano and bulk nickel-zinc ferrite sample at room temperature (300 K) and low temperature (5 K)

Figure 5.1 shows the room temperature Mössbauer spectra of nano nickel-zinc ferrite ($Ni_{0.58}Zn_{0.42}Fe_2O_4$) sample.

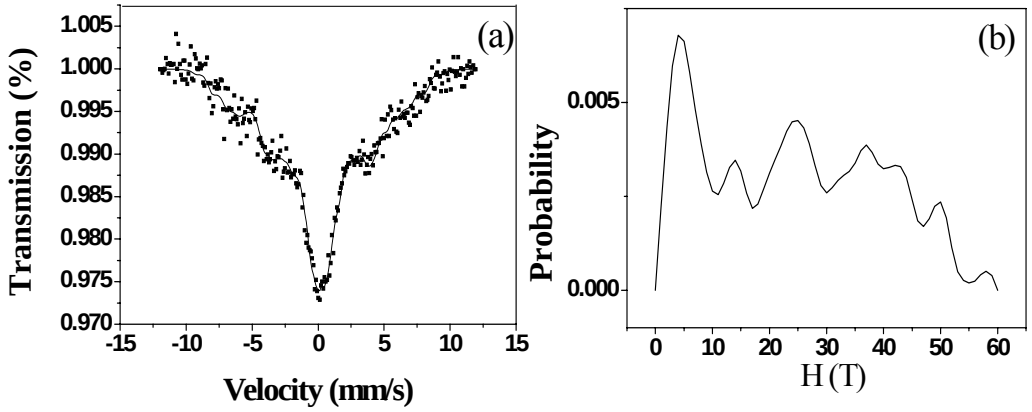

Figure 5.1 *(a) Mössbauer spectra of nano $Ni_{0.58}Zn_{0.42}Fe_2O_4$ sample at room temperature (b) p-H distribution curve*

Mössbauer spectrum of nano $Ni_{0.58}Zn_{0.42}Fe_2O_4$ (N_0) sample exhibits collective magnetic excitations (Figure 5.1a). Here the dots represent the experimental data and solid lines through the data points are least square fit (Figure 5.1a). The spectrum of nano $Ni_{0.58}Zn_{0.42}Fe_2O_4$ sample was fitted with DIST programme and show a wide range of hyperfine magnetic field (HMF) distribution (Figure 5.1b). HMF distribution shows a maximum near 4 T, extending up to ~ 58 T. The average hyperfine field for nano $Ni_{0.58}Zn_{0.42}Fe_2O_4$ sample is 44.43 T.

Room temperature Mössbauer spectrum of bulk $Ni_{0.58}Zn_{0.42}Fe_2O_4$ (S_0) sample shows the ferrimagnetic phase (Figure 5.2). The spectrum reveals the hyperfine magnetic

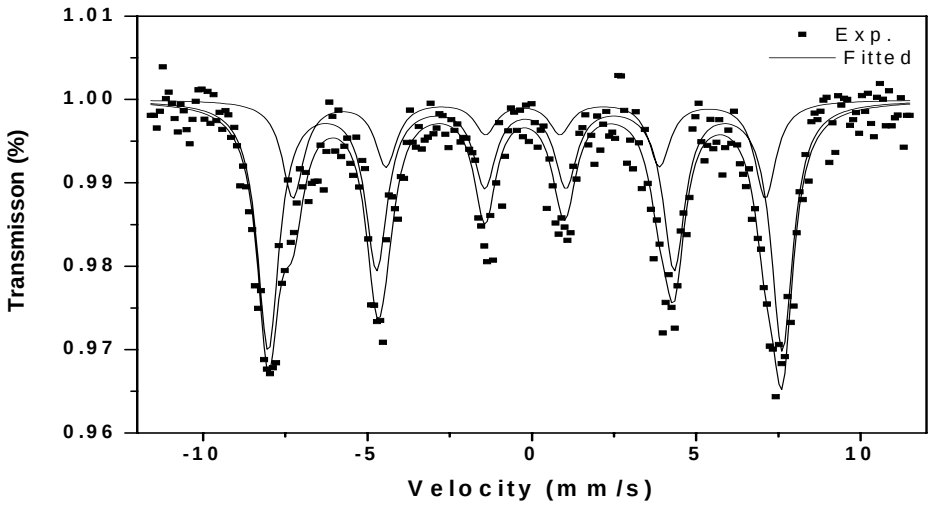

Figure 5.2 *Room temperature Mössbauer spectrum of bulk $Ni_{0.58}Zn_{0.42}Fe_2O_4$ sample*

sextets corresponding to the tetrahedrally and octahedrally coordinated iron cations. The solid lines obtained after fitting the spectrum indicate the position of the tetrahedral (A) and octahedral (B) site. The spectrum was fitted using two magnetic components of hyperfine fields: 44.5 T and 48.0 T corresponding to Fe^{3+} ions at site (A) and (B) respectively. The values of the hyperfine fields are in agreement with previously published data on bulk nickel-zinc ferrite sample [11]. The corresponding Mössbauer parameters obtained by fitting the spectra at room temperature are listed in table 5.1. The degree of inversion calculated from the subspectral area ratio of the Mössbauer spectrum was $\lambda = 0.581$.

Table 5.1 Mössbauer parameters: isomer shift (I.S.), the average magnetic hyperfine field (H), width (WID), quadrupole splitting (Q.S.) and relative area (I) obtained by fitting the room temperature Mössbauer spectrum of bulk sample

Sample	Subspectrum	WID (mm/s)	I.S. (mm/s)	Q. S. (mm/s)	H (T)	AREA (%)
S_0	(A)	0.78±0.07	0.18±0.00	0.19±0.07	44.50±0.27	27.88 %
	(B)	0.80±0.00	0.20±0.00	-0.01±0.00	48.41±0.11	72.12 %
				$I_{(A)}/I_{(B)}$ = 0.386, λ = 0.582		

The low-temperature Mössbauer spectra of both nano and bulk $Ni_{0.58}Zn_{0.42}Fe_2O_4$ sample are compared in figure 5.3. As clearly shown, the superparamagnetic relaxation of nano

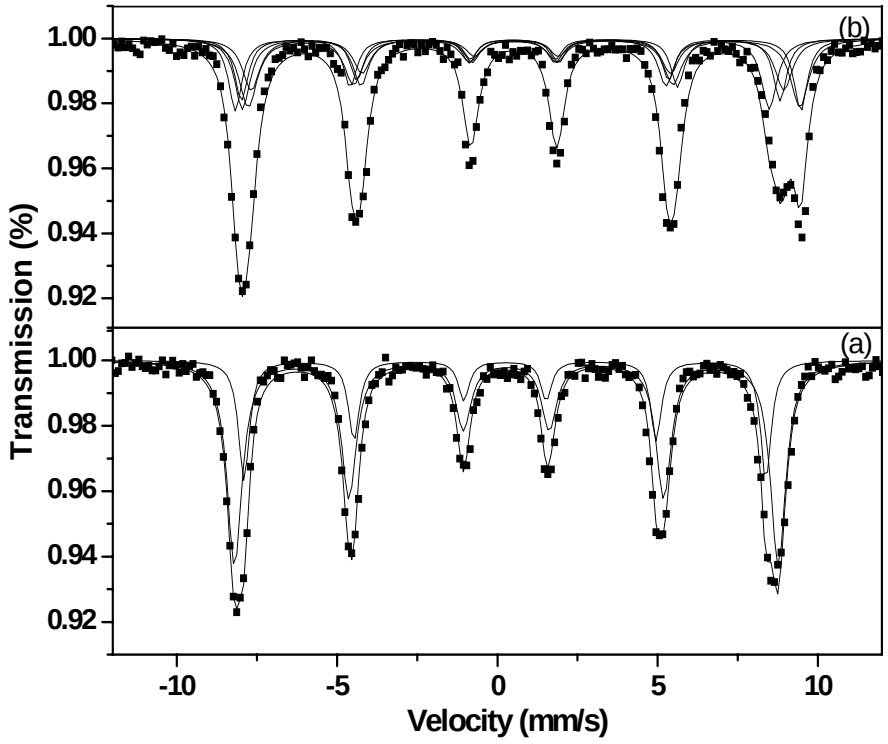

Figure 5.3 *Zero field Mössbauer spectra of $Ni_{0.58}Zn_{0.42}Fe_2O_4$ sample taken at 5 K (a) bulk sample (b) nano sample*

particles is suppressed at 5 K, and the spectrum consists of broadened sextets only. The spectrum of the bulk $Ni_{0.58}Zn_{0.42}Fe_2O_4$ sample at room temperature (Figure 5.2) and low-temperature (Figure 5.3a) show similar magnetic sextet distributions, except for large

hyperfine field values at 5 K, as expected. The low temperature spectrum of the bulk $Ni_{0.58}Zn_{0.42}Fe_2O_4$ sample consists of two sextets with the average magnetic hyperfine fields $H_{(A)}$ = 50.39 T and $H_{(B)}$ = 52.41 T that are well comparable with those of the bulk material [12].

The broad shape of Mössbauer spectral lines for the nano $Ni_{0.58}Zn_{0.42}Fe_2O_4$ sample as compared to bulk sample provides clear evidence of a wide distribution of magnetic fields acting at the Fe^{3+} nuclei in the nanoparticles. To analyze the complex spectra of nano $Ni_{0.58}Zn_{0.42}Fe_2O_4$ particles we take into consideration that the (A) site hyperfine fields in spinel ferrites are not very sensitive to the kind of (B) site nearest neighbors [13]. It is well known that Zn^{2+} prefers the (A) sites and Ni^{2+} prefers the (B) sites [12], and a recent combined study using extended X-ray absorption fine structure and Mössbauer effect confirmed that it is also the case in nano $Ni_{0.58}Zn_{0.42}Fe_2O_4$ particles [14]. The (A) and (B) magnetic ions are engaged in superexchange interactions, giving rise to ferrimagnetic nature of the material. For ^{57}Fe ion at the (A) site, its metallic ion neighbors at (B) sites are all magnetic (on an average, 3Fe-1Ni). Therefore, the hyperfine field at the (A) site ^{57}Fe nuclei should be relatively constant and was fitted by a single hyperfine field at an (A) site. For a (B) site ^{57}Fe, however, its six metallic ion neighbors at (A) site may include any number of non magnetic Zn^{2+} ions (e.g. 6Fe-0Zn, 5Fe-1Zn, 4Fe-2Zn, 3Fe-3Zn, 2Fe-4Zn, 1Fe-5Zn, 0Fe-6Zn) and the hyperfine field is reduced due to the presence of Zn^{2+} ions. Assuming a random distribution of Zn^{2+} ions, the probability of having n Zn^{2+} ions ($0 \leq n \leq 6$) is given by the binomial formula

$$P(n, x) = \binom{6}{n} x^n (1-x)^{6-n} \quad \text{.....(5.1)}$$

where x is the average fraction of (A) site occupied by Zn^{2+} ions. In our case, x = 0.42, and the probabilities are 0.038, 0.165, 0.299, 0.289, 0.157, 0.045, 0.005 for n = 0, 1, 2, 3, 4, 5 and 6 respectively. Mössbauer studies of conventional and nanostructured $Ni_{0.58}Zn_{0.42}Fe_2O_4$ particles have provided evidence for the (B) site hyperfine distribution in accordance with these probabilities [14-16]. For this reason it was found necessary to fit additional hyperfine field components at the (B) site. For the Mössbauer spectra of nano $Ni_{0.58}Zn_{0.42}Fe_2O_4$ particles taken at 5 K, four hyperfine components were found sufficient to fit the absorption due to Fe^{3+} (B) site (Figure 5.3b and Table 5.2). The

probabilities for n = 0, 5 and 6 are not large enough to be significant. On the basis of detailed analysis of a broad (B) site HMF distribution, its low-field component was

Table 5.2 Mössbauer parameters: isomer shift (I.S.), the average magnetic hyperfine field (H), width (WID), quadrupole splitting (Q.S.) and relative area (I) obtained by fitting the Mössbauer spectra at 5 K

Sample	Subspectrum	WID (mm/s)	I.S. (mm/s)	Q. S. (mm/s)	H (T)	AREA (%)
S_0	(A)	0.40±0.00	0.23±0.02	-0.002±0.00	50.39±0.10	29.41 %
	(B)	0.56±0.01	0.28±0.00	0.003±0.00	52.41±0.20	70.59 %
			$I_{(A)}/I_{(B)}$ = 0.416, λ = 0.587			
N_0	(A)	0.58±0.02	0.38±0.01	0.23±0.03	50.94±0.00	21.70%
	(B)					78.30%
	$(B)_1$	0.50±0.00	0.58±0.01	-0.12±0.03	54.64±0.10	19.23%
	$(B)_2$	0.68±0.00	0.66±0.03	-0.33±0.07	53.31±0.10	24.73%
	$(B)_3$	0.50±0.00	0.45±0.02	0.06±0.04	52.07±0.00	16.48%
	$(B)_4$	0.65±0.01	0.60±0.02	-0.04±0.00	51.50±0.00	17.86%
			$<H>_{(B)}$ = 52.88 T			

assigned to those Fe^{3+} (B) site nuclei that experience a local surrounding with the reduced number of magnetic neighbors on the nearest (A) sites. In this context, in the present study, the B_4 component of the (B) site HMF distribution may be attributed to those Fe^{3+} (B) ions located in the surface region of a nano $Ni_{0.58}Zn_{0.42}Fe_2O_4$ particle that possess four nearest (A) site ion neighbors. The average values of the hyperfine fields $H_{(A)}$ = 50.94 T and $H_{(B)}$ = 52.88 T are comparable to that of bulk $Ni_{0.58}Zn_{0.42}Fe_2O_4$ sample.

5.1.1 In-field Mössbauer spectra of nano and bulk nickel-zinc ferrite sample

The determination of the cation distribution in nano $Ni_{0.58}Zn_{0.42}Fe_2O_4$ particles is impossible to make from the low-temperature spectrum, because it is difficult to resolve the subspectra or to assign them to the respective lattice sites. Therefore, in the present case, the iron populations at the (A) and (B) sublattices will be analyzed concurrently with the discussion of in-field Mössbauer data. In the presence of an external magnetic field (H_{ext}) applied parallel to the γ-ray direction, the effective magnetization of the individual particles is aligned along the field. As a consequence of the antiparrallel

alignment of the spins of Fe^{3+} cations at (A) and (B) sites in spinel ferrites, the external field adds to the magnetic hyperfine field at (A) site and subtracts from the hyperfine field at (B) sites [17]. Thus, the use of the large external magnetic fields creates an effective separation of the overlapping subpatterns, thereby allowing for an accurate determination of the cation distribution in ferrites.

In-field Mössbauer spectra for both bulk and nanosized $Ni_{0.58}Zn_{0.42}Fe_2O_4$ particles taken at 5 K are shown in figure 5.4. The Mössbauer spectra of the bulk $Ni_{0.58}Zn_{0.42}Fe_2O_4$

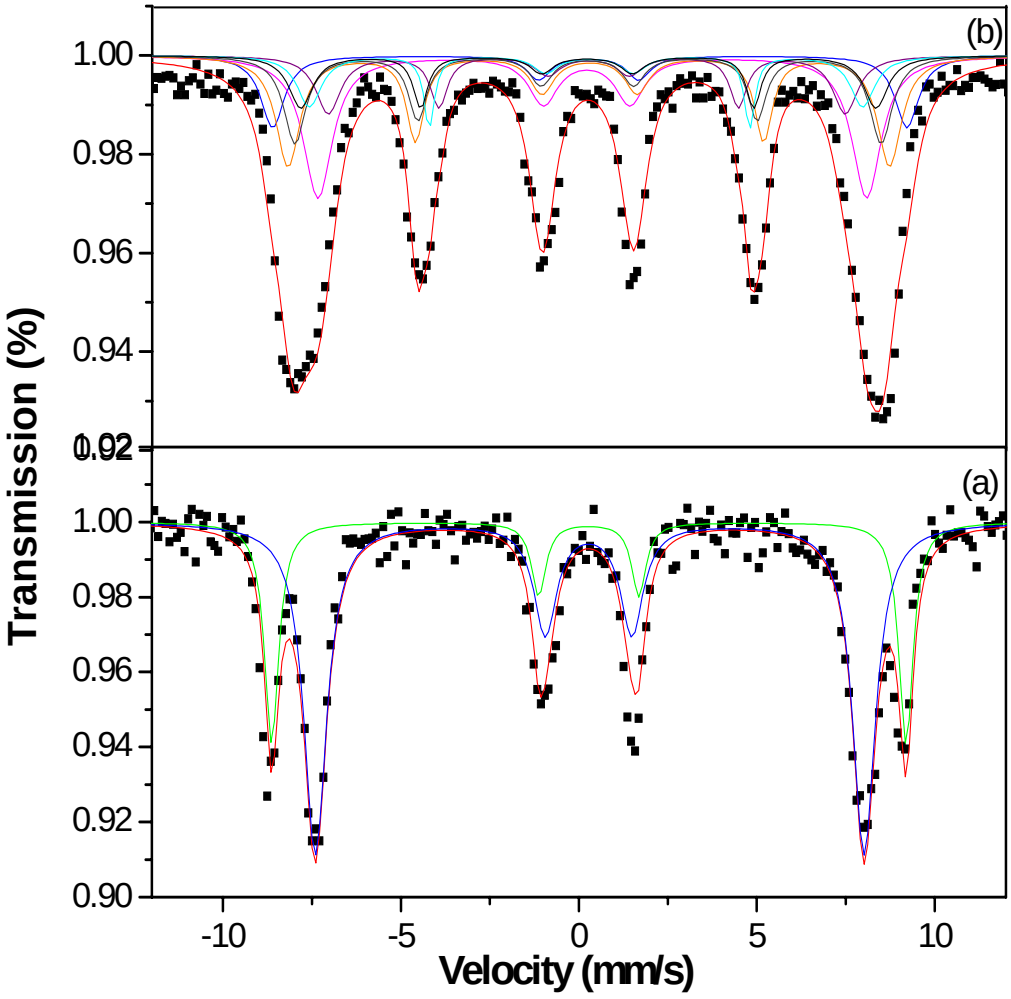

Figure 5.4 *Mössbauer spectra of $Ni_{0.58}Zn_{0.42}Fe_2O_4$ sample recorded at 5 K in an external magnetic field of 5 T (a) bulk sample (b) nano sample*

sample (Figure 5.4a) was fitted by a superposition of two subspectra corresponding to Fe^{3+} (A) and Fe^{3+} (B) ions. The average effective hyperfine field values (Table 5.3) obtained after fitting are well comparable with those of the earlier studies on nickel-zinc bulk material [12]. The quantitative evaluation of this spectrum revealed that the bulk

Table 5.3 Mössbauer parameters: isomer shift (I.S.), effective hyperfine field ($H_{eff.}$) the average magnetic hyperfine field (H), width, quadrupole splitting (Q.S.) and relative area (I), obtained by fitting the high field spectra at 5 K. Ψ is the canting angle, c define as the core and s is used for surface, $I_{(A)2}/I_{(A)3}$ is the relative area of 2 and 3 lines for the (A) site, $I_{(B)2}/I_{(B)3}$ is the relative area of 2 and 3 lines for the (B) site, < H> is the average hyperfine field acting at (B) site, <H_{eff}> is the average effective hyperfine field acting at (B) site in the presence of field, λ is the degree of inversion.

Sample	Subspectrum	WID (mm/s)	I.S. (mm/s)	Q.S. (mm/s)	H_{eff} (T)	H (T)	AREA (%)
S_0	(A)	0.48±0.01	0.28±0.10	0.01±0.00	55.22±0.05	50.23	29.41 %
	(B)	0.77±0.01	0.29±0.01	0.03±0.02	47.77±0.04	52.77	70.59 %
	$I_{(A)}/I_{(B)}$ = 0.413, λ = 0.584, $I_{(A)2}/I_{(A)3} = I_{(B)2}/I_{(B)3}$ =0, $\Psi_{(A)} = \Psi_{(B)} = 0^o$						
N_0	$(A)_c$	0.8[a]	0.28[a]	0.03±0.02	55.22[a]	50.23	9.35 %
	$(B)_c$	0.99±0.01	0.29[a]	0.02±0.01	47.77[a]	52.77	22.89 %
	$(A)_s$	0.82[a]	0.24[a]	-0.02±0.01	52.35±0.06	49.33	20.99 %
	(B)						46.77 %
	$(B)_{s1}$	0.75[a]	0.24[a]	0.02±0.00	51.03±0.10	54.24	15.48 %
	$(B)_{s2}$	0.8±0.10	0.24[a]	0.03±0.02	50.08±0.10	53.28	9.92 %
	$(B)_{s3}$	0.82[a]	0.24[a]	-0.09±0.02	48.18±0.20	51.01	9.92 %
	$(B)_{s4}$	0.84[a]	0.24[a]	-0.05±0.00	45.02±0.01	48.30	11.45 %
$I_{(A)c}/I_{(B)c}$ = 0.408, λ_c= 0.58, $I_{(A)2c}/I_{(A)3c} = I_{(B)2c}/I_{(B)3c}$ =0 $\Psi_{(A)c} = \Psi_{(B)c} = 0^o$, $I_{(A)s}/I_{(B)s}$ = 0.449, λ_s= 0.62, $I_{(A)2s}/I_{(A)3s}$ = 1.7, <$I_{(B)2s}/I_{(B)3s}$>= 1.81, $\Psi_{(A)s} = 50.67^o$, $\Psi_{(B)s} = 52.22^o$, < H_{eff}>$_{(B)s}$ = 48.57 T, < H>$_{(B)s}$ = 51.70 T a is fixed parameter.							

sample exhibits the fully inverse spinel structure with a collinear spin alignment. The degree of inversion was found to be λ = 0.58. The intensity ratio $I_2/I_3 \approx 0$ for both (A) and (B) subspectra indicates that the spins are completely aligned ($\Psi_{(A)} = 0^o$, $\Psi_{(B)} = 0^o$) along the external magnetic field of 5 T. Thus the bulk ferrite exhibits a fully inverse spinel structure with a Néel-type collinear spin arrangement of ions ($Zn_{0.42}Fe_{0.58}\uparrow$) [$Ni_{0.58}Fe_{1.42}\downarrow$]. The degrees of inversion calculated from the subspectral area ratio of the

Mössbauer spectrum without and with an applied magnetic field were found to be λ = 0.587, 0.584 respectively and are in good agreement with each other. Within the experimental error limits, hyperfine fields derived from the zero field Mössbauer spectrum of the bulk $Ni_{0.58}Zn_{0.42}Fe_2O_4$ sample are in agreement with those obtained from the in-field Mössbauer spectrum at 5 K (Tables 5.2 and 5.3).

In-field Mössbauer spectrum of $Ni_{0.58}Zn_{0.42}Fe_2O_4$ nanoparticles (Figure 5.4b) is well fitted by assuming an ordered particle core surrounded by disordered grain boundary (surface) regions. This fitting strategy has already been applied in the fitting of the in field Mössbauer spectra of nanoscale particles $NiFe_2O_4$ [7], $MgFe_2O_4$ [8] and $CuFe_2O_4$ [18]. Thus the present Mössbauer spectra were fitted by a superposition of four subspectra; two accounting for Fe^{3+} nuclei at (A) and (B) sites of the particle core, denoted by $(A)_c$ and $(B)_c$ and two associated with Fe^{3+} ions at (A) and (B) sites in the surface shell of the nanoparticles denoted by $(A)_s$ and $(B)_s$ (Table 5.3). To separate the surface effects from the bulk effects in the spectrum of $Ni_{0.58}Zn_{0.42}Fe_2O_4$, we assumed that the core of nano $Ni_{0.58}Zn_{0.42}Fe_2O_4$ particles possesses the same structure as the bulk sample. Thus, the fit to the spectrum of nano $Ni_{0.58}Zn_{0.42}Fe_2O_4$ particles was made by imposing constraints on the Mössbauer parameters of the subspectra corresponding the particle core (I.S., H, $I_{(A)c}/I_{(B)c}$, $I_{(A)c2}/I_{(A)c3}$, $I_{(B)c2}/I_{(B)c3}$), such that these parameters were fixed and equal to those obtained from the fit of the spectrum of the bulk sample. The absorption due to Fe^{3+} ions at (B) site of the particle shell was fitted by a HMF distribution consisting of four components (Bn_s, n = 4, 3, 2, 1).

The results of the present study are supported by Mössbauer measurements on nickel-zinc ferrite particles with varied concentration of zinc ions, prepared by wet grinding technique [12]. Width (WID) of the outermost (A) site linewidth is smaller than the (B) site linewidth. In nickel-zinc ferrite particles the field gradients at the (A) site ions are more uniform as the (B) sites are occupied to a greater extent by Fe^{3+} ions. Consequently, WID (A) is less than WID (B) site. The values of width for bulk sample are in good agreement with the reported one and the spectrum was well fitted with two sextets. The smaller isomer shift (I.S.) at the (A) site is due to a larger covalency and is in good agreement with the results of other workers [18,19]. The values of I.S. at (A) and (B) sites show that iron is in the Fe^{3+} state [18]. The observed differences between the

I.S. of bulk particles at 5 K and 300 K (Table 5.1 and Table 5.2) are fully explained by the temperature-dependent second-order Doppler shift of the lines. The values of quadrupole splitting (Q.S.) for hyperfine spectra of nano and bulk samples are almost zero within the experimental error and are attributed to the fact that overall cubic symmetry is maintained. The values of I.S. and Q.S. obtained for (A) and (B) sites are in good agreement with earlier study on nickel-zinc ferrite particles [14,19]. The I.S. and Q.S. values obtained also confirm the presence of only Fe^{3+} charge state and not Fe^{2+} charge state in the system. Smaller magnitude of $H_{(A)}$ compared to $H_{(B)}$ in nano $Ni_{0.58}Zn_{0.42}Fe_2O_4$ particles is primarily due to covalency, as suggested for inverse spinel ferrites [12].

We have also studied the hyperfine magnetic field (HMF) distribution in nano sample by fitting the in-field data using DIST programme. Figure 5.5 compares the (B) site HMF distributions derived from the in-field Mössbauer spectra of the bulk and nano $Ni_{0.58}Zn_{0.42}Fe_2O_4$ sample. The in-field data is fitted considering the (A) site as crystalline site and the (B) site as for the distribution of fields. The obtained HMF distributions basically correspond to the (B) site. It may be noted that this is mainly because of the fact that the lines corresponding to (B) site are relatively broad as compared to (A) site as

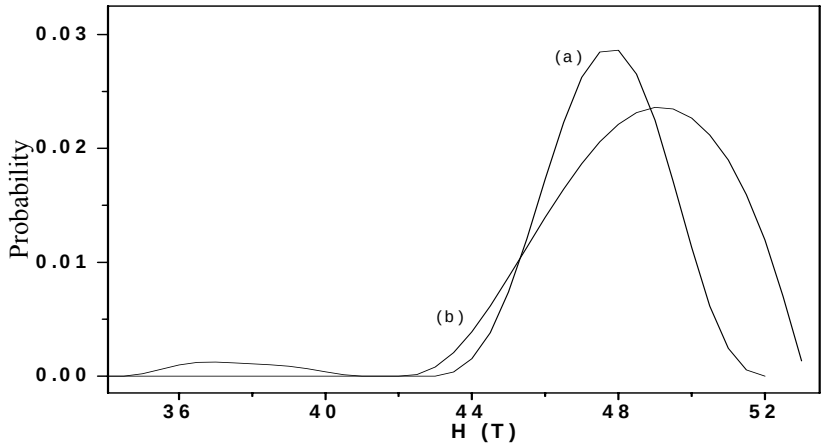

Figure 5.5 *The (B) site hyperfine distribution derived from the Mössbauer spectrum recorded at 5 K in an external magnetic field of 5 T (a) bulk sample (b) nano sample*

described above. It should be emphasized that HMF distributions provide the most detailed information on the local magnetic fields acting on iron nuclei located on a particular iron site. As can be seen, the (B) site iron nuclei located in the bulk $Ni_{0.58}Zn_{0.42}Fe_2O_4$ particles (Figure 5.5a) experience a local fields from a relatively narrow interval (from about 44 to 51 T). This is in contrast to the nanosized particles, where a broad distribution is observed ranging from about 43 to 53 T (Figure 5.5b). This broad HMF distribution indicates a strongly disturbed macroscopic magnetic state of the nano $Ni_{0.58}Zn_{0.42}Fe_2O_4$ particles.

From the relative intensities of sextets, one can easily deduce quantitative information on both the cation distribution and the spin configuration within the nano $Ni_{0.58}Zn_{0.42}Fe_2O_4$ particles. Whereas the core is considered to possess the partly inverse spinel structure ($\lambda_c = 0.58$), the shell region is found to be structurally disordered. The subspectral intensity ratio $I_{(A)s}/I_{(B)s} = 0.449$ indicates that the major feature of the atomic configuration in the shell is a nonequilibrium cation distribution characterized by increased fraction of iron cations on (A) sites, $\lambda_s = 0.62$.

Another striking feature of the present Mössbauer data is the observed difference between the intensity ratios of spectral lines 2 and 3 for the inner core ($I_{(A)c2}/I_{(A)c3}$, $I_{(B)c2}/I_{(B)c3}$) and the surface region ($I_{(A)s2}/I_{(A)s3}$, $I_{(B)s2}/I_{(B)s3}$), which is a direct indication of a nonuniform spin arrangement within a nanoparticle. Whereas the magnetic moments located at (A) and (B) sites of the particle core are assumed to exhibit a perfect alignment with the external field ($I_{(A)c2}/I_{(A)c3} = I_{(B)c2}/I_{(B)c3} = 0$), the spins in the shell region are found to be canted. The average canting angles, calculated from the intensity ratios $I_{(A)s2}/I_{(A)s3}$ and $I_{(B)s2}/I_{(B)s3}$, were found to be $\Psi_{(A)s} = 50.67^o$ and $\Psi_{(B)s} = 52.22^o$, respectively. Thus the spins located on the two sublattices in the surface regions of $Ni_{0.58}Zn_{0.42}Fe_2O_4$ nanoparticles are found to behave differently under an external filed of 5 T.

This result is also consistent with previous work, where different spin canting in the (A) and (B) sublattices of spinel nanostructured was observed [6,7,20-22]. The intensity ratio $(I_{(A)s}+ I_{(B)s}/(I_{(A)c}+ I_{(B)c}+ I_{(A)s}+ I_{(B)s}) = 0.647$ indicates that about 64% of the magnetic cations are located in the surface shell of nano $Ni_{0.58}Zn_{0.42}Fe_2O_4$ particles. Assuming a spherical shape of reverse micelle synthesized nanoparticles and taking their average size as determined by X-ray diffraction pattern (8.4 nm), we estimated the

thickness of the surface shell to be t ≈ 1.3 nm. The estimated thickness of the shell is also comparable to that obtained from magnetic measurements on mechanosynthesized $MnFe_2O_4$ nanoparticles (0.91 nm) [23], ball milled $NiFe_2O_4$ (0.88 nm) [24], nanosized $CoFe_2O_4$ (1.0-1.6 nm) [25], $MgFe_2O_4$ (0.85 nm) [6] and $NiFe_2O_4$ (1 nm) [7]. The non uniform nanostructure of $Ni_{0.58}Zn_{0.42}Fe_2O_4$ particles is schematically presented in figure 5.6.

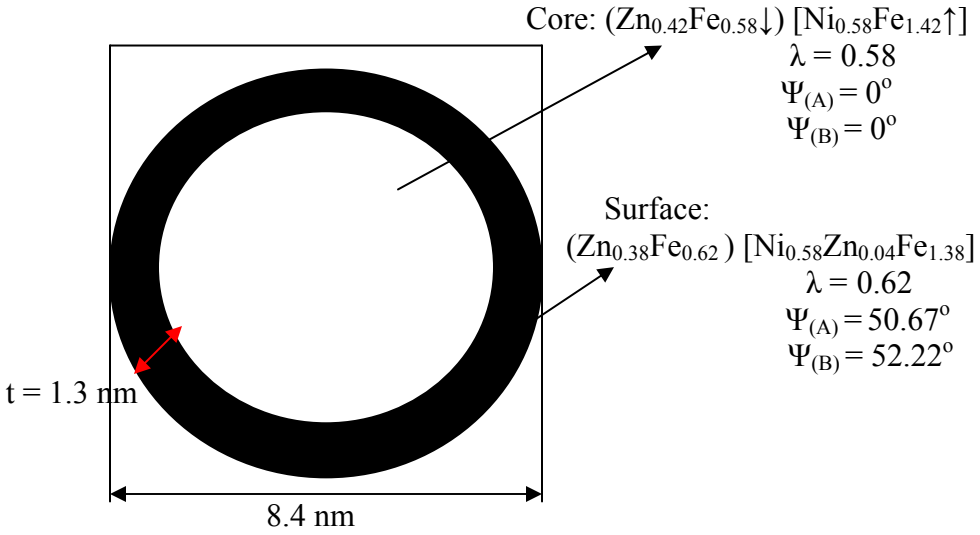

Figure 5.6 *Schematic representation of non uniform structure of nanoparticles*

It is found that the average sublattice magnetic fields experienced by Fe^{3+} ions located in the near surface layers ($H_{(A)s}$= 49.33 T, $H_{(B)s}$= 51.70 T) are reduced in comparison with those acting on iron nuclei in the inner core ($H_{(A)c}$= 50.23 T, $H_{(B)c}$= 52.77 T) of nano sample. This could be explained by the effect of frustrated superexchange interactions due to the above described cation disorder and spin canting in the surface regions of nanoparticles. The reduced magnetic fields have already been reported for nano $Ni_{0.58}Zn_{0.42}Fe_2O_4$ particles [26]. This indicates that the nonequilibrium cation distribution and the canted spin arrangement resulting from the reverse micelle synthesis route are metastable; that is, during the annealing process, they relax toward their equilibrium configuration. Thus, on heating, the reverse micelle synthesized nano $Ni_{0.58}Zn_{0.42}Fe_2O_4$ particles have relaxed to a magnetic state that is similar to the bulk one.

5.2 Mössbauer spectra of nickel-zinc-indium ferrite samples at nano and bulk scale

The room temperature Mössbauer spectra for bulk $Ni_{0.58}Zn_{0.42}In_xFe_{2-x}O_4$ samples are shown in figure 5.7 and 5.8. Bulk samples of $Ni_{0.58}Zn_{0.42}In_{0.1}Fe_{1.9}O_4$ (S_1) and

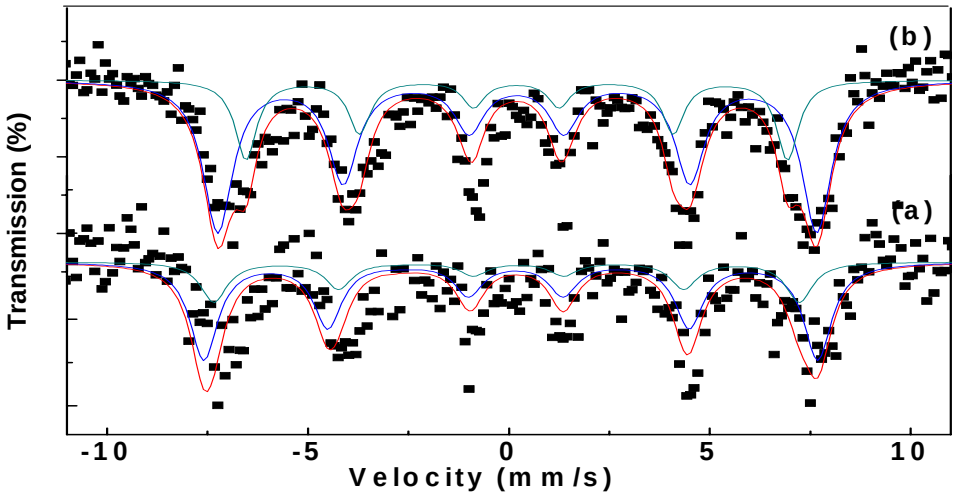

Figure 5.7 *Room temperature Mössbauer spectra of nickel-zinc-indium ferrite bulk samples (a) S_1 (b) S_2*

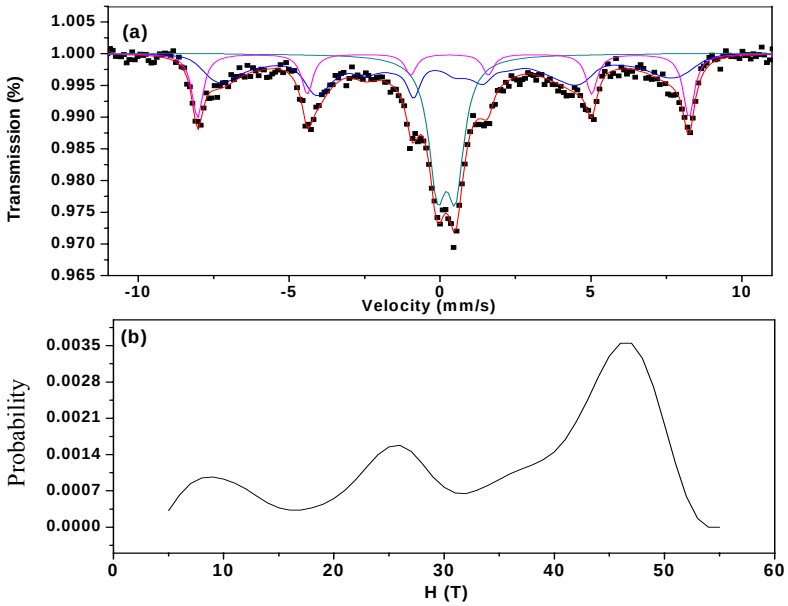

Figure 5.8 *Room temperature Mössbauer spectrum of nickel-zinc-indium ferrite bulk sample (a) S_3 (b) p-H distribution curve*

$Ni_{0.58}Zn_{0.42}In_{0.2}Fe_{1.8}O_4$ (S_2) at room temperature show a well defined Zeeman pattern consisting of two sextets, due to Fe^{3+} ions at (A) and (B) sites. The parameters obtained after fitting are given in table 5.4. S_1 sample consist of sextet with $H_{(A)}$ = 44.02 T, $H_{(B)}$ = 46.17 T and for S_2 sample the parameters are $H_{(A)}$ = 41.76 T, $H_{(B)}$ = 46.17 T. From the

Table 5.4 Mössbauer parameters for nickel-zinc-indium ferrite samples at room temperature

Sample	Subspectrum	WID (mm/s)	I.S. (mm/s)	Q. S. (mm/s)	H (T)	AREA (%)
S_1	(A)	0.80±0.00	0.17±0.00	0.16±0.06	44.02±0.00	27.92 %
	(B)	0.85±0.00	0.20±0.00	-0.06±0.05	46.17±0.17	72.08 %
				$I_{(A)}/I_{(B)}$ = 0.387		
S_2	(A)	0.65±0.05	0.19±0.01	-0.007±0.00	41.76±0.18	27.87 %
	(B)	0.89±0.03	0.20±0.00	-0.019±0.02	46.17±0.07	72.13 %
				$I_{(A)}/I_{(B)}$ = 0.386		

spectra of bulk samples, it is evident that the material is magnetically ordered. The origin of such a high fields in the spinel ferrites is due to superexchange interaction between nuclear spins, where the spin density is transferred via the oxygen ions. As a result, particular iron ion experience local fields that reflect the distribution of magnetic ions in the neighborhood. The Mössbauer spectrum of $Ni_{0.58}Zn_{0.42}In_{0.3}Fe_{1.7}O_4$ (S_3) sample (Figure 5.8) shows collective magnetic excitations, which may be due to decrease in hyperfine field values with increase in indium concentration and smaller particle size of $Ni_{0.58}Zn_{0.42}In_{0.3}Fe_{1.7}O_4$ (S_3) sample than that of $Ni_{0.58}Zn_{0.42}In_{0.1}Fe_{1.9}O_4$ (S_1) and $Ni_{0.58}Zn_{0.42}In_{0.2}Fe_{1.8}O_4$ (S_2) samples. The spectrum was fitted with DIST programme. The spectrum of $Ni_{0.58}Zn_{0.42}In_{0.3}Fe_{1.7}O_4$ (S_3) sample has a wide range of HMF distribution (Figure 5.8b). HMF distribution of $Ni_{0.58}Zn_{0.42}In_{0.3}Fe_{1.7}O_4$ (S_3) sample shows a maximum at 45.90 T. The average hyperfine field for $Ni_{0.58}Zn_{0.42}In_{0.3}Fe_{1.7}O_4$ (S_3) sample is 35.03 T.

Room temperature Mössbauer spectra of $Ni_{0.58}Zn_{0.42}In_{0.1}Fe_{1.9}O_4$ (N_1) and $Ni_{0.58}Zn_{0.42}In_{0.2}Fe_{1.8}O_4$ (N_2) samples having an average particle size 15 nm (Figure 5.9) show well defined sextet with a small superparamagnetic doublet. In case of N_1 and N_2

samples, the doublet can only be observed when the superparamagnetic relaxation of the nanoparticles occurs at a rate faster than the Mössbauer measurement time, giving a time

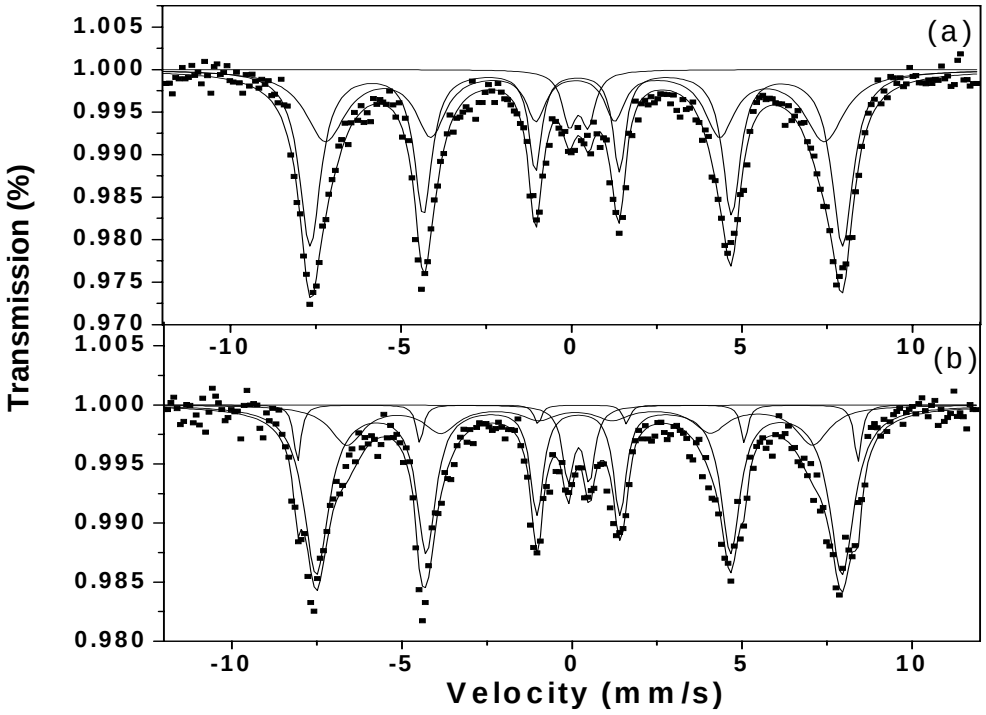

Figure 5.9 *Room temperature Mössbauer spectra of nickel-zinc-indium ferrite nano samples (a) N_1 (b) N_2*

average zero magnetization. Due to a distribution of energy barriers, some nanoparticles relax faster and the other slower at a given temperature. Consequently, the sextet peak and doublet peak can appear simultaneously. The experimental data for sample $Ni_{0.58}Zn_{0.42}In_{0.1}Fe_{1.9}O_4$ (N_1), was fitted with the superposition of three subspectra, two accounting for Fe^{3+} in the tetrahedral sites (A) and octahedral sites (B) of the spinel structure, third associated for the doublet (M1). In addition to these, a fourth spectrum (M2) is used for sample $Ni_{0.58}Zn_{0.42}In_{0.2}Fe_{1.8}O_4$ (N_2) for the traces of hematite. The corresponding Mössbauer parameters such as isomer shift (I.S.), quadrupole splitting (Q.S.), hyperfine magnetic field and linewidth obtained by fitting the spectra are listed in the table 5.5.

Table 5.5 Mössbauer parameters for nano nickel-zinc-indium ferrite samples at room temperature

Sample	Subspectrum	WID	I.S. (mm/s)	Q.S. (mm/s)	H (T)	Area Ratio
N_1	(A)	0.70±0.02	0.11±0.00	-0.01±0.00	45.33±0.00	40.44%
	(B)	0.45±0.00	0.15±0.00	-0.03±0.00	48.38±0.00	54.38%
	M1	0.50±0.00	0.21±0.00	0.55±0.01	-	5.18 %
N_2	(A)	1.18±0.11	0.16±0.01	0.12±0.01	42.40±0.01	20.64%
	(B)	0.46±0.10	0.20±0.01	0.02±0.02	47.88±0.01	66.45%
	M1	0.40±0.01	0.19±0.01	0.61±0.02	-	6.45%
	M2	0.25±0.02	0.23±0.01	-0.13±0.02	51.05±0.01	6.46%

The room temperature Mössbauer spectra of $Ni_{0.58}Zn_{0.42}In_{0.1}Fe_{1.9}O_4$ (N_3), $Ni_{0.58}Zn_{0.42}In_{0.2}Fe_{1.8}O_4$ (N_4) and $Ni_{0.58}Zn_{0.42}In_{0.3}Fe_{1.7}O_4$ (N_5) samples revealed that the particle size affects the magnetic hyperfine field. Mössbauer spectra of N_3, N_4 and N_5 samples show collective magnetic excitations (Figures 5.10 and 5.11). The spectra of N_3 and N_4 samples having an average particle size 8.7 nm and 8.3 nm respectively were fitted with one discrete sextet and one doublet, while the spectrum of $Ni_{0.58}Zn_{0.42}In_{0.3}Fe_{1.7}O_4$ (N_5, 8.0 nm) sample was fitted using one doublet. Figure 5.10 (c-d) shows the p (B) distribution curve derived from the Mössbauer spectra. The average hyperfine field for nano $Ni_{0.58}Zn_{0.42}Fe_2O_4$ (N_0) sample is 44.43 T. As indium ions are introduced in the system, the most intense peak shifts from 44.43 T to 30.0 T (Figure 5.10c). For $Ni_{0.58}Zn_{0.42}In_{0.2}Fe_{1.8}O_4$ (N_4) sample, the relaxed spectra show peak at 3.9 T (Figure 5.10d).

Figure 5.11 shows that the spectrum of $Ni_{0.58}Zn_{0.42}In_{0.3}Fe_{1.7}O_4$ (N_5) sample leads to partly collapsed magnetic hyperfine splitting and to the appearance of a central doublet, which may be due to superparamagnetic behavior of nanosized ferrites. HMF distribution of $Ni_{0.58}Zn_{0.42}In_{0.3}Fe_{1.7}O_4$ (N_5) sample shows a maximum near 3 T (Figure 5.11b).

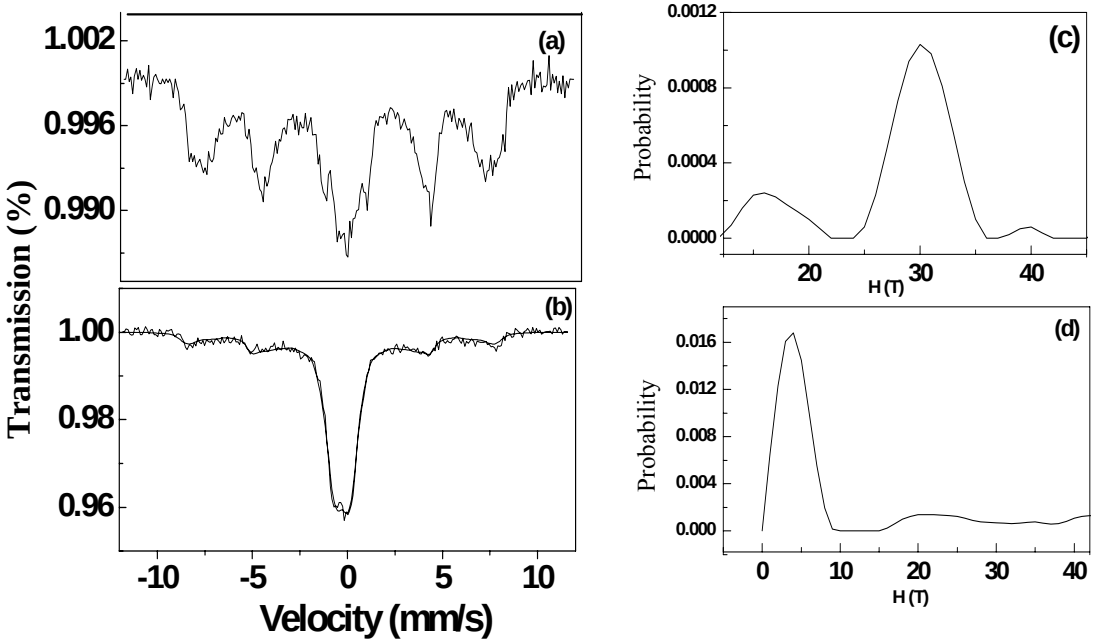

Figure 5.10 *Room temperature Mössbauer Spectra of nano samples (a) N_3 (b) N_4 (c) p-H distribution curve for N_3 sample (d) p-H distribution curve for N_4 sample*

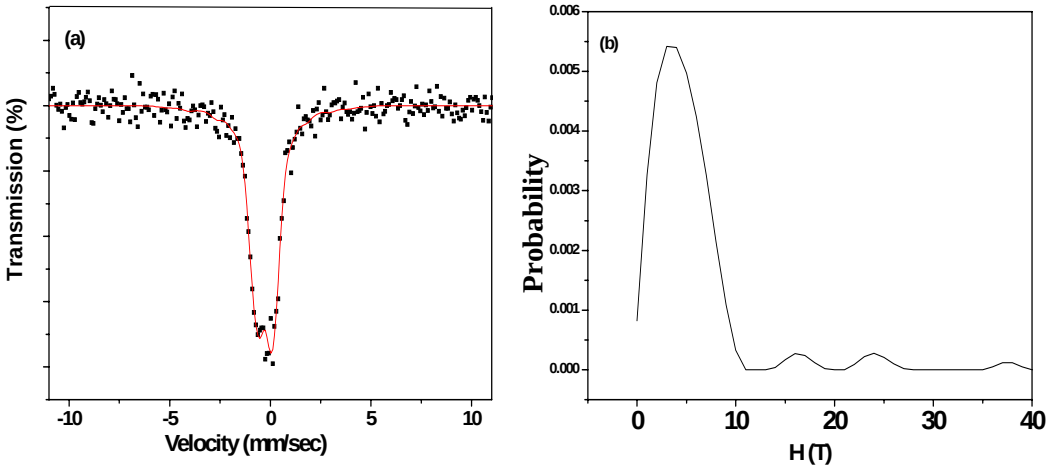

Figure 5.11 *Room temperature Mössbauer spectrum of nano sample (a) N_5 (b) p-H distribution curve*

The broadening of the doublet in case of nanosamples in comparison to bulk samples provide clear evidence of the considerable changes in the quadrupolar interaction and indicates the presence of wide distribution of the electric field gradient (E.F.G) at the Fe^{3+} nuclei. The large surface to volume ratio in nanoparticles is known to create large electric field gradient in ferrites which results in broadened doublet, while the bulk materials has cubic symmetry.

The doublet observed in all nanosamples is attributed to extremely small particles of ferrite undergoing superparamagnetic relaxation at room temperature. In the present case, the spectrum of N_5 sample shows a doublet, which indicates that long range magnetic ordering is vanished and the particles behave like single domain showing superparamagnetism.

The spectra of the $Ni_{0.58}Zn_{0.42}In_{0.1}Fe_{1.9}O_4$ (S_1) and $Ni_{0.58}Zn_{0.42}In_{0.2}Fe_{1.8}O_4$ (S_2) samples at room temperature and low-temperature (5 K) show similar magnetic sextet distributions, except for large hyperfine field values at 5 K, as expected (Figure 5.12). $Ni_{0.58}Zn_{0.42}In_{0.1}Fe_{1.9}O_4$ (S_1) sample consist of sextets with $H_{(A)}$ = 50.14 T, $H_{(B)}$ = 51.84 T,

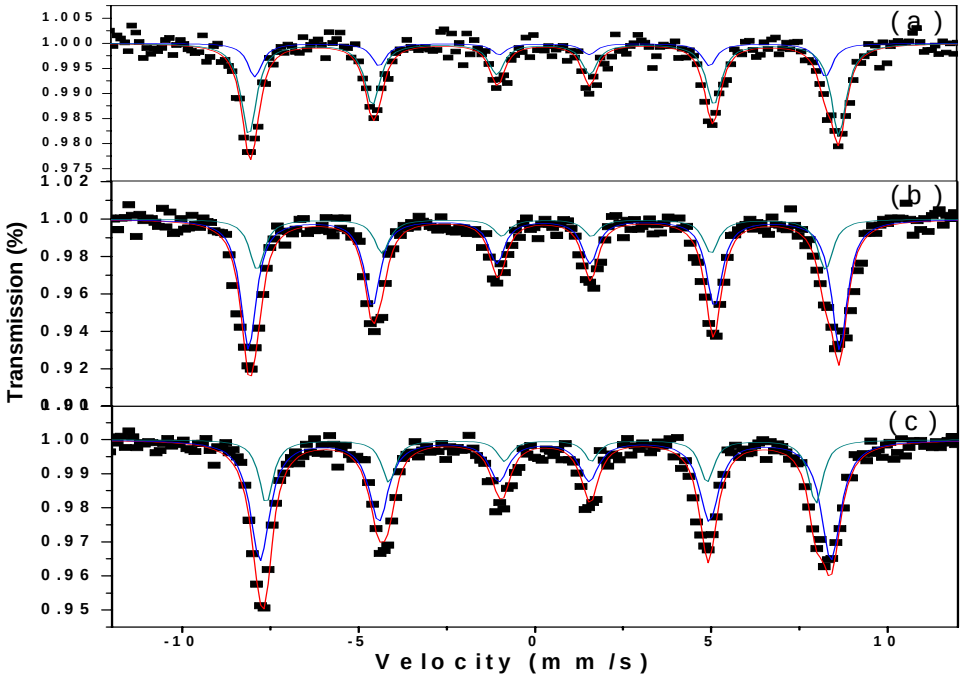

Figure 5.12 *Mössbauer spectra of bulk nickel-zinc-indium ferrite samples at 5 K (a) S_1 (b) S_2 (c) S_3*

while for $Ni_{0.58}Zn_{0.42}In_{0.2}Fe_{1.8}O_4$ (S_2) sample $H_{(A)}$ decreases to 49.95 T and $H_{(B)}$ remains almost constant 51.94 T (Table 5.6). The collective magnetic excitations of $Ni_{0.58}Zn_{0.42}In_{0.3}Fe_{1.7}O_4$ (S_3) sample are suppressed at 5 K and spectrum consists of sextet only (Figure 5.12c). Hyperfine fields at both sites decreases with increase in indium concentration, as obtained in case of $Ni_{0.58}Zn_{0.42}In_{0.3}Fe_{1.7}O_4$ (S_3) sample.

Table 5.6 Mössbauer parameters for bulk nickel-zinc-indium ferrite samples at low temperature 5 K

Sample	Subspectrum	WID (mm/s)	I.S. (mm/s)	Q. S. (mm/s)	H (T)	AREA (%)
S_1	(A)	0.49±0.04	0.23±0.03	-0.11±0.05	50.14±0.10	25.61 %
	(B)	0.53±0.01	0.27±0.01	0.02±0.01	51.84±0.01	74.39 %
			$I_{(A)}/I_{(B)}$ = 0.344			
S_2	(A)	0.51±0.04	0.27±0.00	-0.14±0.02	49.95±0.09	26.88 %
	(B)	0.55±0.00	0.26±0.00	0.01±0.01	51.947±0.00	73.12 %
			$I_{(A)}/I_{(B)}$ = 0.376			
S_3	(A)	0.48±0.02	0.27±0.02	-0.19±0.02	48.32±0.10	27.67 %
	(B)	0.67±0.01	0.28±0.00	0.04±0.01	50.17±0.05	72.33 %
			$I_{(A)}/I_{(B)}$ = 0.382			

Figures 5.13 and 5.14 show that the superparamagnetic relaxation of nano samples are suppressed at 5 K and spectra consists of broadened sextet only. The broad shape of Mössbauer spectral lines for nano nickel-zinc-indium ferrite samples provide clear evidence of a wide distribution of magnetic fields acting at the Fe^{3+} nuclei in the nanoparticles. To analyze the complex spectra of nano samples we consider that the octahedral site field in spinel ferrites is very sensitive to the kind of (A) site nearest neighbors [6]. Measurements on pure and Sb-substituted $LiFe_5O_8$ have shown that even for diamagnetic (B) site ions, the influence of cation disorder on $H_{(A)}$ is quite small [27]. For this reason, in indium substituted nickel-zinc ferrite samples (A) site field is not influenced by (B) site ions. Hence we have fitted (B) site field by taking into consideration that the HMF distribution arises due to (A) site neighbors. Four hyperfine field components were found necessary to fit the absorption due to Fe^{3+}(B). For $Ni_{0.58}Zn_{0.42}In_{0.1}Fe_{1.9}O_4$ (N_1), $Ni_{0.58}Zn_{0.42}In_{0.1}Fe_{1.9}O_4$ (N_3), $Ni_{0.58}Zn_{0.42}In_{0.2}Fe_{1.8}O_4$ (N_4) and

$Ni_{0.58}Zn_{0.42}In_{0.3}Fe_{1.7}O_4$ (N_5) samples we obtained the best fit by employing five sextets in the Mössbauer spectra, one accounting for Fe^{3+} in the (A) sites and four for the (B) sites

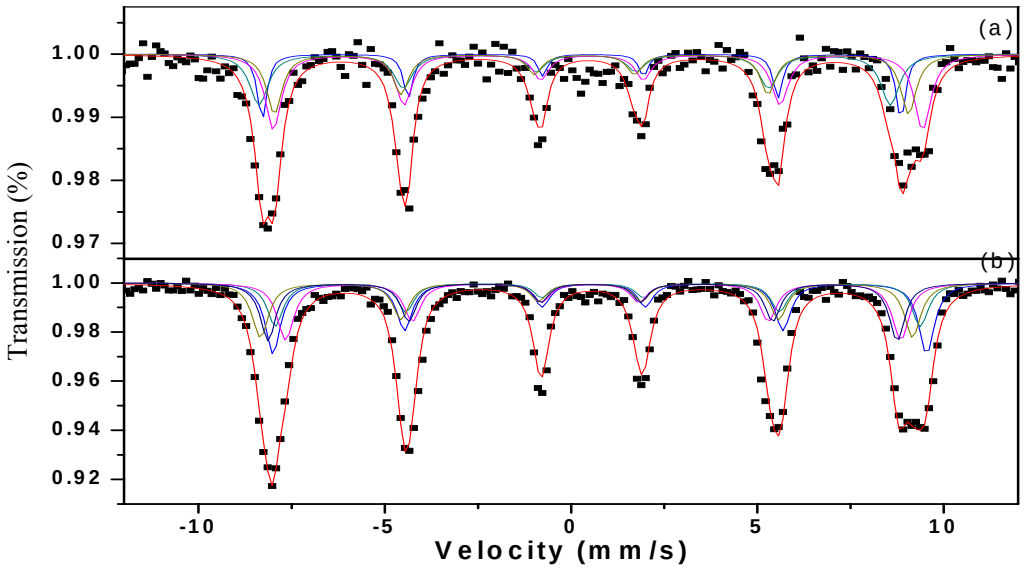

Figure 5.13 *Mössbauer spectra of nano nickel-zinc-indium ferrite samples at 5 K (a) N_1 (b) N_2*

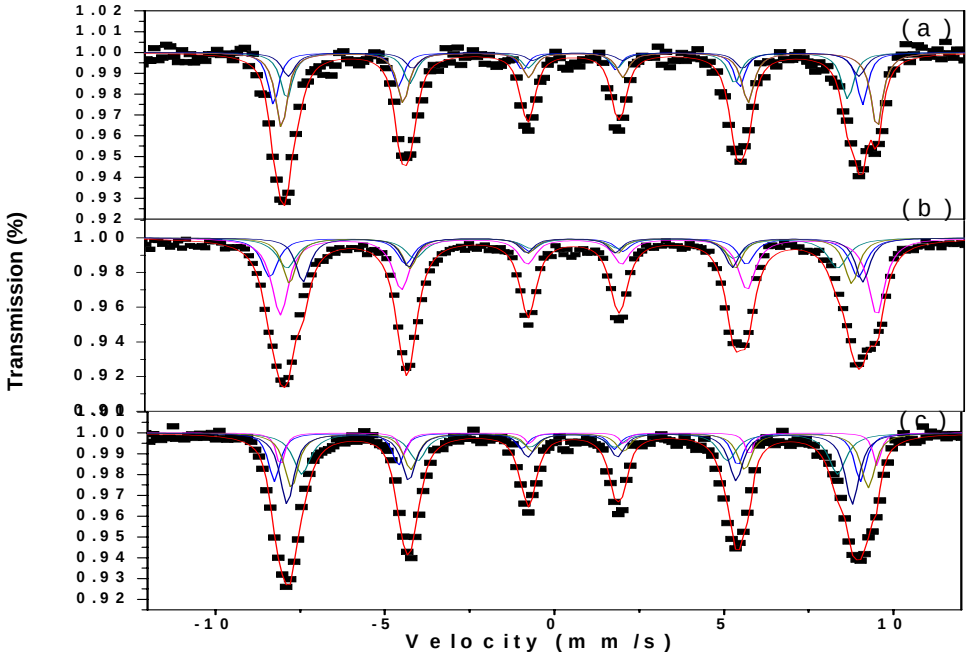

Figure 5.14 *Mössbauer spectra of nano nickel-zinc-indium ferrite samples* at 5 K *(a) N_3 (b) N_4 (c) N_5*

of the spinel structure. In addition to those a sixth spectrum (M) is used for sample $Ni_{0.58}Zn_{0.42}In_{0.2}Fe_{1.8}O_4$ (N_2) for the traces of hematite (Figure 5.13). The hyperfine fields at both crystallographic sites for nano nickel-zinc-indium ferrite particles are reported in table 5.7. Nano nickel-zinc-indium ferrite particles show promising properties as

Table 5.7 Mössbauer parameters for nano nickel-zinc-indium ferrite samples at low temperature 5 K. < H> represents the average hyperfine field acting at the (B) site

Sample	Subspectrum	WID (mm/s)	I.S. (mm/s)	Q. S. (mm/s)	H (T)	AREA (%)
N_1	(A)	0.65±0.00	0.28±0.04	0.27±0.07	52.72 ±0.2	22.73 %
	(B)					77.27 %
	$(B)_1$	0.42±0.00	0.67±0.01	-0.16±0.02	54.21±0.10	22.73 %
	$(B)_2$	0.56±0.00	0.46±0.00	0.08±0.00	53.92±0.30	22.73 %
	$(B)_3$	0.56±0.00	0.36±0.04	-0.08±0.00	52.78±0.30	16.66 %
	$(B)_4$	0.70±0.00	0.51±0.00	-0.13±0.08	51.40±0.00	15.15 %
N_2					$<H>_{(B)}$= 53.07	
	(A)	0.50±0.00	0.54±0.01	-0.05±0.02	51.04±0.10	15.39 %
	M	0.53±0.00	0.60±0.01	-0.06±0.10	54.89±0.76	19.63 %
	(B)					59.29 %
	$(B)_1$	0.52±0.00	0.58±0.13	-0.05±0.00	55.18±0.90	15.39 %
	$(B)_2$	0.54±0.00	0.58±0.01	-0.03±0.00	53.39±0.08	20.96 %
	$(B)_3$	0.50±0.00	0.50±0.01	0.06±0.01	52.32±0.00	19.63 %
	$(B)_4$	0.50±0.00	0.45±0.00	0.12±0.00	51.16±0.17	9.02 %
					$<H>_{(B)}$=53.01	
N_3	(A)	0.55±0.00	0.59±0.03	-0.13±0.00	50.76±0.25	17.93%
	(B)					82.07%
	$(B)_1$	0.43±0.03	0.67±0.01	-0.10±0.01	54.03±0.08	31.35%
	$(B)_2$	0.38±0.03	0.41±0.01	0.03±0.02	53.44±0.10	19.21%
	$(B)_3$	0.50±0.00	0.61±0.04	0.11±0.07	51.75±0.00	11.53%
	$(B)_4$	0.44±0.04	0.44±0.01	0.15±0.03	50.90±0.00	19.98%
					$< H>_{(B)}$ = 52.53	
N_4	(A)	0.50±0.00	0.65±0.01	-0.35±0.03	50.75±0.00	16.26%
	(B)					83.74%
	$(B)_1$	0.61±0.01	0.63±0.00	-0.12±0.02	54.13±0.05	34.55%
	$(B)_2$	0.57±0.02	0.45±0.02	0.35±0.04	53.38±0.06	16.67%
	$(B)_3$	0.50±0.00	0.50±0.02	0.06±0.03	51.00±0.14	16.87%
	$(B)_4$	0.70±0.02	0.40±0.02	0.35±0.06	49.99±0.31	15.65%
					$< H>_{(B)}$ = 52.12	
N_5	(A)	0.63±0.02	0.48±0.01	0.08±0.02	48.95±0.00	21.92%
	(B)					78.08%
	$(B)_1$	0.28±0.05	0.68±0.01	-0.06±0.01	54.50±0.09	8.10%
	$(B)_2$	0.41±0.02	0.39±0.01	0.02±0.01	53.52±0.07	16.97%
	$(B)_3$	0.50±0.00	0.71±0.01	-0.06±0.01	52.70±0.10	23.09%
	$(B)_4$	0.50±0.00	0.48±0.01	0.08±0.01	51.65±0.00	29.92%
					$< H>_{(B)}$ = 53.09	

hyperfine field is found to be close to that of the bulk materials.

5.2.1 In-filed Mössbauer spectra of nickel-zinc-indium ferrite samples at nano and bulk scale

To evaluate the relative repartition of iron ions in the (A) and (B) sites, Mössbauer spectroscopy has to be performed under a magnetic field. In-field Mössbauer spectrum of the bulk nickel-zinc-indium ferrite (Figure 5.15) samples was fitted by a superposition of two subspectra corresponding to Fe^{3+}(A) and Fe^{3+}(B) ions.

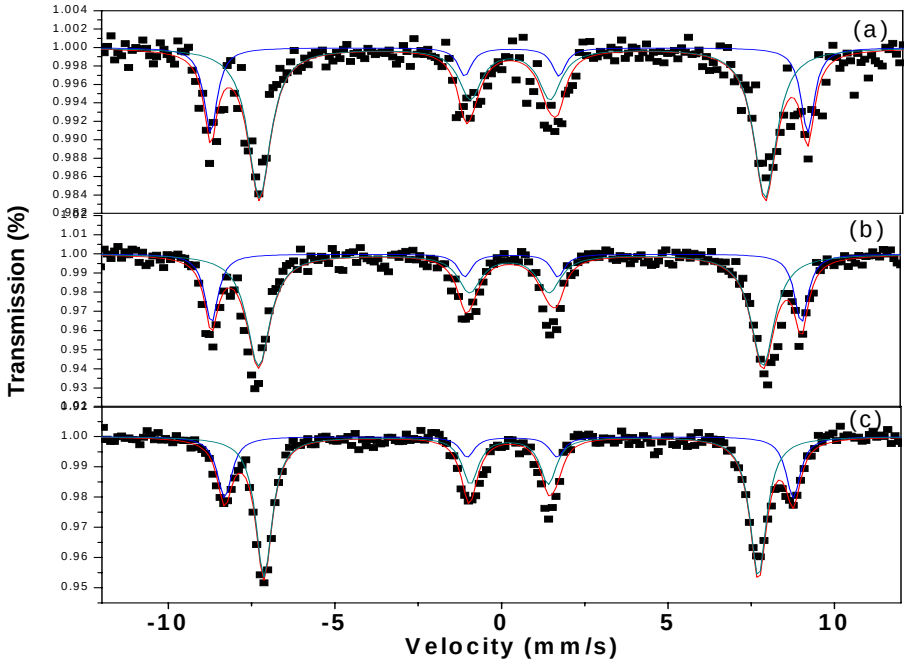

Figure 5.15 *Mössbauer spectra of bulk nickel-zinc-indium samples recorded at 5 K in an external magnetic field of 5 T (a) S_1 (b) S_2 (c) S_3*

Estimate of the cation distribution in the present series has been made on the basis of area occupied by Fe^{3+} ions at (A) and (B) sites obtained from in-field Mössbauer spectra. The relative strength of preference of occupation of sites has been taken into consideration while making this distribution. Accordingly, indium has been assigned to the tetrahedral site first. The cation distribution can be written as: $(Zn_{0.42}In_{x\tau}Fe_{0.58-x\tau})[Ni_{0.58}In_{(1-\tau)x}Fe_{1.42+x\tau-x}]$, where τ is the distribution parameter which represents the fraction of indium (In^{3+}) ions present at the tetrahedral site. The values of effective hyperfine field, isomer

shift, cation distribution and of area ratio obtained for $Ni_{0.58}Zn_{0.42}In_{0.1}Fe_{1.9}O_4$ (S_1), $Ni_{0.58}Zn_{0.42}In_{0.2}Fe_{1.8}O_4$ (S_2), $Ni_{0.58}Zn_{0.42}In_{0.3}Fe_{1.7}O_4$ (S_3) samples are given in table 5.8. The intensity ratio $I_2/I_3 \approx 0$ for both tetrahedral and

Table 5.8 Mössbauer parameters for bulk nickel-zinc-indium ferrite samples at 5 K in presence of 5 T field

Subspectrum		WID	I.S. (mm/s)	Q.S.(mm/s)	H_{eff} (T)	H (T)	AREA (%)
S_1	(A)	0.49±0.01	0.25±0.00	-0.07±0.02	55.41±0.20	50.41	25.33 %
	(B)	0.82±0.02	0.27±0.02	0.06±0.03	46.94±0.12	51.94	74.67 %
		$I_{(A)c}/I_{(B)c} = 0.333$, $\tau_c = 1$, $I_{(A)2}/I_{(A)3} = I_{(B)2}/I_{(A)3} = 0$, $\Psi_{(A)} = \Psi_{(B)} = 0^o$					
		$(Zn_{0.42}In_{0.1}Fe_{0.48})$ $[Ni_{0.58}Fe_{1.42}]$					
S_2	(A)	0.50±0.01	0.24±0.00	-0.14±0.02	54.92±0.11	49.92	26.50 %
	(B)	0.85±0.01	0.27±0.01	0.03±0.01	46.94±0.10	51.94	73.50%
		$I_{(A)c}/I_{(B)c} = 0.361$, $\tau_c = 0.52$, $I_{(A)2}/I_{(A)3} = I_{(B)2}/I_{(B)3} = 0$, $\Psi_{(A)} = \Psi_{(B)} = 0^o$					
		$(Zn_{0.42}In_{0.1}Fe_{0.48})$ $[Ni_{0.58}In_{0.1}Fe_{1.32}]$					
S_3	(A)	0.52±0.01	0.27±0.00	-0.09±0.01	52.89±0.05	47.88	27.95 %
	(B)	0.59±0.01	0.28±0.00	0.05±0.01	45.98±0.00	50.98	72.05 %
		$I_{(A)}/I_{(B)} = 0.387$, $\tau_c = 0.37$, $I_{(A)2}/I_{(A)3} = I_{(B)2}/I_{(B)3} = 0$, $\Psi_{(A)} = \Psi_{(B)} = 0^o$					
		$(Zn_{0.42}In_{0.11}Fe_{0.47})$ $[Ni_{0.58}In_{0.19}Fe_{1.23}]$					

octahedral subspectra indicate that the spins are completely aligned ($\Psi_{(A)} = 0^o$, $\Psi_{(B)} = 0^o$) along the external magnetic field of 5 T. Thus, the bulk nickel-zinc-indium ferrite samples exhibit a fully inverse spinel structure with a Néel-type collinear spin arrangement of ions, showing that samples attain bulk properties after heat treatment. Although, sample $Ni_{0.58}Zn_{0.42}In_{0.3}Fe_{1.7}O_4$ (S_3) attains bulk properties, the particle size of this sample is in nanoscale. Cation distribution obtained clearly show that indium ions were found to prefer the (A) sublattice for small concentration (10 %), while with further increase in concentration some of the indium ions partially occupy octahedral sites.

As annealed samples exhibits the properties similar to that of bulk samples we have fitted the in-field Mössbauer spectra of nickel-zinc-indium ferrite nano samples (N_3, N_4, N_5) (Figure 5.16) by assuming an ordered particle core like bulk particles surrounded by disordered grain boundary regions. Thus the present Mössbauer spectra were fitted by

a superposition of four subspectra; two accounting for Fe^{3+} nuclei at (A) and (B) sites of the particle core and two associated with Fe^{3+} ions at (A) and (B) sites in the surface shell of the nanoparticles. To separate the surface effects from the bulk effects in the spectrum of nano samples, we assumed that the core of N_3, N_4 and N_5 samples possess the same structure as the S_1, S_2 and S_3 samples. Thus, the fit to the spectrum of N_3, N_4 and N_5 samples was made by imposing constraints on the Mössbauer parameters of the subspectra corresponding to the particle core (I.S., H, $I_{(A)c}/I_{(B)c}$, $I_{(A)c2}/I_{(A)c3}$, $I_{(B)c2}/I_{(B)c3}$), such that these parameters were fixed and equal to those obtained from the fit of the spectrum of the S_1, S_2 and S_3 samples. The absorption due to Fe^{3+} ions at (B) site of the particle shell was fitted by a HMF distribution consisting of four components (Bn_s, n = 4, 3, 2, 1). The hyperfine parameters of (A) and (B) site ferric ions resulting from fitting of the spectra are presented in table 5.9.

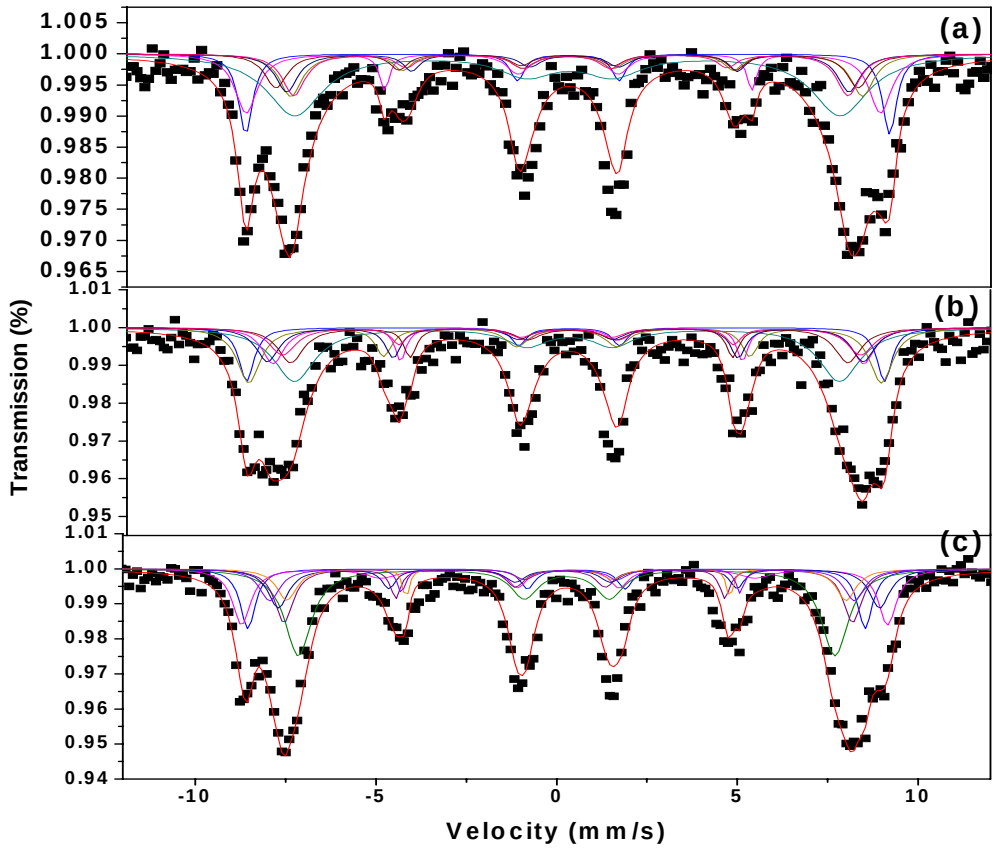

Figure 5.16 *Mössbauer spectra of nano nickel-zinc-indium ferrite samples recorded at 5 K in an external magnetic field of 5 T (a) N_3 (b) N_4 (c) N_5*

Table 5.9 Mössbauer parameters: isomer shift (I.S.), effective hyperfine field ($H_{eff.}$) the average magnetic hyperfine field (H), quadrupole splitting (Q.S.) and relative area (I), obtained by fitting the high field spectra at 5 K. Ψ is the canting angle, c define as the core and s is used for surface, $I_{(A)2}/I_{(A)3}$ is the relative area of 2 and 3 lines for the (A) site, $I_{(B)2}/I_{(B)3}$ is the relative area of 2 and 3 lines for the (B) site, < H> is the average hyperfine field acting at (B) site, $<H_{eff}>$ is the average effective hyperfine field acting at (B) site in the presence of field, a is fixed parameter.

	Subspectrum	WID	I.S. (mm/s)	Q.S. (mm/s)	H_{eff} (T)	H (T)	A23	AREA (%)
N_3	$(A)_c$	0.48[a]	0.25[a]	-0.02±0.01	55.41[a]	50.41	0	10.88 %
	$(B)_c$	1.89[a]	0.27[a]	-0.06±0.02	46.94[a]	51.94	0	32.64 %
	$(A)_s$	0.75[a]	0.18±0.01	-0.13±0.04	54.57±0.10	50.57	0.80	15.06 %
	$(B)_{s1}$	0.75[a]	0.22±0.05	-0.01±0.00	50.10±0.20	53.97	1.12	9.21 %
	$(B)_{s2}$	0.77[a]	0.37±0.04	0.24±0.01	49.20±0.10	53.26	0.90	11.30 %
	$(B)_{s3}$	0.75[a]	0.33±0.05	-0.18±0.00	48.40±0.20	53.97	1.00	10.04 %
	$(B)_{s4}$	0.76[a]	0.27±0.05	0.12±0.02	47.71±0.20	51.83	0.84	10.88 %

$I_{(A)2c}/I_{(A)3c} = I_{(B)2c}/I_{(B)3c} = 0$
$I_{(A)s}/I_{(B)s} = 0.363$, $\tau_s = 0.75$, $I_{(A)2s}/I_{(A)3s} = 0.8$,
$<I_{(B)2s}/I_{(B)3s}> = 0.96$, $\Psi_{(A)s} = 35.28^o$, $\Psi_{(B)s} = 38.43^o$, $< H_{eff}>_{(B)s} = 49.99$ T , $< H>_{(B)s} = 52.85$ T,
Core: ($Zn_{0.42}In_{0.1}Fe_{0.48}$) [$Ni_{0.58}Fe_{1.42}$], **Surface :**($Zn_{0.42}In_{0.07}Fe_{0.51}$) [$Ni_{0.58}In_{0.03}Fe_{1.39}$]

N_4	$(A)_c$	0.50±0.05	0.24[a]	-0.103	54.92[a]	49.92	0	9.01 %
	$(B)_c$	1.40[a]	0.27[a]	-0.08	46.94[a]	51.94	0	24.92 %
	$(A)_s$	0.77[a]	0.20±0.02	-0.04±0.04	54.45±0.16	50.67	1.07	8.02 %
	$(B)_{s1}$	0.77[a]	0.18±0.05	-0.01±0.00	51.29±0.45	54.60	1.75	12.61 %
	$(B)_{s2}$	0.74[a]	0.31±0.00	-0.09±0.07	50.83±0.38	54.50	1.38	12.01 %
	$(B)_{s3}$	0.89[a]	0.28±0.09	0.15±0.00	49.76±0.00	53.72	1.00	10.21 %
	$(B)_{s4}$	0.87[a]	0.32±0.03	-0.06±0.00	47.97±0.20	51.74	1.20	13.21 %

$I_{(A)2c}/I_{(A)3c} = I_{(B)2c}/I_{(B)3c} = 0$
$I_{(A)s}/I_{(B)s} = 0.375$, $\tau_s = 0.45$, $I_{(A)2s}/I_{(A)3s} = 1.0$,
$<I_{(B)2s}/I_{(B)3s}> = 1.3$, $\Psi_{(A)s} = 39.25^o$, $\Psi_{(B)s} = 44.28^o$, $< H_{eff}>_{(B)s} = 50.86$ T $< H>_{(B)s} = 53.64$ T,
Core: ($Zn_{0.42}In_{0.1}Fe_{0.48}$) [$Ni_{0.58}In_{0.1}Fe_{1.32}$], **Surface:** ($Zn_{0.42}In_{0.09}Fe_{0.49}$) [$Ni_{0.58}In_{0.11}Fe_{1.31}$]

N_5	$(A)_c$	0.50[a]	0.27[a]	-0.55±0.03	52.89[a]	47.88	0	10.89%
	$(B)_c$	0.90[a]	0.28[a]	-0.01±0.00	45.98[a]	50.98	0	28.31%
	$(A)_s$	0.60[a]	0.27[a]	-0.09±0.04	55.34±0.14	51.40	0.85	14.82%
	$(B)_{s1}$	0.68[a]	0.39±0.03	0.44±0.07	51.53±0.24	55.49	1.00	12.10%
	$(B)_{s2}$	0.68[a]	0.26±0.04	-0.24±0.08	50.10±0.39	54.16	0.90	9.68%
	$(B)_{s3}$	0.62[a]	0.21±0.03	0.22±0.06	48.71±0.28	52.77	0.90	14.82%
	$(B)_{s4}$	0.67[a]	0.28±0.03	-0.04±0.02	47.93±0.19	51.98	0.90	9.38%

$I_{(A)2c}/I_{(A)3c} = I_{(B)2c}/I_{(B)3c} = 0$
$I_{(A)s}/I_{(B)s} = 0.322$, $I_{(A)2s}/I_{(A)3s} = 0.85$, $\tau_s = 0.56$, $<I_{(B)2s}/I_{(B)3s}> = 0.9$, $\Psi_{(A)s} = 36.32^o$,
$\Psi_{(B)s} = 37.80^o$, $< H_{eff}>_{(B)s} = 49.56$ T, $< H>_{(B)s} = 53.80$ T, a is fixed parameter.
Core: ($Zn_{0.42}In_{0.11}Fe_{0.47}$) [$Ni_{0.58}In_{0.19}Fe_{1.23}$], **Surface:** ($Zn_{0.42}In_{0.17}Fe_{0.41}$) [$Ni_{0.58}In_{0.13}Fe_{1.29}$]

The subspectral intensity ratio $I_{(A)s}/I_{(B)s}$ indicates that the major feature of the atomic configuration in the nanoparticle shell is a nonequilibrium cation distribution. The observed difference between the intensity ratios of spectral lines 2 and 3 for the inner core ($I_{(A)c2}/I_{(A)c3}$, $I_{(B)c2}/I_{(B)c3}$) and the surface region ($I_{(A)s2}/I_{(A)s3}$, $I_{(B)s2}/I_{(B)s3}$) is a direct indication of a nonuniform spin arrangement within a nanoparticle. All spins in the particle core are fully aligned in a direction of the external field ($I_{(A)c2}/I_{(A)c3} = I_{(B)c2}/I_{(B)c3} = 0$), whereas the spins in the shell region are found to be canted. The average canting angles, calculated from the intensity ratios $I_{(A)s2}/I_{(A)s3}$ and $I_{(B)s2}/I_{(B)s3}$ are shown in table 5.9. Thus the spins located on the two sublattices in the surface regions of nano nickel-zinc-indium ferrite particles are found to behave differently under an external field of 5 T. The cation distribution obtained at the surface of nanosamples is also given in table 5.9. Assuming a spherical shape of reverse micelle synthesized nanoparticles and taking their average size as determined by X-ray diffraction, we estimated the thickness of the surface shell to be t ≈ 1.0 nm, 1.3 nm, 0.85 nm for $Ni_{0.58}Zn_{0.42}In_{0.1}Fe_{1.9}O_4$ (N_3), $Ni_{0.58}Zn_{0.42}In_{0.2}Fe_{1.8}O_4$ (N_4) and $Ni_{0.58}Zn_{0.42}In_{0.3}Fe_{1.7}O_4$ (N_5) samples respectively. Figure 5.17 shows the schematic diagram of nano samples.

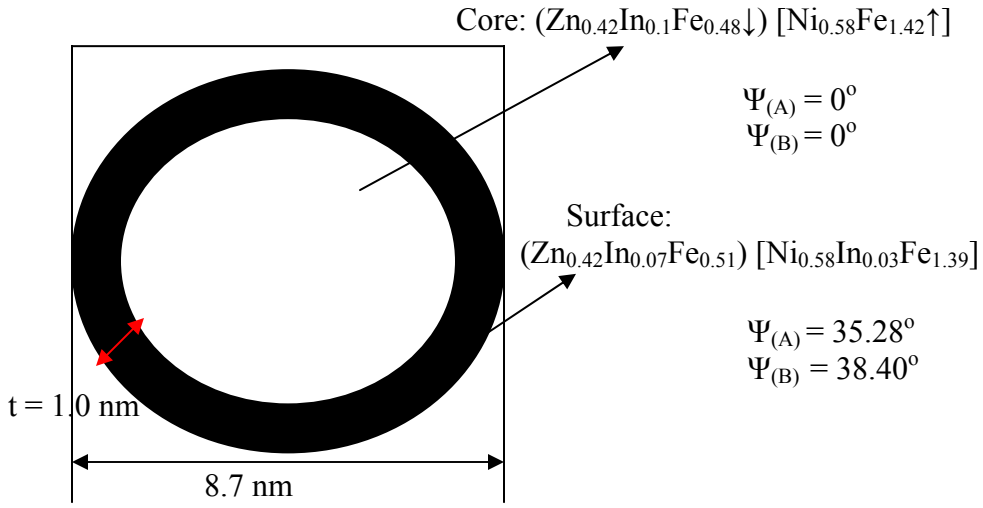

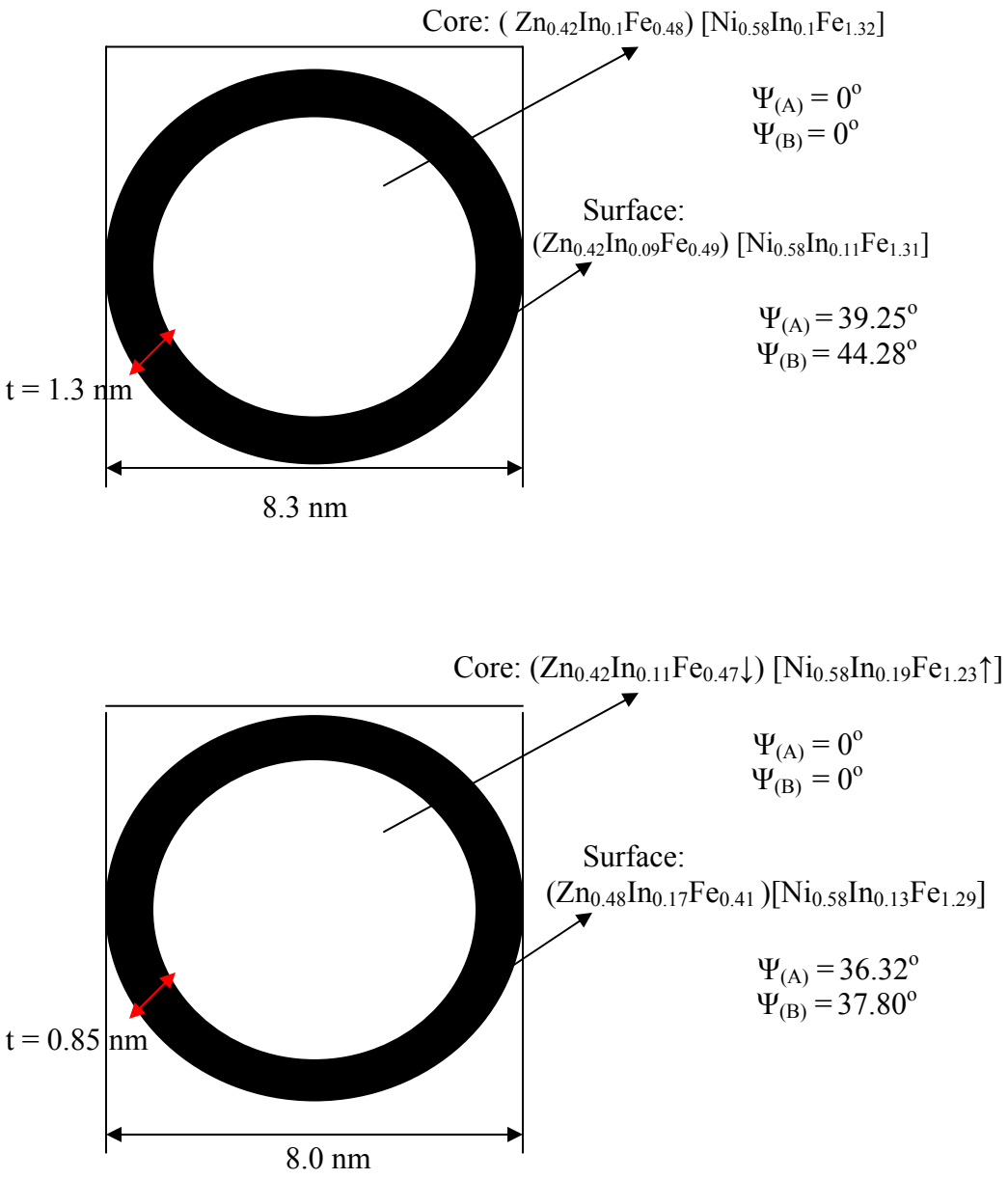

Figure 5.17 *Schematic diagram of nanoparticles*

Figure 5.18 compares the (B) site HMF distributions derived from the in-field Mössbauer spectra of the samples. The in-field data is fitted with DIST program considering the (A) site as crystalline site and the (B) site as for the distribution of fields. As can be seen, the (B) site HMF distributions derived from the in-field Mössbauer spectra of the bulk nickel-zinc-indium ferrite particles experience a local field from a relatively narrow

interval, in contrast to the nanosized particles, where a broad distribution is observed. This broad HMF distribution indicates a strongly disturbed macroscopic magnetic state of the nickel-zinc-indium ferrite nanoparticles.

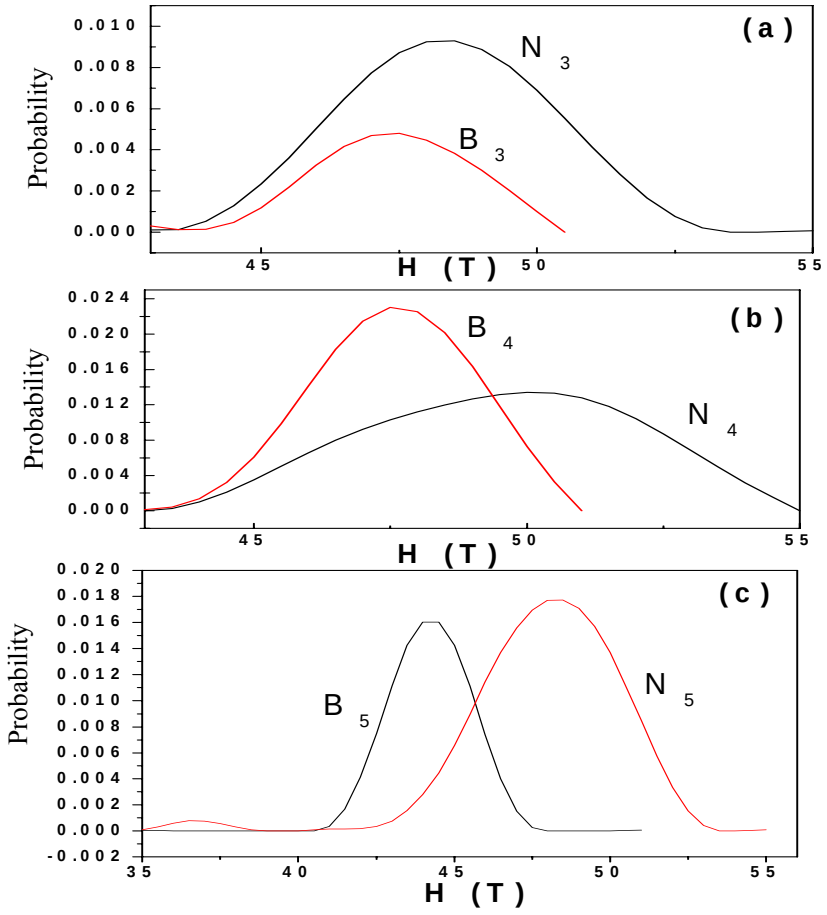

Figure 5.18 *The (B) site hyperfine distribution derived from the Mössbauer spectra recorded at 5 K in an external magnetic field of 5 T (a) N_3, B_3 (b) N_4, B_4 (c) N_5, B_5*

5.3 Variation of Mössbauer parameters with indium concentration

5.3.1 Isomer shift (I.S.)

From the Mössbauer spectra taken at different temperatures, it is observed that there is no systematic change in the values of isomer shift corresponding to Fe^{3+} ions at (A) as well as (B) site, with the increase in concentration of indium (In^{3+}) ions in the

system. This indicates that substitution of diamagnetic ions in the system produces negligible influence on the 's' electron density around Fe^{3+} nuclei at both the sites. The values of I.S. obtained for (B) and (A) sites are in good agreement with earlier study on nickel-zinc ferrite particles [14,19]. The values of I.S. for the (A) and (B) sites are consistent with high spin Fe^{3+} charge state [18]. The observed differences between the isomer shift of bulk particles at 5 K and 300 K are fully explained by the temperature-dependent second-order Doppler shift of the lines. A small paramagnetic doublet appeared in the nano $Ni_{0.58}Zn_{0.42}In_{0.1}Fe_{1.9}O_4$ (N_1) and $Ni_{0.58}Zn_{0.42}In_{0.2}Fe_{1.8}O_4$ (N_2) samples on magnetic sextet, showing I.S. values are consistent with Fe^{3+} valence state.

5.3.2 Quadrupole splitting (Q.S.)

The values of Q.S. obtained for (A) and (B) sites are in good agreement with earlier study on nickel-zinc ferrite particles [14,19]. The Q.S. values obtained also confirm the presence of only Fe^{3+} charge state and not Fe^{2+} charge state in the system. The values of Q.S. for hyperfine spectra of all the samples are almost zero within the experimental error. This does not necessarily signify the absence of an electric field gradient (E.F.G.) at Fe^{3+} nuclei. Although the spinel ferrites, studied in the present case, have got an overall cubic symmetry, yet (A) and (B) sublattice may individually experience a non-cubic charge distribution and will, therefore, result in an electric field gradient at ^{57}Fe ions occupying these two sublattice. It can be explained as follows:

In a cubic system having Fe^{3+} ions at both the sites, the (A) site shows Q.S. on account of an asymmetric charge distribution due to twelve (B) site neighbors. On the other hand, a Fe^{3+} ion present at an octahedral (B) site has got trigonal symmetry and such sublattice will, therefore, exhibit a non-zero electric field gradient at the nucleus. This electric field gradient arises due to

(a) departure of the six nearest anion neighbors from their ideal octahedral symmetry, and

(b) non-spherical distribution of the charges on the next nearest cation and anion neighbors at the octahedral site.

Thus, almost negligible value of the quadrupole splitting obtained in the present study can not be attributed to the absence of electric field gradient at the nucleus rather it can be

explained in terms of the presence of the chemical disorder in the compositions which can mask the shifts in the hyperfine field produced by the quadrupole interaction [28]. The chemical disorder will produce a distribution of electric field gradient of varying magnitude, direction, sign and asymmetry. The resulting distribution of the quadruple shifts will result in a noticeable broadening of the individual lines. Because of the overall cubic symmetry of the spinel ferrites, it is expected that this distribution will give rise to approximately equal probability for shifts of the opposite sign. This will not therefore, result in an observable shift of the broadened Zeeman lines.

5.3.3 Magnetic hyperfine field

All the spectra of bulk and nano samples at different temperatures have been resolved into sextets belonging to (A) and (B) sites respectively. The sextets are labeled as (A) and (B) sites on the basis of the values of their isomer shift and magnetic hyperfine fields. Since Fe^{3+} ions present at (B) site experience larger hyperfine fields, the outer sextets have been assigned as the (B) site in case of zero field Mössbauer spectrum.
The internal magnetic field on a nucleus can arise due to various interactions [29,30] and can be written as

$$H_{int} = H_{core} + H_{STHF} + H_{THF} + H_D \quad \text{.....(5.2)}$$

where, H_{core} is the field due to the polarization of the core s-electrons. H_{THF} and H_{STHF} are the transferred and supertransferred hyperfine fields respectively. The term, H_D is the dipolar field.

It is known that the basic contribution to the magnetic field, H_{core}, is brought about by the Fermi contact interaction of the nucleus with the s electrons of the ionic core, which are unpaired because of the polarization of the core by the uncompensated spins [30]. The degree of the polarization of the core and its associated contribution to the magnetic field at the nucleus depend mainly on the effective magnetic moment of the ion. H_{core} remains almost constant unless the number and the type of cations changed. Therefore, the field due to the core polarization experienced by Fe^{3+} nuclei present at (A) site will be almost equal to that experienced by Fe^{3+} nuclei present at (B) site. The transferred hyperfine field, H_{THF} which results from a direct exchange interaction between metal cations and oxygen anions also contributes to internal magnetic field upto

some extent. The value of this field depends upon the inter-nuclear distance between the metal cations and oxygen anions. For Fe^{3+} ions present at (A) site, the inter-nuclear distance from O^{2-} ions is less as compared to that of Fe^{3+} ions present at (B) site. It gives rise to the covalency of Fe^{3+}—O^{2-} bond which leads to a greater degree of spin delocalization at (A) site and hence to a smaller value of the hyperfine field. This is one of the reasons, why (A) site field is generally less than (B) site field. The effect of covalency on the value of the hyperfine field at (A) site has also been reported by several workers [29,31,32].

The third term, H_{STHF}, which represents the field produced due to the super-exchange interactions between two cations through an oxygen anion, also contributes significantly. The value of the hyperfine field at Fe^{3+} nucleus present at a particular site will thus, depend upon the strength of the super exchange interactions, which this cation experiences with other cations both within and outside the sublattice to which it belongs. Larger is the strength of this interaction, higher will be the supertransferred hyperfine field. Fe^{3+} ions present at (A) sites, generally, do not experience as strong super-exchange interaction as those present at (B) sites and hence they experience smaller values of internal hyperfine fields.

The fourth term, H_D, represents the dipolar field produced by the surrounding magnetic ions and is a function of both the cation distribution as well as magnetic moments of the cations. It will change if one of the surrounding ions is replaced by an ion with different magnetic moment. The term H_D is generally quite small for iron group ions even in non-cubic systems [33,34]. However, in rare earth systems, where the orbital momentum is quenched, H_D can be quite large, whereas H_D is equal to zero for spherically symmetric charge distribution.

From the values of the hyperfine fields (Table 5.9), it is observed that the internal magnetic field decreases systematically at (A) as well as at (B) site with increase in indium ions concentration. This variation of hyperfine field in bulk nickel-zinc-indium ferrite ($Ni_{0.58}Zn_{0.42}In_xFe_{2-x}O_4$, x = 0, 0.1, 0.2, 0.3) samples can be explained using eqn. (5.2). The decrease in the hyperfine field can be attributed to effect on H_D and H_{STHF}, whereas H_{core} and H_{THF} will remain constant for all values of x. The replacement of Fe^{3+} ions of higher magnetic moment by diamagnetic indium ions effectively decreases the

dipolar magnetic field H_D. The variation of hyperfine field with indium concentration at different temperatures could be understood on the basis of Neel's molecular field theory and the supertransferred hyperfine field. It is found that $H_{(B)}$ decreases with the increase of indium ions concentration upto 0.1. We attribute this to the fact that all the indium ions occupy solely the (A) site. The magnetic hyperfine field at the (A) site is due to the net magnetization of the nearest neighbor (B) site through A-B superexchange and the very weak A-A interaction. Since indium moments order diamagnetically with the magnetic moments of Fe^{3+} ions, hence reduce the magnetization at the (A) site. Consequently the hyperfine field at the (B) site decreases. With further increase in indium concentration, decrease in hyperfine field at (A) site indicates that indium ions occupy partially (B) sites for $x > 0.1$. Thus, the decrease in various magnetic linkages due to the substitution of indium ions mainly reduces H_D and H_{STHF} and results in a net decrease of hyperfine field. A similar decrease in hyperfine magnetic field with the successive incorporation of diamagnetic ions in place of Fe^{3+} ions in many kinds of ferrites has been reported [20,35-37]. It is found that the average hyperfine fields experienced by Fe^{3+} ions located in the near surface layer (Table 5.9) are increased in comparison with those acting in the inner core of particles. This feature must be underlined, because it is completely different from that reported by the majority of authors [6,7,26]. This anomalous behavior of hyperfine field at nanoparticle surface can be understood on the basis of cation redistribution.

It has been observed that the linewidth values corresponding to (A) and (B) sites have been found to increase with increasing concentration of indium ions. The broadening of the spectral components is obviously caused by superimposition of several Zeeman sextiplets corresponding to the Fe^{3+} ions located at various different magnetically nonequivalent positions formed as a result of the addition of diamagnetic ions. In addition, the changes in the environment would affect isomer shift values slightly, displacing sextets with respect to one another and cause general broadening of these lines.

5.4 Variation of hyperfine field with particle size

It is also evident from Mössbauer spectra that decrease in particle size yields a reduction in the hyperfine fields and broadening of the Mössbauer lines. According to

Morup et al [38-40], the fluctuation of magnetization vectors in a direction close to an easy direction of magnetization leads to a particle size dependent magnetic hyperfine field. If the correlation time of the collective magnetization fluctuations is short relative to the observation time, the measured value of the magnetic field and consequently the hyperfine field will be reduced according to the relation:

$$H_{hf}(V, T) = H_{hf}(V = \infty, T)\left[1-\frac{k_B T}{2KV}\right] \quad \text{.....(5.3)}$$

where k_B is the Boltzmann's constant, V is the particle volume and $V = \infty$, refers to a large crystals at temperature T in the absence of collective magnetic excitations. Therefore, according to eqn. (5.3) the hyperfine field decreases with the decrease in particle size since particles with different volumes will show different hyperfine splitting.

The most striking feature of the particle size reduction on the Mössbauer spectra is due to the superparamagnetic relaxation. The latter arises if the particle sizes are so small that thermal energy can overcome the anisotropy energy and change the orientation of the magnetization of a particle from one easy axis to another [5]. In fact, a material can be observed as superparamagnetic in the Mössbauer spectrum, if the relaxation time for the reversal of magnetization in a particle is smaller than the Larmor precession time of the nuclear magnetic moment in the local field. From literature, it is found that for an assembly of particles with nonuniformity of sizes, the experimental Mössbauer spectra will be given by the superposition of spectra with different relaxation time (τ), since τ is very sensitive to volume. For extremely small particles with uniaxial anisotropy, the energy barrier, which separates the two easy directions of magnetization, may be smaller than the thermal energy even at room temperature. This leads to spontaneous fluctuations of the magnetization direction having relaxation time given by [41],

$$\tau = \tau_0 \exp\left(\frac{KV}{k_B T}\right) \quad \text{.....(5.4)}$$

where τ_0 (10^{-9}-10^{-12} s) is a constant and KV is the total anisotropy energy of the particle. The superparamagnetic relaxation of a single domain magnetic particle may be defined by a technique with characteristic time (τ_{obs}) at temperature above the so called blocking temperature (T_B) defined by

$$T_B = \left(\frac{KV}{k_B \ln(\tau_{obs} / \tau)} \right) \text{……(5.5)}$$

Above the blocking temperature, the relaxation time $\tau << \tau_{obs}$ (10^{-8} s) for ^{57}Fe Mössbauer spectroscopy and the internal magnetic field at the nucleus is averaged out giving rise to usually a quadrupolar doublet in the Mössbauer pattern. Below blocking temperature, $\tau >> \tau_{obs}$, a characteristic sextet Mössbauer pattern is observed. Near the blocking temperature when $\tau \sim \tau_{obs}$, a partially collapsed sextet with broad lines is seen.

The low value of hyperfine field obtained in case of $Ni_{0.58}Zn_{0.42}In_{0.1}Fe_{1.9}O_4$ (N_3) and $Ni_{0.58}Zn_{0.42}In_{0.2}Fe_{1.8}O_4$ (N_4) samples in comparison to $Ni_{0.58}Zn_{0.42}In_{0.1}Fe_{1.9}O_4$ (N_1) and $Ni_{0.58}Zn_{0.42}In_{0.2}Fe_{1.8}O_4$ (N_2) samples can be understood on the basis of particle size effect. Also, increase in hyperfine field with indium concentration upto 0.1, for $Ni_{0.58}Zn_{0.42}In_{0.1}Fe_{1.9}O_4$ (N_1) sample, could be explained on the basis of larger particle size in comparison to $Ni_{0.58}Zn_{0.42}Fe_2O_4$ (N_0) sample. In case of $Ni_{0.58}Zn_{0.42}In_{0.1}Fe_{1.9}O_4$ (N_1) and $Ni_{0.58}Zn_{0.42}In_{0.2}Fe_{1.8}O_4$ (N_2) samples the addition of indium creates an increasing distortion in the iron environment due to the next nearest neighbor effect, a distortion which lowers the electronic symmetry. The doublet thus splits into a sextet with increasing indium content. This substitution causes a complete rearrangement in the cation distribution among the various valence states and coordination sites. The appearance of a well split sextet indicates the presence of a long range magnetically ordered phase with $kV > E_{th}$. Thus the cation distribution results in a higher effective magnetic anisotropy barrier, bringing magnetic ordering at room temperature.

5.5 Mössbauer spectra of $Ni_{0.58}Zn_{0.42}In_{0.3}Fe_{1.70}O_4$ particles at different temperatures

Figure 5.19 shows the Mössbauer spectra of nano $Ni_{0.58}Zn_{0.42}In_{0.3}Fe_{1.7}O_4$ (N_5) sample recorded at different temperatures. The zero-field Mössbauer spectra of 8.0 nm particles show a transition from a blocked state at low temperature to a superparamagnetic state at high temperature. At 5 K, the spectrum has relatively narrow lines. When temperature increases; one observes a broadening of the lines and a small decrease of the hyperfine field. The thermal variation of the hyperfine field is approximately linear, in agreement with Morup's law for an assembly of particles in the

frozen state. Using the mean volume derived from the transmission electron microscopy, the anisotropy constant (K), estimated from the thermal variation of the hyperfine field, is 2.12 x 10^5 erg/cm^3. The hyperfine field at 0 K, H_{hf} (0), is found close to 50.9 T. The anisotropy constant determined for $Ni_{0.58}Zn_{0.42}In_{0.3}Fe_{1.7}O_4$ (N_5) sample by Mössbauer spectroscopy is larger than that observed for bulk γ-Fe_2O_3 particles (5 x 10^4 erg/cm^3) [42]. This drastic enhancement is attributed to the surface anisotropy contribution for nanocrystals [43,44]. As a matter of fact; it has been well described for cobalt ferrite [45,46] and γ-Fe_2O_3 [47] nanocrystals that the effective anisotropy constant markedly increases with decreasing particle size.

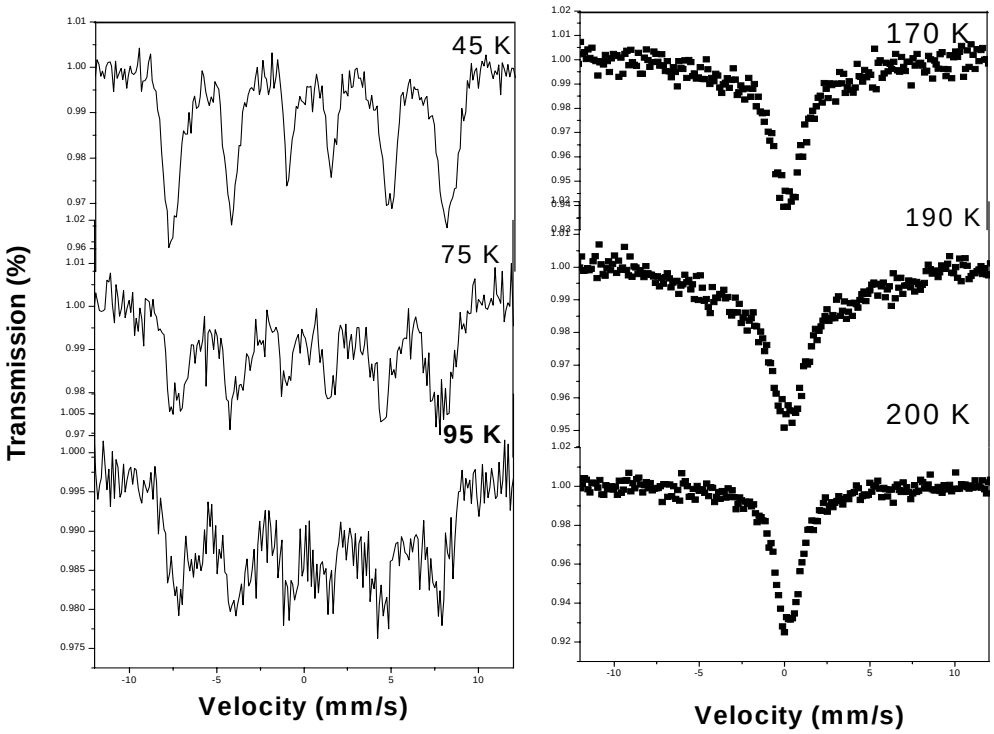

Figure 5.19 *Mössbauer spectra of nano $Ni_{0.58}Zn_{0.42}In_{0.3}Fe_{1.7}O_4$ sample taken at different temperatures*

Conclusion

Due to the ability of ^{57}Fe Mössbauer spectroscopy to reveal the noncollinearity of the spin arrangement and to discriminate between probe nuclei on equivalent crystallographic sites provided by the spinel structure, valuable insight into a local disorder in reverse micelle synthesized nickel-zinc ferrite and nickel-zinc-indium ferrite nanosamples was obtained. Nano $Ni_{0.58}Zn_{0.42}In_{0.1}Fe_{1.9}O_4$ (15 nm) and $Ni_{0.58}Zn_{0.42}In_{0.2}Fe_{1.8}O_4$ (15 nm) samples exhibit ferromagnetically coupling at room temperature, while nano samples having average particle size in the range of 8 nm show collective magnetic excitations. The room temperature Mössbauer spectra of bulk samples exhibit the ferrimagnetic phase. At 5 K, the superparamagnetic relaxation of nano samples is suppressed and the spectra consist of broadened sextets only. The broad shape of Mössbauer spectral lines for the nanosamples as compared to bulk samples provides clear evidence of a wide distribution of magnetic fields acting at the Fe^{3+} nuclei in the nanoparticles. Hyperfine magnetic field distributions at octahedral site derived from the in-field Mössbauer spectra shows that bulk samples experience a local field from a relatively narrow interval, in contrast to the nanosamples, where a broad distribution is observed.

In bulk samples, indium ions were found to prefer the (A) sublattice for small concentration $Ni_{0.58}Zn_{0.42}In_{0.1}Fe_{1.9}O_4$ (10 %), while with further increase in concentration some of the indium ions partially occupy octahedral sites. From detailed investigation of Mössbauer spectra it is concluded that hyperfine field decreases with increase in indium ions concentration except for $Ni_{0.58}Zn_{0.42}In_{0.1}Fe_{1.9}O_4$ (15 nm) sample, which is explained on the basis of larger particle size in comparison to $Ni_{0.58}Zn_{0.42}Fe_2O_4$ (8.4 nm) sample. From the variation of hyperfine field with indium concentration, it can be concluded that $Ni_{0.58}Zn_{0.42}In_{0.3}Fe_{1.7}O_4$ nanoparticles behaves like bulk sample after heat treatment at 1673 K, although the particle size remains in nanoscale.

The comparative in-field Mössbauer study of the bulk and nanosized ferrite samples enables us to separate the surface effects from the bulk effects in nanoparticles. It, thus, was revealed that the surface shell of nano samples is structurally and magnetically disordered due to the nearly random distribution of cations and the canted spin arrangement. This is in contrast to the ordered core of the nanoparticles, and of bulk

particles, which exhibits an inverse spinel structure with a collinear spin alignment ($\Psi_{(A)s} = \Psi_{(B)s} = 0^o$). Mössbauer study on these nano system shows that the cation distribution not only depends on the particle size but also on the preparation route. The anomalous increase in hyperfine field values in nanoparticle surface is attributed to the cation distribution.

At 5 K, nano samples show promising properties: hyperfine field close to that of the bulk materials. Such interesting behavior appears to be clearly related to, good crystallinity of the nanoparticles. From the data it can be concluded that hyperfine field values are strongly influenced by the size of the particles and by surface defects. Therefore these properties depend to a large extent on the synthesis process.

The thickness of the surface shell obtained for nanosamples corresponds to about 4-5 near surface cation layers and is comparable to the lattice constant of nickel-zinc-indium ferrite particles.

The nonequilibrium cation distribution and the canted spin arrangement resulting from the reverse micelle synthesis route are metastable; that is, during the annealing process, they relax toward their equilibrium configuration. Thus, on heating, the reverse micelle synthesized nano samples have relaxed to a magnetic state that is similar to the bulk one. To our knowledge, this is the first report which highlights the properties of bulk nickel-zinc ferrite and nickel-zinc-indium ferrite samples obtained after annealing the reverse micelle synthesized particles at high temperature. This approach offers several advantages because of possible high-temperature application of reverse micelle synthesized ferrites.

References

[1] Morrison S. A., Cahill C. L., Carpenter E. E., Calvin S., Swaminathan R., Mchenry M. E. and Harris V. G. *J. Appl. Phys.* **2004**, 95, 6392.

[2] Vestal C. R. and Zhang Z. J. *Int. J. of Nanotechnology* **2004***,* 1, 240.

[3] Uskoković V., Drofenik M. and Ban I. *J. Magn. Magn. Mater.* **2004**, 284, 294.

[4] Hochepied J. F., Bonville P. and Pileni M. P. *J. Phys. Chem. B* **2000,** 104*,* 905.

[5] Šepelák V., Baabe D., Litterst F. J. and Becker K. D. *J. Appl. Phys*. **2000**, 88, 5884.

[6] Šepelák V., Feldhoff A., Heitjans P., Krumeich F., Menzel D., Litterst F. J.,

Bergmann I. and Becker K. D. *Chem. Mater*. **2006**, 18, 3057.

[7] Šepelák V., Bergmann I., Feldhoff A., Heitjans P., Krumeich F. Menzel D., Litterst F. J., Campbell S. J. and Becker K. D. *J. Phys. Chem. C* **2007**, 111, 5026.

[8] Brands R. A., Lauer J. and Herlach D. M . *J. Phys.* **1984**, F14, 55.

[9] Sawatzky G. A., Van D. W. F. and Morrish A. H. *Phys. Rev.* **1969**, 183, 383.

[10] Tućek J. and Zbaril R. *Czech J. Phys*. **2005,** 55, 893.

[11] Srivastva R. C., Khan D. C. and Das A. R. *Phys. Rev.* B **1990**, 41, 125147.

[12] Leung L. K., Evans B. J. and Morrish A. H. *Phys Rev. B* **1973,** 8, 29.

[13] Yang D., Lavoie K. L., Zhang Y., Zhang Z. and Ge S. *J. Appl. Phys*. **2003**, 93, 7492.

[14] Albuquerque A. S., Ardisson J. D., Macedo W. A. A. and Alves M. C. M. *J. Appl. Phys*. **2000**, 87, 4352.

[15] Dooling T. A. and Cook D. C. *J. Appl. Phys.* **1991**, 69, 5352.

[16] Amer M. A. and Hiti M. El. *J. Magn. Magn. Mater.* **2001**, 234, 118.

[17] Long G. J. *Mössbauer spectroscopy Applied to Inorganic Chemistry* Vol. 2 New York, Plenum Press, **1987**.

[18] Margulies S. and Ethrman J. R. *Nucl. Instrum methods* **1961**, 12, 131.

[19] Sorescu M., Diamandescu L., Ramesh P. D., Roy R., Daly A. and Bruno Z. *Mater. Chem. Phys.* **2007**, 101, 410.

[20] Chkoundali S., Ammar S., Jouini N., Fiévet F., Molinié P., Danot M., Villain F. and Grenéche J-M. *J. Phys.: Condens. Matter.* **2004**, 16, 4357.

[21] Oliver S. A., Hamdeh H. H. and Ho J. C. *Phys. Rev. B* **1999**, 60, 3400.

[22] Ngo A. T., Bonville P. and Pileni M. P. *J. Appl. Phys.* **2001**, 89, 3370.

[23] Muroi M., Street R., McCormick P. G. and Amighian J. *Phys. Rev. B* **2001**, 63, 184414.

[24] Zhang Y. D., Ge S. H., Zhang H., Hui S., Budnick J. I., Hines W. A., Yacaman M. J. and Miki M. *J. Appl. Phys*. **2004**, 95, 7130.

[25] Haneda K. and Morrish A. H. *J. Appl. Phys*. **1988**, 63, 4258.

[26] Upadhyay C., Verma H. C. and Anand S. *J. Appl. Phys*. **2004**, 95, 5746.

[27] Evans B. J. and Swartzendruber L. J. *J. Appl. Phys.* **1971**, 42, 1628.

[28] Daniels J. M. and Rosencweig A. *Cand. J. Phys*. **1970**, 48, 381.

[29] Marshal W. *Phys. Rev.* **1958**, 110, 1280.

[30] Goldanskli V. I., Belov V. F., Devisheva M. N. and Trukhtanov V. A. *Sov. Phys. JEPT* **1966**, 22, 1149.

[31] Goodenough J. B. and Loeb A. L. *Phys. Rev.* **1955**, 98, 391

[32] Fatseas G. A. and Krishnan R. *J. Appl. Phys*. **1968**, 39, 1256.

[33] Bhide V. G. *Mössbauer effect and its applications* New Delhi, Tara-McGraw Hill, **1973.**

[34] Woude V. D. F. *Phys. Status Solidi* **1965**, 17, 417.

[35] Rao K. H. and Mendiratta R. G. *J. Appl. Phys.* **1983**, 54, 1795.

[36] Parvatheeswara B. and Rao K. H. *J. Magn. Magn. Mater*. **2005**, 292, 44.

[37] Puri R. K., Singh M. and Sud S. P. *J. Mater. Sci.* **1994**, 29, 2182.

[38] Morup S., Dumesic J. A. and Topsoe H. *Application of Mössbauer spectroscopy* ed. Cohen R. L., New York, Academic Press, **1980**.

[39] Morup S. and Topsoe H. *Appl. Phys*. **1976**, 11, 63.

[40] Morup S., Topsoe H. and Lipka J. *J. Phys*. **1975**, 37, C6-287.

[41] Neel L. Ann. Geophys. **1949**, 5, 99.

[42] Yang Z. and Yao K. *J. Appl. Phys.* **1983**, 3, 6665

[43] Bodker F., Morup S. and Linderoth S. *Phys. Rev. Lett.* **1994**, 72, 282.

[44] Gazeau F., Bacri J. C., Gendron F., Perzynski R., Raikher Y. L., Stepanov V. and Dubois E. *J. Magn. Magn. Mater.* **1998**, 186, 175-187.

[45] Moumen N. and Pileni M. P. *J. Phys. Chem.* **1996**, 100, 1867

[46] Moumen N. and Pileni M. P. *Chem. Mater.* **1996**, 8, 1128.

[47] Prene P., Tronc E., Jolivet J-P. Livage J., Cherkaoui R. Nogues M. and Dormann J-L. *IEEE Trans. Magn.* **1993**, 29, 2658.

CHAPTER 6

MAGNETIC PROPERTIES OF NANO AND BULK FERRITE SAMPLES

Interest in magnetic properties of nanosized ferrite particles is driven by both technological applications and theoretical researchers. Nanocrystalline magnetic materials display a variety of unusual and interesting magnetic properties that are not present in bulk systems. In nanoparticles with large surface to volume ratio, the spin disorder may eventually modify the magnetic properties. This spin disorder is due to the lower coordination of the surface atoms, broken exchange bonds that produces a spin-glass like state of spatially disordered spins in the surface cations with high anisotropy surface layers. In ferrite nanoparticles, the magnetic ions located at the surface have fewer neighbors than in the core or in the bulk material. Owing to strong modifications in surface/interface effects, electronic states and magnetic interactions in the nanometer range, the nanocrystalline ferrites possess some of the most distinct features such as the enhanced/reduced saturation magnetization, low/high coercivity, superparamagnetic relaxation, spin glass (SG)-like behavior, spin canting [1-3] etc.

In earlier studies, because of the importance of site inversion phenomenon we have focused on the structural change at nano level. Once these site inversion phenomena are understood and controlled, we are able to use our particles for size dependent studies. In this chapter we have studied the magnetic properties of nano and bulk nickel-zinc ferrite particles and the effect of particle size and indium concentration on these properties in detail. We have analyzed the thermal variations of magnetization in high fields in terms of a modified Bloch law, accounting for both finite-size effect and an extra surface contribution at low temperature. It indeed confirms that one should distinguish magnetic nanostructures of the particles, the single-domain core from the surface spins, which can fluctuate freely at high temperature. The magnetic behavior of nanoparticles is strongly affected also by interparticle interactions. The magnetic interactions can be due to dipolar coupling and exchange coupling among surface atoms and play a fundamental role in the physics of these systems [4-6]. The role of interactions on the static and dynamic properties of nickel-zinc ferrite and indium doped nickel-zinc ferrite particles has been investigated by different models.

Magnetic field dependent magnetization measurements, zero field cooled (ZFC) and field cooled (FC) magnetization measurements were carried out on super conducting quantum interference device (SQUID) and vibrating sample magnetometer (VSM).

Variation of magnetization in the presence of high field (5 T) with temperature is studied on a SQUID magnetometer in the cooling cycle. The real and imaginary parts of the ac magnetic susceptibility were measured at frequencies in the range 131.1-1131.1 Hz with field amplitude of 2 Oe on a home made susceptometer [7] in the temperature range 77-300 K.

Results and discussion

6.1 Magnetic behavior of nickel-zinc ferrite nano and bulk sample

6.1.1 ZFC-FC magnetization curves

Figure 6.1 shows the ZFC and FC magnetization curves for nickel-zinc ferrite ($Ni_{0.58}Zn_{0.42}Fe_2O_4$) nanoparticles at different applied fields. In case of ZFC measurements, the magnetization of the sample is random at room temperature and remains random upon cooling to 5 K, because the magnetic dipoles do not have enough thermal energy to rotate. As temperature is increased, the thermal energy k_BT increases and magnetic dipoles align in the direction of applied field resulting in increase in magnetic moment. In case of FC magnetization, as the temperature is increased, thermal energy k_BT provides the energy for the magnetic dipoles to randomize the motion resulting in decrease in the magnetic moment.

It is clearly seen from the figure that the ZFC and FC curves begin to separate at the temperature of irreversibility (T_{SEP}) and the ZFC magnetization (M_{ZFC}) exhibits a broad maxima located at T_{MEAN}. This indicates that the magnetic moment of each particle is blocked along its easy magnetization axis at a temperature T_B (blocking temperature), which depends upon particle volume, anisotropy and orientation. The blocking temperature is a measure of the thermal energy required to overcome the superexchange transition and is defined as the temperature at which the nanoparticles do not relax during the time of measurement; they are blocked. In any real fine particle system, there is always a distribution of particle volume (V) and hence each particle is blocked at different T_B, which is not influenced by easy magnetization axis in the presence of a very low field. Therefore, there might be a distribution of blocking temperature (T_B), which provides wide maxima in ZFC and FC curves.

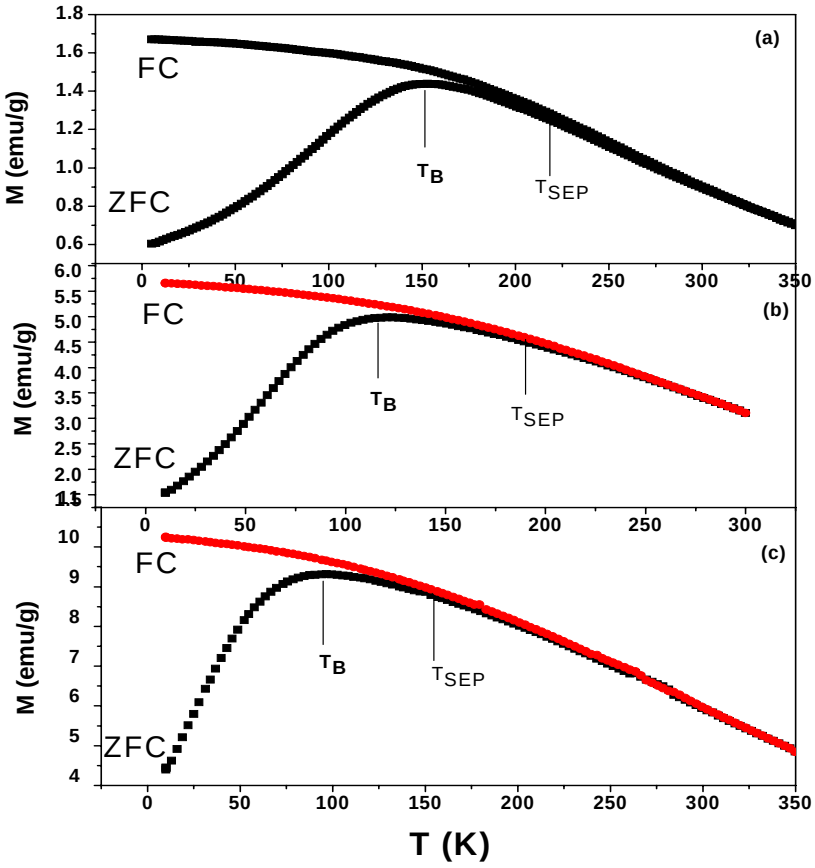

Figure 6.1 *ZFC and FC magnetization curves taken in external field of (a) 50 Oe (b) 200 Oe (c) 500 Oe*

The maxima of ZFC curve is located at T_{MEAN} = 94.54 K for nickel-zinc ferrite nano sample in the presence of 500 Oe field. Here T_{MEAN} is related to the average blocking temperature $<T_B>$ through the distribution of particle volumes. Moreover, M_{ZFC} strongly decreases below T_{MEAN}, since the superparamagnetic-ferromagnetic transition activates the anisotropy, which forces the magnetization along easy axes and are randomly oriented. This decrease in M_{ZFC} is also observed above T_{MEAN}, as we approach superparamagnetic (SPM) regime. From the curves, a clear thermo-magnetic irreversibility can be easily seen from the distinct difference between M_{ZFC} (T) and M_{FC} (T) below certain temperature T_{SEP}. Both, the ZFC and FC curves tend to superimpose at above T_{SEP} (~180 K in the presence of 500 Oe field) leading superparamagnetic (SPM) and spin-glass (SG)-like state [8]. The field dependence of blocking temperature T_B (H) :

150.37 K (50 Oe), 116.25 K (200 Oe), 94.54 K (500 Oe) indicates the superparamagnetic blocking of magnetic clusters [9]. Further, the M_{FC} have almost a nearly constant value below certain temperature which is less than T_{MEAN} and this value is much higher than that of M_{ZFC} values. In fact, the M_{FC} magnetization state is nearly an equilibrium state in which below certain temperature < T_{MEAN}, almost all the particles have only a positive projection of magnetization along the field axis, whereas the M_{ZFC} state is not a true equilibrium state. Also FC curve was nearly flat below T_B, as compared with the monotonically increasing behavior characteristic of non-interacting or superparamagnetic systems, indicating the existence of strong interactions among these nanoparticle systems [10]. However, this feature has been recently found not only to be exclusive of spin glass (SG), but is also shared by other nanoparticle systems having random anisotropy and strong interparticle interactions [11,12]. Different slopes of magnetization versus temperature for the ZFC curve (for small applied field) in the low temperature range show the spin glass behavior of the nickel-zinc ferrite nanoparticles [13].

A noticeable feature of the magnetization-temperature curves is a considerable departure of ZFC and FC branches in large temperature range for the nanoparticle sample, whereas in case of bulk sample, there is no departure up to the available temperature (Figure 6.2). This departure reflects the relaxation behavior due to

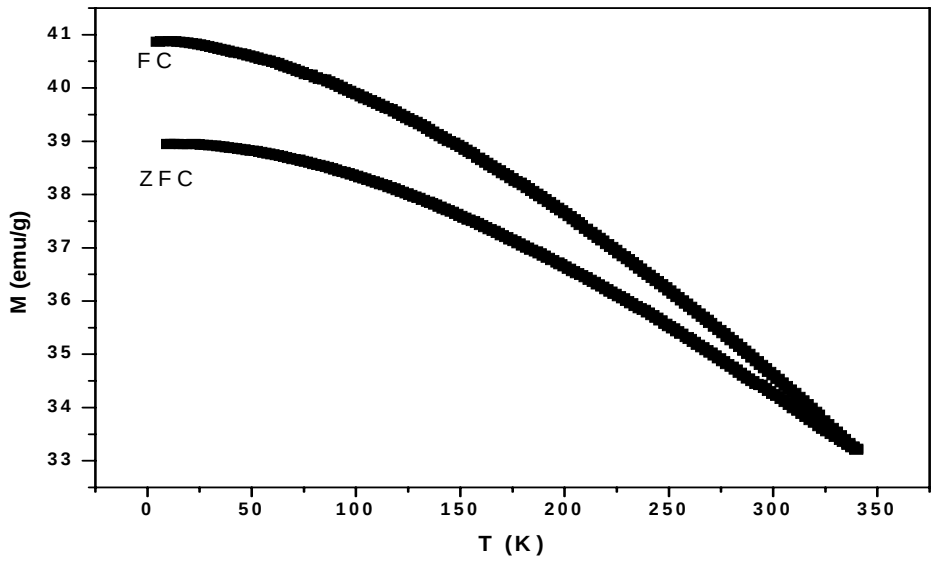

Figure 6.2 *ZFC and FC magnetization curves taken in external field of 500 Oe for bulk sample*

superparamagnetic particles in nanosamples and is in consistent with the X-ray diffraction and Mössbauer data. Such a divergence originates from the blocking of the magnetization orientation by anisotropy barrier in the nanoparticles cooled with a ZFC process [14]. The narrow divergence of ZFC and FC curves for the bulk samples indicate the narrow particle size distribution in the annealed samples which agrees with the grain size obtained from X-ray diffraction pattern and as well as from transmission electron microscopy images.

6.1.2 Variation of magnetization with applied field

Magnetization versus applied magnetic field curves (hysteresis loop/curve measurements) are time dependent measurements of the magnetic moment of a sample with the variation of the magnetic field in a hysteretic fashion. Hysteresis curves provide information such as saturation magnetization (M_s), coercivity (H_c), remanence magnetization (M_R) and squareness ration (M_R/M_s) for a given sample. These values are specific to the temperature at which the hysteresis loop experiment is performed, as the magnetic moment of a sample depends upon the temperature. Saturation magnetization was determined by observing the magnetic moment of the material at the largest applied magnetic field. For nano samples where saturation magnetization has not been attained at the maximum field applied, the saturation magnetization is determined by extrapolating the magnetization (M) versus inverse of field (1/H) curve to 1/H = 0. Remanence magnetization was determined by locating the point on the y-axis, where there was a magnetization in zero applied magnetic field. Coercivity was determined by locating the point on the x-axis, where the magnetization was zero in an applied magnetic field.

Figure 6.3 shows the variation of magnetization with applied field at different temperatures for nano nickel-zinc ferrite sample carried out on SQUID magnetometer. The typical characteristic of superparamagnetic behavior, an absence of hysteresis, almost immeasurable coercivity and remanence are observed in nano sample at 300 K. The magnetization of the nano sample does not saturate even at the maximum field attainable (H = 50 kOe) for all the temperatures studied. The observation of hysteresis loop for nickel-zinc ferrite sample below the blocking temperature (Figure 6.4) clearly

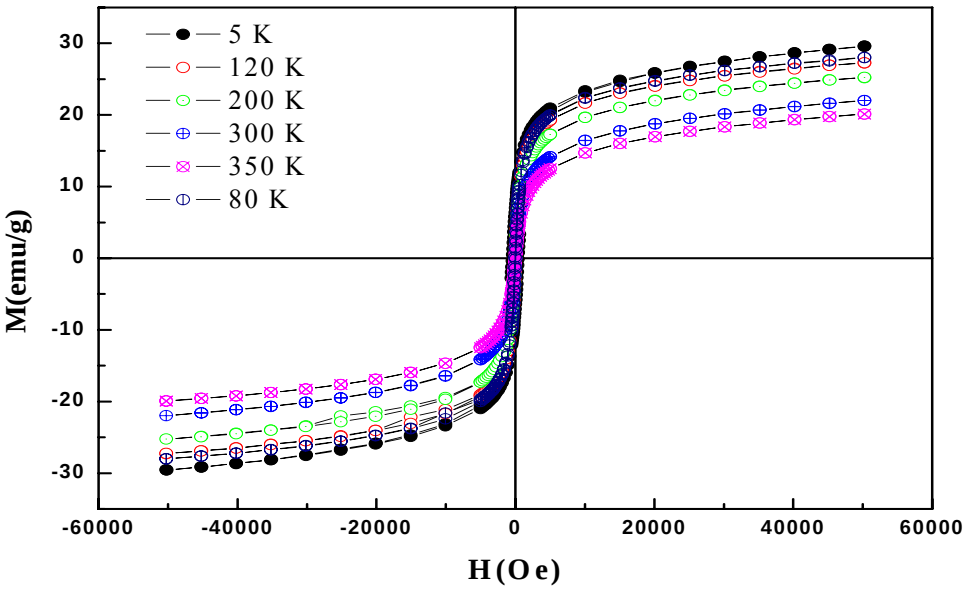

Figure 6.3 *Variation of magnetization with applied field at different temperature for nano nickel-zinc ferrite particles*

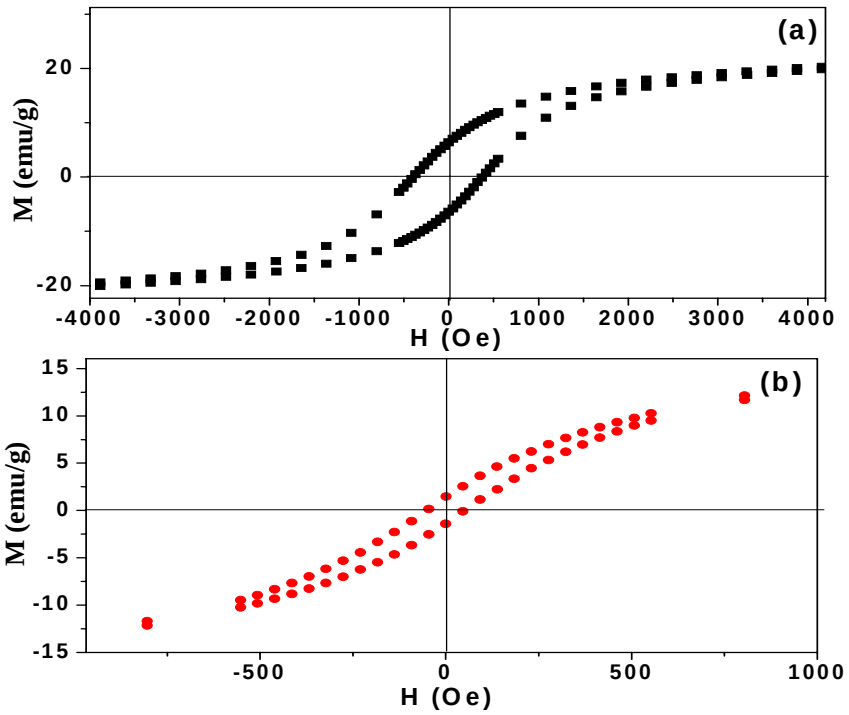

Figure 6.4 *Variation of magnetization with applied field near the origin for nano nickel-zinc ferrite particles below the blocking temperatures (a) 5 K (b) 80 K*

suggests the occurrence of a ferrimagnetic or a ferromagnetic ordering in the nanocrystals. When temperature is increased, the magnetization decreases owing to thermal fluctuations and the hysteresis feature disappear, in agreement with the superparamagnetic character of the particles. These results can be explained by the fact that nanoparticles contain a particle size distribution. This is in contrast to the magnetic behavior of the bulk sample (Figure 6.5), where saturation magnetization has been attained measured on vibrating sample magnetometer. Table 6.1 lists the value of saturation magnetization, the coercivity, remanence and the ratio of remanent magnetization to saturation magnetization at 5 K, 80 K and 300 K for nano sample. The value of saturation magnetization of bulk sample (S_0) at 300 K was obtained from magnetization vs. temperature curve in the presence of high field (Figure 6.6 shown in section 6.1.4).

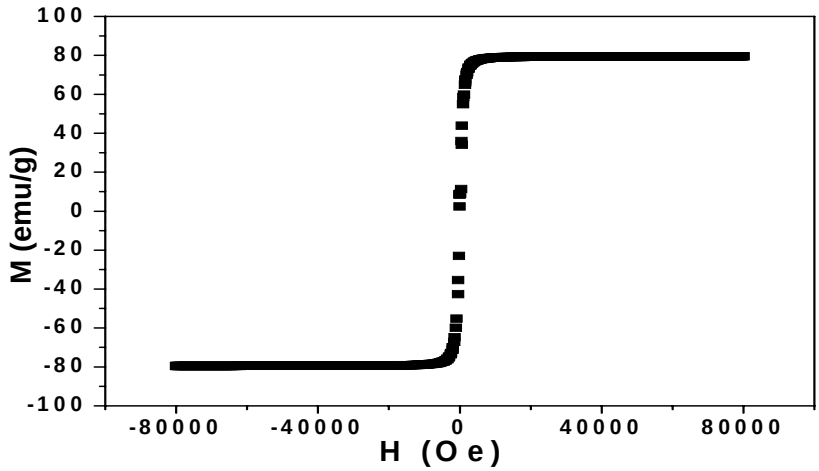

Figure 6.5 *Variation of magnetization with applied field at 5 K for nickel-zinc ferrite bulk sample*

Table 6.1 Magnetic characteristics of nano and bulk nickel-zinc ferrite sample

Sample	M_s (emu/g)	H_c (Oe)	M_R (emu/g)	M_R/M_s
N_0 (300 K)	22.44	-	-	-
(80 K)	28.44	47.09	1.50	0.03
(5 K)	30.15	333.00	7.57	0.25
S_0 (300 K)	59.94			
(5 K)	79.91			

The observed reduction in saturation magnetization and high-field irreversibility in case of nano sample in comparison to bulk sample is explained in the later section. The value of saturation magnetization obtained in our bulk sample is low compared to obtain by Smith [15]. This can be explained on the basis of difference in particle size of our sample (0.1μm) and sample prepared by Smith (1μm: ceramic method), as saturation magnetization increases with increase in particle size [16].

6.1.3 Measurement of shell thickness

Assuming a spherical shape of reverse micelle synthesized nickel-zinc ferrite nanoparticles, in the following, we have estimated the shell thickness (t) using the experimentally determined particle size (D) and saturation magnetization (M_s) value of the nano nickel-zinc ferrite sample. Assuming that the thickness of the dead layer (t) is constant, the magnetization of the particles can be expressed as [17]

$$M_s = M_0\left(1-\frac{6t}{D}\right) \quad \text{.....(6.1)}$$

where M_0 = 79.9 emu/g correspond to the bulk value at 5 K. Fitting the data with D = 8.4 nm, we obtained the thickness of the dead layer which is about 0.9 nm. The value of the shell thickness obtained is in reasonable agreement with that estimated from Mössbauer experiments (1.3 nm).

6.1.4 Finite size effect and effective Bloch law

We discuss now our results, in the framework of a core-shell model, taking into account both the finite-size effects in an effective Bloch formalism and the thermal dependence of the disordered surface contribution. The thermal behavior of the magnetization of ordered magnetic systems is due to low energy collective excitations, the well known spin waves or magnons, and results in a decrease in the spontaneous magnetization with increasing temperature. Such a model, which leads to the Bloch $T^{3/2}$ law well works for infinite systems if the gap, induced in the dispersion relation of spin waves is zero [18]. Nevertheless, the behavior for small clusters and nanoparticles is different from that of bulk particles since the spatial confinement reduces the number of degrees of freedom. It generates an energy gap in the corresponding spin-wave spectrum

[19]. As a result of the existence of this energy gap in the density of states for the spin waves, added to the lowering of the mean number of nearest neighbors, the temperature dependence of the magnetization of the cores of the nanoparticles can be well described with a more general law [20,21].

$$M_s(T) = M_s(0)\,(1-bT^{\alpha}) \qquad \text{……..(6.2)}$$

where $M_s(0)$ is the saturation magnetization as T tends to zero. Note that experimentally $M_s(0)$ has to be extrapolated, getting rid of the additional surface contribution at low temperatures. The Bloch exponent (α) is now size dependent and structure independent whereas the Bloch constant (b) mainly depends on the detailed structure of the core of the nanoparticles.

However, it is important to note that this model would work only if the applied field is large enough to ensure the saturation condition for the core of the nanoparticles in each sample [22]. In order to compensate the nonsaturation for nano sample, a correction is made replacing $M_s(T)$ by $M_s(T)/\{L[\xi(T)]\}$ where $L(\xi(T)) = \coth(\mu H/kT) - (kT/\mu H)$ is calculated at each temperature, by using the value of mean magnetic moment $<\mu>$. This small correction being taken into account, the high temperature variations of $M_s(T)$, which are associated to the regular saturation of the grain core, are fitted with eqn. (6.2). This adjustment leads to $M_s(0)$ (29.1 emu/g), the extrapolated values of M_s for the grain core at T = 0. Figures 6.6 and 6.7 show semilogarithmic representations of the experimental variation of $M_s(T)$ and their corresponding core saturation for bulk and nano sample. For the largest particles, the whole range of temperature can be adjusted by eqn. (6.2) (Figure 6.6). The depression of the core magnetization $M_s(0)-M_s(T)$ is also plotted. The inset of Figure 6.6 clearly shows that the linear relation between $M_s(0)-M_s(T)$ vs. T is followed along the whole experimental range (5-300 K) for bulk sample. In the log-log representation, the variations are linear with a slope α. The values of α (1.5) and b (5×10^{-5}) are in good agreement with the expected Bloch behavior for bulk materials. On the contrary, for nano sample, the extra surface contribution appears clearly below 80 K (Figure 6.7). In case of nano sample, the fit with eqn. (6.2) is performed for $T \geq 80$ K (inset of Figure 6.7). This also leads to α (1.43) and b (7×10^{-5}). The straight line clearly leads to smaller slope and is therefore associated to a deviation

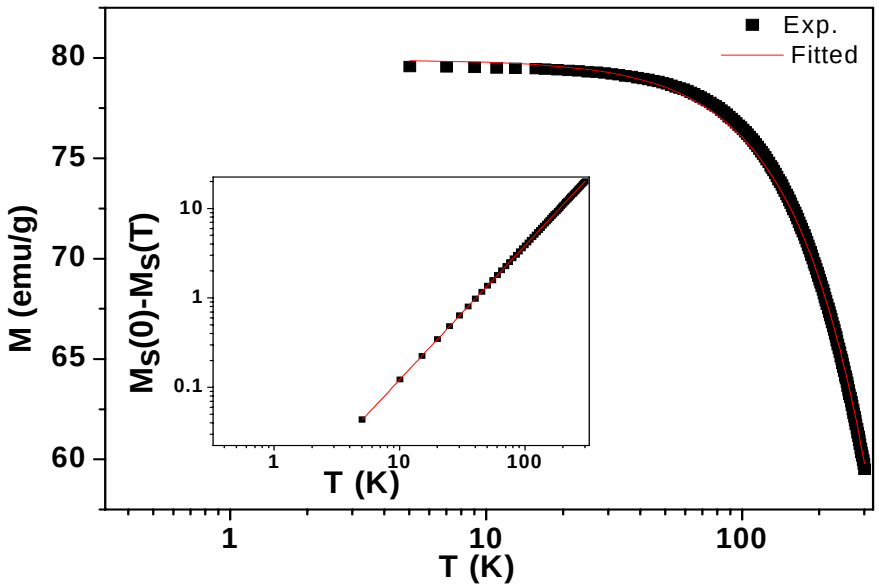

Figure 6.6 *Semilogarithmic plot of the experimental variation of $M_s(T)$ and the core saturation (full line) of bulk sample. Inset shows the depression of the core magnetization $M_s(0)-M_s(T)$ for bulk sample in a double logarithmic representation*

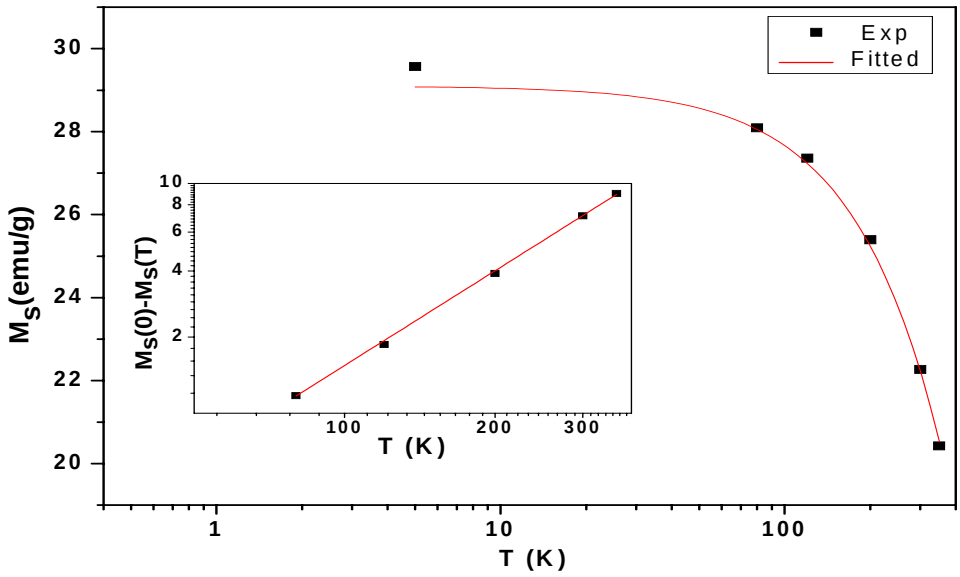

Figure 6.7 *Semilogarithmic plot of the experimental variation of $M_s(T)$ and the core saturation (full line) of nano sample. Inset shows the depression of the core magnetization $M_s(0)-M_s(T)$ for nano sample in a double logarithmic representation*

of the $T^{3/2}$ Bloch law. Several works reported a dependence of α on the particle size in nanomagnets, ferrimagnetic or ferromagnets. It is in the range 0.79-1.14 for magnetic nanocomposites [23], 1.45-1.55 for $ZnFe_2O_4$ particles of 6.6-14.8 nm in size [24], 1.6–1.8 for $MnFe_2O_4$ particles of 5–15 nm in size [25], close to 1.9 [26] and 1.66 [27] for Fe–C and $La_{0.8}Sr_{0.2}MnO_{3-\delta}$ particles with a diameter of 3.1 nm and 8 nm, respectively. This deviation of α from 1.5 is usually associated with the increase in structural disorder with particle size reduction. The observed size dependence of b can be related to the existence of a rather important contribution in ferrite nanoparticles coming from surface canted spins poorly correlated to the monodomain core [28-30]. Indeed at the interface, the reduction of atomic coordination implies that surface spins are more sensitive to thermal fluctuations, which favors an effective b increasing. It is usually found greater in nanoparticles than in bulk, increasing when the size decreases. Some authors attribute this feature to an increased interaction among the neighboring spins [27]. In the particular case of spinel ferrite materials, it can be suspected due to a significant structural deviation from the thermodynamically stable one in terms of cation distribution. The 8.4 nm sized nickel-zinc ferrite particles exhibit the lower diameter, the higher degree of cationic inversion and hence the higher b value.

6.1.5 AC susceptibility measurements

In order to better understand the spin dynamics, we have also investigated the temperature dependence of the real $\chi'(T)$ and imaginary parts $\chi''(T)$ of ac susceptibility measurements for different driving frequencies in the range from 131.1-1131.1 Hz (Figures 6.8a-b) for nano nickel-zinc ferrite sample. It is clearly evident from figures that the data for both $\chi'(T)$ and $\chi''(T)$ exhibit the expected behavior of a blocking/freezing process, i.e. the occurrence of a maximum at a temperature T_B ((i.e. the temperature of the peak position in the ac susceptibility) for both $\chi'(T)$ and $\chi''(T)$ components which shifts towards higher temperature with increasing frequency [31].

In order to identify the dynamic behavior of the blocking/freezing process, we have used the real part $\chi'(T)$ of ac susceptibility in an empirical relation $\{\Phi = \Delta T_B/(T_B \Delta \log_{10} f)\}$, here ΔT_B is the difference between T_B measured in the $\Delta \log_{10}(f)$ frequency interval and f is the ac magnetic field frequency.

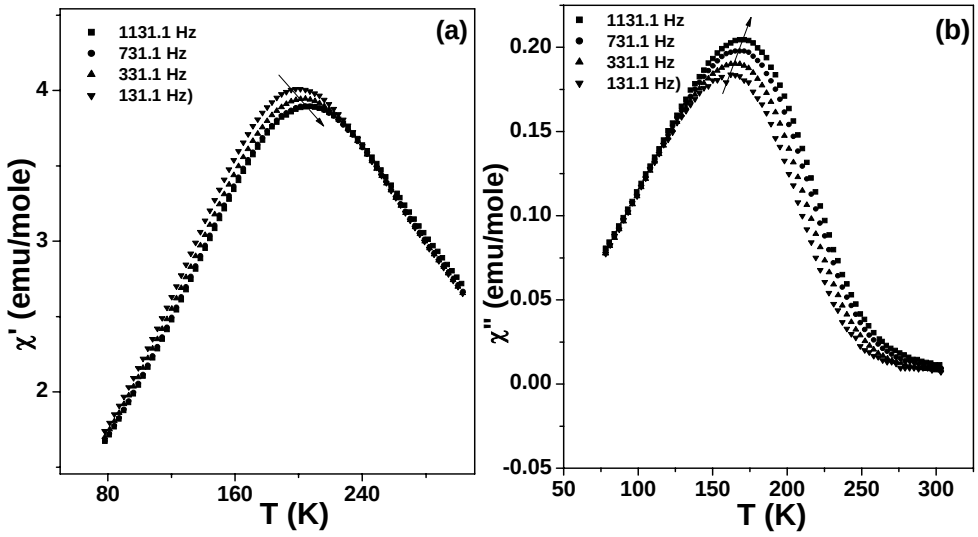

Figure 6.8 *(a) Temperature dependence of the real part χ' (T) of the ac magnetic susceptibility for the nano sample, at different frequencies. The arrow indicates increasing frequencies (b) Imaginary part χ''(T) of the ac magnetic susceptibility. The data were taken with an external magnetic field, H = 2 Oe*

The experimentally found values for the superparamagnetic (SPM) particles are in the range ~0.1–0.13, whereas a much smaller value was found in the present case (0.04) usually observed for spin-glass (~0.005–0.05) behavior of the nanoparticle surface or simply due to non-negligible interparticle interactions [32]. In fact, it is well known that smaller values of Φ usually result from strong interactions and the spin-glass hypothesis [31,33,34]. However, it is often very difficult to distinguish between spin glass and superparamagnetism experimentally [35]. There are two different interpretations in the literature on the phenomenon of the spin glass freezing. For a system consisting of non-interacting superparamagnetic particles, the relaxation time τ follows the Neel–Arrhenius (NA) relation

$$\tau = \tau_0 \exp\left(\frac{E_A}{k_B T_B}\right) \ldots\ldots\ldots\ldots (6.3)$$

where τ is the relaxation time at frequency f, E_A is the anisotropy energy barrier for the reversal of the moments and τ_0 is the characteristic relaxation time, ranging typically from 10^{-9} to 10^{-13} s for superparamagnetic (SPM) particles. In an external magnetic field,

the energy barrier is given by $E_A = K_{eff}V$, where K_{eff} is an effective magnetic anisotropy constant and V is the particle volume. To confirm the validity of the Neel–Arrhenius (NA) relation, we first plot lnτ versus $1/T_B$ for nano system (Figure 6.9).

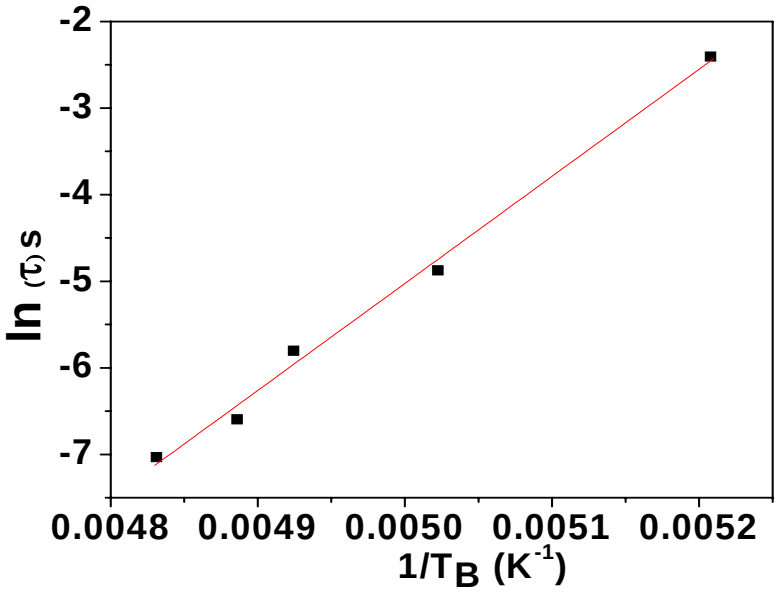

Figure 6.9 *Logarithm of the measuring frequency as a function of the reciprocal of the temperature of peak for nano sample*

From the fitting, we have found an unphysically small value of relaxation time; τ_0~9.4 × 10^{-30} in comparison to 10^{-13} s. This leads us to conclude that the Neel–Arrhenius (NA) relation is not valid and there exist strong interactions among these nanoparticle systems [35], consistent with the results obtained from the dc magnetization data.

As a result, we have tried to fit these data using the Vogel–Fulcher (VG) law [36], that describes the slowing down of a system composed of magnetically interacting particles as the temperature is reduced, and can be expressed in the form

$$\tau = \tau_0 \exp\left(\frac{E_A}{k_B(T_B - T_0)}\right) \quad \text{.....(6.4)}$$

where T_0 is an effective temperature and T_B is the characteristic temperature signaling the onset of the blocking process

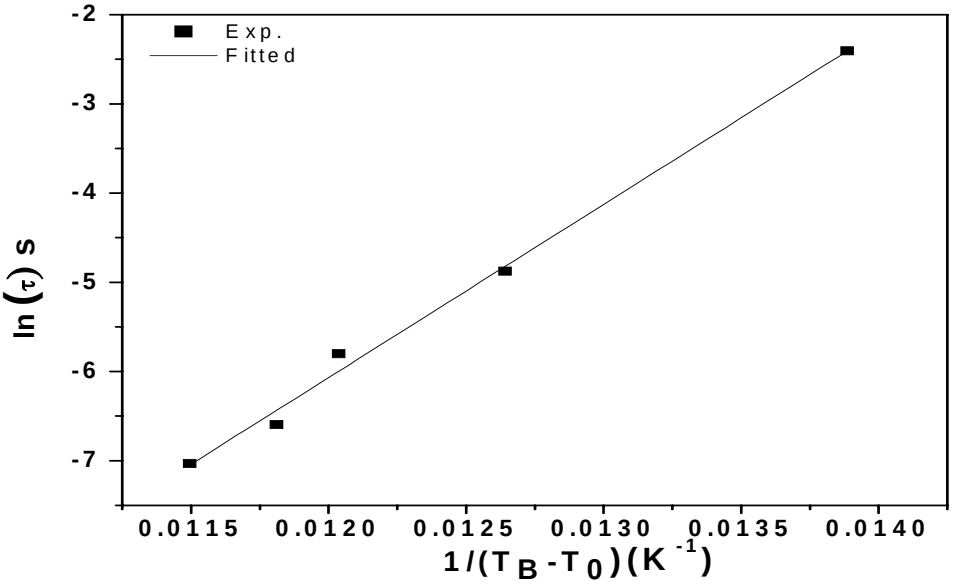

Figure 6.10 *Logarithm of the measuring frequency as a function of the reciprocal of the difference between the temperature of peak and T_0 for nano sample*

For nano sample, the following values of the parameters are obtained after fitting the data (Figure 6.10): $\tau_0 = 1.77 \times 10^{-13}$ s, $E_A = 2.6 \times 10^{-13}$ erg, $T_0 = 120$ K. The finite value of T_0 (~120 K), again suggests interactions between particles via grain boundary spins. This confirms that a blocking of the interacting particles occurs rather than the collective nature of a spin disordered system, such as spin glass. By using the average particle size calculated from X-ray diffraction data, the calculated value of K_{eff} for nickel-zinc ferrite nanoparticles is 8.38 x 10^5 erg cm^{-3}. The values are one order of magnitude larger than K value (~6 x 10^4 erg cm^{-3}) for bulk nickel ferrite [37]. Evidently, nickel-zinc ferrite nanoparticles exhibit large magnetocrystalline anisotropy [38]. This is an expected behavior of nanosized particles, where the surface contribution is expected to enhance the magnetic anisotropy constant.

6.2 Effect of indium doping on the magnetic properties of nickel-zinc ferrite particles

6.2.1 ZFC-FC magnetization curves

Figures 6.11 and 6.12 show the ZFC-FC curves for nickel-zinc-indium ferrite nano and bulk samples respectively. Observation of departure of ZFC and FC branches in large temperature range for $Ni_{0.58}Zn_{0.42}In_xFe_{2-x}O_4$ (N_1-N_5) nanosamples in contrast to bulk samples suggest the relaxation behavior in case of nanoparticle samples due to superparamagnetic particles consistent with the X-ray diffraction and Mössbauer data.

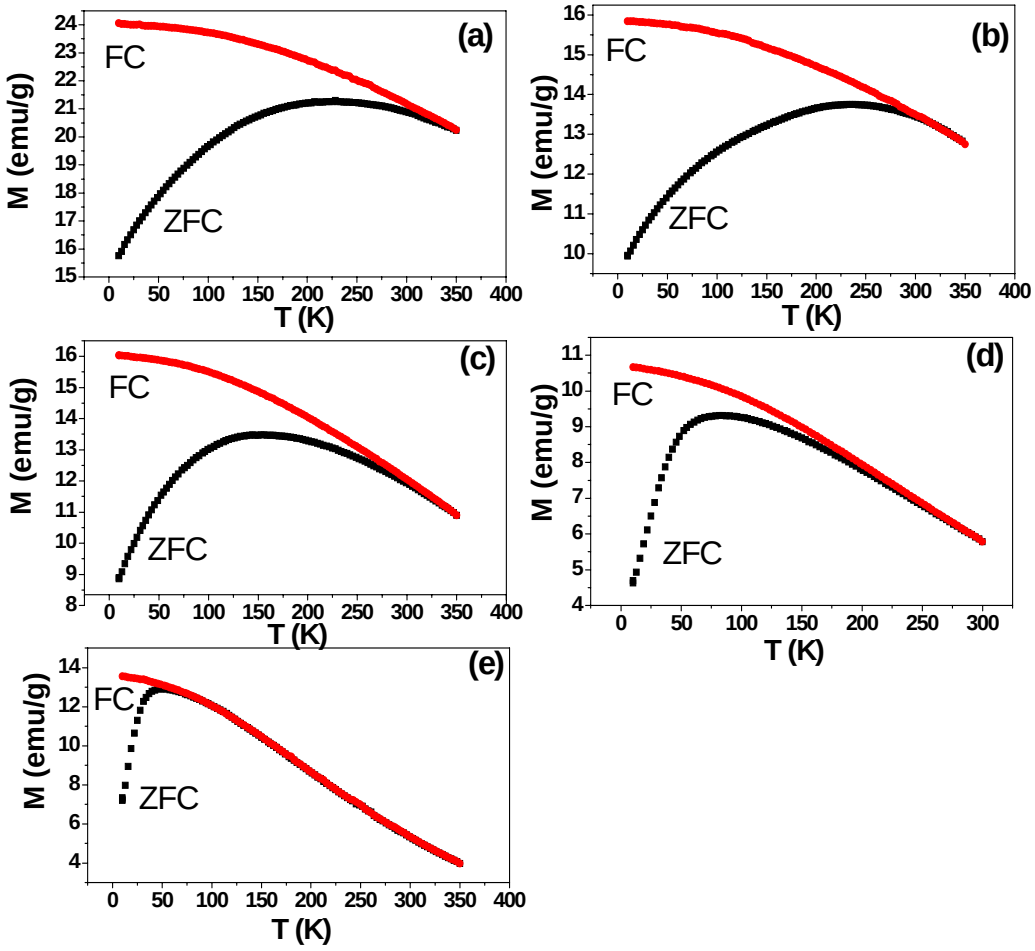

Figure 6.11 *ZFC and FC magnetization curves taken in external field of 500 Oe for nano samples (a) N_1 (b) N_2 (c) N_3 (d) N_4 (e) N_5*

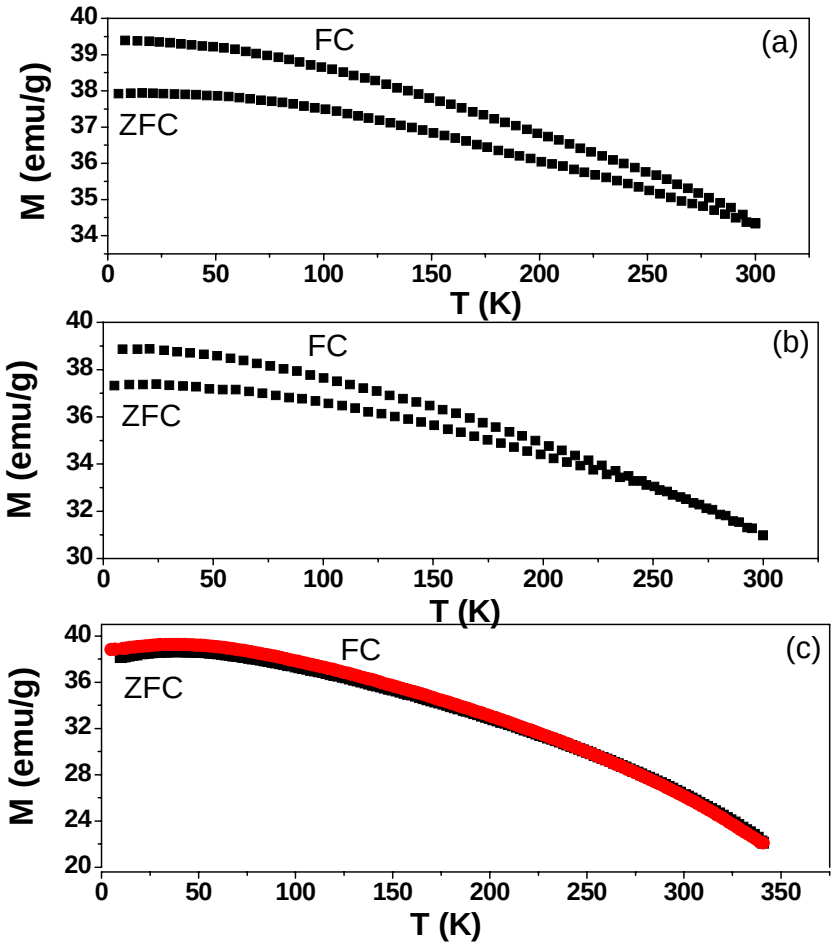

Figure 6.12 *ZFC and FC magnetization curves taken in external field of 500 Oe for bulk samples (a) S_1 (b) S_2 (c) S_3*

The observation of prominent irreversibility for $Ni_{0.58}Zn_{0.42}In_{0.1}Fe_{1.9}O_4$ (N_1, 15 nm), $Ni_{0.58}Zn_{0.42}In_{0.2}Fe_{1.8}O_4$ (N_2, 15 nm) and $Ni_{0.58}Zn_{0.42}In_{0.1}Fe_{1.9}O_4$ (N_3, 8.7 nm) samples is due to anisotropy effect in the ferromagnetic clusters [39].

The FC curves were nearly flat for all nano samples below T_B, indicating the existence of strong interactions among these nanoparticle systems. This hypothesis is somewhat confirmed in regard to the collected transmission electron microscopy images where the smaller particles appear clearly agglomerated. Blocking temperature increases with increase in particle size (Figure 6.11).

According to Stoner-Wohlfarth theory [40], the magnetic anisotropy energy E_A of a single-domain superparamagnetic particle can be expressed as:

$$E_A = KV \sin^2\theta \quad \text{.....(6.5)}$$

where K is the magnetic anisotropy constant, V is the particle volume and θ is the angle between the magnetization vector and easy axis of the nanoparticles. When E_A is comparable with the thermal energy k_BT, the magnetization vector of the nanoparticle start to flip and goes through rapid superparamagnetic relaxation. Above a certain temperature called blocking temperature T_B, the magnetic anisotropy energy is overcome by thermal energy and magnetization vector follows simply the applied field direction. Consequently, the nanoparticles show paramagnetic behavior. Below T_B, the thermal energy no longer overcomes the magnetic anisotropy energy and hence the magnetization vector of each nanoparticle rotates from the field direction back to easy axis without any movement of the nanoparticles. As larger particles exhibit a higher E_A and require a larger thermal energy to become superparamagnetic, hence T_B increases with increasing particles size.

For $Ni_{0.58}Zn_{0.42}In_{0.3}Fe_{1.7}O_4$ (N_5, 8.0 nm) sample, ZFC and FC curves are also taken in the presence of different applied fields (Figure 6.13). It is found that the blocking

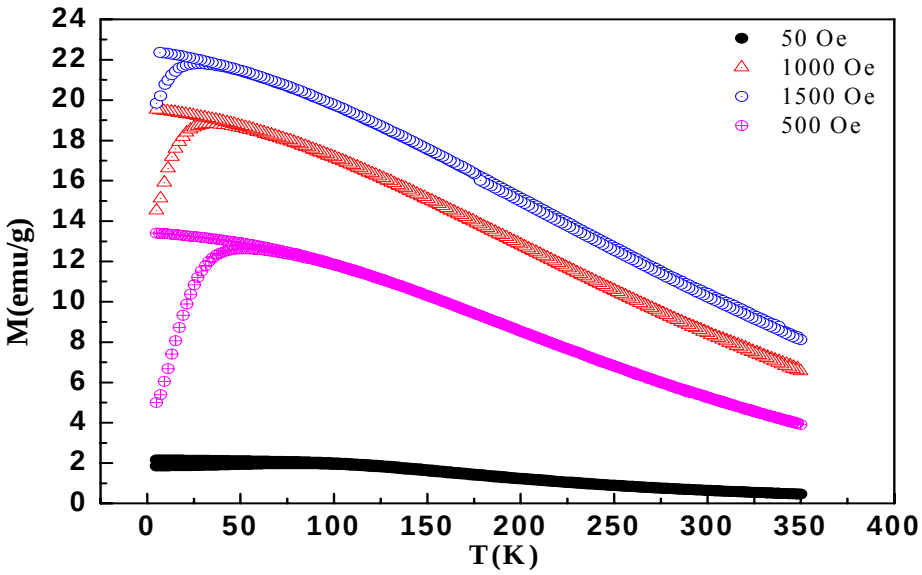

Figure 6.13 *ZFC and FC magnetization curves for $Ni_{0.58}Zn_{0.42}In_{0.3}Fe_{1.7}O_4$ sample taken in various applied external fields*

temperature decreases with the increase in applied field: T_B (H) : 48.53 K (500 Oe), 31.32 K (1000 Oe) and 22.03 K (1500 Oe) for N_5 sample, which indicate the superparamagnetic blocking of magnetic clusters.

6.2.2 Room temperature magnetization measurements

Figure 6.14 shows the room temperature variation of magnetization with field for nickel-zinc-indium ferrite nano samples. The magnetization of $Ni_{0.58}Zn_{0.42}In_{0.1}Fe_{1.9}O_4$ (N_3, 8.7 nm), $Ni_{0.58}Zn_{0.42}In_{0.2}Fe_{1.8}O_4$ (N_4, 8.5 nm) and $Ni_{0.58}Zn_{0.42}In_{0.3}Fe_{1.7}O_4$ (N_5, 8.0 nm)

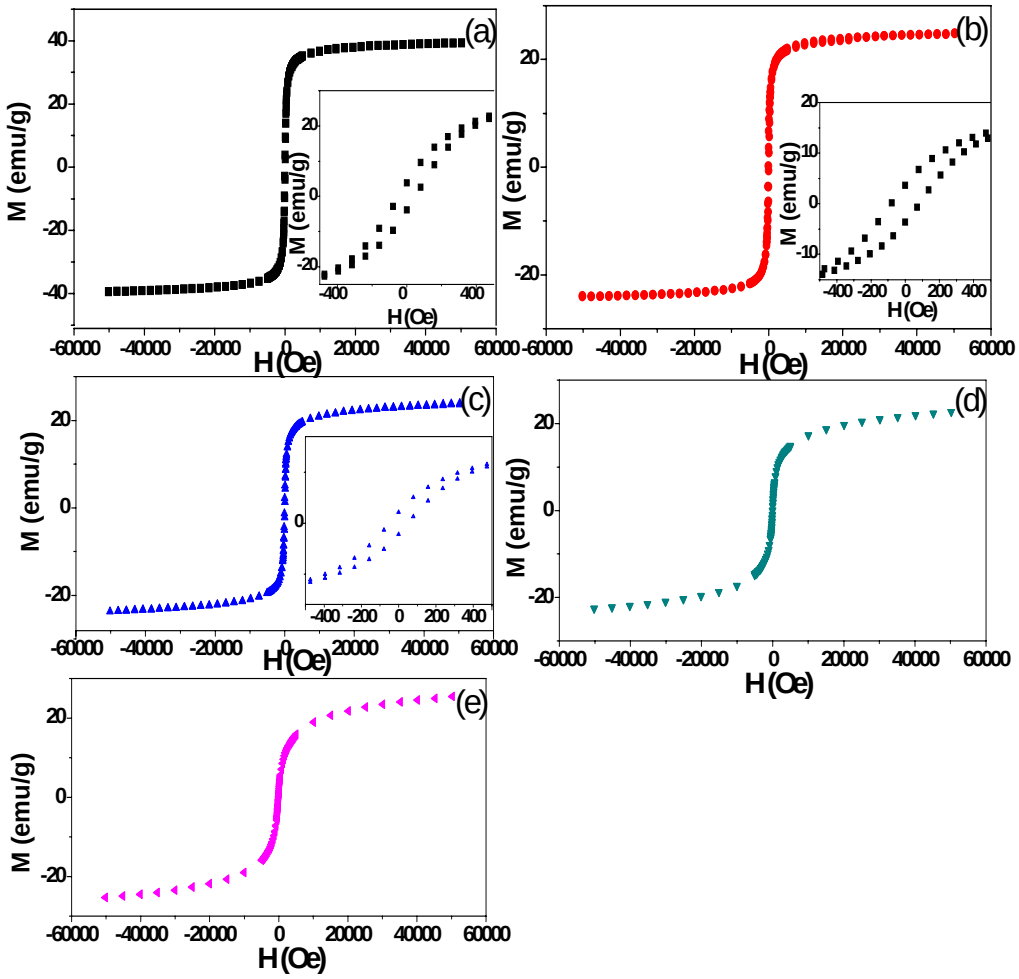

Figure 6.14 *Variation of magnetization with applied field at room temperature for nano nickel-zinc-indium ferrite samples (a) N_1 (b) N_2 (c) N_3 (d) N_4 (e) N_5*

samples does not saturate even at the maximum field attainable (H = 50 kOe), while $Ni_{0.58}Zn_{0.42}In_{0.1}Fe_{1.9}O_4$ (N_1, 15 nm) and $Ni_{0.58}Zn_{0.42}In_{0.2}Fe_{1.8}O_4$ (N_2, 15 nm) samples attain saturation magnetization in the applied field. The M_s value calculated for all samples are given in table 6.2. At room temperature, observation of hysteresis loops (Inset of Figure) for N_1, N_2 and N_3 samples are typical of ferromagnetic ordering,

Table 6.2 Magnetic characteristics of nano and bulk nickel-zinc-indium ferrite sample

Sample	M_s (emu/g)	H_c (Oe)	M_R (emu/g)	M_R/M_s
N_1 (300 K)	39.38	54.00	3.89	0.10
(80 K)	45.66	175.32	13.70	0.30
(5 K)	46.10	273.95	15.03	0.32
N_2 (300 K)	24.85	77.82	5.37	0.20
(80 K)	29.89	226.98	10.33	0.34
(5 K)	30.86	294.63	13.38	0.43
N_3 (300 K)	23.96	48.19	2.23	0.10
(80 K)	33.72	170.56	7.17	0.21
(5 K)	36.20	322.81	10.79	0.29
N_4 (300 K)	22.61	-	-	-
(80 K)	30.11	43.75	1.65	0.05
(5 K)	33.02	378.59	7.45	0.22
N_5 (300 K)	28.58	-	-	-
(80 K)	36.75	-	-	-
(5 K)	40.04	343.75	9.79	0.24
S_1 (300 K)	65.85			
(5 K)	92.12			
S_2 (300 K)	50.67			
(5 K)	76.37			
S_3 (300 K)	37.64			
(5 K)	74.37			

whereas the absence of hysteresis loop for N_4 and N_5 samples is consistent with the superparamagnetic clusters. The low inferred values of coercivity and squareness ratio obtained for N_1, N_2 and N_3 samples at room temperature are in agreement with the well established soft magnetic character of nickel-zinc-indium ferrite particles (Table 6.2) [41].

6.2.3 Magnetization measurements at different temperatures

Figure 6.15 shows the variation of magnetization with applied field at different temperatures for nano samples. The magnetization in N_3, N_4 and N_5 samples does not saturate even at 5 K. The observation of hysteresis loop for N_3, N_4 and N_5 samples below

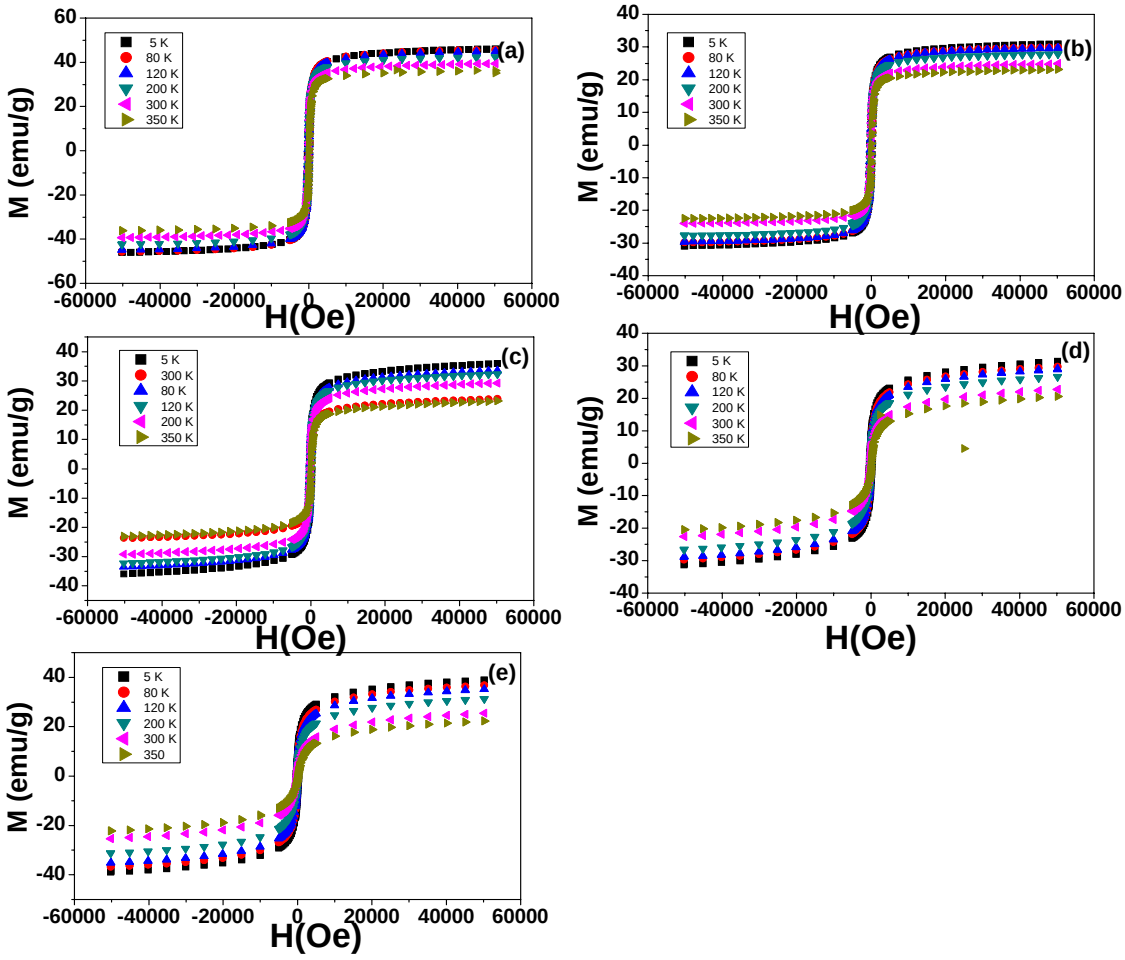

Figure 6.15 *Variation of magnetization with applied field at different temperature for nano nickel-zinc-indium ferrite samples (a) N_1 (b) N_2 (c) N_3 (d) N_4 (e) N_5*

the blocking temperature suggests clearly the occurrence of a ferrimagnetic or a ferromagnetic ordering in the nanocrystals. Table 6.2 lists the value of saturation magnetization, the coercivity, remanence and the ratio of remanent magnetization to saturation magnetization at 5 K, 80 K and 300 K for nano samples. The value of saturation magnetization for bulk samples were obtained from the magnetization vs. temperature curve in the presence of high field (Figure 6.16 shown in the section 6.2.5) (Table 6.2).

6.2.3.1 Variation of saturation magnetization of nickel-zinc ferrite samples with indium concentration

Variation of saturation magnetization of nickel-zinc ferrite particles with indium concentration ($Ni_{0.58}Zn_{0.42}In_xFe_{2-x}O_4$, x = 0, 0.1, 0.2, 0.3) can be understood on the basis of Neel's theory [42]. Neel considered three kinds of exchange interactions between unpaired electrons of two ions lying: (I) both ions at tetrahedral (A) sites (A-A interactions) (II) both ions at octahedral (B) sites (B-B interactions), and (III) one at (A) site and the other at (B) site (A-B interaction). A-B interaction heavily predominates over A-A and B-B interactions. The A-B interaction aligns all the magnetic spins at (A) site in one direction and those at (B) site in the opposite direction. The net magnetic moment of the lattice is therefore the difference between the magnetic moments at (B) and (A) sublattices, i.e. $M = M_B - M_A$. To explain the observed variation in saturation magnetization, the following possibilities may be considered:

(i) In^{3+} ions occupy (B) sites and replace Fe^{3+} ions.

(ii) In^{3+} ions replace (A) site Fe^{3+} ions

(iii) In^{3+} ions occupy (A) sites and push Zn^{2+} ions from (A) to (B) sites.

(iv) In^{3+} ions occupy both (A) and (B) sites.

If indium ions occupy (B) sites and replace Fe^{3+} ions, the magnetization of (B) sublattice decreases keeping the magnetization of (A) sublattice constant. Thus, the resultant magnetization according to $M = M_B - M_A$ is expected to decrease which is contrary to the observed rise in saturation magnetization for $Ni_{0.58}Zn_{0.42}In_{0.1}Fe_{1.9}O_4$ sample. Therefore possibility (i) is ruled out. For lower concentration, if In^{3+} ions occupy

(A) sites and replace Fe^{3+} ions, (A) sublattice magnetization decreases and the resultant magnetization, therefore increases. For higher concentration, x>0.1, if indium ions continues to occupy (A) sites, the magnitude of (A) sublattice would decrease rapidly which in turn weakens A-B exchange interactions considerably and material may turn into paramagnetic. But the moderate values in saturation magnetization for samples x > 0.1, indicate that the A-B exchange interactions still persists for these samples. This shows that at higher concentration, indium ions may partly occupy (B) sites and replace Fe^{3+} ions due to which A-B exchange interactions, though weaken are strong enough to provide some magnetization. The results observed are in accordance with previous study on indium doped ferrites [24-27]. The rapid decrease of the saturation magnetization for $Ni_{0.58}Zn_{0.42}In_{0.2}Fe_{1.8}O_4$ (N_2) sample may also be due to the formation of antiferromagnetic phase with spinel phase [13]. The observed variation of saturation magnetization with indium concentration is in accordance with the results obtained by Mössbauer spectroscopy. The anomalous increase of saturation magnetization in case of $Ni_{0.58}Zn_{0.42}In_{0.3}Fe_{1.7}O_4$ (N_5) sample in comparison to $Ni_{0.58}Zn_{0.42}In_{0.1}Fe_{1.9}O_4$ (N_3) and $Ni_{0.58}Zn_{0.42}In_{0.2}Fe_{1.8}O_4$ (N_4) samples can be explained on the basis of site exchange of surface cations (In^{3+} and Fe^{3+}) among the (A) and (B) sites as observed by Mössbauer spectroscopy. In addition to site exchange of cations, we correlate the enhancement of magnetization of N_5 sample to the spin canting effect i.e. the lowering of (B) site spin canting in N_5 sample compared to N_3 and N_4 samples. Bhowmik et al [43] have also reported the enhancement of saturation magnetization of cobalt ferrite nanoparticle to the site exchange of cations and spin canting effect i.e. lowering of (B) site spin canting.

6.2.3.2 Particle size effect on the saturation magnetization of nickel-zinc-indium ferrite samples

The saturation magnetization of ferromagnetic or ferrimagnetic materials usually decreases with decreasing particle size due to the existence of spin canting in most small magnetic particles. Basically two mechanisms have been suggested to explain the origin of spin canting: one is the surface or interface effect [44-57] and the other is the finite size effect [58-60]. Variations in coordination numbers and distances of surface cations could result in a distribution of net exchange fields [44-46]. The surface effect based on this argument, states that the spin structure of magnetic particles in a large applied

magnetic fields consists of collinear spins in a core and non-collinear spins in a surface layer (or shell). The core magnetic moment aligns with the applied field, upto a particular field in a usual Langevin-like way. But, beyond this field, any increase in the applied field has an effect only on the surface layer of the particles, which is spin glass like. Since this layer does not have a very high response to the applied field, the overall increase in the magnetization of the particles slows down. These effects are strongly manifested in nanocrystalline ferrites, where the superexchange interactions occur through the oxygen ions. It often happens that two magnetic ions are separated by a non-magnetic ion (oxygen in this case i.e., one with all electronic shells closed). It is then possible for magnetic ions to have a magnetic interaction mediated by the electrons in their common non-magnetic neighbors, which is more important than their superexchange interactions and hence include surface spin disorder [61]. These interactions are highly sensitive and depend upon the bond angles and bond lengths [62], which would obviously be different at the surface due to the breaking of the bonds.

It is observed that even a magnetic filed of 50 kOe was not sufficient to align all spins in the field direction for nanoparticles. The particular lack of saturation in N_0, N_3, N_4 and N_5 samples is attributed to surface spin-canting effect. It is clearly seen (Table 6.2) that the saturation magnetization depends strongly on the particle size. The value of saturation magnetization increases with the increasing particle size. Small value of saturation magnetization for N_3 sample in comparison to N_1 sample can be understood on the basis of decrease in particle size. This has already been observed with other ferrite nanoparticles and is due to an increase in the disorder of magnetic moments orientation in the various sites when the ratio surface/volume increases [63]. The reduced magnetization measured for nanosamples in comparison to bulk samples is attributed to the effect of spin canting and small particle size.

6.2.3.3 Variation of coercivity and squareness ratio with particle size

When temperature is increased, the magnetization value decreases owing to thermal fluctuations and the hysteresis feature disappear, in agreement with the superparamagnetic character of the particles. These results can be explained on the basis of particle size distribution.

At room temperature, coercive field (H_c) decreases with decreasing particle size due to the superparamagnetic relaxation effect. The $H_c = 0$ point marks a critical size, D_p, at which the onset of superparamagnetic relaxation takes place within the magnetization measuring time (τ~100 s). On the other hand, at 5 K, H_c increases with decrease in size (Table 6.2), which is the behavior of single-domain superparamagnetic particles caused by thermal effect. At 5 K, particles are blocked and the magnetization will reverse by rotation since the samples N_4 and N_5 are well below their single-domain critical value D_s. The coercive field might be expressed by

$$H_c = 2K_{eff}/M_s \quad \text{.....(6.6)}$$

where M_s is the saturation magnetization of the nanoparticle and K_{eff} is related to the effective anisotropy constant [64]. Above the blocking temperature, the magntocrystalline anisotropy is overcome by thermal activation and K_{eff} can be considered as zero. The nanoparticles do not display any magnetization hysteresis behavior with $H_c = 0$.

From table 6.2, it is seen that the squareness ratio (M_R/M_s) is very small at room temperature. It is due to the increasing fraction of superparamagnetic particles. The M_R/M_s values for all the samples studied at 5 K are slightly smaller than the expected value of 0.5 for particles with uniaxial symmetry, which could originate from interparticle interactions.

6.2.4 Measurement of shell thickness

Assuming a spherical shape of reverse micelle synthesized nickel-zinc-indium ferrite nanoparticles, in the following, we have estimated the shell thickness (t) using eqn. 6.1. Fitting the data with particle size (D) we obtained the thickness of the dead layer. The values of the shell thickness obtained for N_3, N_4 and N_5 samples are 0.8 nm, 0.79 nm and 0.5 nm respectively, are in reasonable agreement with that estimated from Mössbauer experiments.

6.2.5 Finite size effect and effective Bloch' law

We discuss now our results, in the framework of a core-shell model. Figure 6.16 shows the variation of spontaneous magnetization with temperature in the presence of

high field of 50 kOe. For bulk samples, the whole range of temperature can be adjusted by Bloch law (eqn. 6.2). The inset of figure 6.16 clearly shows that the linear relation between $M_s(0)-M_s(T)$ vs. T is followed along the whole experimental range (5-300 K). The values of α and b (Table 6.3) are in good agreement with the expected Bloch behavior for bulk materials. Here the consideration should be given to $Ni_{0.58}Zn_{0.42}In_{0.3}Fe_{1.7}O_4$ (S_3) sample which shows the promising properties although the particle size is in nano scale.

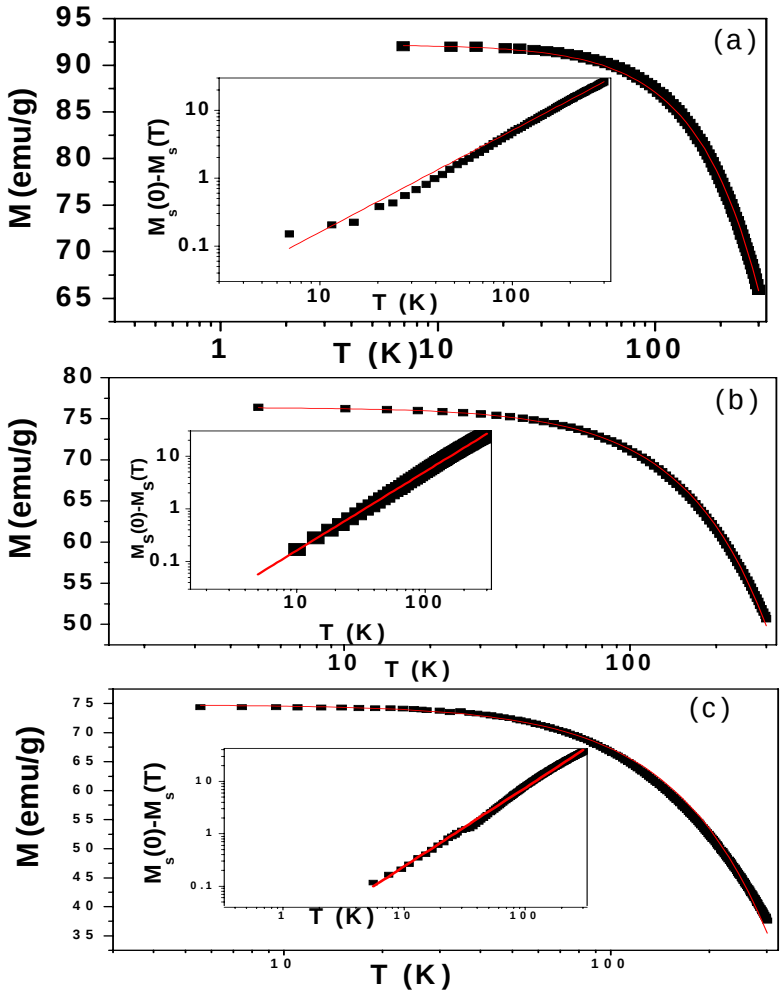

Figure 6.16 *Semilogarithmic plot of the experimental variation of $M_s(T)$ and the core saturation (full line) of bulk samples (a) S_1 (b) S_2 (c) S_3. Inset shows the depression of the core magnetization $M_s(0)-M_s(T)$ for bulk samples in a double logarithmic representation*

Interesting results are obtained in case of nano samples. For nano N_1 and N_2 samples the whole range of temperature is adjusted by Bloch law (Figure 6.17). The inset of Figure 6.17 clearly shows a linear relation between $M_s(0)-M_s(T)$ vs. T, and is followed along the whole experimental range (5-300 K). The values of α and b are in good agreement with those obtained for the corresponding bulk samples (Table 6.3). But this is not the case for N_3, N_4 and N_5 samples. Magnetization measurements show that these samples do not saturate even at the maximum field applied.

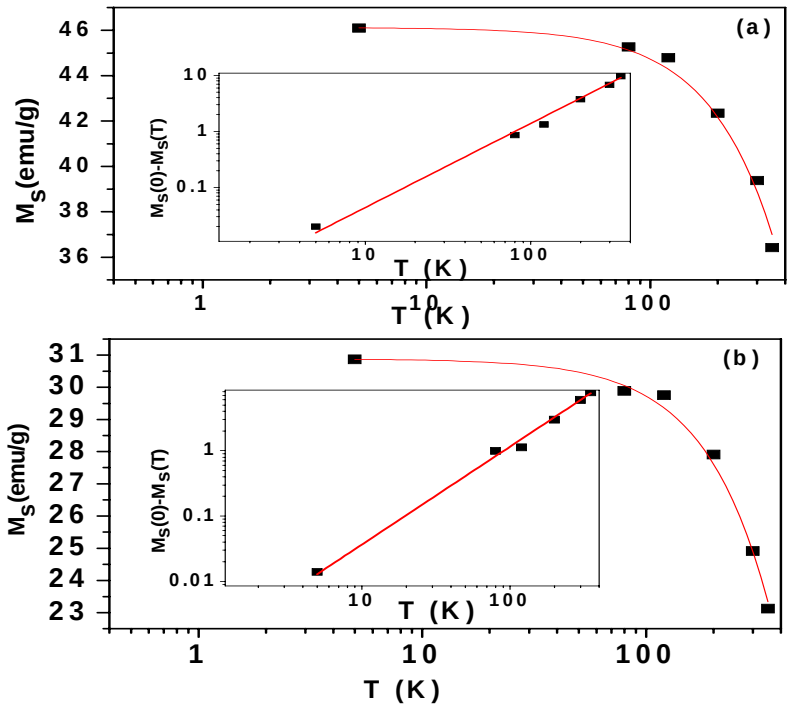

Figure 6.17 *Semilogarithmic plot of the experimental variation of $M_s(T)$ and the core saturation (full line) of nano samples (a) N_1 (b) N_2. Inset shows the depression of the core magnetization $M_s(0)-M_s(T)$ for nano samples in a double logarithmic representation*

In order to compensate the nonsaturation of magnetization for nano N_3, N_4 and N_5 samples, a correction is made replacing $M_s(T)$ by $M_s(T)/\{L[\xi(T)]\}$, where $L(\xi(T)) = \coth(\mu H/kT) - (kT/\mu H)$ is calculated at each temperature, by using the value of mean magnetic moment $<\mu>$. This leads to $M_s(0)$ values as 35.38, 31.24, 38.5 emu/g for N_3, N_4 and N_5 samples respectively. On the contrary, for these nano samples, the extra surface

contribution appears below 80 K (Figure 6.18). The straight lines (T ≥ 80 K) clearly lead to smaller slope and larger values of b (Table 6.3).

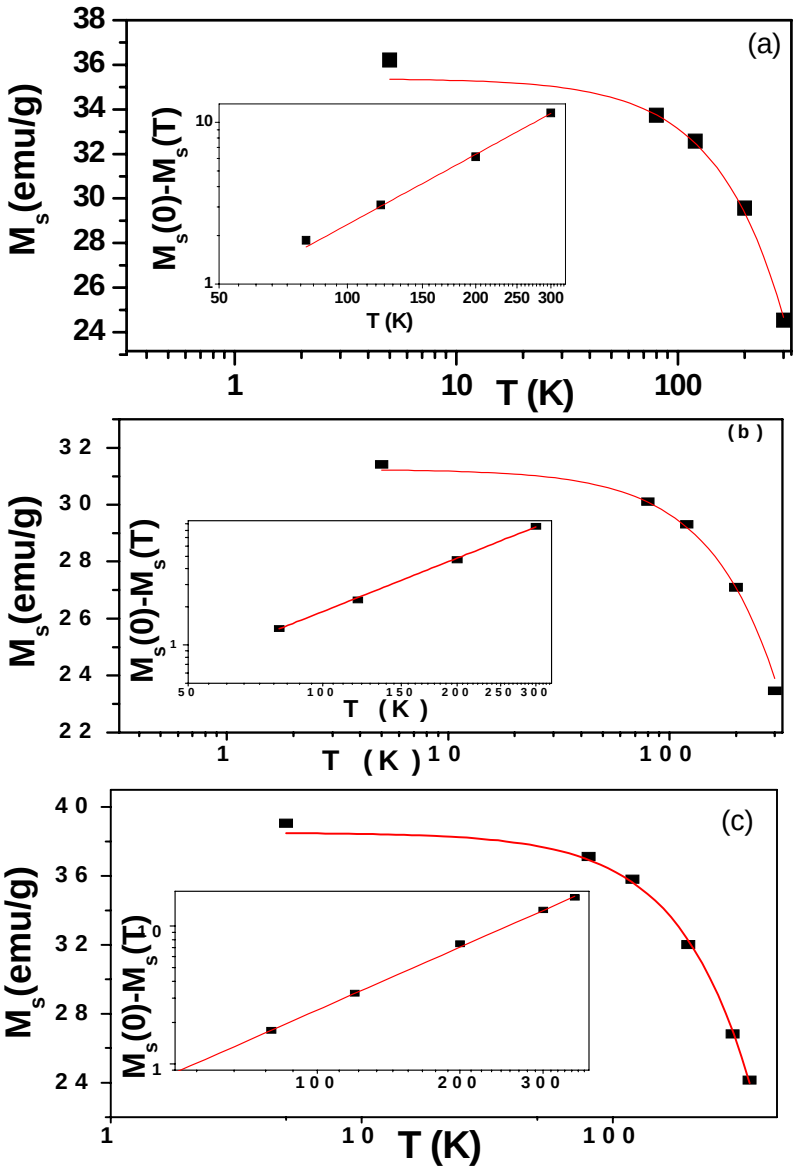

Figure 6.18 *Semilogarithmic plot of the experimental variation of $M_s(T)$ and the core saturation (full line) of nano samples (a) N_3 (b) N_4 (c) N_5. Inset shows the depression of the core magnetization $M_s(0)-M_s(T)$ for nano samples in a double logarithmic representation*

Table 6.3 $M_s(0)$: saturation magnetization of the nanoparticle core extrapolated at $T=0$; α: the temperature exponent obtained from a fit of $M_s(0)-M_s(T)$ to eqn. (6.2), and *b*: Bloch constant calculated for our samples using eqn. (6.2).

Sample	M_s (0) (emu/g)	α	b x 10^{-5} ($K^{-3/2}$)
S_1	-	1.50	6.01
S_2	-	1.50	7.20
S_3	-	1.50	9.10
N_1	-	1.50	3.10
N_2	-	1.50	4.12
N_3	35.38	1.42	9.21
N_4	31.24	1.40	9.23
N_5	38.50	1.40	10.00

The qualitative theoretical expectation is that the reduced coordination at the surface will cause the spins at the surface to be more susceptible to thermal excitation, which leads to larger magnetization temperature dependencies. This qualitative expectation is borne out by our data. Since reduced coordination is a factor, it follows that the nature of the coordination is also important, and this is also supported by different dependencies of the Bloch parameters with size.

For N_3, N_4 and N_5 samples the b values are larger than the corresponding bulk ones. In case of N_3, N_4 and N_5 samples the observed size dependence of b can be related to the existence of a rather important contribution in ferrite nanoparticles, coming from surface canted spins poorly correlated to the monodomain core. Some authors attributed this feature to increased interactions among the neighboring spins and structural deviation from the thermodynamically stable one in terms of cation distribution. This deviation of α from 1.5 is usually associated with the structural disorder increase with particle size reduction. The N_3, N_4 and N_5 samples exhibit the lower diameter, the higher degree of cationic inversion and hence higher b value.

In conclusion it appears that M (T) behavior is richly dependent on size, interface, and the magnetic behavior. Despite this complexity, the form of Bloch law continues to hold.

6.2.6 AC susceptibility measurements

In order to better understand the spin dynamics, we have also investigated the temperature dependence of the real χ'(T) and imaginary parts χ'' (T) of ac susceptibility measurements for nano N_3, N_4 and N_5 samples. The shift of T_B per decade of f (Table 6.6) is slightly less than the typical value of 0.1 for noninteracting superparamagnetic clusters. We have tried to fit these data using the Neel–Arrhenius (NA) relation eqn. (6.3). To confirm the validity of the Neel–Arrhenius relation, we first plot lnτ versus $1/T_B$ for nano system (Figure 6.19). From the fitting, we have found an unphysically small value of relaxation time ~ 10^{-28}-10^{-38} s in comparison to 10^{-13} s. This leads us to conclude

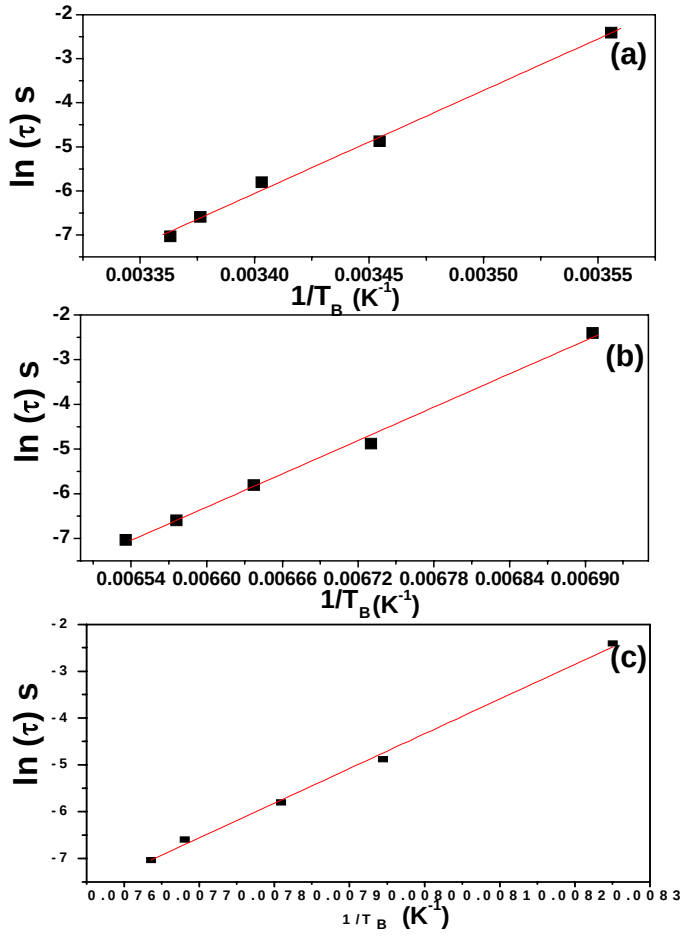

Figure 6.19 *Logarithm of the measuring frequency as a function of the reciprocal of the temperature of peak for nano samples (a) N_3 (b) N_4 (c) N_5*

that the Neel–Arrhenius (NA) relation is not valid and there exist strong interactions among these nanoparticle systems [25], consistent with the results obtained from the dc magnetization data.

As a result, we have tried to fit these data using the Vogel–Fulcher (VG) law (eqn. 6.4). From the fitting (Figure 6.20), we have found value of relaxation time, τ_0~ 10^{-12} s (Table 6.4). The finite value of T_0, again suggests interactions between particles

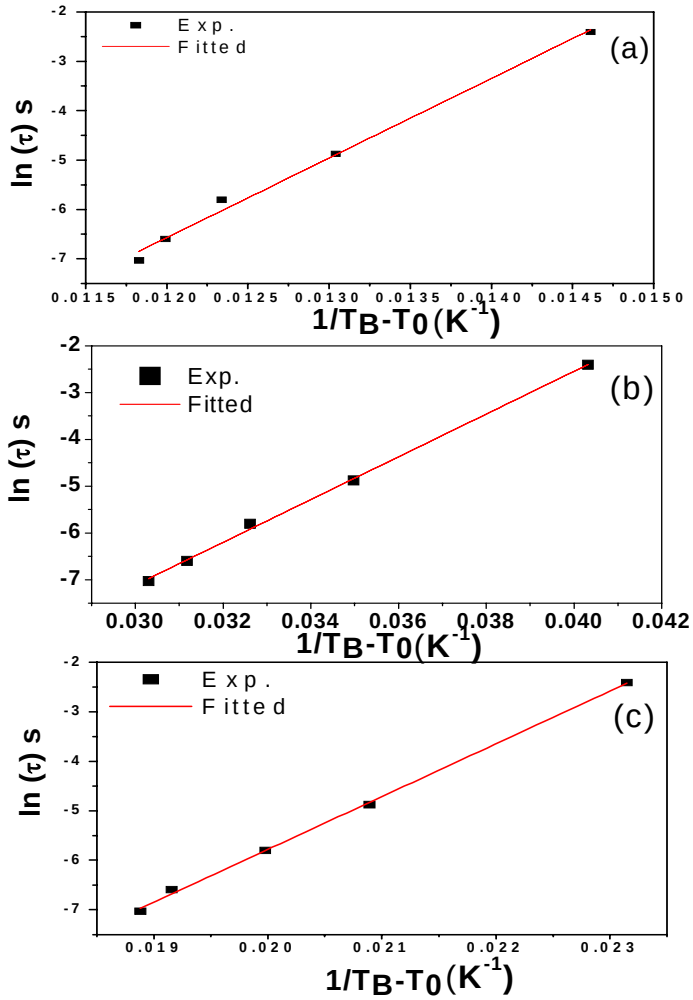

Figure 6.20 *Logarithm of the measuring frequency as a function of the reciprocal of the difference between the temperature of peak and T_0 for nano samples (a) N_3 (b) N_4 (c) N_5*

via grain boundary spins. In an external magnetic field, the energy barrier is given by $E_A = K_{eff}V$, where K_{eff} is an effective magnetic anisotropy constant and V is the particle

volume. By using the average particle size calculated from X-ray diffraction data, the values of K_{eff} for nanosamples are calculated (Table 6.4). The values are one order of magnitude larger than K value (~6 x 10^4 erg cm^{-3}) for bulk nickel ferrite. Evidently, nickel-zinc-indium ferrite nanoparticles exhibit large magnetocrystalline anisotropy. This is an expected behavior of nanosized particles, where the surface contribution is expected to enhance the magnetic anisotropy constant.

Table 6.4 Value of relaxation time (τ_0), anisotropy energy (E_A), effective magnetic anisotropy constant (K_{eff}) and value of T_0 obtained after fitting in eqn. (6.4).

Sample	Φ	τ_0 (10^{-12} s)	E_A (10^{-14} erg)	T_0 (K)	K_{eff} (10^5erg/cm^3)
N_3	0.01	5.49	9.66	212±0.30	2.80
N_4	0.01	9.05	6.30	120±0.20	2.10
N_5	0.01	1.60	14.7	78±0.40	10.70

Conclusion

Magnetic investigation appears a powerful tool to investigate the spin dynamics and magnetic properties of nickel-zinc ferrite particles. The narrow divergence of ZFC and FC curves for the bulk samples in comparison to nano samples indicate the narrow particle size distribution in the annealed samples which agrees with the grain size obtained from X-ray diffraction pattern and as well as from transmission electron microscopy images. Annealed samples exhibit promising properties as saturation magnetization close to bulk samples. The magnetic properties are strongly influenced by the reverse micelle processing: the saturation magnetization of nano nickel-zinc ferrite particles take a value 30.15 emu/g, which is about 62 % lower than 79.91emu/g for bulk sample. Indium ions were found to prefer the tetrahedral sublattice for small concentration ($Ni_{0.58}Zn_{0.42}In_{0.1}Fe_{1.9}O_4$, 10 %), while with further increase in concentration some of the ions partially occupy octahedral sites. Therefore, magnetic properties increase by doping 10 % indium ions in nickel-zinc ferrite particles. Sample $Ni_{0.58}Zn_{0.42}In_{0.1}Fe_{1.9}O_4$ exhibits saturation magnetization close to that of the bulk sample which shows the applicability of this sample for magnetic storage data. Nano

$Ni_{0.58}Zn_{0.42}In_{0.1}Fe_{1.9}O_4$ sample having average particle size in the range 15-25 nm attain saturation magnetization and exhibit ferromagnetic coupling at room temperature. This behavior is promising if such materials are to be used in technological applications.

Nano sample ($Ni_{0.58}Zn_{0.42}In_{0.3}Fe_{1.7}O_4$) with 30 % indium doping shows promising properties with enhanced saturation magnetization in comparison to nano $Ni_{0.58}Zn_{0.42}In_{0.1}Fe_{1.9}O_4$ (N_3) and $Ni_{0.58}Zn_{0.42}In_{0.2}Fe_{1.8}O_4$ (N_4) samples. The nano $Ni_{0.58}Zn_{0.42}In_{0.3}Fe_{1.7}O_4$ particles attain properties similar to that of bulk after heat treatment, even the particle size is in nanoscale.

The magnetic behavior of nickel-zinc-indium ferrite samples such as the blocking temperature and coercivity are unambiguously correlated with the particle size. The squareness ratio M_R/M_s has been found to be too small (< 0.5), which supported the presence of strong interactions in these nanoparticle systems.

For annealed samples the value of α and b are in good agreement with the expected Bloch behavior for bulk samples, while nano $Ni_{0.58}Zn_{0.42}In_{0.1}Fe_{1.9}O_4$ (N_3), $Ni_{0.58}Zn_{0.42}In_{0.2}Fe_{1.8}O_4$ (N_4) and $Ni_{0.58}Zn_{0.42}In_{0.3}Fe_{1.7}O_4$ (N_5) samples present a significant deviation from the Bloch law. We ascribe it to surface disorder and interactions among the nanoparticles. Interactions among the nanoparticles are also well described by the Vogel–Fulcher law.

The three observations in nano samples viz., reduction in saturation magnetization, enhancement in magnetic anisotropy constant and deviation of Bloch's law clearly indicates that outside a core of ordered moments, there exists a surface layer which is in a state of frozen disorder.

From the data it can be concluded that magnetic properties of nickel-zinc-indium ferrite particles are strongly influenced by the size of the particles and by surface defects. These studies will surely facilitate the understanding and controlling of the magnetic properties of nanoparticles.

To our knowledge, this is the first report which highlights the magnetic properties of nickel-zinc-indium ferrite nanoparticles obtained by reverse micelle technique and annealed nano nickel-zinc-indium ferrite samples at high temperature. This approach offers several advantages because of possible high-temperature application of reverse micelle synthesized ferrites. The changes observed in the magnetic properties of particles

with increase in particle size suggest that this could be a useful way to design novel magnetic materials.

References

[1] Ding J., Reylond T., Miao W. F., McCormick P. G. and Street R. *Appl. Phys. Lett.* **1994**, 65, 7074.

[2] Ding J., Miao W. F., Street R. and McCormick P. G. *J. Alloys Compd.* **1998**, 281, 32.

[3] Martinez B., Obradors T., Balcell LI., Rounanet A. and Monty C. *Phys. Rev. Lett.* **1998**, 80, 181.

[4] Lee Penn R. and Banfield J. F. *Science* **1988**, 281, 969.

[5] Banfield J. F., Welch S. A., Zhang H., Ebert T. T. and Lee P. R. *Science* **2000**, 289, 751.

[6] Mendes P. M., Chen Y., Palmer R. E., Nikitin K., Fitzmaurice D. and Preece J. A. *J. Phys.: Condens. Matter* **2003**, 15, S3047.

[7] Bajpaians A. and Banerjee A. *Rev. Sci. Instum* **1999**, 68, 4075.

[8] Cannas C., Concas G., Gatteeschi D., Falqui A., Musinu A., Piccaluga G., Sangregorio C. and Spano G. *J. Phys. Chem. Chem.* **2001**, 3, 832.

[9] Chen Qi and Zhang Z. J. *Appl. Phys. Lett.* **1998**, 73, 3156.

[10] Bitoh T., Ohba K., Takamatsu M., Shirane T. and Hikazawa S. *J. Phys. Soc. Japan* **1995**, 64, 1305.

[11] Mamiya H., Nakatani I. and Furubayashi T. *Phys. Rev. Lett.* **1998**, 80*,* 177.

[12] Battle X., Garcia del M. M. and Labarta A. *Phys. Rev.* B **1997**, 55*,* 644.

[13] Thakur S., Katyal S. C. and Singh M. *J. Magn. Magn. Mater.* **2009**, 321, 1.

[14] Rondinone A. J., Samia A. C. S. and Zhang Z. J. *J. Phys. Chem. B* **1999**, 103, 6876.

[15] Smith J. and Wijn H. P. J. *Ferrites* Amsterdam, Philips library, **1961**.

[16] Oliver S. A., Harris V. G., Hamdeh H. H. and Ho J. C. *Appl. Phys. Lett.* **2000**, 76, 2761.

[17] Zheng M., Wu X. C., Zou B. S. and Wang Y. J. *J. Magn. Magn. Mater.* **1998**, 183, 152.

[18] Kodama R. H. *J. Magn. Magn. Mater*. **1999**, 200, 359.

[19] Hendriksen P. V., Linderoth S. and Lingard P-A. *J. Magn. Magn. Mater.* **1992**, 104-107, 1577.

[20] Didukh P., Greneche J. M., Slawska-Waniewska A., Fanin P. C. and Casas L. *J. Magn. Magn. Mater*. **2002**, 242-245, 613.

[21] Hendriksen P. V., Linderoth S. and Lingard P-A. *J. Phys.: Condens. Matter.* **1993**, 5, 5675.

[22] Aquino R., Depeyrot J., Sousa M. H., Tourinho F. A., Dubois E. and Perzynski R. *Phys. Rev. B* **2005**, 72, 184435.

[23] Chakravorty D., Banerjee S., Pal M., Brahma P., Roy S., Roy B. and Das D. *Frontiers in Material Physics Vol. 1* New Delhi, Allied publishers, **2001**.

[24] Ammar S., Jouini N., Fiévet F., Beji Z., Smiri Leila., Moliné P., Danot M. and Grenéche Jean-Marc. *J. Phys.: Condens. Matter* **2006**, 18, 9055.

[25] Puri R. K., Singh M. and Sud S. P. *J. Mater. Sci.* **1994**, 29, 2182.

[26] Linderoth S., Balcells L., Laborta A., Tejada J., Hendriksen P. V. and Sethi S. A. *J. Magn. Magn. Mater.* **1993**, 124, 269.

[27] Roy S., Dubenko I., Edorh D. D. and Ali N. *J. Appl. Phys.* **2004**, 96, 1202.

[28] Cullity B. D *Introduction to Magnetic Materials* New York, Addison-Wesley, **1972**.

[29] Wernsdorfer W., Orozco E. B., Hasselbach K., Benoit A., Barbara B., Demoncy N., Loiseau A., Pascard H. and Mailly D. *Phys. Rev. Lett.* **1997**, 78, 1791.

[30] Hendriksen P. V., Linderoth S. and Lindgard P-A. *Phys. Rev. B* **1993**, 48, 7259.

[31] Dormann J. L., Fiorani D. and Tronc E. *Adv. Chem. Phys.* **1997**, 98, 326.

[32] Toro J. A. de, Lopez de la T. M. A., Riveiro J. M., Puche R. S., Gomez-Herrero A. and Otero-Diaz L. C. *Phys. Rev. B* **1999**, 60, 918.

[33] Goya G. F. *IEEE Trans. Magn.* **2002**, 38, 2610.

[34] Toro J. A. de, Lopez de la T. M. A., Arranz M. A., Riveiro J. M., Marinez J. L., Palade P. and Filoti G. *Phys. Rev.* B **2001**, 64, 094438.

[35] Mydosh A. *Spin Glasses: An Experimental Introduction* London, Taylor and Francis, **1993**.

[36] Shtrikman S. and Wohlfarth E. P. *Phys. Lett.* A **1981**, 85, 467.

[37] Morrish A. H. *The Physical Principles of Magnetism* New York, Wiley, **1965**.

[38] Pal M., Brahma P., Chakravorty D., Bhattacharyya D. and Maiti H. S. *J. Magn.*

Magn. Mater. **1996**, 164, 256.

[39] Mukherjee S., Ranganathan R., Anil Kumar P. S., and Joy P. A. *Phys. Rev. B* **1996**, 54, 9267.

[40] Stoner E. C. and Wohlfarth E. P. *IEEE Tran. Magn.* **1991**, 27, 3475.

[41] Chkoundali S., Ammar S., Jouini N., Fiévet F., Molinié P., Danot M., Villain F. and Grenéche J-M. *J. Phys.: Condens. Matter* **2004**, 16**,** 4357.

[42] Neel L. *Ann. Phys.* **1948**, 3,137.

[43] Bhowmik R. N., Ranganathan R., Sarkar S., Bansal C. and Nagarajan R. *Phys. Rev. B* **2003**, 68, 134433.

[44] Kodama R. H., Berkowitz A. E., McNiff E. J. and Foner S. *Phys. Rev. Lett.* **1996**, 77, 394

[45] Parker F. T., Spada F. E., Cox T. J. and Berkowitz A. E. *J. Appl. Phys.* **1995**, 77 5833.

[46] Lin D., Nunez A. C., Majkrzak C. F. and Berkowitz A. E. *J. Magn. Magn. Mater.* **1995**, 45, 343

[47] Coey J. M. D. *Phys. Rev. Lett.* **1971**, 27, 1140

[48] Coey J. M. D. *Can. J. Phys.* **1987**, 65, 1210

[49] Berkowitz A. E., Lahut J. A., Jacobs I. S., Levinson L. M. and Forester D. W. *Phys. Rev. Lett.* **1975**, 34, 594.

[50] Berkowitz A. E., Lahut J. A., Jacobs I. S., Levinson L. M. and Forester D. W. *AIP Conf. Proc.* **1971**, 10, 966.

[51] Berkowitz A. E., Lahut J. A., Jacobs I. S., Levinson L. M. and Forester D. W. *IEEE Trans. Magn.* **1980**, 16**,** 184.

[52] Morrish A. H., Haneda K. and Schurer P. J. *J. Physique Coll.* **1976***,* 37, C6 301

[53] Haneda K. and Morrish A. H. *Surf. Sci.* **1978**, 77, 584.

[54] Ochi T., Watanabe K., Kiyama M., Shinjo T., Bando Y. and Takada T. *J. Phys. Soc. Japan* **1981**, 50, 2777.

[55] Morrish A. H. and Haneda K. *J. Appl. Phys.* **1981**, 52, 2496.

[56] Okada T., Sekizawa H., Ambe F., Ambe S. and Yamadaya T. *J. Magn. Magn. Mater.* **1983**, 31–34, 105.

[57] Morrish A. H. and Haneda K. *J. Magn. Magn. Mater.* **1983**, 35, 105.

[58] Pankhurst Q. A. and Pollard R. J. *Phys. Rev. Lett.* **1991**, 67, 248.

[59] Parker F. T., Foster M. W., Margulies D. T. and Berkowitz A. E. *Phys. Rev. B* **1993**, 47, 7885.

[60] Morales M. P., Serna C. J., Bødker F. and Mørup S. *J. Phys.: Condens. Matter* **1997**, 9, 5461.

[61] Chundnovsky E. M. and Gunther L. *Phys. Rev. Lett*. **1998**, 60, 661.

[62] Caizer C. and Stefanescu M. *J. Phys. D: Appl. Phys.* **2002**, 35, 3035.

[63] Hamdeh H. H., Ho J. C., Oliver S. A., Willey R. J., Oliveri G. and Busca G. *J. Appl. Phys.* **1997**, 81, 1851.

[64] Chikazumi S. *Physics of Ferromagnetism* 2nd ed. New York, Oxford University Press, **1997**, pp. 510.

CHAPTER 7

SUMMARY AND FUTURE PLANS

This work demonstrates the versatility of the reverse micelle technique as a reaction control system for producing nanoparticles. A significant portion of this research involved elucidation of the effect of altering the reaction parameters on subsequent the nanoparticle product. In these reaction systems in which metal cations form a metal oxide framework, the primary lesson is the importance of controlling the presence of ambient oxygen. In ferrite systems each of the metal cations can form other stable oxide compounds, and therefore limiting the presence of excess oxygen, limits the progression of competing reaction pathways. The benefits of having developed a good understanding of the reverse micelle reaction parameters can be seen in the ease at which the process was adapted to the nickel-zinc ferrite nanoparticles and indium doped nickel-zinc ferrite nanoparticles.

Work presented in this thesis describes studies on structural, magnetic and Mössbauer spectroscopy characterization of nano and bulk samples of pure nickel-zinc ferrite having basic composition $Ni_{0.58}Zn_{0.42}Fe_2O_4$ and indium doped nickel-zinc ferrite particles ($Ni_{0.58}Zn_{0.42}In_xFe_{2-x}O_4$, x = 0.1, 0.2, 0.3) synthesized via reverse micelle technique. Bulk samples in this study are prepared by annealing the reverse micelle synthesized nanoparticles at high temperature 1473 K. Prepared bulk and different size nanoparticles have been characterized using X-ray diffraction (XRD), transmission electron microscopy (TEM) and Fourier transform infrared (FTIR) spectroscopy studies. ^{57}Fe Mössbauer measurements have been made in the temperature range from 5-300 K for determining the cation distribution and hyperfine parameters. The cation distribution of nano and bulk particles has been studied by using in-field Mössbauer spectroscopy. The magnetic behavior of the compositions has been studied using vibrating sample magnetometer (VSM) and superconducting quantum interference device (SQUID) magnetometer. To study the dynamic behavior of nanoparticles, ac susceptibility measurements have been performed on a home made susceptometer.

7.1 Summary and important findings

Reverse micelle technique has been found to be appropriate for the synthesis of nanostructured nickel-zinc ferrite and nickel-zinc-indium ferrite particles with uniform size. X-ray diffraction studies suggest the formation of nano samples via reverse micelle

technique and the persistence of the spinel phase upto 1473 K. Transmission electron microscopy shows that the nano samples synthesized via reverse micelle technique have spherical size and narrow particle size distribution, while in case of annealed samples monodisperse particles are obtained. Fourier transform infrared spectroscopy spectra confirmed that the structure remains cubic spinel after indium substitution. The carbonization of the surfactant at high temperature results in extra bands in bulk samples in comparison to nano samples.

The simultaneous application of Mössbauer spectroscopy and magnetic investigation appears a powerful tool to investigate the structure, spin dynamics and magnetic properties of nanoparticles. The comparative in-field Mössbauer study of the bulk and nanosized particles enables us to separate the surface effects from the bulk effects in nanoparticles. Due to the ability of ^{57}Fe Mössbauer spectroscopy to reveal the noncollinearity of the spin arrangement and to discriminate between probe nuclei in equivalent crystallographic sites provided by the spinel structure, valuable insight into a local disorder in reverse micelle synthesized nanoparticles was obtained. It, thus, was revealed that the surface shell of nanoparticles is structurally and magnetically disordered due to the nearly random distribution of cations and the canted spin arrangement. This is in contrast to the ordered core of the nanoparticles, which exhibits an inverse spinel structure with a collinear spin alignment like bulk particles. In case of nickel-zinc-indium ferrite bulk samples, indium ions were found to prefer the tetrahedral sublattice for small concentration (10 %), while with further increase in concentration some of the ions partially occupy octahedral sites. Mössbauer study on these nano system shows that the cation distribution not only depends on the particle size but also on the preparation route. The nonequilibrium cation distribution and the canted spin arrangement resulting from the reverse micelle synthesis route are metastable; that is, during the annealing process, they relax toward their equilibrium configuration. Thus, on heating, the reverse micelle synthesized nano samples have relaxed to a magnetic state that is similar to the bulk one.

Quantitative information on the distribution of local magnetic field, ions and on the canted spin arrangement within the nanoparticles provided by Mössbauer spectroscopy is complemented by investigations of their magnetic behavior on the macroscopic scale. The magnetic properties are strongly influenced by the reverse

micelle processing: the saturation magnetizations of nanosamples are lower than bulk samples. Magnetic properties of nickel-zinc-indium ferrite particles are strongly influenced by the size of the particles and by surface defects. Magnetic properties increase by doping 10 % indium ions in nickel-zinc ferrite particles in accordance with Mössbauer study. Nano $Ni_{0.58}Zn_{0.42}In_{0.1}Fe_{1.9}O_4$ sample having average particle size in the range 15-25 nm attain saturation magnetization and exhibit ferromagnetic coupling at room temperature. This behavior is promising if such materials are to be used in technological applications.

Nano sample ($Ni_{0.58}Zn_{0.42}In_{0.3}Fe_{1.7}O_4$) with 30 % indium doping shows promising properties with enhanced saturation magnetization in comparison to nano $Ni_{0.58}Zn_{0.42}In_{0.1}Fe_{1.9}O_4$ (N_3) and $Ni_{0.58}Zn_{0.42}In_{0.2}Fe_{1.8}O_4$ (N_4) samples. The nano $Ni_{0.58}Zn_{0.42}In_{0.3}Fe_{1.7}O_4$ (N_5) particles attain properties similar to that of bulk after heat treatment, even the particle size is in nanoscale.

The thickness of the surface shell obtained for nanosamples from magnetization experiments are found to be in agreement with that estimated from Mössbauer measurements.

For annealed samples the value of Bloch exponent (α) and Bloch constant (b) are in good agreement with the expected Bloch behavior for bulk samples, while nano $Ni_{0.58}Zn_{0.42}In_{0.1}Fe_{1.9}O_4$ (N_3), $Ni_{0.58}Zn_{0.42}In_{0.2}Fe_{1.8}O_4$ (N_4) and $Ni_{0.58}Zn_{0.42}In_{0.3}Fe_{1.7}O_4$ (N_5) samples present a significant deviation from the Bloch law. We ascribe it to surface disorder and interactions among the nanoparticles. Interactions among the nanoparticles are also well described by the Vogel–Fulcher law.

The three observations viz., reduction in saturation magnetization in the nanoparticle sample, enhancement in magnetic anisotropy constant and deviation of Bloch's law for nano samples clearly indicates that outside a core of ordered moments, there exists a surface layer which is in a state of frozen disorder.

To our knowledge, this is the first report which highlights the properties of indium doped nickel-zinc ferrite particles obtained by reverse micelle technique. This approach offers several advantages because of possible high-temperature application of reverse micelle synthesized ferrites. This is the first study where a core-shell structure of nanoparticles is

obtained by in-field Mössbauer spectroscopy using NORMOSS software. The changes observed in the magnetic properties of particles with increase in particle size suggest that this could be a useful way to design novel magnetic materials.

7.2 Future suggestions

- In the future attempts, this technique could develop a tool/synthesis procedure to obtain nanoparticles with higher yield in smaller time frames. This means these reaction methodologies can be utilized to produce material in sufficient quantity to be used in bulk sized amounts.
- Further, the measurements such as high resolution transmission electron microscopy (HRTEM) would be very helpful to enhance the validity of the conclusions derived and also to understand the core-shell structure of these nano systems more clearly.
- In this thesis, structural and magnetic properties are studied in detail. It would be interesting to study the effect of indium concentration on electrical and dielectric properties of nickel-zinc ferrite particles.
- $Ni_{0.58}Zn_{0.42}Fe_2O_4$ sample shows its application in high frequency region. At room temperature the $Ni_{0.58}Zn_{0.42}Fe_2O_4$ sample exhibits superparamagnetic properties which can be suitable in biomedicine and biotechnology as contrast agents for magnetic resonance imaging (MRI) and as drug delivery carriers. It would be interesting to study the biomedical application of the prepared nanoferrites.